UNIVERZITA JANA EVANGELISTY PURKYNĚ

MASARYKOVA UNIVERZITA

PŘÍRODOVĚDECKÁ FAKULTA

HABILITAČNÍ PRÁCE

STUDIUM SLUNEČNÍCH ERUPCÍ
MODELY A POZOROVÁNÍ

Michal Varady

Ústí nad Labem, 2014

UNIVERZITA JANA EVANGELISTY PURKYNĚ

MASARYKOVA UNIVERZITA

PŘÍRODOVĚDECKÁ FAKULTA

HABILITAČNÍ PRÁCE

STUDIUM SLUNEČNÍCH ERUPCÍ
MODELY A POZOROVÁNÍ

RNDr. Michal Varady, Ph.D.

Ústí nad Labem, srpen 2014

Abstract The habilitation thesis is devoted to studies of solar flares both theoreticaly, using the means of computer modelling, and observationally. The theoretical part is devoted to the modelling of various aspects of solar flares using several approaches. They combine the test-particle method to simulate the high-energy non-thermal particle transport, scattering and energy dissipation, hydrodynamics to calculate the dynamic response of flaring chromosphere combined with the non-LTE radiative transfer – radiation hydrodynamics, calculating the profiles of selected optically thick spectral lines. In this part we also present modelling of various aspects and new ideas concerning the high-energy non-thermal particle transport from the acceleration to the thermalisation site, resulting flare heating and corresponding properties of the non-thermal hard X-ray emission emmanating from the chromosphere thick-target regions. The results are discused in context of contemporary flare models. In the observational part of the habilitation we present results of plasma diagnostics in a post-flare loop system and observational signs of ongoing reconnection of magnetic fields in the solar corona. The habilitation thesis consists of an introduction into the solar flare physics and a commented collection of 14 papers which are devoted to the topics mentioned above.

Abstrakt Habilitační práce se zabývá studiem slunečních erupcí jak teoreticky, s využitím metodiky počítačového modelování, tak zpracováním pozorovacích dat. Teoretická část je věnována modelování různých aspektů slunečních erupcí s využitím několika metod. V těchto modelech jsou zkombinovány metody využívající testovací částice pro simulaci transportu, rozptylu a disipace kinetické energie vysokoenergetických netermálních částic v okolním plazmatu, hydrodynamiku k popisu dynamické odezvy erupční chromosféry zkombinovanou s non-LTE přenosem záření – zářivá hydrodynamika, modelující profily vybraných opticky tlustých spektrálních čar. V této části rovněž prezentujeme modelování některých aspektů a nových myšlenek, které se týkají transportu vysokoenergetických netermálních částic z místa své akcelerace do oblasti termalizace, výsledného erupčního ohřevu a odpovídajících vlastností tvrdé netermální rentgenovské emise vystupující z oblastí chromosférického tlustého terče. Výsledky jsou diskutovány ve světle současných erupčních modelů. V observační části se zabýváme diagnostikou plazmatu v systému poerupčních smyček a observačními znaky probíhající rekonexe magnetických polí ve sluneční koróně. Tuto habilitační práce tvoří úvod do problematiky slunečních erupcí a komentovaný soubor 14-ti publikovaných prací na výše uvedená témata.

Obsah

Předmluva

Slunce, jakožto Zemi nejbližší hvězda, je prakticky jediným zdrojem energie pro ekosystém naší planety. Slunce zdaleka není klidnou hvězdou. Díky existenci časově proměnných, vysoce strukturovaných magnetických polí, jež prostupují žhavé plazma sluneční atmosféry, představuje atmosféra Slunce fascinující dynamické prostředí v těsné blízkosti Země. Projevy tohoto prostředí označujeme souhrným termínem sluneční aktivita. Sem zahrnujeme například výrony koronální hmoty, erupce, aktivní protuberance, výskyt rázových a magnetohydrodynamických vln nejrůznějších modů a podobně. Podle současných představ, všechny tyto jevy získávají energii na úkor časově proměnných magnetických polí pronikajících plazmatem sluneční atmosféry.

Díky blízkosti obou těles a typickým hodnotám energií uvolněných ve sluneční atmosféře při velkoškálových jevech, mohou mít projevy sluneční aktivity vážné důsledky nejen ve sluneční atmosféře, ale také v bezprostředním kosmickém okolí Země – v magnetosféře a mohou dokonce, vesměs negativně, ovlivnit technická zařízení instalovaná na zemském povrchu. Dopad těchto jevů je samořejmě amplifikován významem moderních technologií, na nichž je naše současná civilizace závislá. Pro určení míry ovlivnění zemského okolí sluneční činností se relativně nově začal používat termín – kosmické počasí. Toto jsou hlavní důvody stále rostoucího zájmu o pochopení jak naše nejbližší hvězda funguje, jaká je fyzikální podstata energetických jevů ve sluneční atmosféře, jak jsou spouštěny, zda je možné předpovědět kdy nastanou, jak velká energie se při nich uvolní a zda ovlivní naši planetu a její bezprostřední okolí. Tento zájem se odráží v stále rostoucím počtu projektů kosmických misí, které byly a jsou věnovány pozorování Slunce v posledních několika dekádách (GOES, SMM, Yohkoh, SOHO, TRACE, Hinode, RHESSI, SDO, STEREO, IRIS). Tyto kosmické observatoře, z nichž některé nesou dokonce několik přístrojů, od dalekohledů, magnetometrů, spektrometrů, koronografů po detektory částic slunečního větru, nepřetržitě pozorují Slunce bez rušivých vlivů zemské atmosféry. Kosmická pozorování Slunce jsou pak zcela nenahraditelná ve spektrálních oborech, kde pozorování nelze uskutečnit z povrchu Země díky neprostupnosti zemské atmosféry pro dané vlnové délky. Ukazuje se, že právě data tohoto druhu jsou zcela klíčová pro pochopení fyzikální podstaty jevů probíhajících ve sluneční atmosféře. Jedná se zejména pozorování na krátkých vlnových délkách, tedy v oblastech γ-záření, tvrdého a měkkého rentgenového záření, extrémně ultrafialového záření a nově také blízkého UV záření.

Předkládaná habilitační práce je věnována studiu nejenergetičtějších projevů sluneční aktivity – slunečním erupcím a to jak s využitím numerických simulací, tak i s použitím pozorovacích dat v různých spektrálních oborech získaných jak z kosmických, tak z pozemských slunečních observatoří. Těžiště práce je v modelování vybraných procesů ve slunečních erupcích. Sluneční erupce jsou nesmírně komplexní jevy, kde hrají fundamentální roli velmi různorodé procesy probíhající na všech prostorových škálách. To je důvodem proč dodnes neexistují počítačové simulace, které by modelovaly erupční procesy v celé jejich komplexnosti: od rekonexe magnetických polí v koróně, urychlování častic a jejich transport a termalizaci v chromosféře, přes dynamickou odezvu chromosféry na energii deponovanou netermálními částicemi až po předpověď časově proměnného spektra elektromagnetického záření emitovaného erupčním plazmatem. Místo tohoto všeobjímajícího přístupu se jde cestou modelování individuálních procesů, které jak sluneční komunita věří, hrají v erupcích zásadní roli. Typicky jsou to magnetohydrodynamický přístup pro modelování velkoškálové rekonexe ve sluneční koróně, metody testovacích částic pro modelování urychlování, transportu, rozptylu a disipace kinetické energie svazků částic v erucích. Dále potom hydrodynamika pro popis transportu plazmatu podél magnetických siločar erupčních arkád a non-LTE přenos záření pro modelování spektrálních čar v opticky tlusté erupční chromosféře. Kódy typu particle–in–cell se potom používají pro studium kinetických efektů spojených například s transportem svazků částic plazmatem nebo pro studium rekonexe na mikroskopické úrovni.

V předkládané habilitační práci jsou v úvodní 1. kapitole shrnuta základní fakta o sluneční atmosféře a je představen tzv. „standardní“ model erupcí. V kontextu tohoto modelu jsou pak interpretována typická pozorování erupcí v různých spektrálních oborech. Dále jsou diskutovány některé problémy „standardního“ modelu a představeny jeho modifikace a alternativy. V 2. kapitole komentujeme a uvádíme do kontextu s literaturou práce týkající se modelování procesů ve slunečních erupcích, na jejiž vzniku jsem se podílel. 3. kapitola je věnována pracem, které se týkají zpracování pozorování erupcí. Přílohou habilitační práce jsou kopie 14 prací, na nichž jsem se autorsky podílel a na něž se odkazuji ve 2. a 3. kapitole.

Kapitola 1

Sluneční erupce

1.1 Úvod

První doložené pozorování sluneční erupce je z 1. září 1859, kdy R. C. Carrington a nezávisle R. Hodgson při rutinním zákresu sluneční fotosféry pozorovali v bílém světle poměrně vzácný jev, tzv. bílou erupci (white–light flare) (Carrington 1859; Hodgson 1859), kdy se kontinuum v erupční chromosféře zvýší natolik, že svou intenzitou přezáří okolní fotosféru. S vynálezem a rozvojem úzkopásmových filtrů ve 30. letech 20. století se sluneční erupce rutinně pozorovaly až do 60. let 20 století zejména v chromosférické vodíkové čáře Hα a byly proto po řadu desetiletí považovány za výsostně chromosférické jevy (Švestka 1976). Rozvoj raketové techniky po 2. světové válce umožnil v 60. a hlavně v 70. letech 20. století uskutečnit zcela nová převratná pozorování erupcí žhavého koronálního erupčního plazmatu v rentgenovém a ultrafialovém oboru (Bray et al. 1991). Ta odhalila, že v chromosférických optických čarách pozorujeme pouze velmi malou část erupčního procesu, přičemž klíčové jevy, umožňující správné fyzikální uchopení celého procesu, probíhají v koróně. Pro pozorování větších erupcí v chromosférické čáře Hα je typická časově proměnná tzv. dvoustužková struktura erupce (two-ribbon flare), pro pozorování jejich horké, koronální části v extrémním ultrafialovém oboru (EUV) nebo měkkém rentgenovém oboru (SXR) jsou typické smyčkovité struktury kopírující koronální magnetická pole, které jsou ukotvené ve zjasněných stužkách v chromosféře (viz obr. 1.1).

Sluneční erupce jsou často označovány za největší výbuchy ve sluneční soustavě, při nichž se na časových škálách desítek až stovek sekund uvolní energie až $\sim 10^{25}$ J, a které jsou, ve svých nejextrémnějších případech, pozorovatelné ve všech oborech elektromagnetického spektra, od kilometrových rádiových vln až po γ-záření. Pro sluneční erupce jsou typická zejména rychlá zjasnění integrovaného toku SXR z celého slunečního disku až o 4, v ojedinělých případech i o 5 řádů. Právě maximální dosažená hodnota integrovaného toku SXR ze slunečního disku při erupci se používá jako hlavní kritérum pro klasifikaci třídy erupce (viz obr. 1.2). Důsledky těchto jevů, které se primárně odehrávají ve sluneční atmos-

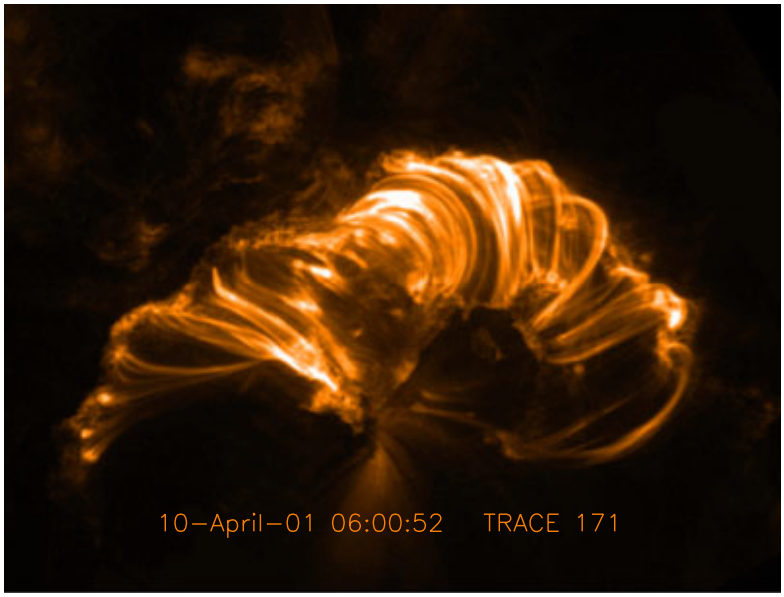

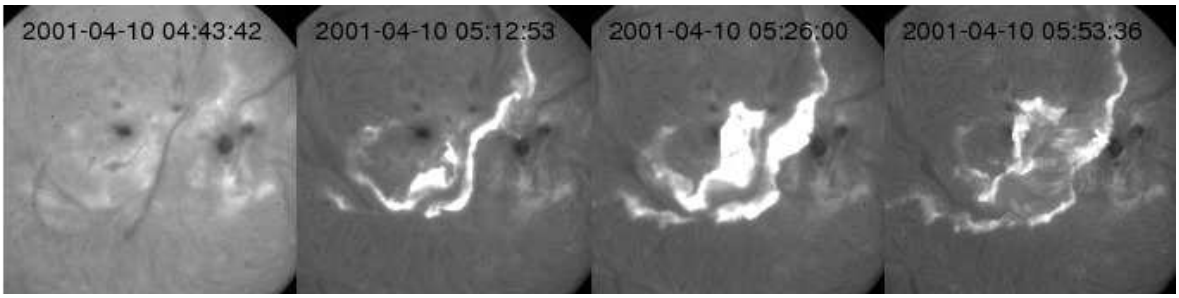

Obrázek 1.1: *Nahoře:* Arkáda horkých erupčních smyček příslušejících erupci třídy X2.3 z 10. dubna, 2010 pozorovaná kosmickým dalekohledem TRACE v kanálu 171 Å – odpovídající teplota $\sim$ 1 MK. *Dole:* Časový vývoj stejné erupce pozorovaný v v chromosférické čáře Hα. Na obrázku je patrná tzv. dvoustužková morfologie erupce (Asai et al. 2012).

féře, mohou mít nezanedbatelný dopad jak v těsném okolí Země, tak i na jejím povrchu a jsou jedním z hlavních iniciátorů proměnnosti tzv. kosmického počasí.

Sluneční erupce jsou nesmírně komplexní jevy zahrnující celou řadu fyzikálně těsně provázaných procesů probíhajících na všech prostorových škálách. Procesy na mikroškálách (např. vlny a nestability v plazmatu) určují transportní koeficienty a atomové procesy (ionizace, populace hladin a podobně) určují vlastnosti vystupujícího záření. Kromě toho zde dochází turbulentní rekonexi magnetických polí a ke vzniku lokalizovaných silných pulzů elektrického pole, které urychluje nabité částice (Bárta et al. 2011b). Na makroškálách s typickými velikostmi desítek až stovek Mm probíhá rekonfigurace globálních magnetických polí, transport vysokoenergetických svazků nabitých částic, depozice energie v oblasti chro-

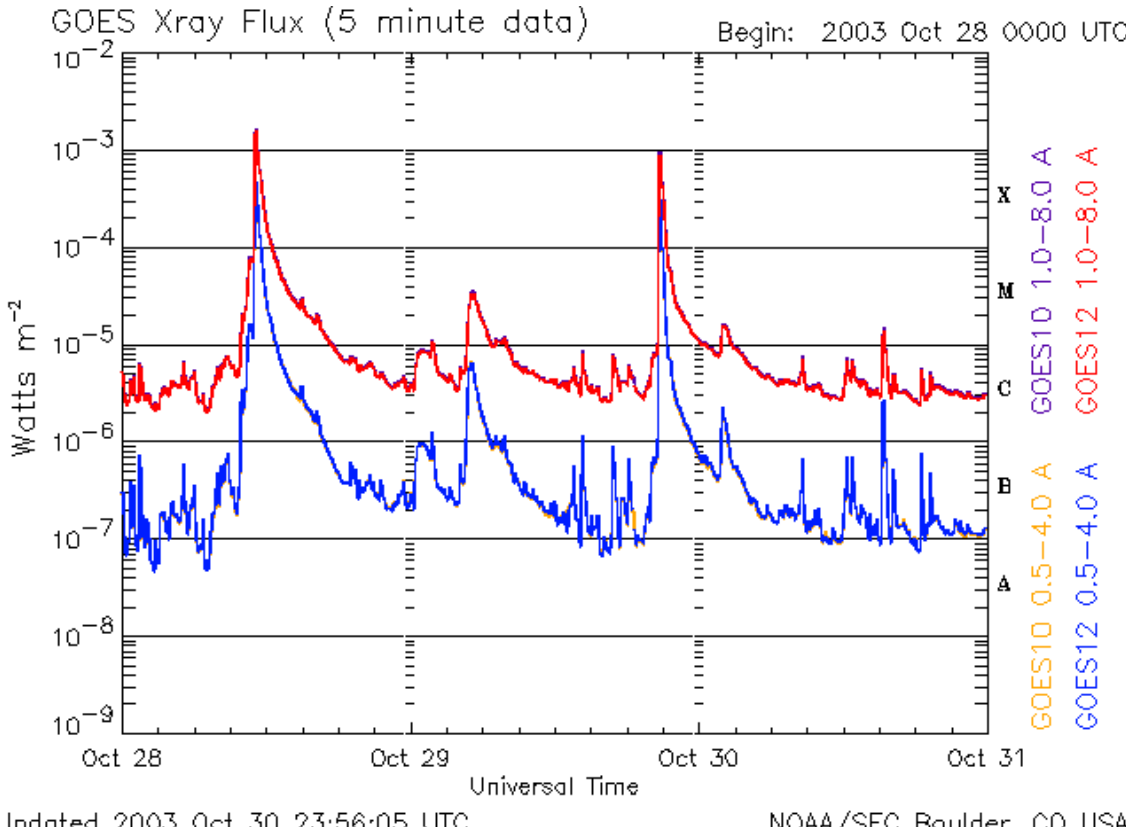

Obrázek 1.2: Typická prudká zjasnění toku měkkého rentgenového záření provázející sluneční erupce na pozorování družic GOES. Maximální tok SXR dosažený při erupci určuje třídu erupce, která se označuje jedním z písmen A, B, C, M, X kódujích řád toku a číslem označující velikost toku. Největší erupci na obrázku odpovídá třída X17.2.

mosférického tlustého terče a transport plazmatu podél magnetických siločar v erupčních smyčkách. Rekonexe globálních magnetických polí erupcí nezřídka ovlivní prakticky celou sluneční atmosféru díky šíření mohutných magnetohydodynamických vln, které lze pozorovat v EUV oboru jako tzv. EIT vlny nebo v optickém oboru jako tzv. Moretonovy vlny (Nitta et al. 2013; Veronig et al. 2011).

V této kapitole nejprve stručně popíšeme strukturu sluneční atmosféry a roli jakou hrají její jednotlivé vrstvy ve slunečních erupcích. Dále budeme diskutovat tzv. „standardní model“ erupcí v kontextu moderních multispekrálních pozorování. Tento model tvoří rámec většiny autorových prací. V závěru se pak budeme věnovat některým otevřeným teoretickým otázkám a problémům současné fyziky erupcí, na něž „standardní model“ není schopen dát uspokojivou odpověď. Zde se omezíme na oblasti, k jejichž poznání se autor této habilitační práce snažil svou dosavadní vědeckou prací přispět.

1.2 Sluneční atmosféra v erupcích

Ve sluneční atmosféře lze identifikovat několik oblastí, které se zásadně liší fyzikálními podmínkami (teplotou, hustotou, plazmovým parametrem β, ionizací), které v nich panují. Vzhledem k tomu, že počáteční podmínkou řady modelů prezentovaných v této práci je právě model sluneční atmosféry, jehož dolní část je dána jedním z modelů publikovaných v práci Vernazza et al. (1981) (viz teplotní profil na obr. 1.3), stručně představíme jednotlivé oblasti sluneční atmosféry, jejich vlastnosti a specifikujeme jaké role hrají v erupcích.

1.2.1 Fotosféra

Sluneční fotosféra (z řeckého slova pro světlo) je oblast, která emituje většinu záření ve viditelném oboru. Fotosféře dominuje plazma s vysokým β, které se mění ze zcela neprůhledného na prakticky průhledné pro viditelné vlnové délky. Přesněji jde o tenkou oblast s tloušťkou ~ 500 km zdola ohraničenou optickou hloubkou $\tau_{5000} = 1$ (pro 5000 Å), které se v modelech sluneční atmosféry přiřazuje výška $h = 0$ km a teplotním minimem. V modelu atmosféry VAL C (Vernazza et al. 1981), který používáme se částicová hustota a teplota fotosféry mění od $\sim 10^{17}$ cm^{-3} a ~ 6200 K v hloubce ~ 0 km do $\sim 10^{15}$ cm^{-3} a ~ 4200 K v teplotním minimu jemuž odpovídá hloubka ~ 500 km. Erupce se ve fotosféře projevují seismickými vlnami, které poměrně nedávno objevili Kosovichev & Zharkova (1998). V poslední době roste počet pozorování seismických vln excitovaných i poměrně malými erupcemi (Donea & Lindsey 2005).

1.2.2 Chromosféra

Chromosféra je vrstva s tloušťkou několika málo Mm. V případě modelů Vernazza et al. (1981) (viz obr. 1.3) je tloušťka chromosféry ~ 2 Mm a je vymezená na jedné straně teplotním minimem a na druhé teplotou přibližně 20 kK, kde se ionizace vodíku mění z prakticky neutrálního plynu na téměř zcela ionizované plazma, β parametr z vysokého na nízký a plazma z vysoce kolizního na téměř bezkolizní. Současně se chromosférické plazma stává směrem ke své horní hranici opticky tenkým v UV, optickém a mm oboru. Pozorování ukazují, že chromosféra je nesmírně nehomogenní a dynamickou oblastí, která zprostředkovává přenos energie pro ohřev koróny (Ayres et al. 2009). Z hlediska erupcí je chromosféra oblastí, kde se termalizují vysokoenergetické svazky částic a v impulzní fázi erupcí je tedy silným zdrojem tvrdého rentgenového záření (HXR). Z pozorování je rovněž známo, že jde o oblast, kde se v erupcích emituje maximum zářivého výkonu a to v optickém, případně blízkém UV oboru (Neidig 1989; Fletcher et al. 2010). Pozorování erupcí v chromosféře dominují data pořízená v optických čarách vodíku (zejména Hα 6562,8 Å a několik dalších čar Balmerovy série) a v jasných optických čarách jiných prvků jako Ca II H 3969,6 Å, K 3968,5 Å a Mg II h 2795 Å, k 2803 Å (Švestka 1976). Vzhledem k tomu, že chromosférické plazma je pro většinu spektrálních čar v optickém oboru opticky tlusté, představuje

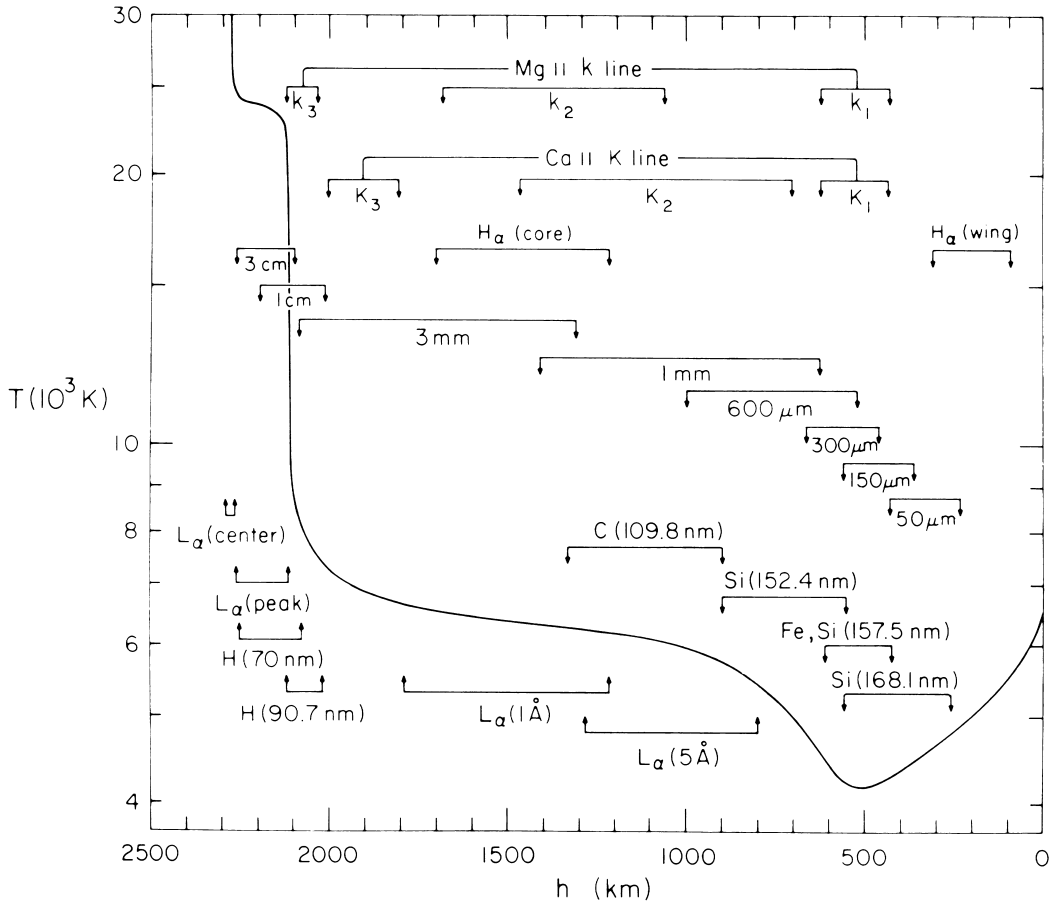

Obrázek 1.3: Teplotní profil sluneční atmosféry podle modelu VAL C (Vernazza et al. 1981). V obrázku jsou znázorněny oblasti formace vybraných spektrálních čar.

jejich modelování, zejména v komplikovaných podmínkách erupcí velmi složitý problém. V poslední době se objevily nové alternativní modely slunečních erupcí, kde chromosféra hraje roli sekundární akcelerační oblasti (Karlický 1995; Fletcher & Hudson 2008; Brown et al. 2009; Varady et al. 2013, 2014).

1.2.3 Přechodová oblast

Je tenká, fyzikálně nesmírně komplikovaná oblast tloušťky pouze několika stovek kilometrů, která odděluje horní chromosféru teploty přibližně 20 kK a korónu s typickými teplotami kolem 2 MK. Vzhledem k tloušťce přechodové oblasti a teplotám plazmatu v chromosféře a koróně tvoří prakticky diskontinuitu v teplotě a jsou pro ni typické veliké gradienty teploty (Mariska 1993). Také tato oblast musí zprostředkovat přenos netepelné energie nutné pro ohřev korony. V přechodové oblasti se tvoří velké množství opticky tenkých a diagnosticky

významných čar zejména v EUV oboru (Mariska 1993). Přechodová oblast v erupcích je oblastí kudy, podle „standardního modelu“, prochází veškeré energie uvolněná v koróně dolů do chromosféry. Vzhledem k velkým teplotním gradientům a malé hustotě plazmatu lze v přechodové oblasti očekávat nemaxwellovská rozdělení energie částic plazmatu (Dzifčáková & Kulinová 2011).

1.2.4 Koróna

Sluneční koróna (Aschwanden 2005) je opět velmi dynamickým a nehomogenním prostředím, kterému dominuje zcela ionizované řídké 10^8–$10^9\,\mathrm{cm}^{-3}$ a žhavé plazma $T \sim 2\,\mathrm{MK}$ s nízkým β. Plazma v koróně je koncentrováno podél magnetických smyček a je opticky tenké prakticky pro všechny vlnové délky. Pozorování koróny dominují data v EUV, SXR a rádiovém oboru, nově se také pozorují slabé koronální HXR, někdy dokonce γ zdroje v prostoru nad arkádami erupčních smyček (Masuda et al. 1994; Krucker et al. 2008a), tedy v místech kde se předpokládá urychlování částic. Z hlediska fyziky erupcí je koróna místem, kde podle standardního modelu dochází k primárnímu uvolnění energie při rekonexi magnetických polí a urychlování částic. Vnější koróna plynule přechází do slunečního větru.

1.3 CSHKP model

Za jakýsi „standardní model“ erupcí se v posledních několika dekádách považuje tzv. CSHKP model. Tento model na základě rekonexe koronálních magnetických velmi názorně vysvětluje vlastnosti erupcí pozorované na velkých prostorových škálách. Název CSHKP je zkratkou vzniklou z počátečních písmen příjmení pěti autorů tohoto modelu, jehož jednotlivé ideje pocházejí z prací Carmichael (1964); Sturrock (1966); Hirayama (1974); Kopp & Pneuman (1976). Schématicky je znázorněn na obr. 1.4. V celém erupčním procesu lze na základě pozorování interpretovaných v paradigmatu tohoto modelu identifikovat několik fází: akumulaci energie, přederupci, impulzní a graduální fázi.

1.3.1 Akumulace energie

V současné době panuje všeobecná shoda, že energie uvolněná během slunečních erupcí pochází z magnetických polí, která prostupují žhavé plazma ve sluneční atmosféře. Pozorování přechodové oblasti a koróny v EUV a SXR oborech ukazují, že sluneční atmosféra představuje nesmírně dynamické prostředí, které je zásobováno energií zdola, z konvektivní zóny. Odtud vstupuje energie do fotosféry, buď ve formě stochastických pohybů relativně hustého a chladného plazmatu excitovaných tubulentními vzestupnými a sestupnými proudy v podpovrchové vrstvě nebo formou vynořování nových (případně zanořování starých) magnetických polí, jež je opět důsledkem proudění plazmatu v konvektivní zóně. Protože plazma má ve většině oblastí sluneční atmosféry vysokou elektrickou vodivost, projevuje se známý

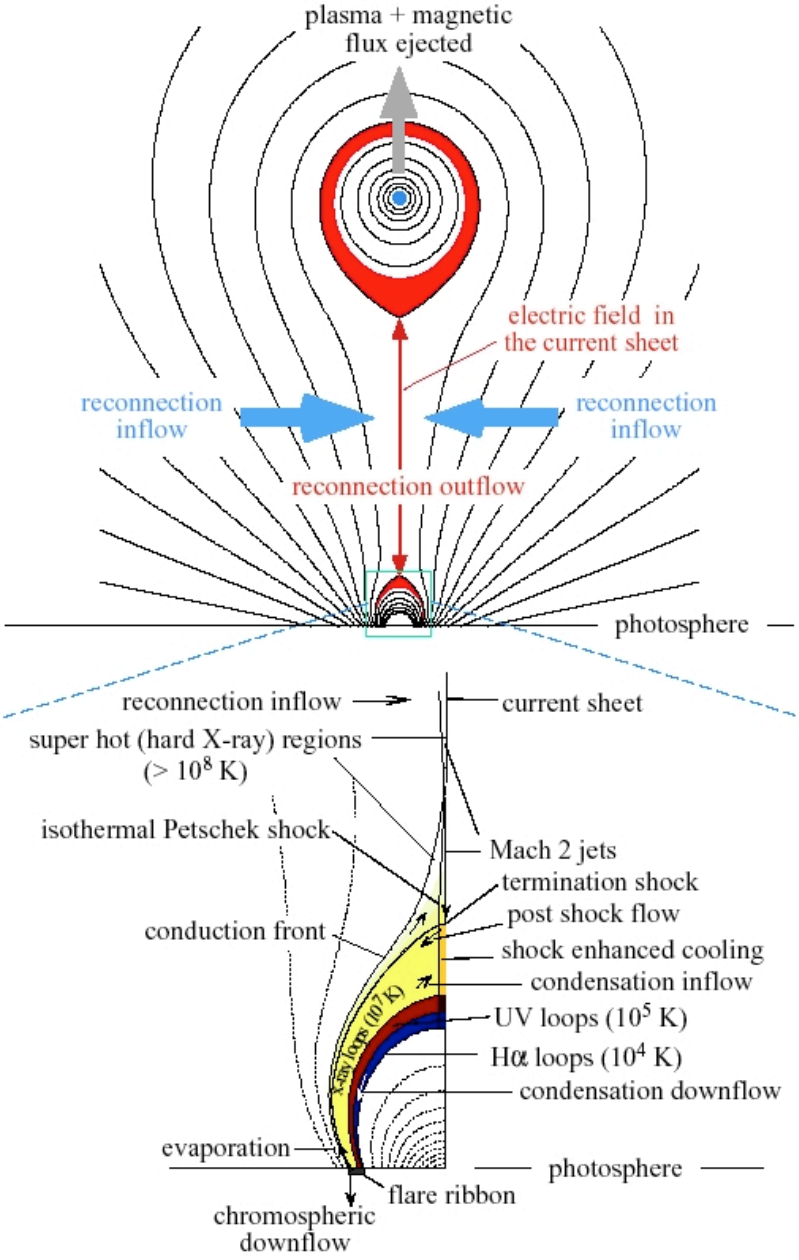

Obrázek 1.4: CSHKP model sluneční erupce (Lin et al. 2002a). *Nahoře:* globální uspořádání přederupčního magnetického pole se zakrouceným magnetickým provazcem (filamentem) ležícím vysoko v koróně. Pohybem provazce směrem vzhůru se vytvoří dlouhá a úzká proudová vrstva, která se dále strukturuje díky rezistivní nestabilitě. *Dole:* Detailní pohled na vznikající arkádu erupčních smyček a její tepelnou strukturu.

efekt zamrzání magnetických polí do plazmatu (Priest 1981). Díky tomuto jevu se energie z podpovrchových vrstev Slunce přenáší do sluneční atmosféry, kde se kumuluje v silně nepotenciálových koronálních magnetických polích s velkou volnou energií a za určitých podmínek může dojít k jejímu uvolnění. Jedna z možných přederupčních konfigurací koronálního magnetického pole je znázorněná v horní části obrázku 1.4 .

1.3.2 Přederupce

U některých erupcí, typicky několik minut před jejich začátkem, se v dané aktivní oblasti pozoruje zvýšená aktivita ve formě krátkých zjasnění v EUV a SXR oborech (Fárník et al. 1996; Veronig et al. 2002). Tato zjasnění zřejmě souvisejí s iniciací erupce. Jedním z možných spouštěcích mechanismů erupcí je iniciace magnetického provazce (twisted flux-rope) ležícího v koróně (viz obr. 1.4) a přibližně kopírujícího fotosférickou neutrální linii. K jeho iniciaci dochází například v důsledku smyčkové nestability (kink instability), která nastartuje vertikální pohyb provazce směrem vzhůru. Tato fáze erupčního procesu je velmi názorně demonstrována na MHD simulacích kombinovaných s pozorováními v pracech Török & Kliem (2005); Williams et al. (2005). Magnetické provazce nad neutrálními liniemi lze často pozorovat na slunečním disku jako filamenty a jejich iniciace vede k výronům koronální hmoty (CME).

1.3.3 Impulzní fáze

V důsledku vertikálního pohybu magnetického provazce se vytvoří uzká a dlouhá proudová vrstva ohraničená magnetickými poli opačných polarit v níž se začne projevovat ostrůvková nestabilita (resistive tearing mode) (Priest 1981), která trhá proudovou vrstvu na řadu menších sekundárních proudových vrstev (opět náchylných vůči ostrůvkové nestabilitě) prokládaných plazmoidy (Bárta et al. 2011b). V takto prakticky fraktálně strukturované proudové vrstvě (Shibata & Tanuma 2001) probíhá rekonexe magnetického pole vedoucí transformaci jeho energie v kinetickou energii částic, Jouleovo teplo, pohybovou energii plazmatu, energii rázových vln a záření. Detaily procesů v proudových vrstvách (na kinetické úrovni) spojené s urychlováním částic, jejichž role je v erupcích klíčová, nejsou dosud zcela známy a jsou předmětem intenzivního studia (Bárta et al. 2011b,a).

Svazky vysokoenergetických nabitých částic urychlených v koronální proudové vrstvě se pohybují podél nově přepojených magnetických siločar, které vytvářejí směrem k fotosféře magnetickou arkádu, jejíž výška roste s časem a polohy ukotvení přepojených siločar se s postupující rekonexí vzdalují od neutrální linie (Kopp & Pneuman 1976). Svazky částic pohybující se směrem k chromosféře procházejí nejprve poměrně řídkým plamatem v koróně a přechodové oblasti, kde lze prakticky zanedbat vliv coulombovských srážek netermálních částic svazku a částic okolní atmosféry. Tato situace se zásadně mění v chromosféře, kde ve standardním přiblížení tzv. tlustého terče dochází díky coulombovským srážkám k rychlé

disipaci kinetické energie částic svazku, emisi netermálního brzdného záření v tvrdém rentgenovém oboru (Brown 1971) a současně k rychlému ohřevu chromosféry na vysoké teploty. Tato fáze erupce, od okamžiku akcelerace částic v koróně a bombardování chromosféry spojené s emisí HXR se nazývá impulzní fází.

Prudký ohřev chromosféry v důsledku termalizace svazků vysokoenergetických částic má za následek vypařování, v impulzní fázi erupce explozivní, horkého chromosférického plazmatu do korony, přičemž vypařené plazma sleduje díky nízkému plazmatickému parametru β tvar přepojených magnetických siločar (Kopp & Pneuman 1976). Vzhledem k postupnému nárůstu hustoty a teploty plazmatu v koronální části erupčních smyček začínají tyto části intenzivně zářit v SXR.

1.3.4 Graduální fáze

Postupující rekonexe postupně odřízne sledovanou horkou erupční smyčku od svazků částic generovaných v koróně a impulzní ohřev chromosféry se posune dál od neutrální linie. Sledovaná smyčka začíná chladnout v důsledku vedení tepla a zářivých ztrát (např. Varady & Heinzel 1997a). Díky vedení tepla z horké koronální časti smyčky směrem k chromosféře může ještě v této fázi erupce pokračovat vypařování chromosférického plazmatu. Tato fáze erupce se nazývá graduální. Nad arkádou chladnoučích smyček může pokračovat rekonexe a tvorba nových horkých smyček až do ukončení rekonekce. Tento model proto předpovídá nárůst výšky arkády erupčních smyček s časem a skutečnost, že horké smyčky leží vždy nad smyčkami chladnějšími.

Od okamžiku kdy v koróně skončí rekonexe magnetických polí, končí přísun energie do erupčních smyček a nastává postupné chladnutí. Observačně se to projeví tak, že se v chladných chromosférických čarách, typicky v Hα, začnou objevovat nejprve nejnižší smyčky arkády. Ty dále chladnou při současném odtoku chladného plazmatu do chromosféry (Varady & Heinzel 1997b; Varady et al. 2000). Tyto smyčky se ve starší literatuře označují termínem smyčkové protuberance, v poslední době se ustálilo označení chladné poerupční smyčky.

1.4 Observační vlastnosti erupcí

CSHKP model je velmi úspěšný z hlediska interpretace pozorování erupcí zejména na velkých prostorových škálách ve všech oborech elektromagnetického spektra. V následujících odstavcích shrneme klíčová observační fakta, která dokládají procesy a konfigurace předpokládané „standardním modelem“.

1.4.1 Rekonexe v koróně

První a klíčová pozorování prokazující existenci před rekonekčních konfigurací polí v koróně a probíhající rekonexi samotnou pocházejí z rentgenového dalekohledu SXT na kosmické

sluneční observatoři Yohkoh (Tsuneta et al. 1991). Jedná se zejména o objev tzv. přilbicovitých struktur (cusp structures) (Tsuneta et al. 1992), které odpovídají tvaru magnetického pole v okolí rekonekčního X nebo Y-bodu (Priest 1981), v němž se předpokládá probíhající rekonexe. Znakem magnetické rekonexe probíhající v koróně podle „standardního modelu" je mimo jiné rostoucí výška X, Y-bodu a arkády erupčních smyček. V literatuře existuje řada pozorování dokládající toto chování (Cheng 1980; Švestka et al. 1987; Varady et al. 2000). Dopplerovské indikace toků plazmatu nevyhnutelně provázejících rekonexi magnetických polí se podařilo získat například v práci Kotrč et al. (1998). Pozorování rekonfigurace magnetických polí v koróně jsou v současné době celkem běžná (Liu & Wang 2009; Su et al. 2013) a lze je dokonce použít k odhadům volné energie v koronálním magnetickém poli před a po erupci (např. Schrijver et al. 2008). Nově se ukazuje překvapivý fakt, že rekonexe koronálních polí může vést k pozorovatelné změně konfigurace polí fotosférických (Liu et al. 2012).

1.4.2 Urychlování, transport a termalizace svazků částic

Nejvýznamnějším průkazem přítomnosti vysokoenergetických svazků částic, zejména elektronových, v erupcích jsou pozorování silných zdrojů netermálního HXR záření vycházejícího z chromosféry z míst, která odpovídají ukotvení erupčních smyček (viz modré kontury v chromosférických erupčních stužkách na obr. 1.5). Tato pozorování lze přirozeně vysvětlit jako interakci vysokoenergetických elektronových svazků s relativně hustým chromosférickým plazmatem při níž je emitováno netermální brzdné záření v tvrdém rentgenovém oboru. Velmi úspěšnou, dnes již klasickou, teorii emise HXR z oblastí ukotvení erupčních smyček, tzv. model tlustého terče, vypracoval Brown (1971). Tento model předpokládá, že kinetická energie netermálních elektronů je disipována výhradně coulombovskými srážkami (Emslie 1978) na relativně malé vzdálenosti. Pomocí přiblížení tlustého terče a ze znalosti spektra a intenzity HXR vycházejícího z chromosféry lze určit parametry primárního elektronového svazku. Zpracování chromosférických HXR pozorování ukazují, že elektronové svazky mají energetická spektra blízká buď jednoduchým, nebo lomeným mocninným spektrům. V případě jednoduchých mocninných spekter lze pak tok netermálních elektronů $F(E)$ v jednotkách elektron $\mathrm{cm}^{-2}\,\mathrm{s}^{-1}\,\mathrm{eV}^{-1}$ vyjádřit vztahem

$$F(E) = (\delta_\mathrm{p} - 2)\frac{\mathcal{F}_0}{E_0^2}\left(\frac{E}{E_0}\right)^{-\delta} \quad , \quad \text{pro} \quad E \geq E_0 \, ,$$

kde E_0 je dolní energetická mez, δ mocninný index spektra a $\mathcal{F}_0$ celkový energetický tok elektronového svazku, který má ve slunečních erupcích tytpické hodnoty $\sim 10^9 - 10^{12}$ erg $\mathrm{cm}^{-2}\,\mathrm{s}^{-1}$. Analýzou HXR pozorování erupcí lze tedy získat parametry elektronových svazků, které lze pak s výhodou použít jako vstupní data do erupčních modelů. V další kapitole uvidíme, že práve toto je cesta, kterou jsme použili v našich modelech.

Skutečnost, že při ohřevu chromosféry v erupcích hrají důležitou roli svazky vysokoenergetických částic dnes již není v literatuře zpochybňována. Na druhou stranu stále nepanuje

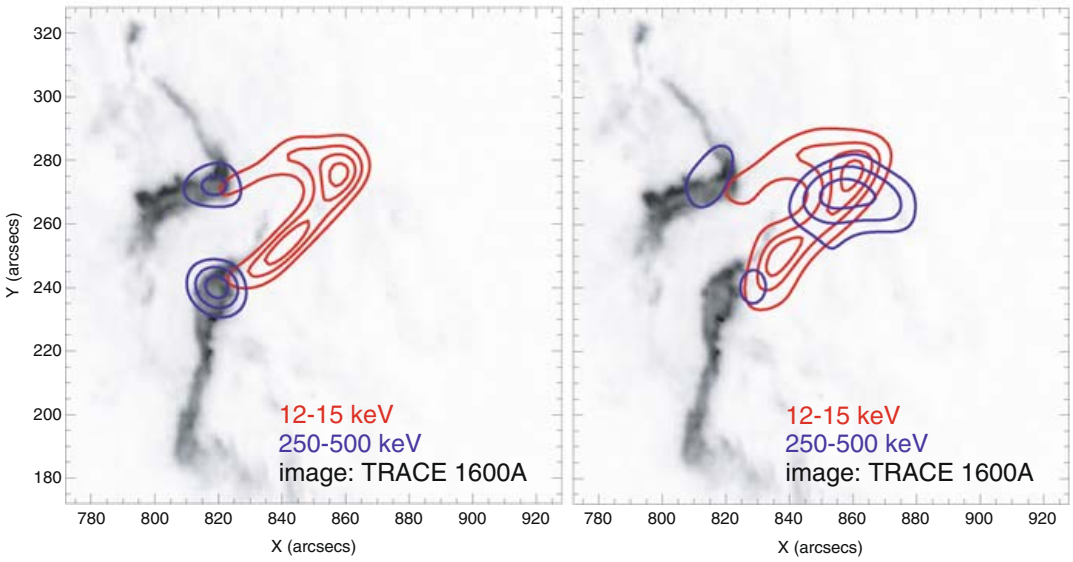

Obrázek 1.5: RHESSI pozorování erupce v HXR oboru na energiích 12 – 15 keV (červené kontury) a 250 – 500 keV (modré kontury) přeložené přes TRACE UV pozorování chromosférických erupčních vláken ve spektrálním okně 1600 Å (Krucker et al. 2008a).

shoda nad tím, zda jsou svazky s takovýmito ohromnými energiemi opravdu urychlovány výhradně v koróně a pak, z hlediska urychlování částic, pasivně transportovány korónou a přechodovou oblastí do chromosféry. Pozorování svědčící o přítomnosti svazků částic v koróně jsou zejména z rádiového a HRX oboru. V 90. letech objevil Masuda et al. (1994) zdroj HXR záření v koróně, v oblasti nad arkádou erupčních smyček (modré kontury v koróně v pravém panelu obr. 1.5). Se zvýšením citlivosti nových přístrojů (RHESSI) se pozorování netermálních koronálních zdrojů stala více méně běžnými (Krucker et al. 2008b). Navíc se díky RHESSI datům pozorují v oblasti erupčních smyček nízkoenergetické tepelné zdroje HXR (viz červené kontury na obr. 1.5). Netermální koronální zdroje HXR jsou interpretovány jako místa, kde částicové svazky mířící směrem k chromosféře interagují s magnetickým polem uzavřených erupčních smyček, v místech kde se mohou vyskytovat tzv. kolabující magnetické pasti, které mohou přispívat k urychlování netermálních elektronů (Karlický & Bárta 2006). Další indikace pocházejí z radiových pozorování, kde vzplanutí typu III nebo U jsou interpretovány jako důsledky průletů vysokoenergetických elektronových svazků plazmatem sluneční atmosféry (Bastian et al. 1998). Přímou souvislost ohřevu chromosféry a vysokoenergetickcých svazků částic mimo jiné dokládá observačně prokázaná časová korelace intenzit Hα jader a toku HXR (Radziszewski et al. 2007, 2011).

1.4.3 Chromosférické vypařování a topologie erupčcích smyček

Nevyhnutelným důsledkem interakce vysokoenergetických svazků částic a hustého chromosférického plazmatu je prudký ohřev chromosféry a expanze hustého a horkého chromosférického plazmatu do koróny tzv. explozivní chromosférické vypařování. Analýzy Dopplerovských posuvů v impulzních fázích erupcí v horkých EUV čarách ($T > 1$ MK) ukazují, že rychlosti plazmatu při jeho explozivní evaporaci do koróny dosahují hodnot $\sim$ 100 – 200 km s^{-1} (např. del Zanna et al. 2006). V chladnějších čarách ($T \sim 10$ kK) dosahují rychlosti evaporace pouze několika desítek km/s. Dokonce i po ukončení impulzního ohřevu smyček, tedy v graduálních fázích erupcí, se pozoruje vypařování chromosférického plazmatu, byť s rychlostmi plazmatu podstatně menšími ($\sim$ 1 – 10 km s^{-1}), přičemž v chladnějších EUV čarách se systematicky pozorují rychlosti menší, než v čarách horkých (např. Czaykowska et al. 2001). Tento jev se nazývá tzv. jemné vypařování (gentle evaporation). Důsledkem explozivní evaporace je rychlé zformování tzv. horkých erupčních smyček dobře známých z pozorování erupcí v SXR oboru. Teplota plazmatu v těchto smyčkách dosahuje hodnot od jednotek MK až do 30 MK a hustota od $\sim 10^9$ cm^{-3} (Varady et al. 2000) v extrémních případech téměř 10^{12} cm^{-3} (Veronig & Brown 2004).

Dalším výrazným argumentem ve prospěch CSHKP modelu založeného na rekonexi koronálních magnetických polí je pozorovaný nárůst výšky arkád erupčních smyček s probíhající rekonexí a observační potvrzení, že horké smyčky leží nad smyčkami chladnějšími (Cheng 1980; Švestka et al. 1987; Varady et al. 2000) a pozorování postupného vzdalování se jasných chromosférických Hα jadérek (kernels) nebo stužek (ribbons) od neutrální linie. Bylo dokonce ukázáno, že rychlost příčného pohybu erupčních stužek vzhledem k neutrální linii koreluje s některými vlastnostmi HXR emise z oblasti ukotvení erupčních smyček (Fletcher & Hudson 2002).

1.4.4 Chladnutí a rozpad poerupčních smyček

Poslední vývojovou fází erupcí je chladnutí horkých erupčních smyček (Varady et al. 2000), které se díky zářivým ztrátám a vedení tepla (Varady & Heinzel 1997a) postupně objevují v čarách s nižší a nižší formační teplotou. Při teplotách kolem $\sim$ 100 kK, kde křivka opticky tenkých zářivých ztrát pro koronální plazma dosahuje maxima, dochází ke katastrofickému chladnutí a současnému rychlému odtoku plazmatu z arkády poerupčních smyček. Tento jev je později pozorován typicky v čáře Hα, zejména na okrajích slunečního disku (Varady & Heinzel 1997b). Dříve byl označován jako smyčková protuberance.

1.5 Alternativy a modifikace CSHKP modelu

CSHKP model velmi přirozeně a názorně interpretuje observační vlastnosti erupcí a z tohoto pohledu je považován za nesmírně úspěšný. Na stranu druhou, pokud hlouběji analyzujeme

jeho důsledky z hlediska fundamentální fyziky a vezmeme v úvahu hodnoty některých veličin, které vycházejí z pozorování a jednoduchých odhadů, model se dostává do velmi obtížně překonatelných problémů. Tyto problémy v poslední době získávají na naléhavosti zejména díky nové generaci pozorování erupcí přístroji pracujícími v oboru tvrdého rentgenového záření, jako byl například teleskop HXT/Yohkoh (Kosugi et al. 1991), nebo v současné době stále ještě funkční RHESSI (Lin et al. 2002b) a která nejsou kompatibilní s klasickým CSHKP modelem. Řešení těchto problémů je jednou z hlavních, v současné době řešených otázek fyziky erupcí. Situaci kolem CSHKP modelu výstižně formuloval v rámci konferenční diskuse Hudson (2012): „Proč standardní model erupcí tak skvěle vysvětluje pozorování, když z fyzikálního hlediska nemůže fungovat?“

V tomto článku identifikujeme hlavní problémy CSHKP modelu, jejich důsledky a představíme některé pokusy o jejich řešení, které se ubírají dvěma cestami. Jednou jsou pokusy o jeho modifikaci (Karlický 1995; Vlahos et al. 2004; Turkmani et al. 2005, 2006; Brown et al. 2009; Gordovskyy & Browning 2011; Turkmani & Brown 2012; Karlický & Kontar 2012). Ty předpokládají existenci sekundární akcelerační oblasti, kde se netermální částice urychlují během svého transportu z primární urychlovací oblasti, o níž se v souladu s CSHKP modelem předpokládá, že je umístěna v koróně. Druhou cestou jsou pak pokusy o navržení modelu zcela nového, které přemisťují oblast klíčového urychlování svazků částic z řídké korány do husté chromosféry, tedy do oblasti kde jsou svazky částic zároveň termalizovány (Fletcher & Hudson 2008).

1.5.1 Hlavní problémy CSHKP modelu

Nejmarkantnějším problémem klasického CSHKP modelu je tzv. problém počtu (netermálních) elektronů[1] v erupcích (Brown & Melrose 1977). Vezmeme-li v úvahu pozorované intenzity a spektra netermálního brzdného HXR emitovaného v oblastech termalizace elektronových svazků, lze za předpokladu kolizního tlustého terče snadno určit odpovídající spektra a toky elektronových svazků (Brown 1971). Vzhledem k tomu, že účinnost produkce netermálního brzdného HXR je velmi nízká, vycházejí nesmírně vysoké typické hodnoty toků netermálních elektronů v erupcích. Například Guo et al. (2013) určovali hodnoty elektronových toků pro řadu erupcí a jejich výsledky se pohybují od $\sim 10^{34}$ do $\sim 10^{36}$ s^{-1}. Typické hodnoty energetických toků elektronových svazků ve slunečních erupcích jsou uváděny v mezích 10^9 až 10^{12} erg cm^{-2} s^{-1}. Pro charakteristické doby trvání impulzní fáze erupcí $\sim 10^2$ až 10^3 s dostáváme celkový počet netermálních elektronů, které musí být v erupcích urychleny na energie $\gtrsim 10-20$ keV až 10^{39}. Toto množství řádově převyšuje počet elektronů v koronální části erupčních smyček a blíží se odhadům celkového počtu elektronů v koróně. Podle standardního CSHKP modelu, který předpokládá jedinou akcelerační oblast v koróně musí být toto množství „shromážděno“ a urychleno v koróně, následně transportováno korónou a přechodovou oblastí do chromosféry a zde termalizováno.

[1] V anglické literatuře 'electron number problem'.

Další nesmírně vážný problém představuje samotný transport takovýchto enormních svazků částic plazmatem koróny a přechodové oblasti. Průlet svazku nabitých částic plazmatem, podle principu elektromagnetické indukce (a z důvodu zachování kvazineutrality plazmatu), způsobí vznik elektrického proudu (tzv. zpětný proud), který eliminuje účinky proudu generovaného transportem nabitých částic (Hoyng et al. 1978; van den Oord 1990; Varady et al. 2007; Karlický 2009; Holman 2012). Elektrické pole vytvářející zpětný proud brzdí svazky částic a vedle coulombovských srážek tak přispívá k jejich termalizaci. Tento efekt roste s tokem elektronových svazků, závisí však také na distribuční funkci elektronů formujících zpětný proud (Karlický 2009). Pro velké a střední toky by za předpokladu, kdy pro zpětný proud platí Ohmův zákon s klasickou Spitzerovskou rezistivitou (Spitzer 1962), tedy v případě kdy je zpětný proud tvořen pomalým driftovým pohybem elektronů bulku a rozdělovací funkce je blízká posunutému Maxwellovu rozdělení, by tento efekt nejenže dominoval disipaci energie coulombovskými srážkami, ale také by vedl k posunutí maxima energie deponované svazky do oblasti nad chromosféru (Varady et al. 2005). Další třídu problémů představuje vznik Langmuirovských vln a řady nestabilit (např. Weibelovy nestability), které dále znesnadňují transport netermálních částic plazmatem sluneční atmosféry (Karlický 2009; Matthews et al. 1996). Vzhledem k těmto problémům je v současné době snaha modifikovat, nebo nahradit CSHKP model tak, aby byly z koróny transportovány svazky částic s podstatně nižšími toky.

Skutečnost, že CSHKP model je nutné modifikovat nebo nahradit napovídají také nová RHESSI pozorování chromosférických netermálních HXR zdrojů. Například Battaglia et al. (2012) se bezúspěšně pokoušeli pomocí kolizního tlustého terče, který je esenciální součástí CSHKP modelu, vysvětlit vertikální rozměry a polohy zdrojů HXR záření měřené na základě pozorování získaných RHESSI (Battaglia & Kontar 2011). Také měření distribuční funkce netermálních elektronů v oblasti tlustého terče (Kontar & Brown 2006) indikují překvapivou izotropii netermálnách elektronů a to i ve vertikálním směru. Tento výsledek je zcela v rozporu s předpověďmi CSHKP modelu, který předpovídá silné směrování svazku směrem k fotosféře.

1.5.2 Modifikace a alternativy

Jak jsme již uvedli, modifikace CSHKP modelu z poslední doby spočívají v jeho doplnění o další (sekundární) akcelerační oblast. V této oblasti jsou netermální elektrony urychlené v primární akcelerační oblasti v koróně urychlovány buď během jejich transportu z koróny, nebo přímo v oblasti kolizního tlustého terče.

Reakcelerace stochastickými elektrickými poli

Jednou takovou modifikací je model analyzovaný v práci Brown et al. (2009) a navržený na základě prací (Turkmani et al. 2005, 2006). Tato modifikace ve shodě s CSHKP modelem předpokládá primární urychlení elektronů svazku v koróně a jejich následný trans-

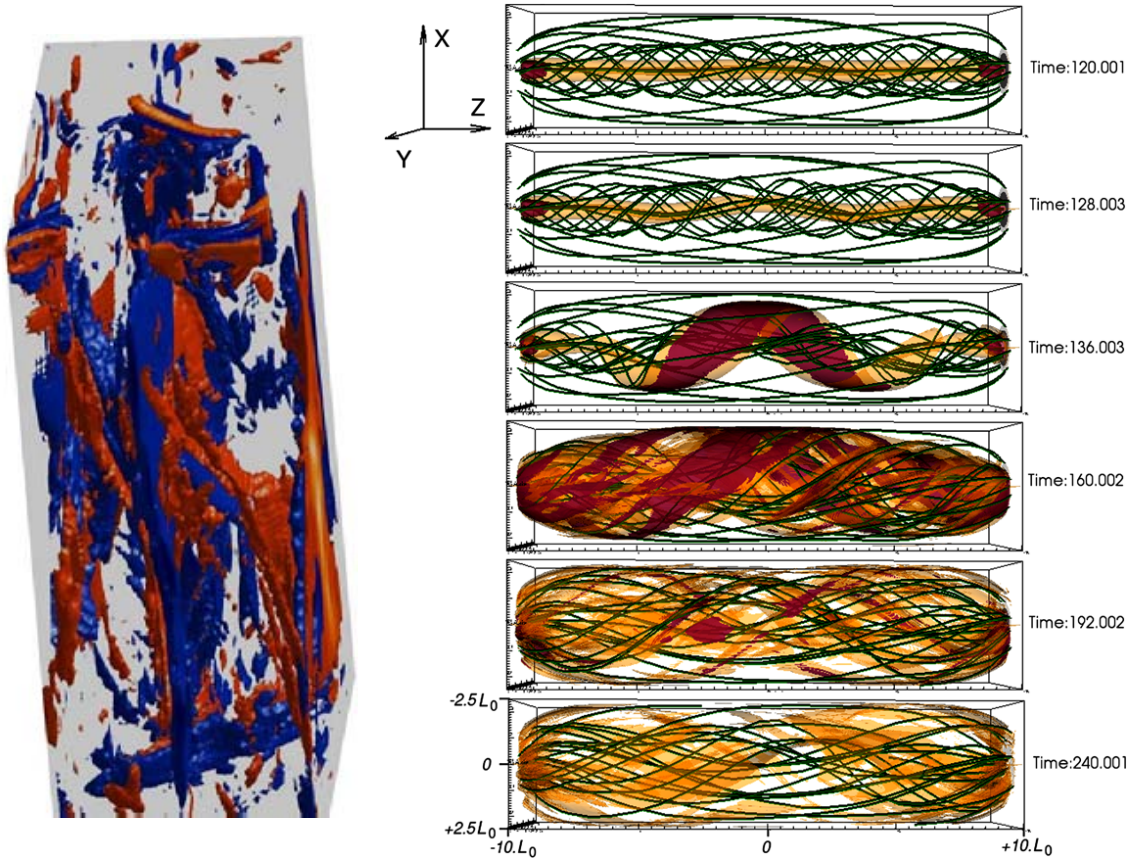

Obrázek 1.6: *Pravý panel:* Ilustrace stochastických rezistivních elektrických polí modelovaných v MHD přiblížení. Pole v červených oblastech urychluje elektrony směrem k hornímu okraji oblasti, modré směrem k dolnímu okraji. Převzato z Turkmani et al. (2006). *Levý panel:* MHD simulace časového vývoje magnetického pole (zelené čáry) ve smyčce, která se zužuje směrem k ukotvením a má nenulovou helicitu. Odstíny hnědé kódují proudové hustoty ve smyčce. Převzato z Gordovskyy et al. (2013).

port do chromosféry. V chromosféře se pak předpokládá sekundární urychlování netermálních elektronů svazku stochastickými elektrickými poli (viz obr. 1.6), které jsou generovány ve stochastických proudových vrstvách, jež jsou vytvářeny v důsledku turbulentních pohybů plazmatu ve fotosféře (Turkmani et al. 2005, 2006). Ukazuje se, že reakcelerace elektronových svazků v oblasti tlustého terče prodlužuje střední doby života jednotlivých netermálních elektronů a umožňuje tak docílit pozorovaných toků HXR a erupčních ohřevů pro podstatně nižší elektronové toky generované v primární akcelerační oblasti v koróně. Tato modifikace tak dovoluje podstatně oslabit požadavky na účinnost koronálního akcelerátoru. V našich pracech (Varady et al. 2014, 2013) jsme tyto závěry potvrdili pro stochastická elektrická pole s nenulovými i nulovými středními hodnotami.

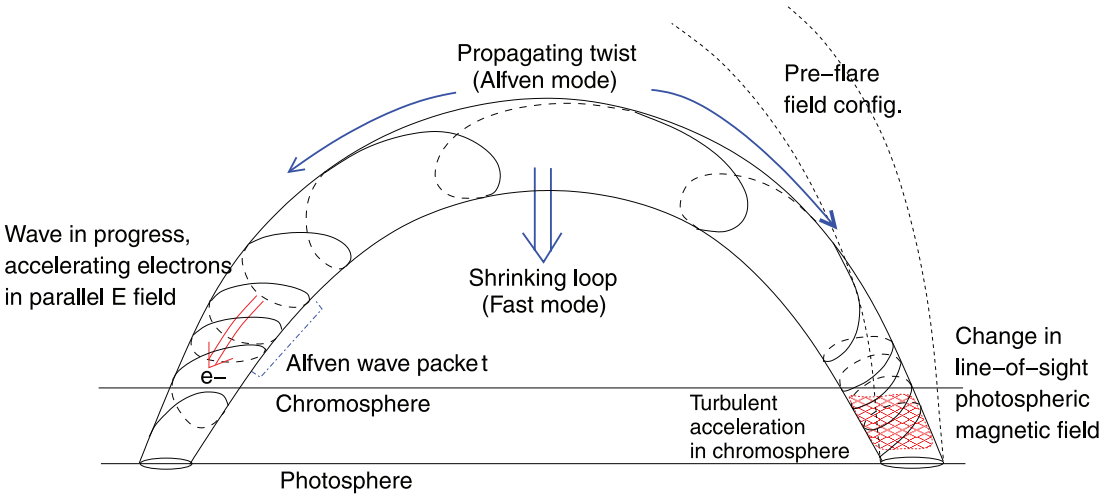

Obrázek 1.7: Alternativní model erupce navržený autory Fletcher & Hudson (2008), který předpokládá, že dominantní část energie uvolněná při rekonexi magnetických polí v koróně je do chromosféry transportována nikoli ve formě vysokoenergetických svazků elektronů s extrémními toky, ale ve formě Alfvénových vln. Převzato z Fletcher & Hudson (2008).

Reakcelerace ve smyčkách s helikálním magnetickým polem

V práci Karlický (1995) je navžen další mechanismus, který vede k sekundární reakceleraci netermálních elektronů, primárně urychlených v koróně, podél celé jejich trajektorie z koróny do chromosféry. Zde je sekundární reakcelerace způsobena malými statickými elektrickými poli, která jsou generována v důsledku nenulové helicity magnetického pole v erupčních smyčkách (např. Gordovskyy & Browning 2011, 2012; Gordovskyy et al. 2013). V důsledku strmého poklesu elektrické vodivosti plazmatu v chromosféře a předpokládané konvergence magnetického pole v této oblasti, dosahují velikosti elektrických polí v chromosféře svého maxima. Na rozdíl od stochastické reakcelerace jsou statická elektrická pole orientována podél celého proudového vlákna stejným směrem a výsledkem tedy je nesymetrický ohřev v místech obou ukotvení vlákna v chromosféře, protože netermální elektrony šířící se z vrcholu smyčky jsou na jednu stranu statickým polem urychlovány, na druhou stranu brzděny. Důsledky tohoto mechanismu na produkci a spektra HXR a na erupční ohřev chromosféry byly studovány pro různé parametry statických polí v práci (Varady et al. 2014).

Reakcelerace díky interakcím svazek – plazma

Další mechanismus reakcelerace netermálních elektronových svazků šířících se plazmatem erupčních smyček k chromosféře navrhli Karlický & Kontar (2012), kteří použili elektromagnetický 3-D particle–in–cell (PIC) kód ke studiu chování netermálních elektronů v systému obsahujícím monoenergetický elektronový svazek a plazma. Vedle disipace energie

netermálních elektronů v důsledku coulombovských srážek shledali, že nezanedbatelná populace netermálních elektronů ($\simeq 10 - 30\%$) je při transportu v koróně urychlována nad svou původní energii díky interakci svazku s Langmuirovými vlnami, které se nevyhnutelně vygenerují ve studovaném systému (viz také Varady et al. 2007).

Alternativní model s transportem energie z koróny Alfvénovými vlnami

V současné době zřejmě nejdiskutovanější alternativou CSHKP modelu je model navržený autory Fletcher & Hudson (2008) (viz obr. 1.7). Tento model zcela opouští paradigma dominantního koronálního akcelerátoru, jakožto zdroje urychlených částic, které transportují výraznou část energie uvolněné při rekonexi koronálních polí ve formě intenzivních vysokoenergetických svazků částic do chromosféry, kde jsou termalizovány. Podobně jako CSHKP sice předpokládá akumulaci magnetické energie v koróně, ale přisuzuje prvořadou roli při transportu energie akumulované v koróně a uvolněné během rekonexe mohutným pulzům Alfvénových torzních vln. Netermální částice urychlené v koronální proudové vrstvě při rekonexi hrají z hlediska energetické bilance zcela druhořadou roli. Autoři popisují dva způsoby urychlování elektronů. Samotné šíření Alfvénových torzních vln v koróně může vést k urychlování elektronů na deka-keV energie a v okamžiku interakce Alfvénových vln s hustou chromosférou dochází nejen k jejich odrazu, ale také ke konverzi vlnových módů, přičemž se vytvoří kaskáda vln s vysokými vlnovými čísly. Přitom dochází ke stochastickému urychlování elektronů v husté sluneční chromosféře, které pak emitují pozorované netermální brzdné HXR. Tento model se tak elegantně vyrovnává s problémem počtu elektronů v erupcích, protože elektrony jsou urychlovány oblasti, kde je jich dostatený počet a současně jsou ve stejné oblasti termalizovány.

Kapitola 2

Modelování erupčních procesů

Modelování procesů probíhajících ve slunečních erupcích je v současné době těžištěm mé odborné práce. Ve své habilitaci uvádím pouze dvě kategorie modelů: zářivou hydrodynamiku (RHD) a částicové modelování transportu a termalizace netermálních částic v plazmatu, prostoupeném magnetickým polem v erupčních smyčkách. Nejprve se budeme zabývat zářivou hydrodynamikou (Mihalas & Mihalas 1984), která spojuje hydrodynamiku a non-LTE přenos záření a umožňuje tak modelovat časově závislé erupční profily opticky tlustých čar ve vizuálním oboru, tedy čar s potenciálně vysokou diagnostickou hodnotou. Tohoto tématu se týkají **práce 1 – 5**, přičemž pro poslední práci je klíčová modifikace částicového kódu pro neutrální svazek.

Dále se budeme zabývat modelováním některých aspektů souvisejících s transportem a depozicí energie v erupcích prostřednictvím netermálních částic. Ty podle většiny současných představ přenášejí energii z oblasti své akcelerace v koróně do oblasti tlustého terče v chromosféře, kde jsou termalizovány. V **pracech 6** a **7** modelujeme vliv zpětného proudu na erupční chromosférický ohřev. Zde také detailně, na mikroskopických škálách, zkoumáme formování zpětného proudu 1-D particle-in-cell (PIC) kódem. Výsledky těchto studií jsou pak použity v **práci 8**, kde pomocí vytvořených modelů účinků zpětného proudu na termalizaci elektronových svazků a RHD zkoumáme jeho vliv na formování optických čar. V souvislosti s problémy klasického CSHKP modelu erupcí (viz čl. 1.5.1), opět metodou testovacích částic, studujeme v **pracech 9** až **11** důsledky některých modifikací modelu kolizního tlustého terče. Tyto problémy jsou stále velmi aktuální a nadále na nich pracujeme.

Kromě těchto témat jsem dále spolupracoval jako školitel konzultant na Ph.D. projektu zabývajícím se řešením soustavy magnetohydrodynamických rovnic (MHD) pomocí metod konečných prvků (FEM) (Skála et al. 2011), jehož cílem bylo zmapovat potenciál FEM při zkoumání jemných struktur vznikajících v oblasti koronální rekonekční proudové vrstvy. Ty podle současných představ hrají klíčovou roli při urychlování částic. V letošním roce jsem začal vést dalšího Ph.D. studenta (Mgr. David Kramoliš) s nímž řeším problematiku urychlování nabitých částic v rekonekčních proudových vrstvách pomocí částicového kódu, který přepíná mezi guiding center approximation (GCA) a full orbit integrací podle lokál-

ních parametrů časově proměnného elektromagnetického pole. Vstupem do těchto simulací je předpočítaný časový vývoj konfigurací elektromagnetického pole získaný pomocí MHD simulací (Bárta et al. 2011a,b).

2.1 Zářivá hydrodynamika erupcí

Dominantní část energie vyzářená během slunečních erupcí pochází z chromosféry (Neidig 1989; Fletcher et al. 2010). Erupce se zde projevují jako silná lokalizovaná zjasnění v místech ukotvení horkých erupčních smyček, které v koróně a přechodové oblasti září zejména v EUV a SXR oborech. Skutečnost, že v dolní atmosféře lze tyto smyčky považovat za prakticky vertikální, spolu s anizotropií, kterou do problému vnáší přítomnost magnetického pole, jež určuje tvar smyčky (předpokládá se nízký plazmový β parametr), umožňuje modelovat procesy v erupčních smyčkách a chromosférickou emisi v prvním přiblížení jako 1-D problém. Zářivá a termodynamická odezva chromosféry na depozici erupční energie transportované ve formě vysokoenergetických svazků nabitých částic, zejména elektronů, z akcelerační oblasti, jež podle klasického CSHKP modelu leží v koróně, do nižších vrstev atmosféry se modeluje dvěma způsoby.

Jednou možností jsou tzv. semi-empirické modely, jejichž základem jsou buď pozorovaná spektra erupcí, nebo pozorování erupční oblasti spektroheliografy či úzkopásmovými filtry v několika spektrálních čarách. Časový vývoj erupční atmosféry se pak modeluje jako série fyzikálně vzájemně neprovázaných stavů tak, že se pozorovaná spektra fitují spektry vypočtenými, kterým odpovídají různé stavy erupční atmosféry (Machado et al. 1980; Fang et al. 1995). Problémem této metody je otázka jednoznačnosti získaných teplotních, hustotních a ionizačních profilů erupční chromosféry. Druhou cestou k získání teoretických erupčních spekter a časového vývoje profilů termodynamických parametrů chromosféry jsou časově závislé zářivě hydrodynamické modely počítané „ab initio“. Jejich výstupem jsou časově závislá self-konzistentně modelovaná erupční spektra, která mohou být přímo porovnána s pozorováními. Výsledky prezentované v této práci jsou získané právě touto metodikou.

Podle prakticky všech v současnosti uvažovaných erupčních modelů, je chromosférické plazma v impulzní fázi bombardováno svazky vysokoenergetických netermálních částic s časově rychle proměnným energetickým tokem a spektrem a je tak vystaveno intenzivnímu, prostoročasově proměnnému depozitu energie. Důsledkem je, že erupční chromosféra je nesmírně dynamickým prostředím, kde se stav plazmatu mění na sub-sekudových časových škálách modulovaných časovým vývojem energetického toku netermálních částic. Situaci dále komplikuje přítomnost svazků netermálních částic, díky nimž je v impulzní fázi erupce chromosférické plazma nemaxwellovské. Mimo jiné, právě tuto skutečnost se na rozdíl od ostaních autorů snažíme ve svých modelech zohlednit.

Historicky první, přelomové práce v oblasti ab initio RHD modelů slunečních erupcí byly vytvořeny v 80. letech. Popis modelů, výsledky a zkušenosti byly publikovány v sérii

klasických prací McClymont & Canfield (1983a,b); Canfield et al. (1983); An et al. (1983); Fisher et al. (1985a,b,c). Pro erupční ohřev byly využity analytické vztahy pro depozici energie vysokoenergetických elektronových svazků s mocninnými spektry způsobenou coulombovskými srážkami netermálních částic s částicemi okolního plazmatu v přiblížení tzv. studeného terče (Emslie 1978). Tyto modely v hlavních rysech popsaly dynamiku erupční chromosféry, pohyb chromosférické kondenzace směrem k fotosféře, explozivní evaporaci žhavého chromosférického plazmatu do koróny a formování některých opticky tlustých chromosférických čar v erupcích. V poslední době byly zdokonalené 1-D RHD modely publikovány skupinou z University of Washington v pracech (Abbett & Hawley 1999; Allred et al. 2006). Tyto modely využívají RHD kód RADYN vyvinutý na University of Oslo (Carlsson & Stein 1995, 1997).

2.1.1 HYDRAD

Téměř všechny výsledky prezentované této kapitole byly získány s využitím kódu HYDRAD, nebo jeho částí. Tento kód v minulosti vyvinula a nyní udržuje a zdokonaluje naše skupina z AsÚ AV v Ondřejově a UJEP v Ústí nad Labem ve složení M. Varady, J. Kašparová, P. Heinzel, Z. Moravec a M. Karlický. HYDRAD je hybridní 1-D RHD model erupční smyčky, kde erupční ohřev je dán výstupem z kódu modelujícího transport netermálních částic sluneční atmosférou metodou testovacích částic (TPC)[1]. HYDRAD je popsán v **práci 1** a jeho non-LTE část pro transport záření pak detailněji v **práci 2**. V **práci 1** je rovněž demonstrován potenciál kódu modelovat časový vývoj ($\sim$ 10 s) vodíkových čar Hα a Hβ odpovídající elektronovému svazku s časovým vývojem spektra a energetického toku odvozeným z HXR pozorování reálné erupce. Kód vznikl propojením několika původně autonomních kódů, které selfkonzistentně modelují následující aspekty erupcí:

(i) kód s testovacími částicemi simuluje šíření a termalizaci netermálních svazků částic s mocninnými spektry tvořených elektrony, protony, případně neutralizovanými iontovými svazky

(ii) 1-D hydrodynamika pro popis odezvy chromosférického plazmatu s nízkým β na erupční ohřev zprostředkovaný disipací kinetické energie svazků vysokoenergetických částic

(iii) časově závislý non-LTE přenos záření pro 5-ti hladinový + kontinuum model atomu vodíku, jehož výstupem je časový vývoj ionizace vodíku v chromosféře a intenzit vodíkových čar

Všechny kódy mohou pracovat jak v propojeném režimu tak samostatně.

[1] Test–Particle Code

Model erupčního ohřevu je klíčovou částí každého erupčního kódu. HYDRAD je unikátní tím, že pro výpočet erupčního ohřevu využívá TPC, který zcela přirozeně a selfkonzistentně simuluje celou řadu aspektů dynamického ohřevu chromosféry vysokoenergetickými svazky částic s mocninným energetickým spektrem. Proces transportu, termalizace a rozptylu svazků vysokoenergetických nabitých částic z místa jejich urychlení ve slunečním plazmatu lze popsat v difuzním přiblížení v 6-D dimenzionálním fázovém prostoru pomocí Fokker-Planckovy (FP) rovnice. MacKinnon & Craig (1991) ukázali a ověřili, že řešení této rovnice není nutné provádět síťovými metodami v 6-D fázovém prostoru, ale je možné tuto rovnici přepsat na soustavu stochastických obyčejných diferenciálních rovnic, které je možno se znalostí difúzních koeficientů FP rovnice řešit metodou Monte-Carlo (Bai 1982). Modelování erupčního ohřevu pomocí testovacích částic je unikátním rysem našeho kódu. Tento přístup nejen přirozeně a zcela konzistentně zahrnuje efekty související s transportním časem částic a časovou proměnností atmosféry, ale také umožňuje modelovat vliv konvergence magnetického pole smyčky, zahrnout efekty různých modelů zpětného proudu, procesy reakcelerace částic během jejich transportu nebo modelovat procesy termalizace neutralizovaných svazků vysokoenergetických svazků protonů a iontů (Karlický et al. 2000; Brown et al. 2000). Vzhledem k tomu, že jedním z možných výstupů TPC jsou distribuční funkce netermálních částic v různých hloubkách, je tento kód ideálním prostředkem k detailnímu studiu HXR emise v oblasti tlustého terče (viz čl. 2.3 a přiložené **práce 9**, **10**, **11**). Navíc se pro realistické modelování konkrétních erupcí nabízí spektra a toky netermálních elektronů určené například z RHESSI pozorování HXR emitovaného chromosférickými zdroji inverzními metodami (Holman et al. 2003). Současnou verzi TPC vytvořil a udržuje na základě algoritmu převzatého z monoenergetické verze kódu (Karlický 1990) autor této habilitace a Z. Moravec.

Dynamika plazmatu v erupčních smyčkách se standardně popisuje pomocí 1-D soustavy hydrodynamických rovnic, v jedno- nebo dvou-tekutinovém přiblížení. Typické zdrojové členy vyskytující v HD rovnicích popisujících procesy v erupčních smyčkách zohledňují vliv gravitačního pole, vedení tepla, které se díky anizotropii vnesené do plazmatu magnetickým polem uvažuje pouze podél magnetických siločar, klidný ohřev zajišťující stabilitu počáteční hydrostatické atmosféry, zářivé ztráty a v neposlední řadě erupční ohřev, který nastartuje časový vývoj simulace a je výstupem TPC. Klíčovými faktory těchto modelů jsou počáteční podmínky prezentované modelem přederupční atmosféry a časoprostorové rozložení erupčního ohřevu v atmosféře. V našich simulacích používáme jednotekutinové přiblížení a přederupční fotosféru, chromosféru a dolní přechodovou oblast aproximujeme modelem VAL C (Vernazza et al. 1981) na nějž navazujeme typický teplotní profil horní přechodové oblasti a koróny tak, že je počáteční atmosféra v hydrostatické rovnováze. Délka výpočetní domény je rovna délce erupční smyčky nebo její polovině v případě osově symetrických problémů. Hydrodynamickou část kódu vytvořil a udržuje autor habilitace. Numericky je advekce řešena explicitním kódem využívajícím LCPFCT algoritmus a stěpení časového kroku (Oran & Boris 1987). Vedení tepla je modelováno semi-implicitním Crank-Nicolsonovým algoritmem. Další detaily HD části kódu jsou popsány v **pracech 1** a **3**.

Protože zářivé pole v chromosféře, zejména ve viditelném oboru silně interaguje s plazmatem a výrazně tak ovlivňuje jeho stav, zdaleka zde neplatí jednoduchý předpoklad lokální termodynamické rovnováhy (LTE) a je proto nezbytné ho modelovat v komplikovaném časově závislém non-LTE přiblížení (Mihalas & Mihalas 1984). Časově závislá verze kódu pro přenos záření vychází z jeho statické verze popsané v práci Heinzel (1995). V současnosti používáme 5-ti hladinový + kontinuum model atomu vodíku a při výpočtu spektálních profilů vodíkových čar zohledňujeme skutečnost, že chromosférické plazma je díky přítomnosti netermálních elektronů svazku nemaxwellowské (Henoux et al. 1995). Časově závislou verzi non-LTE kódu vytvořili P. Heinzel a J. Kašparová a je popsána v **práci 2**. Zde jsou také prezentovány první výsledky kódu – časový vývoj profilu spektrální čáry Hα z typického klidného absorpčního profilu v typicky erupční profil s jasnými křídly v emisi pro 3 hladinový + kontinuum model atomu vodíku a monoenergetický elektronový svazek. Důležitým výstupem tohoto kódu z hlediska TPC a HD kódů je non-LTE ionizace vodíku v erupční atmosféře, která ovlivňuje jak její dynamiku, tak i termalizaci svazků vysokoenergetických částic.

Kód HYDRAD byl vybrán jako jeden z klíčových kódů pro modelování erupční chromosféry v rámci v současné době probíhajícího evropského grantu FP-7 F-CHROMA. Kód je stále intenzivně rozvíjen a jsou připravovány rozsáhlé erupční simulace. V rámci projektu F-CHROMA nyní naši skupinu na AsU AV v Ondřejově posílila postdoktorandka Wenjuan Liu (Ph.D. na Montana State University).

2.1.2 Odezva vodíkových čar v erupcích na ohřev svazky částic

Jak jsme již uvedli výše, poměry v chromosféře jsou v impulzní fázi erupcí nesmírně komplikované. V **práci 3** jsme studovali vliv elektronových svazků s mocninnými energetickými spektry s různými indexy a časově proměnnými energetickými toky různé velikosti a profilů na formování vodíkových čar Hα, Hβ a Hγ v 5-ti hladinovém + kontinuum modelu atomu vodíku na krátkých časových škálách do $\sim$ 5 s od zahájení ohřevu chromosféry. Hlavní motivací práce bylo zjistit jakým způsobem se přenášejí rychlé změny toku elektronového svazku do intenzit vodíkových čar, zda netermální elektrony výrazně ovlivňují jejich profily a jestli lze z pozorování Balmerových čar jednoznačně usuzovat na to, že tyto čáry vznikají v oblasti nemaxwellovského plazmatu, tedy v místech kde je maxwellovské plazma narušené svazkem netermálních částic s mocninným spektrem. Hlavním cílem naší práce bylo pokusit se ověřit, zda existuje diagnostická metoda prokazující existenci elektronových svazků v oblasti formování vodíkových čar pouze z jejich optických pozorování, jak naznačují někteří pozorovatelé (např. Kashapova et al. 2008).

Naše modely vedly k zjištění, že intenzita všech studovaných Balmerových čar sleduje modulaci toku elektronových svazků na sub-sekundových škálách se sub-sekundovým zpožděním. K identickým závěrům jsme došli v **práci 1**, kde jsme demonstrovali potenciál kódu HYDRAD modelovat časový vývoj intenzit čar Hα a Hβ na delších časových škálách desítek sekund. Tyto výsledky jsou v souladu s pozorováními časové korelace proměnnosti

Balmerových čar s modulací toku elektronového svazku získaného z RHESSI pozorování v některých chromosférických erupčních jádrech (Radziszewski et al. 2007, 2011).

V **práci 3** jsme dále studovali vliv elektronových svazků na formování profilů Balmerových čar. Analýzou jejich kontribučních funkcí bylo zjištěno, že přítomnost netermálních elektronů vede k podstatnému nárůstu emise ze sekundární formační oblasti čar ležící v chromosféře nad oblastí primární, ležící těsně nad fotosférou. Velká pozornost byla věnována hledání diagnostiky, která by pouze na základě pozorování Balmerových čar, případně poměrů jejich intenzit, dokázala jednoznačně prokázat elektronové svazky v místě jejich formace. Přestože jsme ukázali, že netermální elektrony výrazně ovlivňují jejich formování, žádná zcela jednoznačná diagnostika tohoto druhu nebyla potvrzena. Určitým znakem přítomnosti elektronového svazku v oblasti formování čar může být rychlá modulace jejich intenzit. K získání jistoty je však nutno i tuto silnou indicii porovnat s HXR nebo rádiovými daty s prostorovým rozlišením.

Elektronové svazky jsou v erupčním kontextu nejčastěji uvažovaným médiem přenášejícím energii z rekonekční koróny do oblasti tlustého terče v chromosféře. Na druhou stranu z pozorování některých erupcí v γ oboru (Lin et al. 2003) lze usuzovat, že svazky částic obsahují také těžké částice jako jsou protony a ionty urychlené na energie až desítek GeV. Někteří autoři proto předpokládají, že stejnou roli jako elektronové svazky mohou hrát v erupcích také svazky neutralizovaných protonů a iontů, tedy tzv. neutrální svazky (Martens 1988; Simnett & Haines 1990; Sakai & Nagasugi 2007).

V **práci 5** se zabýváme modelováním spektrální odezvy balmerovských čar na bombardování chromosféry neutralizovanými svazky protonů a iontů. Modelování erupčního ohřevu umožnila modifikace TPC založená na myšlence (Karlický et al. 2000; Brown et al. 2000), že urychlené protony a ionty s sebou strhávají elektrony z bulku, takže paralelní rychlosti (vzhledem k magnetickému poli) protonů, iontů a urychlených elektronů z bulku jsou totožné. Dostáváme tak neutralizovaný svazek částic. Díky své malé hmotnosti jsou však elektrony na rozdíl od mnohem hmotnějších iontů a protonů navíc předmětem silného rozptylu, ale protože paralelní rychlosti těžkých částic a elektronů musí být stejné dochází během transportu k přenosu energie od těžkých částic k elektronům. Podle našich simulací přejdou asi 3% energie těžkých částic na elektrony, takže celková energie deponovaná netermálními elektrony taženými protony a ionty je asi 55× větší než jejich počáteční kinetická energie odpovídající rychlosti těžkých částic. Díky elektrickému spřažení protonů a iontů s elektrony představují neutralizované svazky jeden z mechanismů jak transportovat elektrony do hlubokých vrstev atmosféry, kde přes netermální srážkové koeficienty výrazně zvyšují emisi zejména v křídlech čáry Hα. Díky lokalizaci erupčního ohřevu v dolní chromosféře zároveň nepozorujeme v kontribuční funkci pro čáru Hα sekundární formační oblast typickou pro ohřev elektronovými svazky. Vzhledem k tomu, že čára je formována hluboko v chromosféře jsou výsledky velmi citlivé na model zářivých ztrát v opticky tlustém prostředí dolní atmosféry. V kontextu nových pozorování hloubek formace tvrdých HXR zdrojů v překvapivě hlubokých vrstvách atmosféry (Martínez Oliveros et al. 2012), představují neutrální svazky médium, které dokáže přenést energii netermálních částic i do těchto vrstev.

2.1.3 Modelování FIR a rádiových tepelných kontinuí v erupcích

Nově instalované antény přístroje ALMA (Atacama Large Milimeter Array) pro pozorování v mm rádiových vlnách a ve vzdálené infračervené oblasti (FIR) jsou díky svým vlastnostem, zejména díky bezprecedentnímu prostorovému a časovému rozlišení, velkým příslibem mimo jiné i pro sluneční fyziku včetně fyziky erupcí (Karlický et al. 2011; Krucker et al. 2013). U erupcí se v těchto oborech očekává emise vzniklá superpozicí dvou zářivých mechanismů: netermální vysokofrekvenční část mikrovlného spektra bude zřejmě generována zejména synchrotronovým mechanismem, tedy zářením urychlených (relativistických) elektronů a pozitronů pohybujících se v magnetickém poli a v nízkofrekvenční oblasti bude patrně dominovat termální kontinuum vznikající v důsledku erupčního ohřevu chromosféry (Vial et al. 2007). Relativní důležitost obou emisních procesů v erupcích odhadli (Ohki & Hudson 1975). První pozozorování erupcí v těchto spektrálních oborech se v současné době netrpělivě očekávají, protože se předpokládá, že otevřou zcela nové spektrální okno, kterým bude možno pozorovat jak netermálních elektrony, tak ohřev plazmatu přímo v oblasti termalizace elektronových svazků.

S ohledem na budování ALMA, rostla poptávka po modelech emise generované ve slunečních erupcích v spektrálních oborech mm vln a FIR. V **práci 4** jsme s využitím našeho kódu vytvořili dynamický model formování erupčních mikrovlných tepelných kontinuí. Studovali jsme vliv elektronových svazků s vysoce proměnným, pulzně se měnícím tokem na formování tepelných kontinuí v oblasti 35 μm – 1 cm a identifikovali oblast v chromosféře, kde tato kontinua vznikají. V našich simulacích jsme zahrnuli vliv srážek netermálních elektronů svazku s atomy vodíku. Ukázali jsme, že zahrnutí netermálních kolizních koeficientů má na jejich formování prakticky zanedbatelný vliv, nicméně intenzita těchto kontinuí je korelována s tokem elektronových svazků na sub-sekundových časových škálách. Dále bylo zjištěno, že jasnost tepelných kontinuí výrazně roste s vlnovou délkou. V klidné VAL C atmosféře vznikají tepelná kontinua s vlnovou délkou pod 1 mm v oblasti těsně nad fotosférou. V erupcích se oblast formace pro delší vlnové délky rozšiřuje směrem vzhůru do oblasti depozitu erupční energie. Nezávislé statické modely mikrovlných tepelných kontinuí v erupcích publikovali Heinzel & Avrett (2012) na základě semi-empirických modelů erupční atmosféry získaných pomocí non-LTE kódu pro přenos záření Pandora.

2.2 Zpětný proud v erupcích

Standardní CSHKP erupční model předpokládá transport energie ve formě vysokoenergetických elektronových svazků s extrémními částicovými toky plazmatem sluneční atmosféry z koróny do chromosféry. Ten nevyhnutelně vede ke vzniku enormních elektrických proudů, které se vytvoří v důsledku masivního transportu elektrického náboje spojeného s přenosem energie svazky elektronů. V elektricky vodivém plazmatu jsou tyto proudy v důsledku zákona elektromagnetické indukce a požadavku na zachování elektrické neutrality plazmatu prak-

ticky okamžitě přesně vybalancovány opačnými, takzvanými zpětnými, proudy, které jsou tvořeny volnými elektrony plazmatu sluneční atmosféry (Knight & Sturrock 1977; Hoyng et al. 1978; van den Oord 1990; Holman 2012). Většina modelů zpětného proudu předpokládá, že indukované elektrické pole urychlující volné elektrony v okolní atmosféře vytvoří na subsekundových časových škálách opačný proud, který neutralizuje účinky proudu neseného svazkem. Volné elektrony nesoucí zpětný proud pak díky srážkám s ionty přispívají k ohřevu okolního plazmatu. Současně pak indukované elektrické pole brzdí elektrony svazku a vedle coulombovských srážek tak přispívá k jeho termalizaci. Vliv zpětného proudu je tedy vedle coulombovských srážek dalším faktorem, který ovlivňuje erupční ohřev sluneční atmosféry.

Účinky zpětného proudu na šíření a termalizaci elektronových svazků byl studován řadou autorů, nicméně výsledky těchto studií jsou velmi nejednoznačné v závislosti na zvolených metodách a úhlech pohledu. Zatímco některé práce přisuzují zpětnému proudu významný dopad na termalizaci svazků, dokonce významnější než mají coulombovské srážky, alespoň v některých oblastech atmosféry (např. Emslie 1980; Brown & McClymont 1987), jiné (Rowland & Vlahos 1985) dospívají k opačnému závěru. Problematika vlivu zpětného proudu na erupční ohřev je nesmírně komplikovaná zejména z toho důvodu, že pro určení velikosti elektrického pole generujícího zpětný proud je nutné znát distribuční funkci elektronové složky plazmatu. Zřejmě právě z těchto důvodů nebyly efekty zpětného proudu na erupční ohřev nikdy zahrnuty ve standardních 1-D hydrodynamických erupčních modelech, přestože jak uvádí Brown & McClymont (1987) zahrnutí zpětného proudu ovlivňuje například hloubku průniku elektronového svazku do chromosféry, poměr energetických depozitů do chromosféry a koróny a podobně. Máli tedy skutečně zpětný proud velký vliv na termalizaci elektronových svazků, lze při jeho zahrnutí očekávat nezanedbatelné důsledky zejména v HXR oboru na tvar energetických spekter a v optickém oboru na formování spektrálních čar.

V literatuře lze vysledovat několik přístupů k této problematice. Nejednodušší přiblížení je založeno na předpokladu platnosti Ohmova zákona pro zpětný proud buď s klasickou – Spitzerovou (Spitzer 1962) elektrickou vodivostí plazmatu (Emslie 1981; Brown & McClymont 1987; McClements 1992; Syniavskii & Zharkova 1994; Holman 2012), nebo anomální elektrickou vodivostí plazmatu (Duijveman et al. 1981; Cromwell et al. 1988; Matthews et al. 1996). Tyto práce zkoumají formování a účinky zpětného proudu buď pomocí jednoduchých analytických modelů, nebo numerickým řešením Fokker-Planckovy rovnice. V tomto takzvaném ohmickém přiblížení se předpokládá, že zpětný proud je nesen elektrony bulku jejichž driftové rychlosti jsou dostatečně malé, aby platily předpoklady odvození klasických nebo anomálních elektrických vodivostí plazmatu. Toto přiblížení v principu zcela zanedbává možný vznik vysokorychlostních 'bezkolizních' populací tzv. runaway elektronů, přestože někteří autoři obdrželi poměrně vysoká elektrická pole v řádu jednotek až desítek procent pole Dreicerova (Duijveman et al. 1981). Tyto bezkolizní elektronové populace mohou nést významnou část zpětného proudu (Norman & Smith 1978). Pokud nastává tento případ, klasické a anomální transportní koeficienty přestávají platit a ohmické přiblížení přeceňuje účinky zpětného proudu na erupční ohřev.

Protipólem ohmických modelů, které předpovídají největší účinky zpětného proudu na erupční ohřev vysokoenergetickými elektronovými svazky jsou modely, které při splnění určitých podmínek v plazmatu předpokládají vznik silné turbulence generované šířením elektronových svazků a zachycení elektronů bulku právě touto turbulencí. V tomto modu je pak zpětný proud nesený poměrně malou populací vysokorychlostních, prakticky bezkolizních elektronů (Rowland & Vlahos 1985). V důsledku minimálních kolizních ztrát elektronů formujících zpětný proud, lze očekávat malý vliv na termalizaci elektronů svazku.

Abychom získali představu o elektronové distribuční funkci a mohli odhadnout v jakém z výše popsaných modů se šíří zpětný proud, pokusili jsme se v pracech **pracech 6** a **7** odhadnout charakter elektronové distribuční funkce plazmatu a na mikroskopické úrovni pochopit formování zpětného proudu vyvolaného šířením monoenergetického svazku vysokoenergetických elektronů s využitím modifikovaného 1-D particle-in-cell (PIC) kódu (Birdsall & Langdon 1991). Vzhledem k tomu, že časové škály odpovídající kolektivním jevům v plazmatu doprovázející vznik zpětného proudu jako je excitace Langmuirových vln jsou řádově mnohem kratší než časové škály pro srážky, modelovali jsme nejprve kolektivní jevy a proces fomování zpětného proudu na čele svazku v bezkolizní aproximaci pro chladné plazma. Tyto simulace ukázaly, že zpětný proud stejné velikosti jako proud nesený svazkem se ve studovaném systému skutečně zformuje na nesmírně krátkých časových škálách několika period plazmových vln. V druhé, kolizní aproximaci, jsme studovali vznik zpětného proudu pro plazma odpovídající sluneční chromosféře. Ukázalo se, že působením srážek se zanedbáním kolektivních jevů se stacionární zpětný proud vytvoří na delší časové škále ($\sim 10^{-6}$ s) a elektronová distribuční funkce rozštěpí na dvě populace: bulk s nulovou střední rychlostí a poměrně malou populaci (ze simulací řádově procenta populace bulku) rychlých elektronů nesoucích zpětný proud, což odpovídá závěrům práce Rowland & Vlahos (1985). Ve třetí aproximaci jsme se pokusili zahrnout jak srážky, tak i kolektivní jevy. Nejdůležitým výsledkem této simulace bylo, že výsledná elektronová distribuční funkce se výrazně liší od počátečního maxwellovského rozdělení. Zpětný proud tedy není tvořen prostým posunutím maxwellovského rozdělení v rychlostním prostoru, jak se někdy předpokládá v jednoduchých ohmických modelech, ale že změna distribuční funkce je silně rychlostně závislá, což je opět odpovídá závěrům získaným v práci Rowland & Vlahos (1985). Poslední dva modely umožnily určit velikost stacionární elektrické pole, které je nutné k udržení stacionárního zpětného proudu. Získané hodnoty v závislosti na modelu odpovídají desetinám až desítkám procent polí získaných z ohmického přiblížení. Z našich jednoduchých PIC simulací lze tedy usoudit, že ohmická aproximace zpětného proudu výrazně přečeňuje jeho skutečný vliv na termalizaci elektronových svazků.

Protože naše práce v tomto směru byla motivována snahou zahrnout makroskopické účinky zpětného proudu do našich RHD modelů erupcí, využili jsme výsledky získané z PIC simulací a potenciálu TPC. Ten umožňuje snadno určit prostoročasovou velikost elektrického proudu podél erupční smyčky. Pokud předpokládáme, že zpětný proud je tvořen pouze určitou malou populací elektronů bulku, lze odhadnout střední hodnotu jejich rychlosti a z pohybové rovnice, s využitím vztahu pro závislost účinného průřezu elektronů na rychlosti

– viz také Codispoti et al. (2013) a ve stacionárním případě dopočítat odpovídající hodnotu elektrického pole, které pak necháme působit na netermální elektrony svazku.

Energetické depozity pro různé toky svazků vypočtené v tomto přiblížení jsou zobrazeny v **práci 6** a srovnány s výsledky pro čistě ohmický model. Z prezentovaných grafů je patrné, že čistě ohmický model zpětného proudu vede, v závislosti na energetickém toku svazku, k posunu maxima energetického depozitu prakticky až do přechodové vrstvy a ke snížení energie deponované do chromosféry o několik řádů. Tento efekt roste s energetickým tokem svazku. Modelujeme-li vliv zpětného proudu v přiblížení popsaném v **práci 7** dostáváme sice, opět v závislosti na energetickém toku, poměrně výrazné přerozdělení deponované energie v choromosféře, ale celková energie deponovaná do chromosféry svazkem zůstává prakticky konstatní.

Získaný model energetického depozitu ovlivněného zpětným proudem byl pak použit v **práci 8**, kde jsme analyzovali vliv zpětného proudu na formování vodíkové Hα čáry. Největší změny v časovém vývoji intenzity čáry Hα vlivem zpětného proudu jsme zaznamenali v jejím centru, v prvních dvou sekundách časového vývoje. To je dáno výrazným zvýšením energetického depozitu v horní chromosféře působením zpětného proudu. Kromě zpětného proudu jsme rovněž uvažovali vliv netermálních kolizních koeficientů a formování čáry Hα v atmosféře bombardované protonovými svazky. Pro ně je vliv zpětného proudu zanedbatelný (Brown et al. 1990).

2.3 Modifikace CSHKP modelu a jejich důsledky

V článku 1.5 jsme poukázali na celou řadu problémů klasického CSHKP modelu erupcí vyplývajících z jeho analýzy z hlediska fundamentální fyziky. V důsledku toho se v posledních letech v literatuře objevila řada prací navrhující jeho modifikace, zejména v tom smyslu, že elektrony primárně urychlené v koronální proudové vrstvě jsou ještě dodatečně urychlovány během svého transportu do chromosféty statickými elektrickými poli (např. Gordovskyy et al. 2013; Gordovskyy & Browning 2012, 2011; Karlický 1995) nebo přímo v oblasti jejich termalizace, tedy v chromosférickém tlustém terči stochastickými elektrickými poli (např. Brown et al. 2009; Turkmani et al. 2006). Tyto práce navrhují zmíněné modifikace a v různé míře detailu zkoumají jednotlivé mechanismy, které vedou k sekundárnímu urychlování částic, většinou pomocí MHD modelů, studiem kinematiky jednotlivých částic nebo analytickými úvahami vedoucími k odhadům jejich vlivu. Nezabývají se však jejich důsledky na erupční ohřev, spektra a intenzitu HXR a polohy a velikosti HXR chromosférických zdrojů, tedy obecně na jejich pozorovatelné vlastnosti.

Náš relativistický kód s testovacími částicemi, na rozdíl od řešení FP rovnice metodou sítí, umožňuje velmi přirozeně simulovat efekty nejrůznějších dodatečných vlivů, které působí na netermální částice během jejich transportu, samozřejmě k působení coulombovských kolizí, jejichž vliv řeší kód primárně. Této vlastnosti jsme využili v **pracech 9**, **11** a **10**, kde se zabýváme důsledky dvou reakceleračních mechanismů diskutovaných v článku 1.5.2

na rozdělovací funkce netermálních elektronů, velikosti a prostorová rozložení erupčních ohřevů v chromosféře, spektra a intenzity HXR a polohy a velikosti HXR zdrojů v atmosféře. Ve všech uvedených pracech je základem VAL C atmosféra s konvergentním magnetickým polem směrem k fotosféře se zrcadlovým poměrem $R_m = 5$. Pouze v **práci 11** používáme modifikovaný plně ionizovaný VAL C. Hlavním cílem těchto prací bylo odhadnout efektivitu uvedených modifikací a předpovědět jejich observační důsledky.

V **práci 9** jsme zkoumali vliv statických polí generovaných proudovými hustotami $j = 1 - 6$ A m^{-2} a stochastických polí v oblasti tlustého terče se středními hodnotami polí $\overline{E} = 0$, 10^{-1} V m^{-1} a variancemi var$(E) = 0 - 5$ V m^{-1}. Vliv sekundární reakcelerace na kinematiku elektronových svazků je dobře patrný na jejich rozdělovacích funkcích, kde se kromě populací brzděných, rozptýlených a odražených částic (pro model bez reakcelerace), objevují nově populace vysokonergetických částic a to i v případě čistě stochastických polí s nenulovou variancí, ale nulovou střední hodnotou. Simulace ukázaly, že velikost energetického depozitu vertikálně integrovaného přes chromosféru je více než o půl řádu vyšší pro maximální uvažované hodnoty stochastického pole a o řád vyšší pro statické pole a maximální uvažovanou proudovou hustotu, obojí ve srovnání s čistě kolizním modelem bez sekundární akcelerace. Pokud jde o produkci HXR záření dostali jsme pro maximální hodnoty polí nárůst intenzity na energii 25 keV o jeden a půl řádu opět ve srovnání s modelem bez reakcelerace (pro identický energetický tok generovaný v koróně). Jedním z důležitých závěrů této práce je, že sekundární akcelerace s hodnotami reakceleračních polí ve studovaném rozsahu umožňuje snížit elektronové toky transportované z koronální primární akcelerační oblasti o více než jeden řád a současně zachovat celkovou energii deponovanou do chromosféry a intenzitu HXR srovnatelnou s hodnotami získanými pro extrémní toky odvozené pro klasický kolizní erupční model (Brown 1971).

Dále bylo zjištěno, že reakcelerace netermálních elektronů těmito, relativně malými, elektrickými poli posouvá maxima chromosférických depozitů energie přibližně o 750 km směrem fotosféře do výšky zhruba 600 km pro maximální hodnoty polí. Toto je nesmírně zajímavý výsledek ve světle nových přelomových simultánních pozorování přístrojů RHESSI a STEREO (Martínez Oliveros et al. 2012), která byla použita k měření hloubek zdrojů HXR a viditelného záření v chromosféře u bílých erupcí. Tato měření ukázala, že jejich poloha koresponduje s polohou zdroje bílého světla a leží v hloubce 500 – 130 km. Tento výsledek je pokládán erupční komunitou za zásadní. V současné době není znám žádný mechanismus v rámci klasického CSHKP modelu s kolizním tlustým terčem, který by byl schopen dopravit elektronové svazky do míst se slupcovou hustotou odpovídající naměřeným hloubkám. Srovnáme-li náš model stochastických polí s poli prezentovanými v Turkmani et al. (2006) zjistíme, že v této práci jsou zhruba o řád vyšší, nicméně jejich rozložení v atmosféře má nižší filling faktor. Je možné, že modifikací našeho modelu směrem k vyšším polím a nižším filling faktorům bychom byli schopni dopravit netermální elektrony ještě do větších hloubek.

V **práci 10** jsme zkoumali vliv sekundární reakcelerace na velikost chromosférických HXR zdrojů. Poměrně nová měření měření z dat družice RHESSI dávají vertikální rozměry HXR zdrojů od 1,3 do 8 obloukových sekund, tedy přibližně od 1 Mm do téměř 6 Mm

(Battaglia & Kontar 2011). Na druhou stranu, klasický kolizní model tlustého terče předpovídá jeho velikost v řádu maximálně stovek kilometrů. Naším cílem bylo zjistit, zda sekundární akcelerace elektronových svazků může vyřešit tento problém. Bohužel se ukázalo, že reakceklerace vede naopak ještě k dalšímu zúžení HXR zdrojů. Na druhou stranu může být validita tohoto výsledku značně ovlivněna skutečností, že atmosféra do níž deponujeme energii svazku je statická a nevykazuje žádnou hydrodynamickou odezvu. Vzhledem k tomu, že integrační doby družice RHESSI pro pořizování dvourozměrných obrazů HXR zdrojů jsou desítky sekund, za tuto dobu může v erupční atmosféře dojít ke značné vertikální redistribuci hmoty a v důsledku také k vertikálním pohybům HXR zdrojů. Tyto pohyby se pak vzhledem k integračním časům RHESSI projeví na dvourozměrných obrazech jako zvětšení velikosti zdrojů. V současné době provádíme simulace se zapojením hydrodynamickécho kódu a snažíme se ověřit tuto hypotézu.

V **pracech 9** a **10** deponujeme energii reakcelerovaných elektronových svazků do klidné (ohřevem neporušené) VAL C atmosféry, kde dolní chromosféra je tvořena téměř neutrálním vodíkem. Samozřejmě v erupcích dochází při ohřevu chromosféry k její hydrodynamické odezvě, ohřevu, ionizaci a makroskopickému transportu plazmatu. Cílem **práce 11** bylo ověřit zda skutečnost, že je atmosféra zcela ionizovaná významně ovlivní výsledky obdržené v předešlých dvou pracech. Tento test jsme provedli pro model stochatické reakcelerace s nenulouvou variancí a s nulovou střední hodnotou pole a zjistili jsme že tato skutečnost výsledky zásadním způsobem neovlivní.

Kapitola 3

Pozorování erupcí

V této kapitole se budeme zabývat zpracováním pozorování erupcí a diagnostikou erupčního plazmatu. Tato témata jsou náplní **prací 12 – 14**. Ty jsou založeny na zpracování dat z kosmických slunečních observatoří SOHO (z přístrojů EIT, LASCO, CDS), Yohkoh (SXT) a z pozemských pozorování Slunce ondřejovskými přístroji Multichannel Flare Spectrograph (MFC) v čáře Hα a radioteleskopem na frekvenci 3 GHz. **Práce 12** se zabývá detailní analýzou a diagnostikou rozpadající se arkády poerupčních smyček a jedná se o jednu z prvních prací využívajících data ze CDS, která se zabývá zpracováním pozorování erupčních dat. Další dvě **práce 13** a **14** se týkají hledáním observačních indicií potvrzujících probíhající magnetickou rekonexi ve sluneční koróně. V těchto pracech jsou detailně popsány procesy, které vedly ke spuštění erupčního procesu pro dvě pozorování erupcí.

3.1 Diagnostika a chladnutí systému poerupčních smyček

Klíčovým východiskem pro porozumění procesům probíhajících v erupčních smyčkách a pro modelování jejich časového vývoje jsou observačně zjištěné hodnoty termodynamických parametrů erupčního plazmatu. Mimo jiné to jsou elektronová hustota n_e a teplota plazmatu a dále pak diagnosticky významná míra emise definovaná vztahem

$$EM \equiv \int_V n_\mathrm{e}^2 \,\mathrm{d}V \,, \quad \text{neboli} \qquad EM = n_\mathrm{e}^2 V_\mathrm{em} = \overline{n_\mathrm{e}^2} V_\mathrm{app} \,,$$

kde v prvním vztahu integrujeme přes zářící objem plazmatu. Objemy V_em a V_app jsou skutečný a zdánlivý objem plazmatu, které přispívají k pozorované emisi. V_app v praxi odhadujeme z pozorování dané struktury s konečným prostorovým rozlišením. $\overline{n_\mathrm{e}}$ je potom střední hodnota elektronové hustoty v pozorované struktuře. Rozdíl mezi těmito dvěma objemy a elektronovými hustotami n_e a $\overline{n_\mathrm{e}}$ je dán skutečností, že zkoumané struktury často nejsme schopni prostorově zcela rozlišit.

Máme-li k dispozici nezáviská měření elektronové hustoty plazmatu a míry emise, můžeme určit tzv. geometrický filling faktor pozorované struktury, který vyjadřuje, zda je pozorovaná struktura zcela rozlišena, nebo obsahuje další, menší nerozlišitelné struktury, i podél zorného paprsku, mezi nimiž je prostor, který k emisi nepřispívá. V této souvislosti se ve sluneční fyzice se často mluví o tzv. špagetové struktuře plazmových koronálních smyček, které jsou podle tohoto modelu tvořeny mnoha tenkými oddělenými zářícími vlákny, přičemž plazma v prostoru mezi nimi přispívá k celkové intenzitě smyčky jen zanedbatelně. Geometrický filling faktor je v tomto kontextu je definován jako $f \equiv \overline{n_e^2}/n_e^2 \leq 1$, přičemž je-li $f = 1$, je pozorovaná struktura zcela rozlišena.

Práce 12 se zabývá detailní diagnostikou plazmatu v rozpadající se arkádě poerupčních smyček vzniklé při relativně malé erupci třídy C2.9, pozorované na jihozápadním okraji slunečního disku. V této práci jsme profitovali ze skutečnosti, že se více méně nedopatřením, v prvních letech mise se spektrometry na SOHO snažily vyhýbat erupcím z důvodu ochrany detektorů, podařilo napozorovat přístrojem Coronal Diagnostic Spectrometer (CDS) na SOHO, EUV spektra (skany) této poerupční oblasti ve 14-ti diagnosticky významných čarách, s formačními teplotami od 20 kK do 2,2 MK. Data ze CDS byla doplněna pozorováními z SXT (Yohkoh), která byla pořízena ve dvou různých filtrech a umožňovala tak přibližné určení časového vývoje míry emise a teploty horkého plazmatu v systému poerupčních smyček během jeho rozpadu. Navíc poskytly tyto snímky poerupční oblasti výborný vhled do topologie smyček. Vzhledem k tomu, že skany pořizované CDS trvaly přibližně 20 minut byla analýza CDS dat zkomplikovaná rychlým vývojem smyček, který se projevil deformací jejich tvaru. Jak jsme již uvedli, tato práce byla jednou z prvních prací týkající se erupcí, která byla založena na datech ze CDS.

3.1.1 Diagnostika plazmatu

Opticky tenké EUV čáry vznikající v přechodové oblasti a koróně mají nesmírný diagnostický potenciál (Mason et al. 1997). Například poměr intenzit dvou opticky tenkých, dovolených spektrálních čar jejichž kontribuční funkce se překrývají lze za předpokladu ionizační rovnováhy v plazmatu využít k teplotní diagnostice (Mason et al. 1997). Studovaná data ze CDS a poloha oblasti na okraji slunečního disku umožnila touto metodou zkoumat teplotní vertikální stratifikaci systému poerupčních smyček. K tomu byl využit teplotně senzitivní pár čar Fe XVI na 360.8 Å a Si XII na 520.7 Å. Bylo zjištěno, že plazma s nejvyšší teplotou v systému smyček leží nad smyčkou pozorovanou v nežhavější čáře Fe XVI s formační teplotou 2,2 MK. Vzhledem k tomu, že CDS rastry v různých čarách pro daný sken pozorují přesně stejnou oblast na Slunci, lze také pouhým vynesením intenzitních profilů poerupčních smyček získaných ve spektrálních čarách s různou formační teplotou určit, zda smyčky jsou vertikálně teplotně stratifikované nebo ne. Naše analýza jednoznačně prokázala ve shodě s CSHKP modelem erupcí a představami o formování poerupčních smyček (Kopp & Pneuman 1976) vertikální stratifikaci arkády poerupčních smyček, kdy horké smyčky leží

nad smyčkami chladnějšími a potvrdila tak dřívější pozorování ze Skylabu a SMM (Cheng 1980; Švestka et al. 1987) i pro tuto relativně malou erupci, která svou morfologií připomíná smyčkovou erupci (tzv. single loop flare).

Analýzou časového vývoje míry emise a teploty, určené z poměru intenzit oblasti ve dvou různých filtrech dalekohledu SXT (Tsuneta et al. 1991) bylo zjištěno, že hlavní roli při rozpadu pozorovaného systému smyček hrál odtok plazmatu ze systému, kdy během přibližně 10^3 s se střední míra emise snížila na čtvrtinu původní hodnoty. Tomu odpovídá rychlost odtoku plazmatu ze smyček $\sim$ 10 km s^{-1} za předpokladu jejich konstantního průřezu. Tato rychlost se řádově shoduje s později publikovanými výsledky získanými na základě Dopplerovských měření rychlostí odtoku plazmatu z jiné arkády poerupčních smyček pořízených v blízkosti středu slunečního disku pozorovaných opět CDS (Czaykowska et al. 2001). Časový vývoj teploty horké části smyček určený z pozorování SXT v různých filtrech sice vykazoval určité známky chladnutí, ale interpretace jeho vlivu na vývoj smyčky není zdaleka tak přímočará jako v případě míry emise. Detailněji se budeme chladnutím studovaných smyček zabývat dále.

V **práci 12** jsme se rovněž zabývali diagnostikou elektronové hustoty plazmatu ve smyčkách, kde jsme využili diagnostického potenciálu hustotně citlivého páru čar Fe XIV 334.2 Å a 353.8 Å s formační teplotou $\sim 1,8$ MK, který je citlivý v rozsahu od $10^9 - 10^{11}$ cm^{-3} (Mason 1998) a pro nějž jsme měli k dispozici atomová data. Tato metoda je unikátní v tom, že umožňuje přímo měřit n_e a ne zprostředkovaně přes míru emise, kde do jejího určení nevyhnutelně vstupují otázky rozlišení pozorované struktury, tedy geometrický filling faktor. Během celé analýzy jsme kladli velký důraz na správné určení chyb měření zohledním fotonové statistiky, kalibrace detektoru CDS, chyb vzniklých při fitování profilů čar Gausovými profily a překryvů čar. Bylo zjištěno, že ve vrcholu smyčky (pozorovatelné v čarách Fe XIV) je $n_e = 0,8 - 1.4 \times 10^{10}$ cm^{-3}. Poměrně velká chyba odráží reálnou přesnost našeho měření. Tento výsledek řádově odpovídá výsledkům obdrženým ze zpracování dat z dřívějších misí jako Solrad 9 a Skylab (např. Dere & Cook 1979; Cheng 1980).

Intezity dovolených čar určené ze spektrálních fitů byly dále využity k nezávislému určení míry emise plazmatu v dané čáře metodou popsanou v práci Pottasch (1963). Kontribuční funkce jednotlivých čar byly určeny pomocí programového balíku ADAS (Lanzafame et al. 1996). Bohužel do přesnosti této metody se promítá velká nepřesnost ve znalosti zastoupení prvků ve sluneční atmosféře, která dosahuje až 30%. Ze znalosti míry emise a odhadu objemu emitující struktury lze určit střední hodnotu kvadrátu elektronové hustoty a následně využitím hodnot n_e z přímého měření poměrů intenzit, které reflektují elektronové srážkové frekvence v plazmatu, lze určit geometrický filling faktor. Vzhledem k chybám, které se kumulují při určování elektronových hustot plazmatu vstupujících do rovnice definující filling faktor se podařilo získat pouze jeho horní mez $f \leq 0,2$. Tato hodnota byla získána pro plazma s teplotou $T \approx 1,8$ MK, odpovídající formační teplotě čar Fe XIV 334.2 Å a 353.8 Å. Lze tedy vyvodit, že pozorovaná arkáda poerupčních smyček měla výrazně filamentární strukturu, která nebyla rozlišena použitým přístrojem. Tento výsledek je důležitý také z toho pohledu, že elektronová hustota určená z míry emise, například zpra-

covánim pozorování téže struktury ve dvou různých filtrech, se může významně lišit od skutečné hodnoty a výrazně ovlivnit teoretické interpretace takových pozorování. Toto byl jeden z důležitých závěrů této práce.

3.1.2 Chladnutí poerupčních smyček

Získané hodnoty teploty a elektronové hustoty ve smyčkách byly použity k odhadu času chladnutí horkých smyček poerupční arkády z počáteční teploty přibližně 2,8 MK (teplota smyček pozorovaných v SXR) na teplotu $\simeq$ 20 kK (smyčky pozorované v čáře He I). K výpočtu byla použita metoda diskutována v pracech (Varady & Heinzel 1997a,b) vycházející z toho, že poerupční plazma v koróně chladne vlivem vedení tepla, které díky silné teplotní závislosti koeficientu vedení tepla ($\kappa \propto T^{2.5}$) dominuje za vysokých teplot a u menších smyček, a zářivým ztrátám, které dominují pro velké a husté smyčky za nižších teplot ($R \propto EM$). Abychom se vyhnuhli náročnému hydrodynamickému modelování procesu chladnutí se současným odtokem plazmatu ze smyčky, použili jsme velmi hrubé přiblížení statického, plně ionizovaného plazmatu, tedy $n_e(s,t) = konst$. Tímto způsobem jsme získali čas chladnutí horkých smyček poerupčního systému $\sim$ 750 s. Vzhledem k masivnímu odtoku plazmatu ze smyček během jejich rozpadu lze očekávat, že reálná hodnota času chladnutí bude o něco vyšší. Teoretický odhad času chladnutí je srovnatelný s pozorovaným časem rozpadu systému od okamžiku počátku našeho pozorování.

3.2 Pozorování magnetické rekonekce v koróně

Práce 13 a **14** jsou věnovány multispekrálním studiím, které se zbývají inicializací erupčních procesů a hledáním známek probíhající rekonexe ve sluneční atmosféře. Tyto práce vznikaly v éře japonské sluneční observatoře Yohkoh (Ogawara et al. 1991), kdy se hledaly observační důkazy magnetické rekonexe v kóróně s využitím multispektálních dat, zejména však v té době dat z přelomového rentgenového dalekohledu SXT (Tsuneta et al. 1991), zobrazujícího termální měkké rentgenové záření koronálních a erupčních smyček. Práce tohoto typu se pokoušely rozplést komplikované před-rekonekční a rekonekční topologie magnetických polí a pomocí měření Dopplerovských rychlostí ze spektrálních čar ve vizuálním oboru kombinovaných s rádiovými a SXR daty najít znaky probíhající rekonexe. Dalším cílem těchto prací bylo nalezení spouštěcích mechanismů erupcí a určení kauzality mezi mnoha prakticky simultánně probíhajícími procesy jako jsou inicializace filamentu a tedy aktivace eruptivní protuberance a výronu koronální hmoty (CME), vynořování nového nebo zanořování starého magnetického toku, vznik SXR erupčních smyček a podobně.

Práce 13 se zabývá analýzou vývoje mohutné eruptivní protuberance (destabilizace filamentu) ze dne 18. září 1995 na severovýchodním okraji disku pozorovanou ondřejovským Multichannel Flare Spektrograph (MFS). Iniciaci této protuberance předcházelo slabé rádiové vzplanutí na 3 GHz pozorované jedním z ondřejovských radioteleskopů, které in-

dikovalo probíhající netermální procesy. Destabilizace filamentu vedla ke spuštění malé erupce třídy B4.2, která byla pozorována v měkkém rentgenovém oboru dalekohledem SXT (Yohkoh). Detailní analýzou simultánních pozorování v SXR oboru a redukcí spektrálních profilů čáry Hα se podařilo přesvědčivě dokázat, že v oblasti pod stoupající eruptivní protuberancí probíhá magnetická rekonexe v několika místech křížení magnetických smyček. Tuto intepretaci potvrdila měření Dopplerovských rychlostí, které v těchto bodech dosahovaly hodnot 50 - 100 km/s, což odpovídá rychlostem vtoku plazmatu do rekonekčního X-bodu.

Pozorování podobného druhu ze dne 27.5. 1999 je zpracováno v **práci 14**. S využitím pokročilých metod pro zpracování obrazu jsme našli dvě lokální minima intenzity přičemž spodní leží v oblasti kde v SXR pozorujeme horkou koronální smyčku, která se v Hα oboru jeví jako transparentní. Za předpokladu, že se nejedná o projekční efekt to znamená, že v bezprostřední blízkosti chladného plazmatu eruptivní protuberance ($T < 20$ kK) dochází uvolňování energie akumulované v magnetickém poli. Topologie, kterou pozorujeme v tomto případě je velmi podobná topologii pozorované v **práci 13** a předpoládáme proto probíhající magnetickou rekonexi v prostoru mezi chladným plazmatem eruptivní protuberance a horkým plazmatem pozorovaným v SXR oboru.

Studie zaměřené na hledání rekonexe ve sluneční koróně s využitím dat ze současných kosmických přístrojů se objevují i v současné literatuře. Velmi pěkným příkladem je práce (Su et al. 2013), která k tomuto účelu využívá EUV snímky z Atmospheric Imaging Assembly (AIA) na Solar Dynamic Observatory (SDO) kombinované s RHESSI pozorováními v HXR. V této práci je na videích dokumentována celá řada procesů, které lze interpretovat jako probíhající rekonexi magnetického pole v koróně.

Literatura

Abbett, W. P. & Hawley, S. L. 1999, ApJ, 521, 906

Allred, J. C., Hawley, S. L., Abbett, W. P., & Carlsson, M. 2006, ApJ, 644, 484

An, C.-H., Canfield, R. C., Fisher, G. H., & McClymont, A. N. 1983, ApJ, 267, 421

Asai, A., Ichimoto, K., Kita, R., Kurokawa, H., & Shibata, K. 2012, PASJ, 64, 20

Aschwanden, M. J. 2005, Physics of the Solar Corona. An Introduction with Problems and Solutions (2nd edition) (Springer–Verlag Berlin Heidelberg New York)

Ayres, T., Uitenbroek, H., Cauzzi, G., et al. 2009, in Astronomy, Vol. 2010, astro2010: The Astronomy and Astrophysics Decadal Survey, 9

Bai, T. 1982, ApJ, 259, 341

Bárta, M., Büchner, J., Karlický, M., & Kotrč, P. 2011a, ApJ, 730, 47

Bárta, M., Büchner, J., Karlický, M., & Skála, J. 2011b, ApJ, 737, 24

Bastian, T. S., Benz, A. O., & Gary, D. E. 1998, ARA&A, 36, 131

Battaglia, M. & Kontar, E. P. 2011, A&A, 533, L2

Battaglia, M., Kontar, E. P., Fletcher, L., & MacKinnon, A. L. 2012, ApJ, 752, 4

Birdsall, C. K. & Langdon, A. B. 1991, Plasma Physics via Computer Simulation (Adam Hilger, Bristol, England)

Bray, R. J., Cram, L. E., Durrant, C., & Loughhead, R. E. 1991, Plasma Loops in the Solar Corona (Cambridge University Press)

Brown, J. C. 1971, Sol. Phys., 18, 489

Brown, J. C., Karlicky, M., MacKinnon, A. L., & van den Oord, G. H. J. 1990, ApJS, 73, 343

Brown, J. C., Karlický, M., Mandzhavidze, N., & Ramaty, R. 2000, ApJ, 541, 1104

Brown, J. C. & McClymont, A. N. 1987, Ap&SS, 133, 297

Brown, J. C. & Melrose, D. B. 1977, Sol. Phys., 52, 117

Brown, J. C., Turkmani, R., Kontar, E. P., MacKinnon, A. L., & Vlahos, L. 2009, A&A, 508, 993

Canfield, R. C., Fisher, G. H., & McClymont, A. N. 1983, ApJ, 265, 507

Carlsson, M. & Stein, R. F. 1995, ApJ, 440, L29

Carlsson, M. & Stein, R. F. 1997, ApJ, 481, 500

Carmichael, H. 1964, NASA Special Publication, 50, 451

Carrington, R. C. 1859, MNRAS, 20, 13

Cheng, C.-C. 1980, Sol. Phys., 65, 347

Codispoti, A., Torre, G., Piana, M., & Pinamonti, N. 2013, The Astrophysical Journal, 773, 121

Cromwell, D., McQuillan, P., & Brown, J. C. 1988, Sol. Phys., 115, 289

Czaykowska, A., Alexander, D., & De Pontieu, B. 2001, ApJ, 552, 849

del Zanna, G., Berlicki, A., Schmieder, B., & Mason, H. E. 2006, Sol. Phys., 234, 95

Dere, K. P. & Cook, J. W. 1979, ApJ, 229, 772

Donea, A.-C. & Lindsey, C. 2005, ApJ, 630, 1168

Duijveman, A., Hoyng, P., & Ionson, J. A. 1981, ApJ, 245, 721

Dzifčáková, E. & Kulinová, A. 2011, A&A, 531, A122

Emslie, A. G. 1978, ApJ, 224, 241

Emslie, A. G. 1980, ApJ, 235, 1055

Emslie, A. G. 1981, ApJ, 249, 817

Fang, C., Henoux, J. C., Ju, H., et al. 1995, Sol. Phys., 157, 271

Fárník, F., Hudson, H., & Watanabe, T. 1996, Sol. Phys., 165, 169

Fisher, G. H., Canfield, R. C., & McClymont, A. N. 1985a, ApJ, 289, 434

Fisher, G. H., Canfield, R. C., & McClymont, A. N. 1985b, ApJ, 289, 425

Fisher, G. H., Canfield, R. C., & McClymont, A. N. 1985c, ApJ, 289, 414

Fletcher, L. & Hudson, H. S. 2002, Sol. Phys., 210, 307

Fletcher, L. & Hudson, H. S. 2008, ApJ, 675, 1645

Fletcher, L., Turkmani, R., Hudson, H. S., et al. 2010, ArXiv e-prints

Gordovskyy, M. & Browning, P. K. 2011, ApJ, 729, 101

Gordovskyy, M. & Browning, P. K. 2012, Sol. Phys., 277, 299

Gordovskyy, M., Browning, P. K., Kontar, E. P., & Bian, N. H. 2013, Sol. Phys., 284, 489

Guo, J., Emslie, A. G., & Piana, M. 2013, ApJ, 766, 28

Heinzel, P. 1995, A&A, 299, 563

Heinzel, P. & Avrett, E. H. 2012, Sol. Phys., 277, 31

Henoux, J. C., Fang, C., & Gan, W. Q. 1995, A&A, 297, 574

Hirayama, T. 1974, Sol. Phys., 34, 323

Hodgson, R. 1859, MNRAS, 20, 15

Holman, G. D. 2012, ApJ, 745, 52

Holman, G. D., Sui, L., Schwartz, R. A., & Emslie, A. G. 2003, ApJ, 595, L97

Hoyng, P., Knight, J. W., & Spicer, D. S. 1978, Sol. Phys., 58, 139

Hudson, H. S. 2012, private communication

Karlický, M. 1990, Sol. Phys., 130, 347

Karlický, M. 1995, A&A, 298, 913

Karlický, M. 2009, ApJ, 690, 189

Karlický, M. & Bárta, M. 2006, ApJ, 647, 1472

Karlický, M., Bárta, M., Dąbrowski, B. P., & Heinzel, P. 2011, Sol. Phys., 268, 165

Karlický, M., Brown, J. C., Conway, A. J., & Penny, G. 2000, A&A, 353, 729

Karlický, M. & Kontar, E. P. 2012, A&A, 544, A148

Kashapova, L. K., Kotrč, P., & Kupryakov, Y. A. 2008, Annales Geophysicae, 26, 2975

Knight, J. W. & Sturrock, P. A. 1977, ApJ, 218, 306

Kontar, E. P. & Brown, J. C. 2006, ApJ, 653, L149

Kopp, R. A. & Pneuman, G. W. 1976, Sol. Phys., 50, 85

Kosovichev, A. G. & Zharkova, V. V. 1998, Nature, 393, 317

Kosugi, T., Makishima, K., Murakami, T., et al. 1991, Sol. Phys., 136, 17

Kotrč, P., Karlický, M., Šimberová, S., Knížek, M., & Varady, M. 1998, Sol. Phys., 182, 393

Krucker, S., Battaglia, M., Cargill, P. J., et al. 2008a, A&A Rev., 16, 155

Krucker, S., Giménez de Castro, C. G., Hudson, H. S., et al. 2013, A&A Rev., 21, 58

Krucker, S., Hurford, G. J., MacKinnon, A. L., Shih, A. Y., & Lin, R. P. 2008b, ApJ, 678, L63

Lanzafame, A. C., Summers, H. P., & Brooks, D. H. 1996, in Astronomical Society of the Pacific Conference Series, Vol. 109, Cool Stars, Stellar Systems, and the Sun, ed. R. Pallavicini & A. K. Dupree, 267

Lin, J., van Ballegooijen, A. A., & Forbes, T. G. 2002a, Journal of Geophysical Research (Space Physics), 107, 1438

Lin, R. P., Dennis, B. R., Hurford, G. J., et al. 2002b, Sol. Phys., 210, 3

Lin, R. P., Krucker, S., Hurford, G. J., et al. 2003, ApJ, 595, L69

Liu, C., Deng, N., Liu, R., et al. 2012, ApJ, 745, L4

Liu, R. & Wang, H. 2009, ApJ, 703, L23

Machado, M. E., Avrett, E. H., Vernazza, J. E., & Noyes, R. W. 1980, ApJ, 242, 336

MacKinnon, A. L. & Craig, I. J. D. 1991, A&A, 251, 693

Mariska, J. T. 1993, The Solar Transition Region (Cambridge University Press)

Martens, P. C. H. 1988, ApJ, 330, L131

Martínez Oliveros, J.-C., Hudson, H. S., Hurford, G. J., et al. 2012, ApJ, 753, L26

Mason, H. E. 1998, in Lecture Notes in Physics, Berlin Springer Verlag, Vol. 507, Space Solar Physics: Theoretical and Observational Issues in the Context of the SOHO Mission, ed. J. C. Vial, K. Bocchialini, & P. Boumier, 143

Mason, H. E., Young, P. R., Pike, C. D., et al. 1997, Sol. Phys., 170, 143

Masuda, S., Kosugi, T., Hara, H., Tsuneta, S., & Ogawara, Y. 1994, Nature, 371, 495

Matthews, S. A., Brown, J. C., & Melrose, D. B. 1996, A&A, 305, L49

McClements, K. G. 1992, A&A, 258, 542

McClymont, A. N. & Canfield, R. C. 1983a, ApJ, 265, 497

McClymont, A. N. & Canfield, R. C. 1983b, ApJ, 265, 483

Mihalas, D. & Mihalas, B. W. 1984, Foundations of radiation hydrodynamics (Oxford university Press, Inc.)

Neidig, D. F. 1989, Sol. Phys., 121, 261

Nitta, N. V., Schrijver, C. J., Title, A. M., & Liu, W. 2013, ApJ, 776, 58

Norman, C. A. & Smith, R. A. 1978, A&A, 68, 145

Ogawara, Y., Takano, T., Kato, T., et al. 1991, Sol. Phys., 136, 1

Ohki, K. & Hudson, H. S. 1975, Sol. Phys., 43, 405

Oran, E. S. & Boris, J. P. 1987, NASA STI/Recon Technical Report A, 88, 44860

Pottasch, S. R. 1963, ApJ, 137, 945

Priest, E. R. 1981, Solar flare magnetohydrodynamics (D. Reidel Publishing Company, Dordrecht/Boston/Lancaster)

Radziszewski, K., Rudawy, P., & Phillips, K. J. H. 2007, A&A, 461, 303

Radziszewski, K., Rudawy, P., & Phillips, K. J. H. 2011, A&A, 535, A123

Rowland, H. L. & Vlahos, L. 1985, A&A, 142, 219

Sakai, J. I. & Nagasugi, Y. 2007, A&A, 474, L33

Schrijver, C. J., De Rosa, M. L., Metcalf, T., et al. 2008, ApJ, 675, 1637

Shibata, K. & Tanuma, S. 2001, Earth, Planets, and Space, 53, 473

Simnett, G. M. & Haines, M. G. 1990, Sol. Phys., 130, 253

Skála, J., Bárta, M., & Varady, M. 2011, Central European Astrophysical Bulletin, 35, 195

Spitzer, L. 1962, Physics of Fully Ionized Gases (New York: Interscience (2nd edition))

Sturrock, P. A. 1966, Nature, 211, 695

Su, Y., Veronig, A. M., Holman, G. D., et al. 2013, Nature Physics, 9, 489

Švestka, Z. 1976, Solar Flares (Springer-Verlag Berlin Heidelberg)

Švestka, Z. F., Fontenla, J. M., Machado, M. E., Martin, S. F., & Neidig, D. F. 1987, Sol. Phys., 108, 237

Syniavskii, D. V. & Zharkova, V. V. 1994, ApJS, 90, 729

Török, T. & Kliem, B. 2005, ApJ, 630, L97

Tsuneta, S., Acton, L., Bruner, M., et al. 1991, Sol. Phys., 136, 37

Tsuneta, S., Hara, H., Shimizu, T., et al. 1992, PASJ, 44, L63

Turkmani, R. & Brown, J. 2012, in Astronomical Society of the Pacific Conference Series, Vol. 454, Astronomical Society of the Pacific Conference Series, ed. T. Sekii, T. Watanabe, & T. Sakurai, 349

Turkmani, R., Cargill, P. J., Galsgaard, K., Vlahos, L., & Isliker, H. 2006, A&A, 449, 749

Turkmani, R., Vlahos, L., Galsgaard, K., Cargill, P. J., & Isliker, H. 2005, ApJ, 620, L59

van den Oord, G. H. J. 1990, A&A, 234, 496

Varady, M., Fludra, A., & Heinzel, P. 2000, A&A, 355, 769

Varady, M. & Heinzel, P. 1997a, in ESA Special Publication, Vol. 404, Fifth SOHO Workshop: The Corona and Solar Wind Near Minimum Activity, ed. A. Wilson, 705

Varady, M. & Heinzel, P. 1997b, Hvar Observatory Bulletin, 21, 33

Varady, M., Karlický, M., & Kašparová, J. 2005, in ESA Special Publication, Vol. 600, The Dynamic Sun: Challenges for Theory and Observations

Varady, M., Karlický, M., & Kašparová, J. 2007, in Astronomical Society of the Pacific Conference Series, Vol. 368, The Physics of Chromospheric Plasmas, ed. P. Heinzel, I. Dorotovič, & R. J. Rutten, 473

Varady, M., Karlický, M., Moravec, Z., & Kašparová, J. 2014, A&A, 563, A51

Varady, M., Moravec, Z., Karlický, M., & Kašparová, J. 2013, Journal of Physics: Conference Series, 440, 012013

Vernazza, J. E., Avrett, E. H., & Loeser, R. 1981, ApJS, 45, 635

Veronig, A., Vršnak, B., Temmer, M., & Hanslmeier, A. 2002, Sol. Phys., 208, 297

Veronig, A. M. & Brown, J. C. 2004, ApJ, 603, L117

Veronig, A. M., Gomory, P., Kienreich, I. W., et al. 2011, ApJ, 743, L10

Vial, J.-C., Auchère, F., Chang, J., et al. 2007, Advances in Space Research, 40, 1787

Vlahos, L., Isliker, H., & Lepreti, F. 2004, ApJ, 608, 540

Williams, D. R., Török, T., Démoulin, P., van Driel-Gesztelyi, L., & Kliem, B. 2005, ApJ, 628, L163

Příloha A

Zahrnuté práce

K habilitační práci je přiloženo 14 publikací. **Práce 1** až **5** se týkají modelování erupčních procesů metodami zářivé hydrodynamiky a základního popisu kódu HYDRAD. V **pracech 6** až **8** se zabýváme modelováním formování a vlivu zpětného proudu na erupční ohřev a formování vodíkové čáry Hα. V **pracech 9** a **11** využíváme metody testovacích částic a zkoumáme důsledky modifikací klasického CSHKP modelu na energetický depozit, HXR spektra a velikost a polohu zdroje HXR. **Práce 12** až **14** jsou observačního charakteru. **Práce 12** se zabývá detailní diagnostikou plazmatu v arkádách poerupčních smyček v SXR, EUV a Hα oborech, zbylé dvě identifikují místa a jevy ve sluneční koróně, kde může docházek k rekonexi koronálních magnetických polí.

A.1 Seznam zahrnutých prací s vymezením podílu autora

Práce-1 **Varady M.,** Kašparová J., Moravec Z., Heinzel P., Karlický M., 2010, *"Modeling of Solar Flare Plasma and Its Radiation"*, IEEE Transactions on Plasma Science **38**, 2249 – 2253 **70%**

Práce-2 Kašparová J., Heinzel P., **Varady M.,** Karlický M., 2003, *"Time-dependent Flare Models with MALI"*, in Proc. Stellar Atmos. Model., Astronomical Society of the Pacific Conference Series **288**, Edited by I. Hubeny, D. Mihalas and K. Werner, 544 – 547 **20%**

Práce-3 Kašparová J., **Varady M.,** Heinzel P., Karlický M., Moravec Z., 2009, *"Response of optical hydrogen lines to beam heating. I. Electron beams"*, A&A **499**, 923 – 934 **30%**

Práce-4 Kašparová J., Heinzel P., Karlický M., Moravec Z., **Varady M.,** 2009, *"Far-IR and Radio Thermal Continua in Solar Flares"*, Central European Astrophysical Bulletin, **33**, 309 – 317 **20%**

Práce-5 **Varady M.,** Kašparová J., Moravec Z., Karlický M., Heinzel P., 2012, *"Formation of Balmer Lines in Impulsively Heated Flare Atmosphere by Neutral Beams"*, Hinode-3: The 3rd Hinode Science Meeting, Astronomical Society of the Pacific Conference Series **454**, Edited by T. Sekii, T. Watanabe, and T. Sakurai, p. 341 – 344 **60%**

Práce-6 **Varady M.,** Karlický M., Kašparová J., 2005, *"Problem of the Return Current in Energy Deposit in Flares"*, Proceedings of the 11th European Solar Physics Meeting "The Dynamic Sun: Challenges for Theory and Observations"ESA SP **600**. Editors: D. Danesy, S. Poedts, A. De Groof and J. Andries. Published on CDROM., p.146.1 **50%**

Práce-7 **Varady M.,** Karlický M., Kašparová J., 2007, *"Return Current and Energy Deposit in Flares"*, The Physics of Chromospheric Plasmas ASP Conference Series **368**, Edited by P. Heinzel, I. Dorotovič, and R. J. Rutten. San Francisco: Astronomical Society of the Pacific, 473 –478 **50%**

Práce-8 Kašparová J., **Varady M.,** Karlický, M.; Heinzel, P.; Moravec, Z., 2007, *"Hα with Heating by Particle Beams"*, The Physics of Chromospheric Plasmas ASP Conference Series **368**. Edited by P. Heinzel, I. Dorotovič, and R. J. Rutten. San Francisco: Astronomical Society of the Pacific, 441 – 446 **30%**

Práce-9 **Varady M.,** Karlický M., Moravec Z., Kašparová J., 2014, *"Modifications of thick-target model: re-acceleration of electron beams by static and stochastic electric fields"*, A&A **563**, A51 **50%**

Práce-10 Moravec Z., **Varady M.,** Karlický M., Kašparová J., 2013, *"Simulations of HXR Foot-point Source Sizes for Modified Thick-target Models"*, Central European Astrophysical Bulletin **37**, 535 – 540 **20%**

Práce-11 **Varady M.,** Moravec Z., Karlický M., Kašparová J., 2013, *"Observational consequences of the local re-acceleration thick-target model"*, Journal of Physics: Conference Series **440**, Issue 1, article id. 012013 **60%**

Práce-12 **Varady M.,** Fludra A., Heinzel P., 2000, *"Decaying post-flare loops system observed by SOHO/CDS and Yohkoh/SXT"*, A&A **355**, 769 – 780 **80%**

Práce-13 Kotrč P., Karlický, M.; Šimberová, S., Knížek M., **Varady M.**, 1998, *"Evidence of Magnetic Field Reconnection in the Hα Eruptive Prominence on 18th September 1995"*, Solar Physics **182**, Issue 2, 393 – 409 **10%**

Práce-14 Šimberová, S., Karlický, M.; **Varady M.**, Rank G., 2001, *"Holes in the Hα Eruptive Prominence Structure"*, Solar Physics, **201**, Issue 1, 119-131 **30%**

Příloha B

Kopie zahrnutých prací

IEEE TRANSACTIONS ON PLASMA SCIENCE, VOL. 38, NO. 9, SEPTEMBER 2010 2249

Modeling of Solar Flare Plasma and Its Radiation

Michal Varady, Jana Kašparová, Zdeněk Moravec, Petr Heinzel, and Marian Karlický

***Abstract*—We present a modular and highly versatile test particle–radiative hydrodynamic code which simultaneously models the particle beam energy transport and deposition, the corresponding explosive response of the flare atmosphere and the NLTE (NLTE, plasma and radiation out of the local thermodynamic equilibrium) radiative transfer for partly ionized hydrogen in the chromosphere and photosphere. The computational domain covers the photosphere, the chromosphere, the transition region, and the corona with the initial hydrostatic preflare atmosphere. To demonstrate the potential of the code, we calculate the time evolution of the Balmer line profiles corresponding to the time variation of the electron beam flux derived from the observed flare hard X-ray emission.**

***Index Terms*—Hydrodynamics, particle beam transport, solar radiation, spectral analysis.**

I. Introduction

IN THE CONTEXT of interpreting the nonthermal hard X-ray emission emanating from the footpoints of the flare loops, all contemporary solar flare models assign a fundamental role during the flare-energy release, transport, and deposition to the high-energy nonthermal particle beams with power-law spectra which are accelerated due to the magnetic reconnection of the magnetic fields in the solar atmosphere. In the impulsive phase of the flares, the beams formed by charged particles are guided from the acceleration site (wherever it is located in the solar atmosphere) along the magnetic field lines downward into the transition region, the chromosphere, and, possibly, the photosphere. Here in the lower atmospheric layers, due to the high density of the local plasma, their kinetic energy is efficiently dissipated by Coulomb collisions, the corresponding regions are rapidly heated, and the dramatic changes of the temperature and ionization occur. This results in an explosive evaporation of the locally heated plasma into the corona accompanied by a dramatic evolution of the profiles and intensities of the optical chromospheric lines.

Due to the demandingness of the simultaneous treatment of the hydrodynamics and the NLTE radiative transfer (NLTE-RT) in the deep layers of the solar atmosphere, only a few attempts have been made to model the time evolution of the optical emission of the flares. The first models for the pulse beam heating were developed by Canfield *et al.* [4] and Fisher *et al.* [6]. Recently, Allred *et al.* [1] studied the optical flare emission in several lines and continua using the complex radiative hydrodynamic (HD) simulations of the electron beam heating on a time scale up to several tens of seconds.

The first part of this paper is devoted to the detailed description of our test particle (TP)–radiative HD code. In the second part, an example is shown of how the code can model the time evolution of the hydrogen Balmer lines during the electron beam bombardment of the solar atmosphere, where the parameters of the beam have been derived from the observations of the hard X-ray flare emission.

II. Code Description

The code is based on three originally autonomous codes which have been extensively tested and used in the past: the TP code, originally for monoenergetic beams [10], [11], the 1-D HD code [26], and the time-dependent NLTE-RT code [8], [12], [14]. The TP and the NLTE-RT codes have recently been upgraded and integrated with the 1-D HD code. Because the TP and HD codes are essentially explicit (only the heat conduction is treated implicitly), the integrated TP–radiative HD code can have a modular structure, and therefore, it is highly versatile. The code self-consistently and simultaneously models the following important mechanisms in flares: the transport and gradual thermalization (flare heating) of the charged particle beams propagating from the acceleration site downward through the ambient flare atmosphere (TP code), the response of the originally hydrostatic atmosphere to the beam dissipated energy (1-D HD code), and the NLTE-RT for the hydrogen in the chromosphere and photosphere where the hydrogen is only partly ionized (time-dependent NLTE-RT code). In the following paragraphs, the details of the physics behind the individual codes are given, and their implementation is explained. An application of the code for the case of the Balmer line formation in the atmosphere heated by an electron beam can be found in [15].

A. Particle Beam Transport and Energy Dissipation

The properties of the flare heating are fully given by the initial parameters of the particle beams and by the instant density

Manuscript received December 1, 2009; revised May 7, 2010 and June 30, 2010; accepted June 30, 2010. Date of publication August 5, 2010; date of current version September 10, 2010. This work was supported in part by the Grant Agency of the Czech Republic under Grants 205/07/1100 and P209/10/1680 and in part by the Astronomical Institute under research project AV0Z10030501.

M. Varady is with Katedra fyziky, Přírodovědecká fakulta Univerzity J. E. Purkyně, 400 96 Ústí nad Labem, Czech Republic and also with Astronomický ústav, Akademie věd ČR, 251 65 Ondřejov, Czech Republic (e-mail: mvarady@physics.ujep.cz).

J. Kašparová and P. Heinzel are with Astronomický ústav, Akademie věd ČR, 251 65 Ondřejov, Czech Republic (e-mail: kasparov@asu.cas.cz; pheinzel@sunkl.asu.cas.cz).

Z. Moravec is with Katedra fyziky, Přírodovědecká fakulta Univerzity J. E. Purkyně, 400 96 Ústí nad Labem, Czech Republic (e-mail: zdenek.moravec@ujep.cz).

M. Karlický is with Astronomický ústav, Akademie věd ČR, 251 65 Ondřejov, Czech Republic and also with Astronomický Ústav Univerzity Karlovy v Praze, V Holešovičkách 2, 180 00 Praha, Czech Republic (e-mail: karlicky@asu.cas.cz).

Color versions of one or more of the figures in this paper are available online at http://ieeexplore.ieee.org.

Digital Object Identifier 10.1109/TPS.2010.2057449

and temperature profiles of the solar atmosphere. According to the observations, the beam flux distribution functions can be roughly approximated by a power law

$$F(E,t) = g(t)F(E) = g(t)(\delta-2)\frac{F_{\max}}{E_0^2}\left(\frac{E}{E_0}\right)^{-\delta} \quad (1)$$

where the product $g(t)\cdot F_{\max}$ is the time-modulated beam energy flux, δ is the power-law index, and E_0 is the low-energy cutoff. In our simulations, the beam energy is also limited by a high-energy cutoff, typically, of hundreds of kiloelectronvolts for the electron beams. The beam parameters for the real flares, appearing in (1), can be obtained from the nonthermal hard X-ray bremsstrahlung emanating from the footpoints of the flare loops [3] observed by, e.g., RHESSI [18] or HXT aboard the Yohkoh satellite [17]. The initial pitch-angle distribution of the beam particles has to be chosen. We assume collimated beams with the initial pitch angle equal to one.

The main advantage of the TP approach, in contrast to the analytical formulas for the electron or proton particle beam losses [5] so widely used in other flare codes, is its flexibility and that the TP approximation of the energetic particle propagation naturally includes the effects of the travel time, the changing ionization, and the plasma transport in the flare atmosphere along the particle trajectories. The TP approach also directly allows to include some additional aspects influencing the beam propagation like magnetic mirroring [2], the effects of the return current [20], additional acceleration mechanisms, or the calculations of the corresponding hard X-ray spectra.

Electron Beams: The energy losses of a nonthermal electron with kinetic energy E and velocity v caused by the Coulomb collisions in a partly ionized hydrogen target with electron and neutral (hydrogen) components, per a time step Δt, can be approximated by the following formulas [5]

$$\Delta E_{\rm ee} = -\frac{2\pi e^4}{E}\Lambda(x+\varepsilon)n_{\rm H}v\Delta t \quad (2)$$

$$\Delta E_{\rm en} = -\frac{2\pi e^4}{E}\Lambda'(1-x)n_{\rm H}v\Delta t \quad (3)$$

where $n_{\rm H} = n_{\rm p} + n_{\rm n}$ is the number density of the equivalent hydrogen atoms, $n_{\rm p}$ and $n_{\rm n}$ are the proton and hydrogen number densities, respectively, $x \equiv n_{\rm p}/n_{\rm H}$ is the hydrogen ionization, and $\varepsilon = 1.4\times10^{-4}$ accounts for the contribution to the plasma electron density from the nonhydrogenic atoms. Λ and Λ' are the Coulomb logarithms [5].

The scattering of the electron beam due to the Coulomb collisions is modeled using the Monte Carlo method. The relation between the rms of the scattering angle θ and the corresponding total energy loss $\Delta E = \Delta E_{\rm ee} + \Delta E_{\rm en}$, which holds if $\overline{\theta^2} \ll 1$ (or, equivalently, $\Delta E/E \ll 1$), is according to [2]

$$\overline{\theta^2} = \left(\frac{\Delta E}{E}\right)\left(\frac{4}{\gamma_0+1}\right). \quad (4)$$

where γ_0 is the Lorentz factor. The scaterring angle of the TPs θ is given by a Gaussian distribution, the rms of which is given by (4). The distribution in the azimuthal direction is uniform, $\phi \in \langle 0, 2\pi)$. The new electron pitch angle is then obtained from spherical trigonometry by

$$\cos(\theta_0+\Delta\theta) = \cos\theta_0\cos\theta + \sin\theta_0\sin\theta\cos\phi \quad (5)$$

where θ_0 is the original pitch angle at the beginning of the time step.

The TP code follows the motion of a chain of clusters of beam electrons—TPs along the magnetic field lines of a homogeneous magnetic field. The linear density of the chain has to be sufficient to model adequately the beam energy losses on the time scales of the beam variations. The electron beam with a power-law distribution is implemented in the following way. The energy range between the lower and upper energy cutoff is divided into several (typically, from 10 to 20) energy bins. Each TP consists of weighted sub-TPs occupying the individual energy bins and giving the required initial distribution (1). During the propagation, the sub-TPs lose their energy until the minimum energy threshold is attained by all the sub-TPs in each energy bin. The corresponding TP is then removed from the computational domain and recycled by putting it into a particle reservoir. The TP code treats typically $\sim10^4$ TPs (i.e., $\sim10^5$ sub-TPs) with typical time steps $\sim10^{-5}-10^{-4}$ s. The macroscopic energy deposits in the electron $\mathcal{E}_{\rm ee}$ and neutral hydrogen $\mathcal{E}_{\rm en}$ component of the plasma are obtained by summing the energy losses (2) and (3) obtained in typically ~50 consecutive time steps on a fine equidistant mesh.

B. Hydrodynamics and Beam Propagation

The 1-D one-fluid HD code calculates the state and evolution of low-β plasma along semicircular magnetic field lines

$$\begin{aligned}
\frac{\partial\rho}{\partial t} + \frac{\partial}{\partial s}(\rho v_{\rm s}) &= 0\\
\frac{\partial\rho v_{\rm s}}{\partial t} + \frac{\partial}{\partial s}\left(\rho v_{\rm s}^2\right) &= -\frac{\partial P}{\partial s} + F_{\rm g}\\
\frac{\partial U}{\partial t} + \frac{\partial}{\partial s}(U v_{\rm s}) &= -\frac{\partial}{\partial s}(v_{\rm s}P) - \frac{\partial}{\partial s}\mathcal{F}_{\rm c}\\
&\quad + \Delta\mathcal{E}_{\rm p} - \mathcal{R} + \mathcal{S} \qquad (6)
\end{aligned}$$

where s and $v_{\rm s}$ are the position and velocity of the plasma along the field lines, respectively, and ρ is the plasma density. The gas pressure and total plasma energy are

$$P = n_{\rm H}(1+x+\varepsilon)k_{\rm B}T, \qquad U = \frac{P}{\gamma-1} + \frac{1}{2}\rho v_{\rm s}^2. \quad (7)$$

The time-dependent hydrogen ionization x is given by the NLTE-RT code. The source terms on the right-hand side of the system of equations are as follows: $F_{\rm g}$ is the component of the gravity force in the parallel direction to the field lines, $\mathcal{F}_{\rm c}$ is the heat flux calculated according to the Spitzer classical formula, $\mathcal{R}$ is the radiative losses, and $\mathcal{S}$ includes all kinds of heating, e.g., the total flare heating $\mathcal{H} = \mathcal{E}_{\rm ee} + \mathcal{E}_{\rm en}$, the quiet heating $\mathcal{Q}$ assuring the stability of the initial unperturbed atmosphere, and the viscous heating $\mathcal{V}$

$$\mathcal{S} = \mathcal{H} + \mathcal{Q} + \mathcal{V}. \quad (8)$$

The radiative losses for the optically thin regions are calculated assuming ionization equilibrium according to [24]. The radiative losses for the optically thick regions are calculated using the approximation of [22] based on an analytic fit of the radiative losses of the VAL C atmosphere, i.e., not fully consistent with the RT.

The initial atmosphere, i.e., the temperature and density profiles in the photosphere and chromosphere, corresponds to the hydrostatic VAL C atmosphere derived from a spectroscopic model [27] with a hydrostatic extension into the transition region and corona [26]. The initial hydrogen ionization in the photosphere and chromosphere is precalculated using the NLTE-RT code.

The set of HD equations is solved using a two- or three-level time-step splitting method (optional) [21]. The convection, generally corresponding to the longest time scales in the model, is treated using the LCPFCT algorithm [21]. The thermal conduction is calculated using the Crank–Nicolson algorithm either with the thermal conduction treated together with radiative losses $\mathcal{R}$ and other source terms $\mathcal{S}$—the two-level time-step splitting—or with the thermal conduction and other source terms treated separately—the three-level time-step splitting.

C. NLTE-RT

Using the instant values of T, $n_{\rm H}$, and $\mathcal{E}_{\rm en}$ obtained by the HD and TP codes, a time-dependent NLTE-RT for hydrogen is calculated by the NLTE-RT code. The RT equation is solved in the lower part of the loop in a 1-D plane-parallel approximation

$$\mu\frac{\partial I_{\mu\lambda}}{\partial\tau_\lambda} = I_{\mu\lambda} - S_\lambda \tag{9}$$

where $I_{\mu\lambda}$ is the specific intensity at a given wavelength λ and μ (cosine of the angle between the radiation-propagation direction and the vertical axis, i.e., the magnetic field line), τ_λ denotes the vertical optical depth, and S_λ is the source function. The hydrogen atom is approximated by a five-level-plus-continuum atomic model.

The level populations n_i are determined by the solution of a time-dependent system of the rate equations

$$\frac{\partial n_i}{\partial t} = \sum_{j\neq i} n_j P_{ji} - n_i \sum_{j\neq i} P_{ij} \tag{10}$$

where P_{ij} contains the sums of thermal collisional rates C_{ij} and radiative rates R_{ij} and R_{ij} are preconditioned in the frame of the MALI method [23]. The excitation and ionization of hydrogen by the nonthermal particles of the beam are also included into P_{ij} using the nonthermal collisional rates $C_{ij}^{\rm nt}$ following the approach of Fang *et al.* [7]

$$C_{1j}^{\rm nt} \propto \frac{\mathcal{E}_{\rm en}}{n_1}. \tag{11}$$

For the transitions from the ground level, we thus get

$$P_{1j} = R_{1j} + C_{1j} + C_{1j}^{\rm nt}. \tag{12}$$

In order not to bias the effects of the nonthermal collisional processes by the effects caused by macroscopic plasma velocities, we excluded the advection term $\partial(n_i v_{\rm s})/\partial s$ from (10). The omission of the advection term can be justified by small velocities (~ 10 km $\cdot$ s^{-1}) in the Balmer line formation regions [19] attained during the first few seconds of the flare atmosphere evolution. The system of rate equations (10) is closed by the charge and particle conservation equations

$$n_{\rm e} = n_{\rm p} + \varepsilon n_{\rm H} \qquad \sum_{j=1}^{5} n_j + n_{\rm p} = n_{\rm H} \tag{13}$$

where $n_{\rm e}$ is the electron density. Because the electron density is not known in advance, the system of preconditioned rate equations is nonlinear due to the products of the atomic-level populations (including protons) with $n_{\rm e}$ or $n_{\rm e}^2$. Therefore, the rate equations and conservation conditions (13) are linearized with respect to the level populations and the electron density. The complete system of equations is then solved using the Crank–Nicolson algorithm and Newton–Raphson iterative method [9], [14].

The NLTE transfer is solved on the shortest time step given by the time-step splitting technique in the HD part. The resulting electron density (ionization) is then fed back to the HD and TP parts.

III. Results

To demostrate the capability of the code, we calculated the response of an initially hydrostatic atmosphere to the propagation of an electron beam whose parameters were derived from the Yohkoh/HXT observation of the March 7, 1993 flare [25]. Fig. 1 presents the time evolutions of the calculated $H\alpha$ and $H\beta$ line profiles. The function g(t) modulating the beam flux is shown as a solid line identical in both the bottom panels. The other beam parameters [see (1)] were as follows: the power-law index $\delta = 3$, the maximum beam energy flux $F_{\rm max} = 5\times10^{10}$ erg $\cdot$ cm$^{-2}\cdot$ s^{-1}, the low-energy cutoff $E_0 = 20$ keV, and the high-energy cutoff 200 keV. The results show a close correlation of the time variations in the line intensities and the beam flux. The time lag of the line intensities behind the beam flux can be almost completely explained by the traveling time of the beam electrons from the corona to the chromosphere. On the other hand, the rapid and deep decreases of the beam flux are followed by a much more moderate decrease of the line intensities. A detailed study of the fast time variations of the Balmer lines formed in the electron-heated atmosphere can be found in [15].

IV. Conclusion

In this paper, we have presented a description of a modular highly versatile TP–radiative HD code, which can be used to model the energetic phenomena related to the particle beam heating of the plasma confined by the magnetic field along the field lines (in 1-D geometry) and their optically thick emission. We demonstrated the potential of the code by calculating the time evolution of the Balmer lines formed in an atmosphere

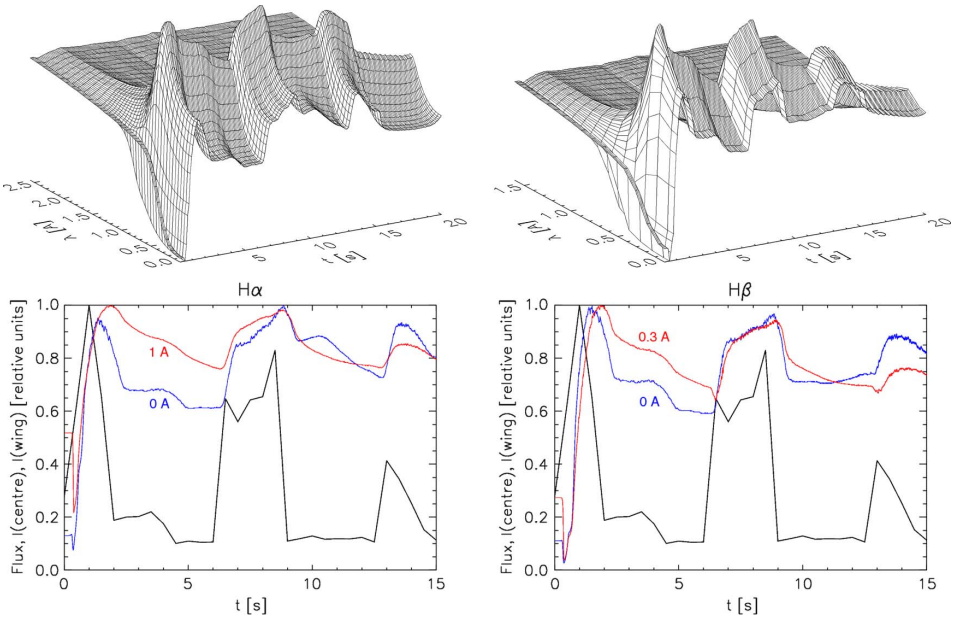

Fig. 1. (Top) Time evolution of (left panel) $H\alpha$ and (right panel) $H\beta$ line profiles in a flare. (Bottom) Time evolution of $H\alpha$ and $H\beta$ line intensities in the line center ($\Delta\lambda = 0$ Å) and line wings ($\Delta\lambda = 1$ Å for $H\alpha$ and $\Delta\lambda = 0.3$ Å for $H\beta$). The line identical in both graphs shows the corresponding electron beam energy flux.

heated by an electron beam whose parameters have been derived from a hard X-ray observation. Due to the TP approach to the propagation and thermalization of the particle beams, the code can be easily modified for other various heating mechanisms (e.g., proton and neutral beams), different nonthermal particle distributions, and additional acceleration or thermalization mechanisms (e.g., the return current), or it can be used to calculate the nonthermal hard X-ray bremsstrahlung. The code has already been used to study some aspects of the time-dependent solar flare emission, such as the detailed formation of the Balmer lines and the role of the nonthermal collisional rates [15], the formation of the thermal far IR continuum [13], and the emission corresponding to the proton beam heating [16]. The code is still being extended, e.g., to include self-consistent radiative losses of other elements and soft X-ray heating.

ACKNOWLEDGMENT

The computations were performed on Ondřejov Cluster for Astrophysical Simulations and Enputron (a computer cluster for extensive computations at J. E. Purkyně University). The authors would like to thank the anonymous referees for the useful criticism and many valuable comments.

REFERENCES

[1] J. C. Allred, S. L. Hawley, W. P. Abbett, and M. Carlsson, "Radiative hydrodynamic models of the optical and ultraviolet emission from solar flares," *Astrophys. J.*, vol. 630, no. 1, pp. 573–586, Sep. 2005.

[2] T. Bai, "Transport of energetic electrons in a fully ionized hydrogen plasma," *Astrophys. J.*, vol. 259, pp. 341–349, Aug. 1982.

[3] J. C. Brown, "The deduction of energy spectra of non-thermal electrons in flares from the observed dynamic spectra of hard X-ray bursts," *Sol. Phys.*, vol. 18, no. 3, pp. 489–502, Jul. 1971.

[4] R. C. Canfield, T. A. Gunkler, and P. J. Ricchiazzi, "The H-alpha spectral signatures of solar flare nonthermal electrons, conductive flux, and coronal pressure," *Astrophys. J.*, vol. 282, pp. 296–307, Jul. 1984.

[5] A. G. Emslie, "The collisional interaction of a beam of charged particles with a hydrogen target of arbitrary ionization level," *Astrophys. J.*, vol. 224, pp. 241–246, Aug. 1978.

[6] G. H. Fisher, R. C. Canfield, and A. N. McClymont, "Flare loop radiative hydrodynamics. V.—Response to thick-target heating. VI.—Chromospheric evaporation due to heating by nonthermal electrons. VII.—Dynamics of the thick-target heated chromosphere," *Astrophys. J.*, vol. 289, pp. 414–441, Feb. 1985.

[7] C. Fang, J. C. Henoux, and W. Q. Gan, "Diagnostics of non-thermal processes in chromospheric flares. 1. $H\alpha$ and CaII K line profiles of an atmosphere bombarded by 10–500 keV electrons," *Astron. Astrophys.*, vol. 274, pp. 917–922, Jul. 1993.

[8] P. Heinzel and M. Karlický, "Pulse-beam heating in flare loops," in *Proc. Coronal Streamers, Coronal Loops, Coronal Sol. Wind Composition, ESA Spec. Publ.*, C. Mattok, Ed., Nov. 1992, vol. 348, pp. 237–240.

[9] P. Heinzel, "Multilevel NLTE radiative transfer in isolated atmospheric structures: Implementation of the MALI-technique," *Astron. Astrophys.*, vol. 299, pp. 563–573, Jul. 1995.

[10] M. Karlický, "Pulse beam heating of the solar atmosphere," *Sol. Phys.*, vol. 130, no. 1/2, pp. 347–360, Dec. 1990.

[11] M. Karlický and J.-C. Henoux, "Return current losses in pulse beam heating of the solar atmosphere," *Astron. Astrophys.*, vol. 264, no. 2, pp. 679–685, Oct. 1992.

[12] J. Kašparová, "Analysis and modelling of hard X-ray and optical signatures of electron beams in solar flares," Ph.D. dissertation, Charles Univ., Prague, Czech Republic, Apr. 2004.

[13] J. Kašparová, P. Heinzel, M. Karlický, Z. Moravec, and M. Varady, "Far-IR and radio thermal continua in solar flares," *Central Eur. Astrophys. Bull.*, vol. 33, pp. 309–317, 2009.

[14] J. Kašparová, P. Heinzel, M. Varady, and M. Karlický, "Time-dependent flare models with MALI," in *Proc. Stellar Atmos. Model., Astron. Soc. Pacific Conf. Ser.*, I. Hubeny, D. Mihalas, and K. Werner, Eds., Jan. 2003, vol. 288, pp. 544–547.

[15] J. Kašparová, M. Varady, P. Heinzel, M. Karlický, and Z. Moravec, "Response of optical hydrogen lines to beam heating. I. Electron beams," *Astron. Astrophys.*, vol. 499, no. 3, pp. 923–934, Jun. 2009.

[16] J. Kašparová, M. Varady, M. Karlický, P. Heinzel, and Z. Moravec, "$H\alpha$ with heating by particle beams," in *Proc. Phys. Chromospheric*

Plasmas, Astron. Soc. Pacific Conf. Ser., P. Heinzel, I. Dorotovič, and R. J. Rutten, Eds., May 2007, vol. 368, pp. 441–446.
[17] T. Kosugi, S. Masuda, K. Makishima, M. Inda, T. Murakami, T. Dotani, Y. Ogawara, T. Sakao, K. Kai, and H. Nakajima, "The hard X-ray telescope (HXT) for the Solar-A mission," *Sol. Phys.*, vol. 136, no. 1, pp. 17–36, Nov. 1991.
[18] R. P. Lin, B. R. Dennis, G. J. Hurford, D. M. Smith, and A. Zehnder, "The Reuven Ramaty high-energy solar spectroscopic imager (RHESSI)," *Sol. Phys.*, vol. 210, no. 1/2, pp. 3–32, Nov. 2002.
[19] T. Nejezchleba, "NLTE solar flare models with stationary velocity fields," *Astron. Astrophys. Suppl.*, vol. 127, no. 3, pp. 607–618, Feb. 1998.
[20] G. H. J. van den Oord, "The electrodynamics of beam/return current systems in the solar corona," *Astron. Astrophys.*, vol. 234, no. 1/2, pp. 496–518, Aug. 1990.
[21] E. S. Oran and J. P. Boris, *Numerical Simulation of Reactive Flow*. New York: Elsevier, 1987.
[22] G. Peres, S. Serio, G. S. Vaiana, and R. Rosner, "Coronal closed structures. IV.—Hydrodynamical stability and response to heating perturbations," *Astrophys. J.*, vol. 252, pp. 791–799, Jan. 1982.
[23] G. B. Rybicki and D. G. Hummer, "An accelerated lambda iteration method for multilevel radiative transfer. I.—Non-overlapping lines with background continuum," *Astron. Astrophys.*, vol. 245, no. 1, pp. 171–181, May 1991.
[24] R. Rosner, W. H. Tucker, and G. S. Vaiana, "Dynamics of the quiescent solar corona," *Astrophys. J.*, vol. 220, pp. 643–645, Mar. 1978.
[25] P. Rudawy, private communication, 2007.
[26] M. Varady, "Observations and modelling of plasma loops in solar corona," Ph.D. dissertation, Charles Univ., Prague, Czech Republic, Jun. 2002.
[27] J. E. Vernazza, E. H. Avrett, and R. Loeser, "Structure of the solar chromosphere. III.—Models of the EUV brightness components of the quiet-sun," *Astrophys. J. Suppl.*, vol. 45, pp. 635–725, Apr. 1981.

Michal Varady was born in Duchcov, Czechoslovakia, in 1965. He received the M.Sc. degree in astrophysics and the Ph.D. degree in theoretical physics and astrophysics from Charles University in Prague, Prague, Czech Republic, in 1996 and 2002, respectively.

Since 1993, he has been with the Astronomical Institute, Ondrejov, Czech Republic. Since 2002, he has also been with the Department of Physics, Faculty of Science, J. E. Purkyně University, Ústí nad Labem, Czech Republic, as an Associate Professor. His research interests include the modeling of processes in solar flares, the analysis of EUV solar spectra, soft and hard X-ray emission, and plasma astrophysics.

Jana Kašparová received the M.Sc. degree in physics and the Ph.D. degree in theoretical physics, astronomy and astrophysics from Charles University in Prague, Prague, Czech Republic, in 1999 and 2004, respectively.

Since 2004, she has been with the Astronomical Institute, Ondrejov, Czech Republic. Her research interests include solar flare processes, non-LTE radiative transfer, continuum and spectral line emission, and hard X-ray emission.

Zdeněk Moravec was born in Ústí nad Labem, Czechoslovakia, in 1968. He received the M.Sc. and Ph.D. degrees in astronomy and astrophysics from Charles University in Prague, Prague, Czech Republic, in 1991 and 1998, respectively.

Until 2000, he was with the Klet Observatory, České Budějovice, Czech Republic, where he was involved in the astrometry of minor planets and comets. He is currently with the Department of Physics, Faculty of Science, J. E. Purkyně University, Ústí nad Labem, Czech Republic, where he is the Head of the computer modeling working group. His research interests include the modeling of processes in solar flares.

Petr Heinzel received the CSc. and DSC. degrees from the Academy of Sciences of the Czech Republic, Prague, Czech Republic, in 1982 and 1993, respectively.

In 2005, he was an Associate Professor of astronomy and astrophysics with Charles University in Prague, Prague, Czech Republic. He was a Visiting Professor with the Paris University, Paris, France, the Wroclaw University, Wroclaw, Poland, the Max-Planck-Institut für Astrophysik, Garching, Germany, and the Harvard-Smithsonian Center for Astrophysics, Cambridge, MA. He is currently the Director of the Astronomical Institute, Ondrejov, Czech Republic. His research interests include solar physics, radiative transfer, plasma spectroscopy, and plasma astrophysics.

Since 2003, Dr. Heinzel has been a member of the editorial board of the journal Solar Physics (Springer).

Marian Karlický was born in Frýdek-Místek, Czech Republic, in 1949. He received the CSc. and DSC. degrees from the Academy of Sciences of the Czech Republic, Prague, Czech Republic, in 1981 and 1992, respectively.

He is currently the Head of the solar flares and prominences working group with the Astronomical Institute, Ondrejov, Czech Republic. He is also currently with Charles University in Prague, Prague, Czech Republic, as an Associate Professor presenting lectures on plasma astrophysics. He was a Visiting Professor or Guest Researcher with the JAXA/ISAS, Fuchinobe, Japan, the INPE, Sao Jose dos Campos, Brazil, the Meudon Observatory, France, the Potsdam Observatory, Germany, and the Glasgow University, Glasgow, U.K. His research interests include solar flares, solar radio bursts, and plasma astrophysics.

Stellar Atmosphere Modeling
ASP Conference Series, Vol. 288, 2003
I. Hubeny, D. Mihalas, & K. Werner, eds.

Time-Dependent Flare Models with MALI

J. Kašparová, P. Heinzel, M. Varady, M. Karlický

Astronomical Institute of Academy of Sciences of the Czech Republic, Fričova 298, Ondřejov, 251 65, Czech Republic

Abstract. Time variations of Hα line-profile intensities produced by electron beams are presented. We show first results of time-dependent simulations of the chromospheric response to a 1 s monoenergetic electron beam. A 1-D hydrodynamic code together with a particle representation of the beam have been used to calculate the atmospheric evolution. The time-dependent radiative-transfer problem has been solved for the resulting atmosphere by the MALI approach, using a Crank-Nicholson semi-implicit scheme. Non-thermal collisional rates have been included in linearized equations of statistical equilibrium.

1. Introduction

It is generally believed that the energy of solar flares is released in the solar corona, then transported by accelerated energetic particles downwards into the transition region and chromosphere. The particles deposit their energy into the ambient plasma mainly via Coulomb collisions, resulting in a rapid heating, accompanied by violent dynamic phenomena in the initially quiet atmosphere.

The aim of our work is to investigate the time-evolution of Hα line-profiles during the impulsive phase of solar flares. Our simulations of the atmospheric response to the heating are split into two independent steps. The flare-plasma evolution, together with particle propagation and thermalization of their energy, is treated by a hybrid hydrodynamic code. Its results are then used as inputs to a code solving the time-dependent non-LTE radiative-transfer problem.

2. Hybrid Hydrodynamic Code

The hybrid hydrodynamic code (Varady 2002) consists of a hydrodynamic and a particle part. The time-evolution of the atmosphere is described by the standard system of 1-D hydrodynamic equations, completed by an equation of state in the one-fluid approximation. Ionization of hydrogen has been approximated by the modified Saha equation (Brown 1973), and radiative losses have been estimated according to the models of Rosner, Tucker, & Vaiana (1978). The particle part of the code simulates interaction of accelerated particle beams with the ambient atmosphere (Bai 1982; Karlický & Hénoux 1992). The deposit of beam energy into the ambient neutrals and electrons is calculated following the approach of Emslie (1978). The energy deposited into electrons is used as a flare-heating term in the energy equation of the hydrodynamic code. The energy deposit into

the neutrals, together with the time-evolution of temperature and total-hydrogen number-density are the inputs into the radiative transfer code.

3. Radiative transfer

We have solved the time-dependent radiative-transfer problem for a 3-level plus continuum atomic model of hydrogen. The time-evolution of the atmosphere's structure was prescribed by the hydrodynamic calculations. Time-dependent equations of statistical equilibrium (ESE) were preconditioned using a diagonal approximate-lambda-operator in the Multilevel Accelerated Lambda Iteration method - MALI (Rybicki & Hummer 1991). According to Nejezchleba (1998), velocities of the order of 10 km s^{-1} cause only minor changes in the level populations n_i. Thus we restrict ourselves to only a static problem where the ESE take the form

$$\frac{\partial n_i}{\partial t} = \sum_{j \neq i} (n_j P_{ji} - n_i P_{ij}) \equiv f_i(\mathbf{n}) \qquad \mathbf{n} = (n_i, n_c, n_e) \tag{1}$$

with n_c and n_e denoting the proton and electron density respectively. The total rates P_{ij} are sums of radiative R_{ij} and collisional C_{ij} rates. The R_{ij} have been preconditioned in the framework of the MALI method. Excitation and ionization by particles in the beam have been taken into account via non-thermal collisional rates $C_{ij}^{\rm nt}$, which are directly proportional to the energy $\mathcal{E}_{\rm H}$ deposited into hydrogen. We have adopted the approach of Fang, Hénoux, & Gan (1993) and included the non-thermal collisional rates from the ground level of hydrogen as follows:

$$C_{1c}^{\rm nt} = 1.73 \times 10^{10} \frac{\mathcal{E}_{\rm H}}{n_1} \quad C_{12}^{nt} = 2.94 \times 10^{10} \frac{\mathcal{E}_{\rm H}}{n_1} \quad C_{13}^{nt} = 5.35 \times 10^{9} \frac{\mathcal{E}_{\rm H}}{n_1} \; . \tag{2}$$

Using the non-thermal rates specified above, the total rates P_{1j} from the ground level are

$$P_{1j} = R_{1j} + C_{1j} + C_{1j}^{\rm nt} \; . \tag{3}$$

The set (1) of ESE is completed by equations of particle and charge conservation

$$\sum n_j + n_c = n_{\rm H} \qquad n_e = n_c + Q n_{\rm H} \; . \tag{4}$$

Here $n_{\rm H}$ corresponds to the total hydrogen density and $Q = 1.4$ represents the contribution to the electron density from non-hydrogenic elements.

3.1. Numerical methods

A semi-implicit difference scheme has been used on the system (1) of ESE

$$F_i^{t+1} \equiv \alpha \Delta t f_i^{t+1} - n_i^{t+1} + (1 - \alpha) \Delta t f_i^t + n_i^t = 0 \; . \tag{5}$$

The parameter α ($0 \leq \alpha \leq 1$) determines the degree of implicitness of the algorithm, Δt is the timestep, and the upper index denotes values corresponding to the two successive time-levels.

Because the electron density n_e is unknown, the preconditioned ESE are non-linear because of the terms containing n_e. Thus, the system of semi-implicit equations (5) together with the conservation conditions (4) is linearized with respect to all level populations, including protons n_c and the electron density, and solved using a Newton-Raphson iteration technique (Heinzel 1995).

$$F_i^{t+1} = F_i^{t+1}\left(\mathbf{n}^\dagger\right) + \sum_j^{NL}\left(\frac{\partial F_i^{t+1}}{\partial n_j}\right)_{\mathbf{n}^\dagger}\delta n_j + \left(\frac{\partial F_i^{t+1}}{\partial n_c}\right)_{\mathbf{n}^\dagger}\delta n_c + \left(\frac{\partial F_i^{t+1}}{\partial n_e}\right)_{\mathbf{n}^\dagger}\delta n_e = 0 \tag{6}$$

Using eq. (5), the final linearized time-dependent ESE system (1) and conservation conditions (4) is

$$-\alpha\Delta t f_i^{t+1}\left(\mathbf{n}^\dagger\right) + \left(n_i^{t+1}\right)^\dagger - (1-\alpha)\Delta t f_i^t - n_i^t =$$

$$\left[\alpha\Delta t\sum_j^{NL}\left(\frac{\partial f_i^{t+1}}{\partial n_j}\right)_{\mathbf{n}^\dagger} - \delta_{ij}\right]\delta n_j + \alpha\Delta t\left(\frac{\partial f_i^{t+1}}{\partial n_c}\right)_{\mathbf{n}^\dagger}\delta n_c + \alpha\Delta t\left(\frac{\partial f_i^{t+1}}{\partial n_e}\right)_{\mathbf{n}^\dagger}\delta n_e \tag{7}$$

$$\begin{aligned} Q\sum_j^{NL}\delta n_j + (1+Q)\delta n_c - \delta n_e &= n_e^\dagger - (1+Q)n_c^\dagger - Q\sum_j^{NL} n_j^\dagger \\ \sum_j^{NL}\delta n_j + \delta n_c &= n_{\mathrm{H}} - \sum_j^{NL} n_j^\dagger - n_c^\dagger \,. \end{aligned}$$

NL is the number of bound levels, and $\dagger$ denotes values from the previous iteration at the time level $t+1$. Having evaluated the corrections $\delta\mathbf{n}$, new populations and electron density are then obtained as

$$\mathbf{n} = \mathbf{n}^\dagger + \delta\mathbf{n} \,. \tag{8}$$

The iteration scheme described above is performed for each timestep until maximum relative changes in the level-populations and electron-density are less than a prescribed value (typically 10^{-3}). After convergence is reached, which is usually within several iterations, the synthetic spectrum is calculated. The converged populations are then used as starting values for the next timestep.

4. First Results

We have simulated the chromospheric response to a 1 s monoenergetic beam of electrons created above the atmosphere with a kinetic energy 30 keV, and an energy-flux of 2.5×10^{10} erg cm^{-2} s^{-1} at the point of injection. The energy flux has the form of a sinusoidal pulse of 1 s duration. At time $t = 0$ s the initial atmospheric temperature- and density-structure is that of the VAL C model atmosphere (Vernazza, Avrett, & Loeser 1981). The resulting time-evolution of the total hydrogen density, temperature and energy-deposition into hydrogen have been used as inputs to the calculation of the time-variation of Hα line

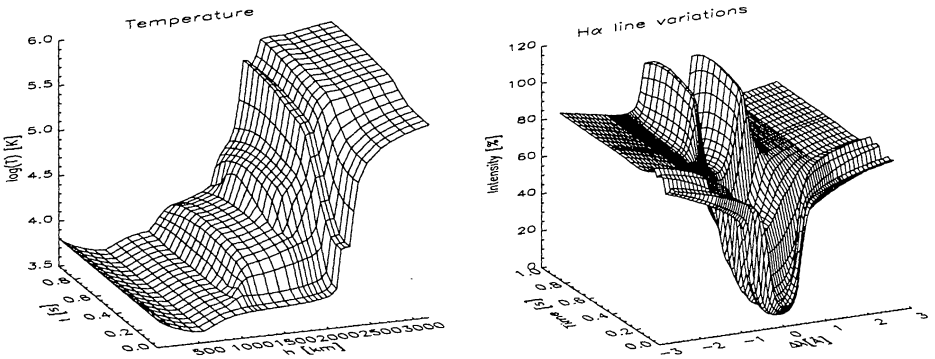

Figure 1. Time evolution of temperature structure and Hα line.

profiles. The timestep Δt of the radiative transfer code has been set to 0.001 s. Figure 1 displays the time-evolution of the Hα profile and the temperature in the part of the atmosphere where the profile of Hα line is calculated. The figure shows that during a time-interval of 1 s, the Hα line evolves from a quiet chromospheric shape to one typical of a flare. The non-thermal rates influence mainly the core of the line where they cause a small dip at $t \sim 0.1$ s.

5. Conclusions

Our results show that time variations of Hα line intensities are mainly caused by the time-evolution of the temperature structure of the atmosphere. For simplicity, velocity fields were not considered in the radiative-transfer code. We plan to include both advection and line-profile anisotropy in future work. The hybrid hydrodynamic code is also capable of computing time-variations of the hard X-ray flux from a thick-target model.

Acknowledgments. This work was supported by grants IAA3003202 and IAA3003203 of GA AV ČR.

References

Bai, T. 1982, ApJ, 259, 341
Brown, J. C. 1973, Solar Phys. 29, 421
Emslie, A. G. 1978, ApJ, 224, 241
Fang, C., Hénoux, J.-C., & Gan, W.Q. 1993, A&A, 274, 917
Heinzel, P. 1995, A&A, 299, 593
Karlický, M., & Hénoux, J.-C. 1992, A&A, 264, 679
Nejezchleba, T. 1998, A&AS, 127, 607
Rosner, R., Tucker, W. H., & Vaiana, G. S. 1978, ApJ, 220, 643
Rybicki, G. B. & Hummer, D. G. 1991, A&A, 245, 171
Varady, M. 2002, PhD Thesis, Charles University, Prague
Vernazza, J. E., Avrett, E. H., & Loeser, R. 1981, ApJS, 45, 635

A&A 499, 923–934 (2009)
DOI: 10.1051/0004-6361/200811559

Astronomy & Astrophysics

Response of optical hydrogen lines to beam heating

I. Electron beams

J. Kašparová[1], M. Varady[2,1], P. Heinzel[1], M. Karlický[1], and Z. Moravec[2]

[1] Astronomický ústav Akademie věd České republiky, v.v.i., Fričova 298, 251 65 Ondřejov, Czech Republic
e-mail: kasparov@asu.cas.cz
[2] Katedra fyziky, Universita J. E. Purkyně, České mládeže 8, 400 24 Ústí nad Labem, Czech Republic
e-mail: mvarady@physics.ujep.cz

Received 20 December 2008 / Accepted 27 March 2009

ABSTRACT

Context. Observations of hydrogen Balmer lines in solar flares remain an important source of information on flare processes in the chromosphere during the impulsive phase of flares. The intensity profiles of optically thick hydrogen lines are determined by the temperature, density, and ionisation structure of the flaring atmosphere, by the plasma velocities and by the velocity distribution of particles in the line formation regions.
Aims. We investigate the role of non-thermal electrons in the formation regions of Hα, Hβ, and Hγ lines in order to unfold their influence on the formation of these lines. We concentrate on pulse-beam heating varying on a subsecond timescale. Furthermore, we theoretically explore possibility that a new diagnostic tool exists indicating the presence of non-thermal electrons in the flaring chromosphere based on observations of optical hydrogen lines.
Methods. To model the evolution of the flaring atmosphere and the time-dependent hydrogen excitation and ionisation, we used a 1-D radiative hydrodynamic code combined with a test-particle code that simulates the propagation, scattering, and thermalisation of a power-law electron beam in order to obtain the flare heating and the non-thermal collisional rates due to the interaction of the beam with the hydrogen atoms. To not bias the results by other effects, we calculate only short time evolutions of the flaring atmosphere and neglect the plasma velocities in the radiative transfer.
Results. All calculated models have shown a time-correlated response of the modelled Balmer line intensities on a subsecond timescale, with a subsecond timelag behind the beam flux. Depending on the beam parameters, both line centres and wings can show pronounced intensity variations. The non-thermal collisional rates generally result in an increased emission from a secondary region formed in the chromosphere.
Conclusions. Despite the clear influence of the non-thermal electron beams on the Balmer line intensity profiles, we were not able on the basis of our simulations to produce any unambiguous diagnostic of non-thermal electrons in the line-emitting region, which would be based on comparison of individual Balmer line intensity profiles. However, fast line intensity variations, well-correlated with the beam flux variations, represent an indirect indication of pulsating beams.

Key words. Sun: flares – radiative transfer – hydrodynamics – line: formation – line: profiles

1. Introduction

In the context of interpreting flare loop hard X-ray footpoint sources (Hoyng et al. 1981; Hudson & Fárník 2002), all contemporary flare models (Sturrock 1968; Kopp & Pneuman 1976; Shibata 1996; Turkmani et al. 2005; Fletcher & Hudson 2008), regardless of their nature, assign a fundamental role during the flare energy release, transport and deposition to the high-energy non-thermal particle beams. In the impulsive phase of flares, the beams formed by charged particles are also guided from the acceleration site (wherever it is located) downwards along the magnetic field lines into the transition region, chromosphere and possibly photosphere. At lower atmospheric layers due to the high density of local plasma, their kinetic energy is efficiently dissipated by Coulomb collisions, the corresponding regions are rapidly heated, and dramatic changes of temperature and ionisation occur. This results in explosive evaporation (Doschek et al. 1996). The manifestations of the early flare processes can be observed in the microwaves, soft and hard-X rays, and optical lines (Tandberg-Hanssen & Emslie 1988). Later on in the thermal (gradual) phase, the heating leads to the evaporation of chromospheric and transition region plasma into the corona which is gradually filled with relatively dense (up to $\sim 10^{10}$ cm^{-3}) and hot ($\sim 10^7$ K) flare plasma (Czaykowska et al. 1999). The radiation from the flare region is now dominated by soft-X rays, EUV, and again by emission in the optical spectral lines.

We concentrate on modelling the formation of optically thick hydrogen spectral lines Hα, Hβ, and Hγ in the early phases of solar flares by the means of numerical radiative hydrodynamics combined with a test particle approach to simulate the propagation, scattering and energy loss of an electron beam with the power-law spectrum and prescribed time-dependent energy flux propagating through the solar atmosphere and depositing its energy into the solar plasma. In this context we address three main questions:

1. Does rapidly varying electron beam flux manifest itself in the Balmer line intensities?
2. How do the non-thermal particles in the Balmer lines formation regions influence the line profiles and intensities?
3. Can an unambiguous diagnostic method be developed that is applicable to observations of Balmer lines recognising the

presence of the non-thermal particles in the line formation regions?

Due to the complexity of simultaneously treating non-LTE radiative transfer in deep layers of the solar atmosphere and the hydrodynamics (radiative hydrodynamics), only a few attempts have been made to model the optical emission of flares. First models of pulse-beam heating were developed by Canfield et al. (1984) and Fisher et al. (1985). Recently, Abbett & Hawley (1999) and Allred et al. (2005) studied emission in several lines and continua using complex radiative hydrodynamic simulations of electron beam heating on a time scale up to several tens of seconds.

In this paper we concentrate on fast time variations on a subsecond time scale. In previous works on this topic, plasma dynamics was neglected. Simplified time-dependent non-LTE simulations of Hα line were then performed e.g. by using a prescribed time evolution of a flare atmosphere from independent hydrodynamic simulations of pulse-beam heating (Heinzel 1991) or by solving approximate energy equation (Ding et al. 2001). Both results showed significant Hα line response to pulse-beam heating on subsecond time scales. Here, we solve 1-D radiative hydrodynamics of a solar atmosphere subjected to a subsecond electron beam heating and study emissions in the Hα, Hβ, and Hγ lines.

The paper is organised as follows: Sect. 2 describes the numerical code and models of beam heating. Results of simulations concerning flare atmosphere dynamics and Balmer line emission are presented in Sect. 3. There, we also analyse several proposed diagnostic methods for recognising the presence of electron beams in line formation regions. Section 4 summarises our results.

2. Model

The model covers three important classes of processes whose importance was identified in flares:

1. propagation of charged, high-energy particle beams with power-law spectra and time-dependent energy flux downwards through the solar atmosphere and their gradual thermalisation due to the Coulomb collisions with the ambient plasma in the solar atmosphere (Bai 1982; Emslie 1978).
2. the hydrodynamic response of low-β solar plasma corresponding to the energy deposited by the beam.
3. time evolution of the ionisation structure and formation of optical emission in the chromosphere and photosphere where non-LTE conditions apply.

The individual classes of flare processes are modelled using three computer codes, each modelling one class of the processes identified above. The codes have been integrated into one radiative hydrodynamic code.

2.1. Flare heating

The flare heating caused by an electron beam propagating from the top of the loop located in the corona ($s = 9.5 \times 10^3$ km corresponding to $T = 1$ MK) downwards is calculated using a test-particle code (TPC) based on Karlický (1990); Karlický & Hénoux (1992). We assume an electron beam with a power-law electron flux spectrum [electrons cm^{-2} s^{-1} per unit energy] (Nagai & Emslie 1984)

$$F(E,t) = g(t)F(E) = g(t)\,(\delta-2)\frac{F_{\max}}{E_0^2}\left(\frac{E}{E_0}\right)^{-\delta}, \qquad (1)$$

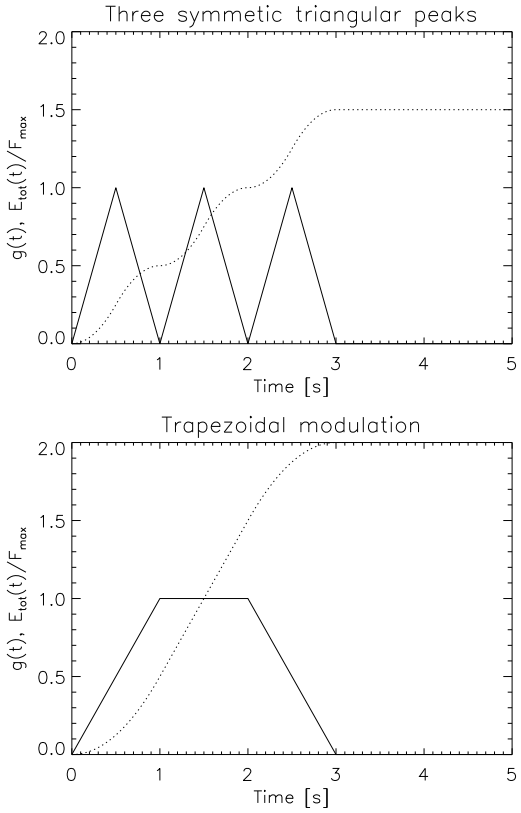

Fig. 1. Time modulations of the beam flux. Solid lines show $g(t)$, dotted lines denote $\int_0^t g(t')\,\mathrm{d}t' = E_{\rm tot}(t)/F_{\max}$, see Eqs. (1) and (2).

where δ is the power-law index, $g(t) \in \langle 0,1\rangle$ is a function describing the time modulation of the beam flux, $F_{\max}$ is the maximum energy flux, i.e. energy flux of electrons with $E \geq E_0$ at $g(t) = 1$. In order to model the electron spectrum by the test particles the beam electron energy is limited by a low and a high-energy cutoff, $E_0 = 20$ keV and $E_1 = 150$ keV, respectively. We present results for two types of time modulation $g(t)$: three symmetric triangular peaks and a trapezoidal modulation (see Fig. 1) and two total deposited energies $E_{\rm tot}$ (see Table 1)

$$E_{\rm tot} = F_{\max}\int_0^{t_1} g(t)\,\mathrm{d}t, \qquad (2)$$

where t_1 is the duration of the energy deposit. The energy fluxes $F_{\max}$ have been chosen in such a way that for both time modulations the total deposited energy $E_{\rm tot}$ is the same. The model parameters are specified in Table 1, their values are consistent with common beam characteristics derived from hard X-ray observations.

The TPC simulates the propagation, scattering and energy loss of an electron beam with a specified energy flux and power-law index as it propagates through partly ionised hydrogen plasma in the solar atmosphere. The losses of the beam electron kinetic energy caused by Coulomb collisions due to electron and neutral (hydrogen) components of solar plasma are given by Emslie (1978)

$$\Delta E_{\rm ee} = -\frac{2\pi e^4}{E}\Lambda(x+\varepsilon)n_{\rm H}v_{\rm e}\Delta t_{\rm B}, \qquad (3)$$

Table 1. Model parameters.

Model	$E_{\rm tot}$ [erg cm^{-2}]	$g(t)$	$F_{\rm max}$ [erg cm^{-2} s^{-1}]	δ
H_TP_D3	9×10^{10}	trapezoid	4.5×10^{10}	3
H_TP_D5	9×10^{10}	trapezoid	4.5×10^{10}	5
H_3T_D3	9×10^{10}	3 triangles	6×10^{10}	3
H_3T_D5	9×10^{10}	3 triangles	6×10^{10}	5
L_TP_D3	1.5×10^{10}	trapezoid	0.75×10^{10}	3
L_TP_D5	1.5×10^{10}	trapezoid	0.75×10^{10}	5
L_3T_D3	1.5×10^{10}	3 triangles	1×10^{10}	3
L_3T_D5	1.5×10^{10}	3 triangles	1×10^{10}	5

$$\Delta E_{\rm en} = -\frac{2\pi e^4}{E}\Lambda'(1-x)n_{\rm H}v_{\rm e}\Delta t_{\rm B}, \tag{4}$$

where E is the kinetic energy of the non-thermal electron, $v_{\rm e}$ is the non-thermal velocity, $n_{\rm H} = n_{\rm p} + n_{\rm n}$ is the number density of equivalent hydrogen atoms, $n_{\rm p}$ and $n_{\rm n}$ are the proton and neutral hydrogen number densities, $x \equiv n_{\rm p}/n_{\rm H}$ is the hydrogen ionisation degree and $\varepsilon = 1.4\times10^{-4}$ accounts for the contribution from the metals to the plasma electron density (Heinzel & Karlický 1992). The metal contribution to electron densities is critical around the temperature minimum where the hydrogen is almost neutral. We account for it in this approximate way. On the other hand, we neglect the helium contribution which can reach maximum 20% of total electron density in higher altitudes. The Coulomb logarithms Λ and Λ' are given by Emslie (1978) and $\Delta t_{\rm B}$ is a constant TPC timestep which has to be chosen to satisfy the condition that the total beam electron energy loss $\Delta E = \Delta E_{\rm ee} + \Delta E_{\rm en}$ per a timestep is negligible relative to its kinetic energy, i.e. $\Delta E/E \ll 1$.

The scattering of the beam due to Coulomb collisions is taken into account using a Monte-Carlo method combined with the analytical expressions for the cumulative effects described by Bai (1982). The relation between the mean square of the beam electron deflection angle $\langle\theta^2\rangle$ and the corresponding energy loss ΔE (which holds if $\langle\theta^2\rangle \ll 1$ or equivalently if $\Delta E/E \ll 1$) is given by formula

$$\langle\theta^2\rangle = \left(\frac{\Delta E}{E}\right)\left(\frac{4}{\gamma_{\rm L}+1}\right), \tag{5}$$

where $\gamma_{\rm L} = 1/\sqrt{1-v_{\rm e}^2/c^2}$ is the Lorentz factor. The new electron pitch angle $\theta_0 + \Delta\theta$ is given by

$$\cos(\theta_0+\Delta\theta) = \cos\theta_0\cos\theta_{\rm s} + \sin\theta_0\sin\theta_{\rm s}\cos\phi, \tag{6}$$

where θ_0 is the original pitch angle at the beginning of the time step, $\theta_{\rm s}$ is given by Eq. (5) and using a 2-D Gaussian distribution. The distribution of the azimuthal angle ϕ is uniform, $\phi \in \langle 0, 2\pi)$.

The TPC in principle follows the motion of statistically important number of test particles representing clusters of electrons in the time varying atmosphere which responses through the 1-D HD code and the non-LTE radiative transfer code to the flare heating by TPC. The test particles with a time-dependent power-law spectra are generated in the corona at the loop-top and at each timestep the positions, energies and pitch angles of the particle clusters are calculated. The macroscopic energy deposits into the electron $\mathcal{E}_{\rm ee}$ and neutral hydrogen $\mathcal{E}_{\rm en}$ component of solar plasma are obtained by summing the energy losses ($\Delta E_{\rm ee}$ and $\Delta E_{\rm en}$) of a huge number of particle clusters for each position in the atmosphere using a fine equidistant grid. This approach allows not only to calculate the total flare heating

$$\mathcal{H} = \mathcal{E}_{\rm ee} + \mathcal{E}_{\rm en}$$

but also to distinguish between the beam energy deposited into the electron and hydrogen component of solar plasma and therefore to calculate the non-thermal contribution to the transition rates in hydrogen atoms which is the crucial point for the present study. The test-particle approach used here naturally takes into account propagation effects of the beam and time evolution of ionisation structure of the atmosphere. This leads us to a more realistic description of beam energy losses as compared to the approach of Abbett & Hawley (1999) or Allred et al. (2005) who used an analytic heating function corresponding to a stationary solution of beam propagation through the atmosphere (Hawley & Fisher 1994).

2.2. 1-D plasma dynamics

The state and time evolution of originally hydrostatic low-β plasma along magnetic field lines is calculated using a 1-D hydrodynamic code. The temperature, density and ionisation profiles of the initial atmosphere correspond to the VAL 3C atmosphere (Vernazza et al. 1981) with a hydrostatic extension into the corona. The half-length of the loop is 10 Mm. The time evolution of the atmosphere is initiated by the energy deposited by the beam. The main processes that determine plasma evolution in flare loops are: convection and conduction (both in 1-D due to the magnetic field), radiative losses and indeed the dominant factor is the flare heating here calculated by the TPC. The evolution of plasma in the flare loop can be described by a system of hydrodynamic conservation laws

$$\frac{\partial\rho}{\partial t} + \frac{\partial}{\partial s}(\rho u) = 0, \tag{7}$$

$$\frac{\partial\rho u}{\partial t} + \frac{\partial}{\partial s}(\rho u^2) = -\frac{\partial P}{\partial s} + F_{\rm g}, \tag{8}$$

$$\frac{\partial E}{\partial t} + \frac{\partial}{\partial s}(uE) = -\frac{\partial}{\partial s}(uP) - \frac{\partial}{\partial s}\mathcal{F}_{\rm c} + \mathcal{S}, \tag{9}$$

where s is the position and u the macroscopic plasma velocity along the magnetic field line and ρ is the plasma density. The gas pressure and the total plasma energy are

$$P = n_{\rm H}(1+x+\varepsilon)k_{\rm B}T, \qquad E = \frac{P}{\gamma-1} + \frac{1}{2}\rho u^2, \tag{10}$$

where $\gamma \equiv c_{\rm p}/c_{\rm v} = 5/3$ is the specific heats ratio, $k_{\rm B}$ the Boltzmann constant. The hydrogen ionisation degree x in the photosphere and chromosphere is calculated at each timestep by the time-dependent non-LTE radiative transfer code. In the transition region and corona we assume $x \equiv 1$. The source terms on the right hand sides of the system of equations are: $F_{\rm g}$ the parallel component of the gravity force in respect to the semicircular field line, $\mathcal{F}_{\rm c}$ the heat flux, calculated using the Spitzer's classical formula, and

$$\mathcal{S} = \mathcal{H} - \mathcal{R} + \mathcal{Q}$$

includes all other considered energy sources and sinks, i.e. the dominant flare heating $\mathcal{H}$ which drives the time evolution of the atmosphere, the quiet heating $\mathcal{Q}$ assuring the stability of the initial quiescent unperturbed (hydrostatic) atmosphere and the radiative losses $\mathcal{R}$. The radiative losses are calculated according to Rosner et al. (1978) for optically thin regions and according to Peres et al. (1982) for optically thick regions.

The 1-D gas dynamics is treated using the explicit LCPFCT solver (Oran & Boris 1987), the Crank-Nicolson algorithm for the heat transfer and the time step splitting technique to couple the individual source terms of the energy equation with hydrodynamics (Oran & Boris 2000).

2.3. Time-dependent non-LTE radiative transfer

Using the instant values of T, $n_{\rm H}$, and $\mathcal{E}_{\rm en}$ obtained by the hydrodynamic and test-particle codes, a time-dependent non-LTE radiative transfer for hydrogen is solved in lower part of the loop in a 1-D plan-parallel approximation. The hydrogen atom is approximated by a five level plus continuum atomic model.

The level populations n_i are determined by the solution of a time-dependent system of equations of statistical equilibrium (ESE)

$$\frac{\partial n_i}{\partial t} = \sum_{j\neq i} n_j P_{ji} - n_i \sum_{j\neq i} P_{ij}, \tag{11}$$

where P_{ij} contain sums of thermal collisional rates C_{ij} and radiative rates R_{ij}, and R_{ij} are preconditioned in the frame of MALI method (Rybicki & Hummer 1991). The excitation and ionisation of hydrogen by the non-thermal electrons from the beam are also included into P_{ij} using the non-thermal collisional rates $C_{ij}^{\rm nt}$ following the approach of Fang et al. (1993)

$$C_{1c}^{\rm nt} = 1.73\times10^{10}\frac{\mathcal{E}_{\rm en}}{n_1}, \qquad C_{12}^{\rm nt} = 2.94\times10^{10}\frac{\mathcal{E}_{\rm en}}{n_1},$$
$$C_{13}^{\rm nt} = 5.35\times10^{9}\frac{\mathcal{E}_{\rm en}}{n_1}, \qquad C_{14}^{\rm nt} = 1.91\times10^{9}\frac{\mathcal{E}_{\rm en}}{n_1}. \tag{12}$$

For transitions from the ground level we thus get

$$P_{1j} = R_{1j} + C_{1j} + C_{1j}^{\rm nt}. \tag{13}$$

Non-thermal collisional rates from excited levels as well as three-body recombination rates are not considered here since Karlický et al. (2004) and Štěpán et al. (2007) found them to be negligible compared to thermal ones.

In order not to bias the effects of the non-thermal collisional processes by effects caused by macroscopic plasma velocities, we excluded the advection term $\partial(n_i u)/\partial s$ from Eq. (11). The omission of the advection term can be justified by small velocities (~10 km s^{-1}) in the Balmer line formation regions (Nejezchleba 1998) attained during the first few seconds of the flare atmosphere evolution. On the other hand, the benefit is a significant simplification of the radiative transfer code. The system of ESE (11) is closed by charge and particle conservation equations

$$n_{\rm e} = n_{\rm p} + \varepsilon n_{\rm H}, \qquad \sum_{j=1}^{5} n_j + n_{\rm p} = n_{\rm H}, \tag{14}$$

where $n_{\rm e}$ is the electron density. The contribution of helium to ionisation is neglected. Because the electron density is not known in advance, the system of preconditioned ESE is nonlinear due to products of atomic level populations (including protons) with $n_{\rm e}$ or $n_{\rm e}^2$. Therefore, the ESE and conservation conditions (14) are linearised with respect to the level populations and electron density. The complete system of equations is then solved using the Crank-Nicolson algorithm and Newton-Raphson iterative method (Heinzel 1995; Kašparová et al. 2003).

The non-LTE transfer is solved on the shortest time step given by the time step splitting technique in the hydrodynamic part, see Sect. 2.2. Resulting electron density (ionisation) is then fed back to the hydrodynamic equations and the TPC.

3. Results of flare simulations

We computed the atmosphere dynamics and time evolution of the Hα, Hβ, and Hγ line profiles resulting from a time-dependent electron beam heating of an initially hydrostatic VAL C atmosphere.

3.1. Flare dynamics

Figures 2 and 3 show the time evolution of temperature, hydrogen ionisation, energy deposit $\mathcal{H}$, and energy deposit to neutral hydrogen $\mathcal{E}_{\rm en}$ of models specified in Table 1. Shortly after the beam injection at the loop top at $t = 0$ s, the chromosphere is at $t \sim 0.25$ s heated mainly at heights between ~1000–2000 km. The temperature rise is higher for models with triangular peak modulation (3T) than for the trapezoidal one (TP) due to the higher energy flux injected into the atmosphere (compare the time evolution of total injected energy in Fig. 1). Since the low-energy electrons are stopped higher in the atmosphere, the total energy deposit for steeper beams (higher δ) is larger than for flatter beams at these heights (compare $\mathcal{H}$ at $t = 0.25$ s in Figs. 2 and 3) and the temperature rise is most significant for models L_3T_D5 and H_3T_D5, see the first panel in Figs. 2 and 3, respectively. This is generally true for all times during the heating; the temperature above $s \sim 1000$ km is larger for larger δ when comparing models with the same time modulation $g(t)$ and $F_{\rm max}$. On the contrary, at lower heights $s < 1000$ km due to the larger heating for flatter beams, see Figs. 2 and 3, the temperature at those atmospheric layers rises more for models with $\delta = 3$ than with $\delta = 5$.

In the low-flux models the heating leads to a gradual increase of temperature above ~1000 km. The steep rise of temperature from chromospheric to coronal values is shifted by about 200 km from the preflare height to $s \sim 1900$ km, see Fig. 2. Heating by a higher flux results in a secondary region of a steep temperature rise at $s \sim 1400$ km which is formed at $t \sim 1$ s, see Fig. 3. Due to the locally efficient radiative losses, the temperature structure in all models up to $s \sim 2000$ km follows the time modulation of the beam flux; i.e. it rises and drops – compare the temperature structure e.g. at $t = 1.5$ s and $t = 2$ s for 3T models and TP models in Figs. 2 and 3 and the time evolution of temperature at two selected heights in Fig. 4.

Similarly to the temperature evolution, ionisation increases above $s \sim 1000$ km shortly after the beam injection, see the middle panel in Figs. 2 and 3. Again, due to beam flux modulation and the dependence of the energy deposit on δ, the increase of ionisation at those layers is most significant for 3T models with $\delta = 5$. As the heating continues, the layers above ~1200 km become completely ionised (at $t \sim 2$ s and $t \sim 1$ s for low and high flux models, respectively – see thick lines in Figs. 2 and 3) and ionisation does not change during further heating – see also Fig. 4.

On the contrary, lower heights, below $s \sim 1000$ km, exhibit most significant increase of ionisation for models with $\delta = 3$. The ionisation at these layers reacts to the beam flux time modulation more for the flatter beams – see Fig. 4 which also demonstrates that the relaxation of ionisation to preheating values lags behind the time evolution of temperature.

This effect previously shown by Heinzel (1991) and Heinzel & Karlický (1992) is due to time evolution of the ratio of the number of recombinations to photoionisations. Detailed behaviour of photoionisations followed by photorecombinations was discussed by Abbett & Hawley (1999, Sect. 4).

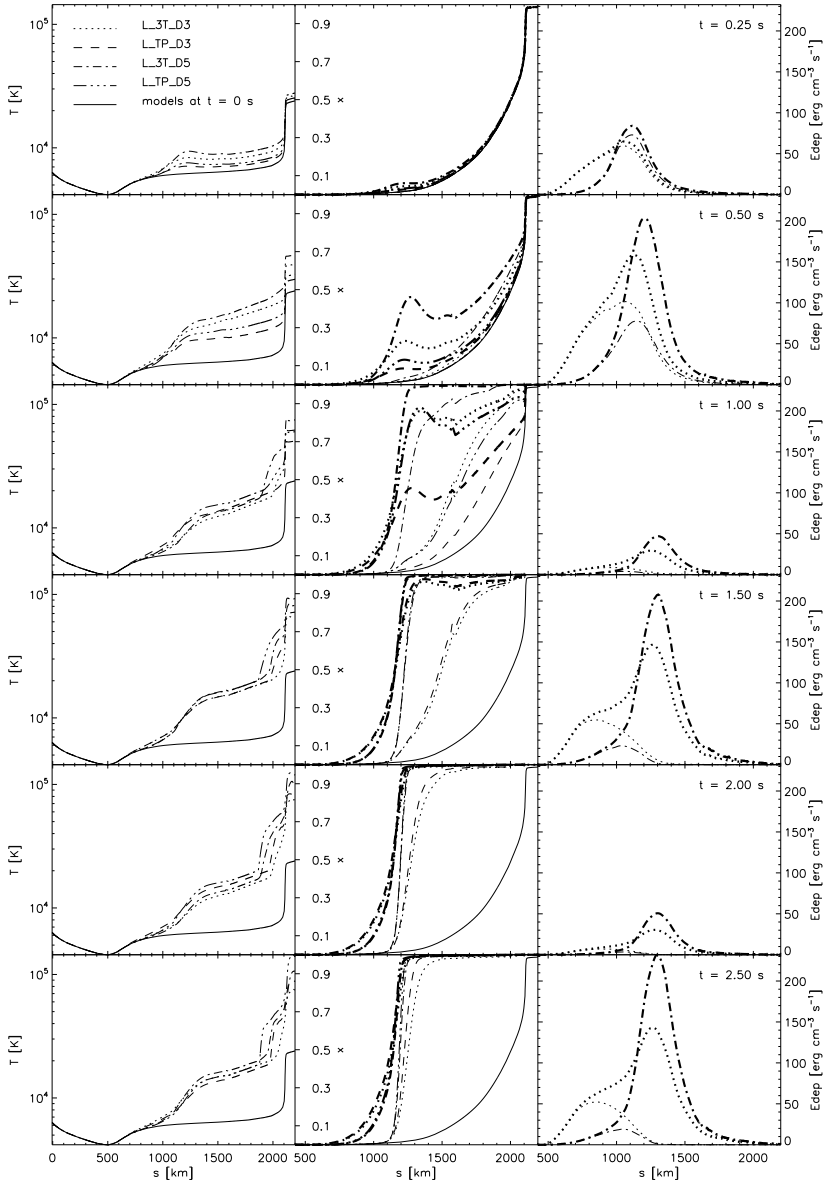

Fig. 2. Temperature, ionisation, and energy deposit corresponding to the low-flux models (L) and their evolution in time (*from top to bottom*). Different line styles denote four low-flux models. Thin solid line shows initial VAL C temperature and ionisation structure. *Left*: temperature. *Middle*: ionisation. Thick lines denote the models with $C^{\rm nt}$, thin lines without $C^{\rm nt}$. *Right*: total energy deposit $\mathcal{H}$ (thick lines) and energy deposit to hydrogen $\mathcal{E}_{\rm en}$ (thin lines). Only deposits corresponding to the triangular modulation models (3T) are displayed.

3.2. Influence of non-thermal collisional rates

To evaluate the influence of the non-thermal collisional rates, two separate runs with and without $C^{\rm nt}$ (Eq. (12)) were made for each model in Table 1.

Taking into account $C^{\rm nt}$ leads only to marginal changes of temperature and density structure of the atmosphere (up to 17%). On the contrary, hydrogen ionisation and emission in Balmer lines may significantly differ in models with and without $C^{\rm nt}$. Generally, the effect of $C^{\rm nt}$ is stronger for models with larger $F_{\rm max}$ or lower δ. In the low-flux models, $C^{\rm nt}$ significantly modify the time evolution of ionisation structure. They lead to a faster complete ionisation of layers above $s \sim 1200$ km and cause an increase of ionisation in the layers below, compare thin and thick lines in Fig. 2. The influence of $C^{\rm nt}$ in the high-flux models is localised mainly in the layers below $s \sim 1000$ km where the flatter beams increase the ionisation. The upper parts of the atmosphere are affected by $C^{\rm nt}$ only temporarily, till $t \sim 0.5$ s, when they contribute to the fast ionisation of those layers – see Fig. 3.

Since $C^{\rm nt}$ are directly proportional to the energy deposit on hydrogen $\mathcal{E}_{\rm en}$ (Eq. (12)), their influence is strongly linked to the $\mathcal{E}_{\rm en}$ as a function of height. Consequently, $C^{\rm nt}$ affect Balmer line intensities according to their formation heights. That can be understood in terms of the contribution function CF to the outgoing intensity I_λ

$$I_\lambda = \int_{s_{\rm min}}^{s_{\rm max}} CF_\lambda \, {\rm d}s = \int_{s_{\rm min}}^{s_{\rm max}} \eta_\lambda(s) {\rm e}^{-\tau_\lambda(s)} \, {\rm d}s, \qquad (15)$$

where η_λ is the emissivity and τ_λ is the optical depth. Figure 5 demonstrates the effect of $C^{\rm nt}$ on the Hα line for a low and high-flux model. In high-flux models, $C^{\rm nt}$ affect mainly the line wings. A new wing formation region appears at heights of maximum of

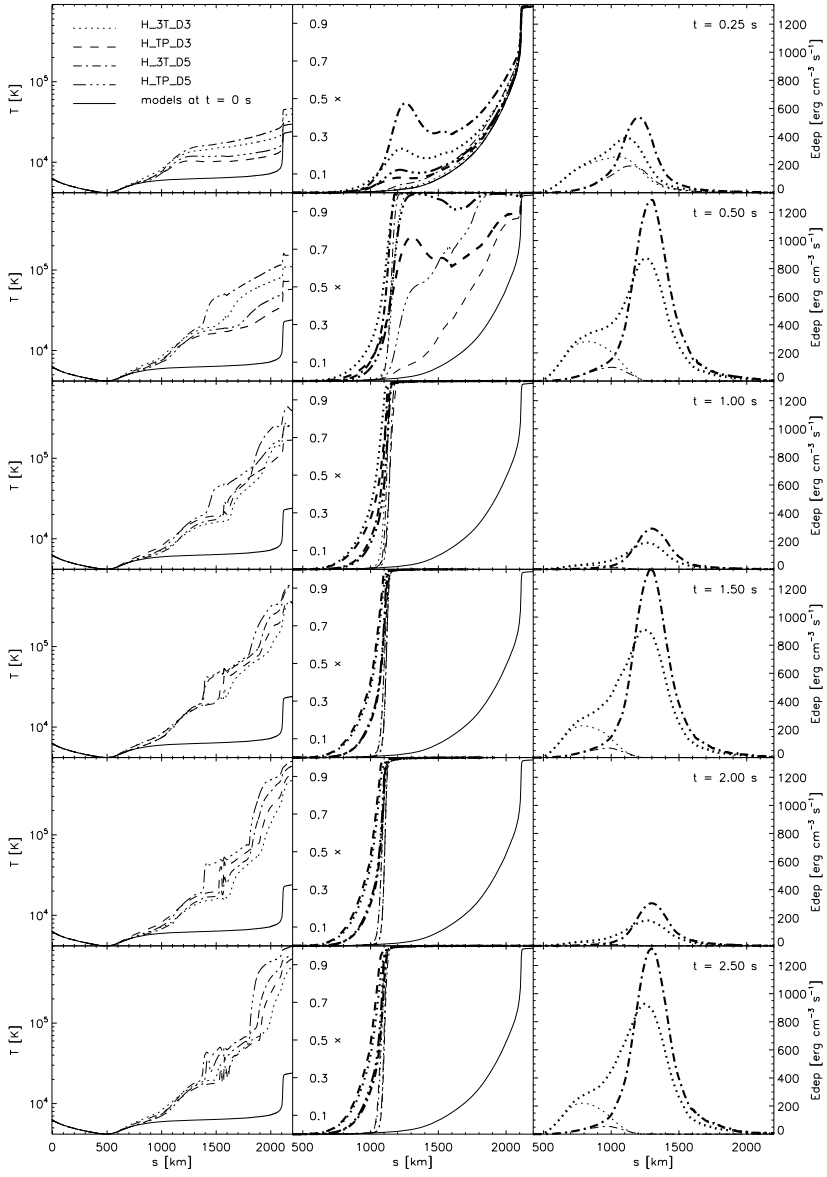

Fig. 3. Temperature, ionisation, and energy deposit corresponding to the high-flux models (H) and their evolution in time (*from top to bottom*). The notation is the same as in Fig. 2.

energy deposit on hydrogen, lower δ producing a stronger contribution to CF. In the low-flux models, $C^{\rm nt}$ influence also the line centre due to change of ionisation of upper layers where e.g. the Hα line centre is formed. The optical depth in the line centre at these heights is decreased and the Hα line centre formation region is shifted deeper. Similarly as in the high-flux models, a new region of wing formation region again appears at the height of the $\mathcal{E}_{\rm en}$ maximum, however the dominant part of the wing emission still comes from the photospheric layers, i.e. from $s \sim 100$ km – see Fig. 5.

3.3. Time variation of line intensities

The intensity variations depend on the maximum beam flux. The low beam flux results in gradual increase of intensities (models L), whereas high beam flux (models H) causes rapid heating of the atmosphere and hence fast and larger increase of line intensities – see Fig. 6 which compares time variations of Hα, Hβ, and Hγ for models L_3T_D3, L_3T_D5, H_3T_D3, and H_3T_D5. (Owing to use of the five level plus continuum atomic model, results concerning Hγ line should be regarded only qualitatively.) Since larger δ results in larger heating of the upper parts of the atmosphere, it leads to higher line centre intensities of Hα and Hβ which are formed in the upper parts of the atmosphere. On the other hand, the whole Hγ line and Hα and Hβ wings are formed in deeper layers, therefore they show more prominent intensity variations for flatter beams ($\delta = 3$) – compare D3 and D5 models in Fig. 6.

Figure 7 demonstrates the time variation and changes induced by $C^{\rm nt}$ of formation regions of the Hα line centre ($\Delta\lambda = 0$ Å), line wing $\Delta\lambda = 1$ Å, Hγ line centre ($\Delta\lambda = 0$ Å), and Hγ line wing ($\Delta\lambda = 0.6$ Å) for L_3T_D3 model. Shortly after the first beam injection into the VAL C atmosphere, at $t \sim 0.1$ s, line intensities decrease by a factor of ~2 and more – see Fig. 6. Such a

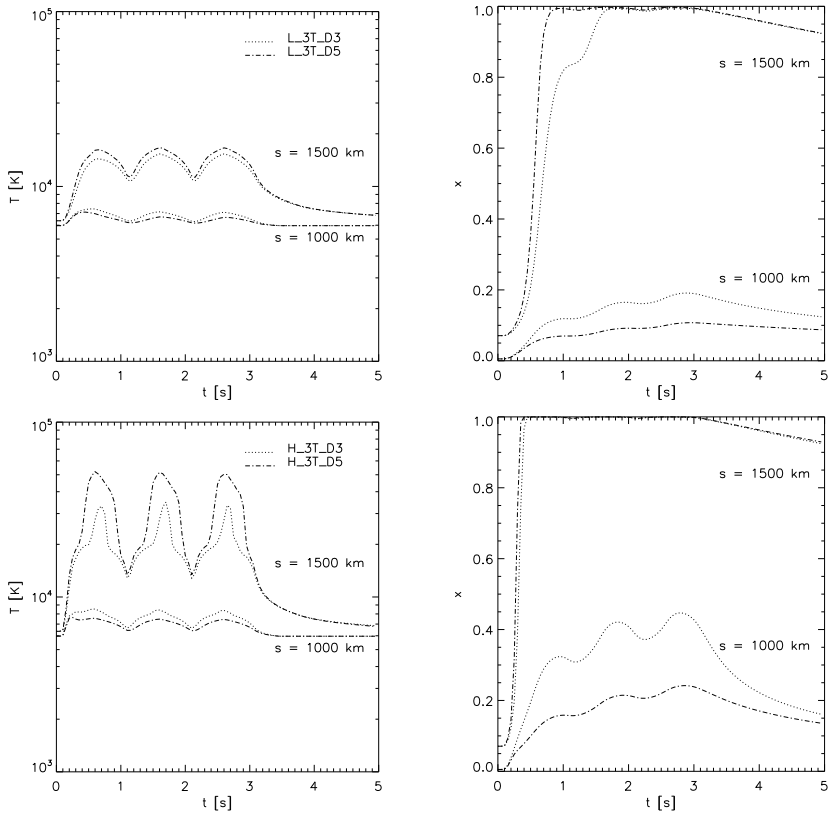

Fig. 4. Time evolution of temperature (*left*) and ionisation (*right*) at two heights s = 1000 and 1500 km. *Top*: low-flux models L_3T_D3 (dotted) and L_3T_D5 (dash-dotted). *Bottom*: high-flux models H_3T_D3 (dotted) and H_3T_D5 (dash-dotted). $C^{\rm nt}$ were included.

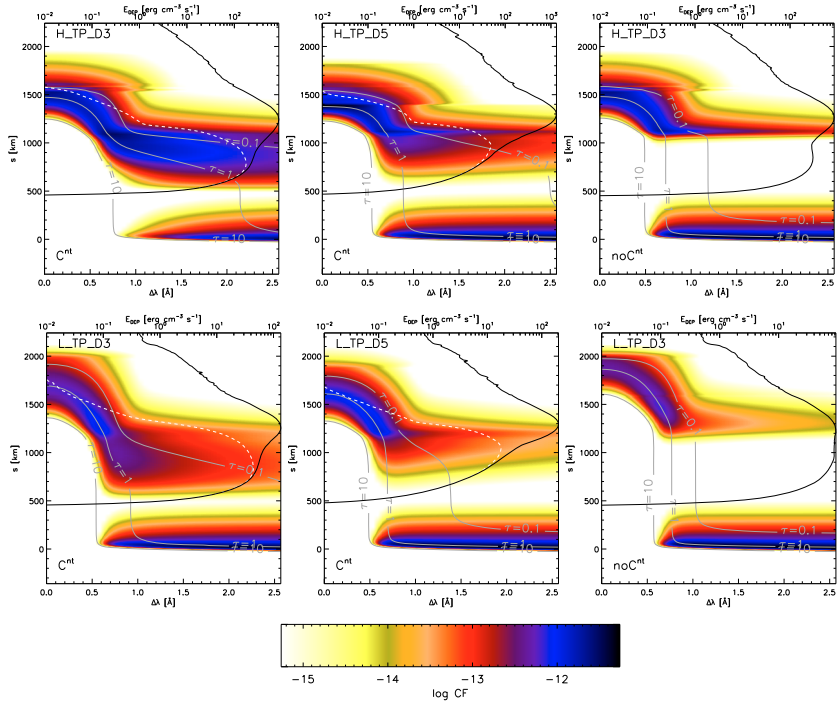

Fig. 5. Hα contribution functions for high (*top*) and low (*bottom*) flux models for trapezoidal beam flux modulation. Black solid curves indicate the total energy deposit, white dashed curves denote the energy deposit on hydrogen. Gray lines display contours of optical depth τ = 0.1, 1, 10. *Top left*: model H_TP_D3 with $C^{\rm nt}$. *Top centre*: model H_TP_D5 with $C^{\rm nt}$. *Top right*: model H_TP_D3 without $C^{\rm nt}$. *Bottom left*: model L_TP_D3 with $C^{\rm nt}$. *Bottom centre*: model L_TP_D5 with $C^{\rm nt}$. *Bottom right*: model L_TP_D3 without $C^{\rm nt}$. Colour scale denotes $\log CF$. All plots correspond to t = 1.8 s – maxima of line intensities, see Fig. 6.

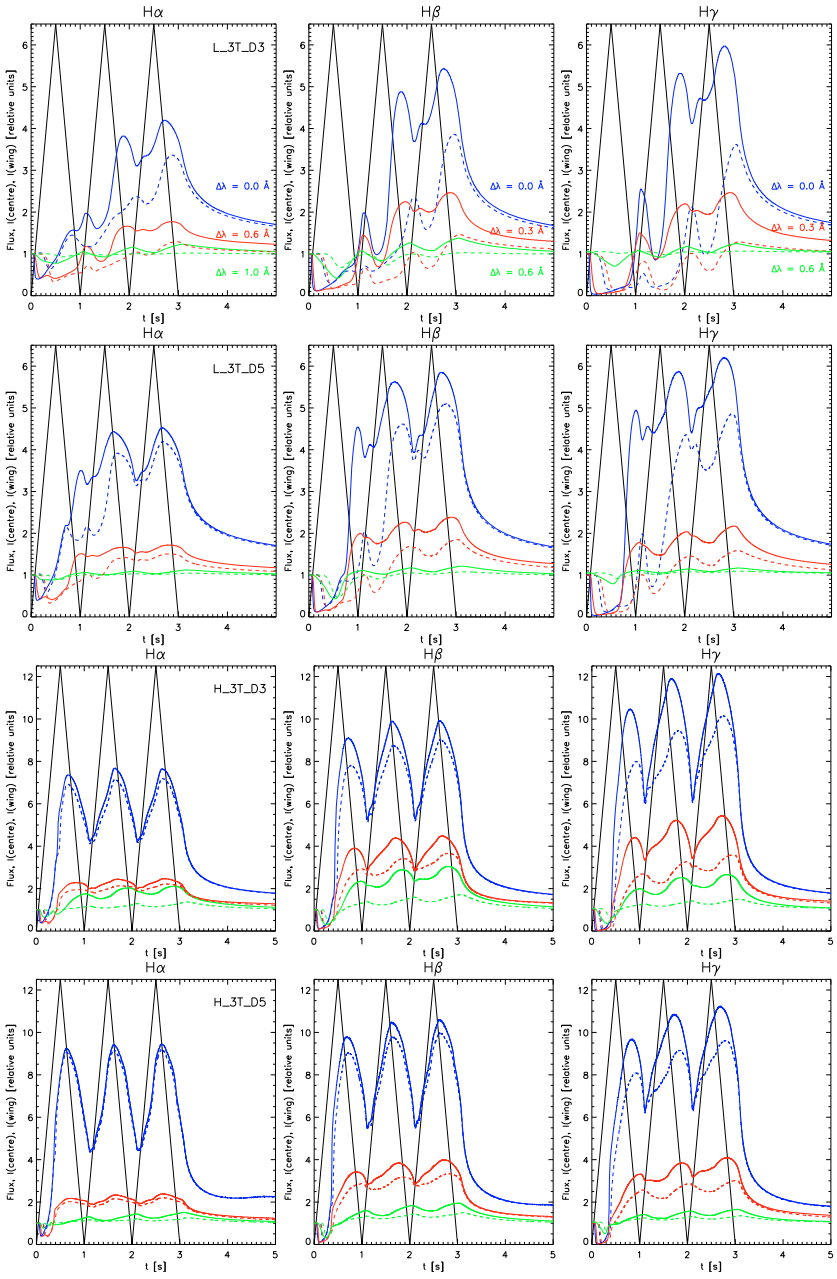

Fig. 6. Time evolution of the Hα, Hβ, and Hγ line intensities in three selected wavelengths for each line. Solid lines denote models with $C^{\rm nt}$, dashed without $C^{\rm nt}$. The black solid line shows the beam flux time modulation in relative units. *From top to bottom*: L_3T_D3, L_3T_D5, H_3T_D5, and H_3T_D5 model.

dip appears due to a temporal increase in optical depth, τ, which is caused by $C^{\rm nt}$. A similar decrease appearing later, at $t \sim 0.4$ s is present also in the models without $C^{\rm nt}$ – compare *CF* with and without $C^{\rm nt}$ in Fig. 7. That dip is a result of relative importance of the thermal collisional rates C_{1j}. This behaviour was explained by Heinzel (1991) for the case of a 3-level model of hydrogen as a consequence of steeper rise of second level population, n_2, in comparison to n_3 with time. Figure 7 also shows that a region of secondary Hα wing emission is formed shortly after the beam injection and its intensity slowly increases in time.

In the case of the high-flux model, the emission from the secondary formation region dominates and photospheric contribution to the wing intensities diminishes; this behaviour is typical for all studied Balmer lines. As regards Hγ line, formation of the Hγ line centre is due to $C^{\rm nt}$ completely moved from the photosphere to the layers above $s \sim 1200$ km. Contrary to the model without $C^{\rm nt}$, no emission from the photosphere contributes to the outgoing intensity. Furthermore, $C^{\rm nt}$ again lead to the prominent secondary wing formation region at $s \sim 1000$ km which occurs in the model without $C^{\rm nt}$ at much later time $t \sim 2$ s – see last panel in Fig. 7.

Intensities of all three studied lines show a good correlation with the beam flux on a time scale of the beam flux variation, i.e. on a subsecond time scale. Depending on the amount of heating, time variations are caused by the time-dependent temperature structure, e.g. Hα line centre in the high-flux models, and influence of $C^{\rm nt}$. Line intensities which are affected by $C^{\rm nt}$ (line centres in the low-flux models and line wings in the high-flux

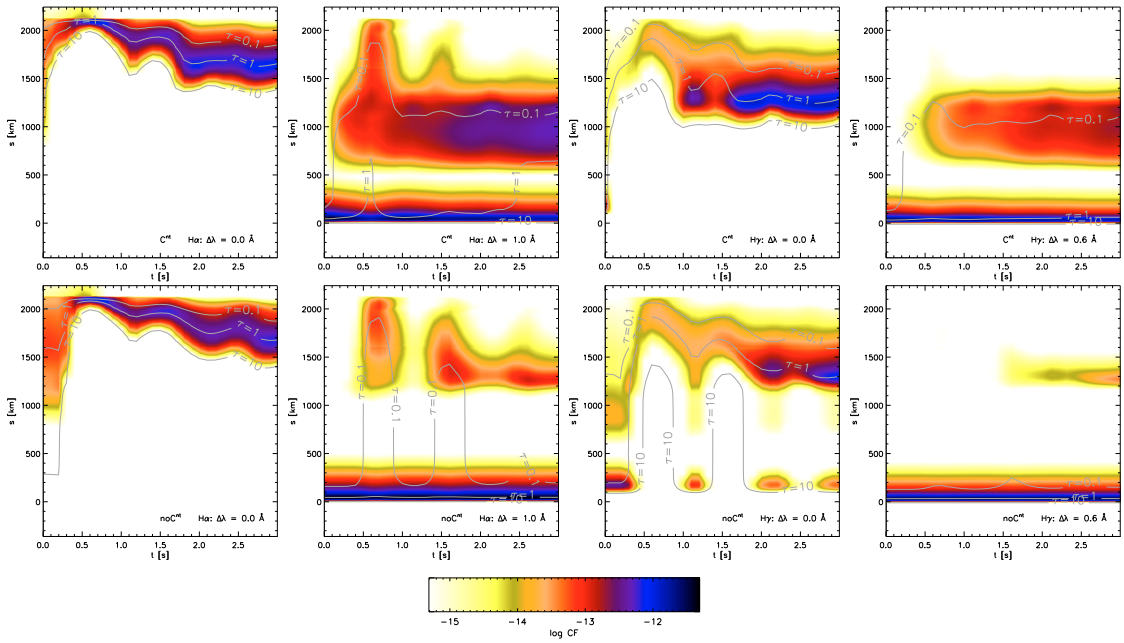

Fig. 7. Time evolution of *CF* of Hα ($\Delta\lambda$ = 0 Å), Hα ($\Delta\lambda$ = 1 Å), Hγ ($\Delta\lambda$ = 0 Å), and Hγ ($\Delta\lambda$ = 0.6 Å) for L_3T_D3 model. Gray lines denote contours of $\tau_\lambda = (0.1, 1, 10)$. *Top*: with $C^{\rm nt}$. *Bottom*: without $C^{\rm nt}$. Colour scale denotes $\log CF$.

models) show more significant time variations. Maxima of line intensities lag behind the beam flux maxima, the time lags are generally larger for line wing intensities than for line centre intensities. Such a time lag is not a beam propagation effect but it is related to different time variations of electron density at different heights. We are aware of the fact that velocities would cause asymmetry of lines and modify the line intensities. Here we concentrate on the beam influence on line formation. For detailed comparison with observed Balmer lines, velocity should be considered in calculating the line intensities.

3.4. Diagnostic tools

Having obtained the time evolution of Balmer line profiles for various electron beam parameters, we can search for observable signatures that could provide a method for diagnostic of the electron beam presence in the Balmer line formation regions. In order to distinguish between the flare energy transport by the nonthermal electrons and other agents (e.g. Alfvén waves – Fletcher & Hudson 2008), we consider a method suitable for such a diagnostics only if $C^{\rm nt}$ lead to significant and systematic differences in measured quantities.

3.4.1. Intensity ratios

Recently, Kashapova et al. (2008) reported on so-called sidelobes in Hα/Hβ intensity ratio (i.e. increased value of Hα/Hβ at $\Delta\lambda \sim 0.5$ Å with respect to other wavelength positions) observed in flare kernels associated with radio and hard X-ray bursts. They attributed the appearance of such sidelobes to the effects of nonthermal electrons.

Using our simulations we are able to check whether the observed sidelobes are a feature related to the electron beams. An example of a sidelobe is shown in Fig. 8 (left). It appears as a

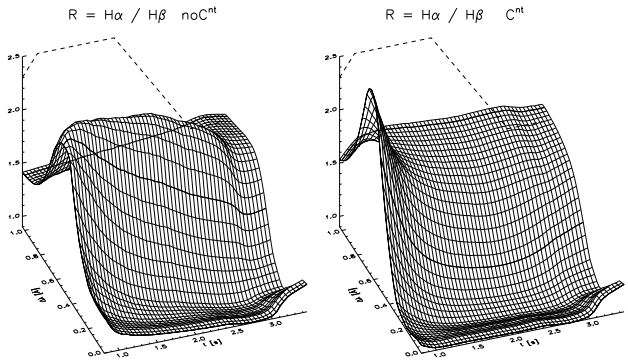

Fig. 8. Intensity ratio $R_{\alpha\beta}(\Delta\lambda, t)$ as a 2D function of wavelength and time for the H_TP_D3 model. *Left*: without $C^{\rm nt}$, *right*: with $C^{\rm nt}$. The black dashed line denotes time modulation of the beam flux. Thick solid lines represent $R_{\alpha\beta}$ at selected $\Delta\lambda = 0, 0.5, 1$ Å which are shown for all models in Fig. 9. For display purposes, the time evolution is shown from $t = 0.8$ s.

local maximum at $\Delta\lambda \approx 0.6$ Å and varies on a timescale similar to the beam flux modulation. Due to velocities, such sidelobes could be asymmetric with respect to the line centre. On the other hand, there are observations of almost symmetric Balmer lines and Hα/Hβ ratios in the flare kernels associated with hard X-ray emission (Kotrč et al. 2008), thus our models which do not consider velocities in radiative transfer can be applied to such situations.

Figure 9 shows the time evolution of Hα/Hβ at several $\Delta\lambda$, $R_{\alpha\beta}(\Delta\lambda, t)$ (indicated also in Fig. 8), for all considered models of the beam heating (see Table 1). In these plots, a sidelobe at a certain $\Delta\lambda$ would appear as an increased line above the others, varying according to the beam time modulation.

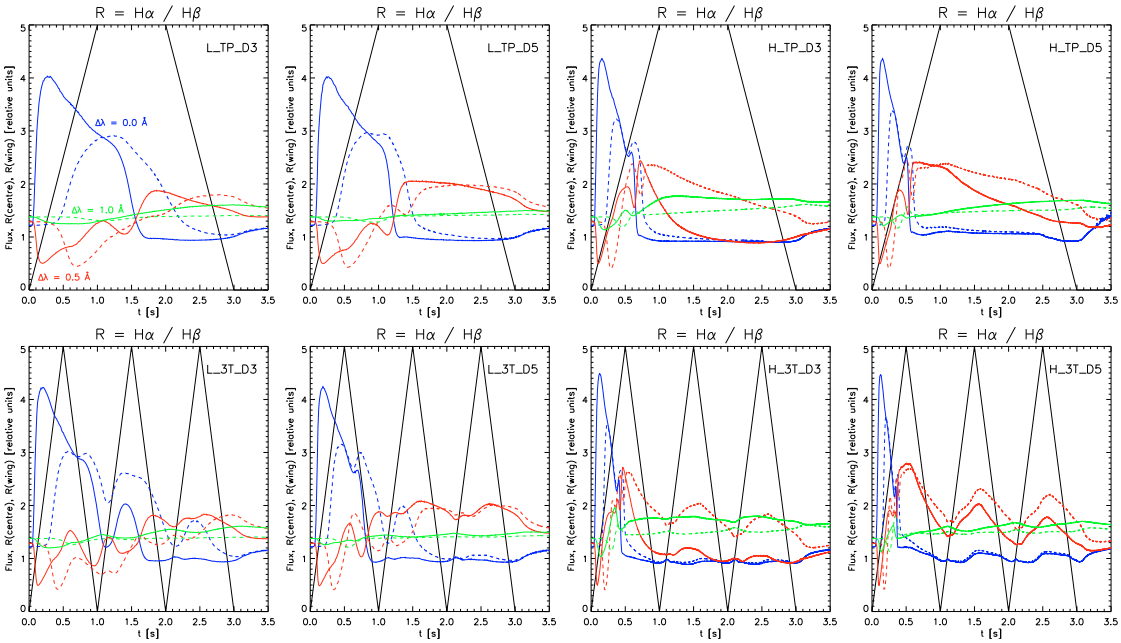

Fig. 9. The intensity ratios $R_{\alpha\beta}(\Delta\lambda, t)$ for three selected wavelengths $\Delta\lambda$. Solid lines denote models with $C^{\rm nt}$ and dashed without $C^{\rm nt}$. The black solid line shows the time modulation of the beam flux. *Top*: trapezoidal time modulation. *Bottom*: modulation by triangular peaks.

To consider a sidelobe being caused by the electron beam, the sidelobe should correspond to a simulation with $C^{\rm nt}$ included. For some beam parameters $R_{\alpha\beta}(0.5\ \text{Å}, t)$ exhibits the reported sidelobe behaviour with the exception of the high-flux models with $\delta = 3$ – see Fig. 8 (right) or the corresponding third panel in the top and bottom row in Fig. 9 – where $R_{\alpha\beta}(0.5\ \text{Å}, t)$ rapidly drops below $R_{\alpha\beta}(\Delta\lambda > 0.5\ \text{Å}, t)$ and no sidelobe exists in $R_{\alpha\beta}$ on a beam timescale. Hα/Hγ ratio shows a similar behaviour to $R_{\alpha\beta}$ whereas Hβ/Hγ ratio is much weakly sensitive to beam parameters.

On the other hand, neglecting the effect of $C^{\rm nt}$, i.e. assuming other agents than electron beams for the flare energy transport, sidelobes at $\Delta\lambda = 0.5$ Å are present at all models. Thus, the observed sidelobes cannot be considered as a unique signature of beam presence in the atmosphere but they are probably related to an impulsive heating.

Note that the maximal sidelobes from our simulations may appear, for some models, at wavelength positions slightly different from $\Delta\lambda \sim 0.5$ Å.

Furthermore, other kinds of intensity ratios, e.g. a relative line intensity with respect to the line centre value such as $R_\alpha(\Delta\lambda, t) = I(\Delta\lambda, t)/I(0\ \text{Å}, t)$, do not show any systematic difference between the models with and without $C^{\rm nt}$ either. Therefore, the intensity ratios do not provide a reliable diagnostic tool suitable for analysing the presence of the electron beams in the Balmer line formation regions.

3.4.2. Wavelength-integrated intensity

Wavelength-integrated intensity $I_{\rm tot}$ (proportional to equivalent width) was recently proposed by Cheng et al. (2006) as a tool for diagnostics of the non-thermal effects in the solar flares. On the basis of static semiempirical models, they propose to judge the relative importance of thermal and non-thermal heating in flares by analysis of $I_{\rm tot}$(Hα) and $I_{\rm tot}$(CaII 8542 Å) which show

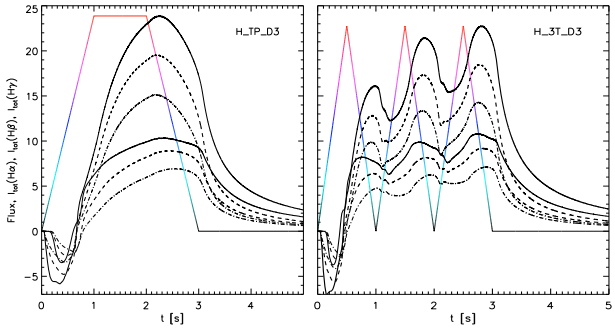

Fig. 10. Time evolution of Hα (solid), Hβ (dashed), and Hγ (dot-dashed) wavelength-integrated intensities. The modulation of the beam flux is shown as colour-changing broken line, the colour indicates the flux value. Thick lines denote models with $C^{\rm nt}$ and thin without $C^{\rm nt}$. Total deposited energy $E_{\rm tot}$ is the same for both models.

significantly different sensitivity to $C^{\rm nt}$. Using this idea, we analyse in detail the wavelength-integrated intensity

$$I_{\rm tot} = k \int_{-\Delta\lambda_{\rm max}}^{+\Delta\lambda_{\rm max}} [I(\lambda, t) - I(\lambda, t = 0)]\ {\rm d}\lambda \qquad (16)$$

of the studied Balmer lines for more general radiative hydrodynamic models. k is a normalisation to scale intensities, here we use line centre intensity at $t = 0$ s.

From our simulations it follows that maximum reached values of $I_{\rm tot}$ are predominantly given by the total deposited energy $E_{\rm tot}$ (see Eq. (2) and Fig. 10). Detailed time evolution of the beam flux is reflected as "loopy structures" in $I_{\rm tot} - I_{\rm tot}$ plots – see the top row of Fig. 11 – and the time variation of $I_{\rm tot}$ correlates with the beam flux variation, see Fig. 10. However, there is

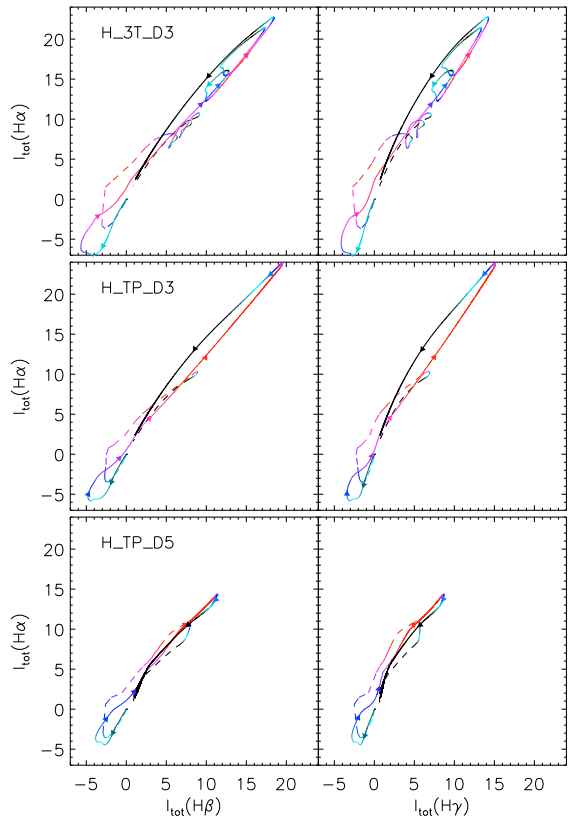

Fig. 11. Time evolution of $I_{\rm tot}$(Hα), $I_{\rm tot}$(Hβ), and $I_{\rm tot}$(Hγ). The colour corresponds to the beam flux value – see also colouring in Fig. 10. Arrows indicate the direction of time evolution. Solid lines denote models with $C^{\rm nt}$, dashed lines the models without $C^{\rm nt}$. *Top*: H_3T_D3 model. *Centre*: H_TP_D3 model. *Bottom*: H_TP_D5 model. Total deposited energy $E_{\rm tot}$ is the same for all panels.

no unique dependence of Balmer line $I_{\rm tot}$ on $F_{\rm max}$, see the right panel of Fig. 10 which shows gradual increase of $I_{\rm tot}$ with local minima and maxima corresponding to the time modulation of the beam flux. Moreover, in the case of the high-flux models, $I_{\rm tot}$ depend also on δ. As a consequence of increased wing emission for lower δ, see Fig. 6, $I_{\rm tot}$ of all studied Balmer lines reach large values for flatter electron spectra (compare centre and bottom panel in Fig. 11).

Taking $C^{\rm nt}$ into account leads to a significant increase of $I_{\rm tot}$ – see Figs. 10 and 11, but similar increase can be caused by stronger heating by other mechanisms than electron beams. Due to this reasons, neither wavelength-integrated intensities of Balmer lines are good indicators of electron beam presence in the Balmer line formation regions.

4. Conclusions

Presented radiative hydrodynamic simulations revealed the complexity of the response of hydrogen Balmer lines to the electron beam heating. At the same time, they proved to be a very useful tool to obtain answers to questions raised in the Introduction.

1. We showed that the Balmer line intensities do vary on beam flux variation time scales, i.e. on a subsecond time scale. The time variations are caused by time evolution of the temperature structure, electron density and influence of the non-thermal collisional rates. Depending on the amount of the beam flux, time evolution of line intensities may also exhibit both fast (pulse like), and gradual (e.g. an increase of intensity on a time scale larger than the beam flux time variation) components, see e.g. the case of model L_3T_D3 in Fig. 6. Such behaviour is known for the Hα line from observations (Trottet et al. 2000). Therefore, we conclude that the fast pulse-like variations seem to be a good indicator of the particle beams, namely when correlated with HXR or radio pulsations.
2. Influence of the non-thermal rates on the Balmer lines depends on the beam parameters, both the energy flux and power-law index. $C^{\rm nt}$ significantly alter the ionisation structure, leading to a modification of the line formation regions which are not ionised due to the heating. Depending on the beam parameters, $C^{\rm nt}$ can affect line centres, wings or both, but generally $C^{\rm nt}$ result in an increased emission from a secondary formation region in the chromosphere.
3. Concerning the diagnostic tools based on Balmer lines, except for the close correlation of the time variation of the beam flux and the line intensities, we did not found any systematic behaviour that would uniquely indicate the presence of the non-thermal electrons in the atmosphere solely from observations of Balmer lines. Complementary information such as hard X-ray emission or spectral lines having different sensitivity to $C^{\rm nt}$, e.g. Ca II (8542 Å), are needed to assess the presence of the non-thermal particles.

In this model study, we analysed the influence of the beam heating and the non-thermal collisional rates on hydrogen Balmer lines in the case of prescribed fast beam flux modulation. The next step is to compare the observed line emission with the simulated one using the non-LTE RHD models for beam parameters inferred from hard X-ray or radio emission. In this way, the role of different flare energy transport mechanisms e.g. such as alternative heating of the chromosphere by Alfvén waves recently proposed by Fletcher & Hudson (2008) can be adequately addressed. We plan to apply our code to fast time variations of Hα and hard X-ray emissions observed during solar flares (e.g. Radziszewski et al. 2007).

Acknowledgements. We thank the referee, S. L. Hawley, for many valuable comments. This work was supported by grants 205/04/0358, 205/06/P135, 205/07/1100 of the Grant Agency of the Czech Republic and the research project AV0Z10030501 (Astronomický ústav). Computations were performed on OCAS (Ondřejov Cluster for Astrophysical Simulations) and Enputron, a computer cluster for extensive computations (Universita J. E. Purkyně).

References

Abbett, W. P., & Hawley, S. L. 1999, ApJ, 521, 906
Allred, J. C., Hawley, S. L., Abbett, W. P., & Carlsson, M. 2005, ApJ, 630, 573
Bai, T. 1982, ApJ, 259, 341
Canfield, R. C., Gunkler, T. A., & Ricchiazzi, P. J. 1984, ApJ, 282, 296
Cheng, J. X., Ding, M. D., & Li, J. P. 2006, ApJ, 653, 733
Czaykowska, A., de Pontieu, B., Alexander, D., & Rank, G. 1999, ApJ, 521, L75
Ding, M. D., Qiu, J., Wang, H., & Goode, P. R. 2001, ApJ, 552, 340
Doschek, G. A., Mariska, J. T., & Sakao, T. 1996, ApJ, 459, 823
Emslie, A. G. 1978, ApJ, 224, 241
Fang, C., Henoux, J. C., & Gan, W. Q. 1993, A&A, 274, 917
Fisher, G. H., Canfield, R. C., & McClymont, A. N. 1985, ApJ, 289, 414
Fletcher, L., & Hudson, H. S. 2008, A&A, 675, 1645
Hawley, S. L., & Fisher, G. H. 1994, ApJ, 426, 387
Heinzel, P. 1991, Sol. Phys., 135, 65
Heinzel, P. 1995, A&A, 299, 563
Heinzel, P., & Karlický, M. 1992, in Eruptive Solar Flares, Proc. Colloq. 133, ed. Z. Svestka, B. V. Jackson, & M. E. Machado, IAU Colloq., 399, 359
Hoyng, P., Duijveman, A., Machado, M. E., et al. 1981, ApJ, 246, L155

Hudson, H. S., & Fárník, F. 2002, in Solar Variability: From Core to Outer Frontiers, ed. J. Kuijpers, ESA SP, 506, 261
Karlický, M. 1990, Sol. Phys., 130, 347
Karlický, M., & Hénoux, J.-C. 1992, A&A, 264, 679
Karlický, M., Kašparová, J., & Heinzel, P. 2004, A&AL, 416, L13
Kashapova, L. K., Kotrč, P., & Kupryakov, Y. A. 2008, Annales Geophysicae, 26, 2975
Kašparová, J., Heinzel, P., Varady, M., & Karlický, M. 2003, in Stellar Atmosphere Modeling, ed. I. Hubeny, D. Mihalas, & K. Werner, ASP Conf. Ser., 288, 544
Kopp, R. A., & Pneuman, G. W. 1976, Sol. Phys., 50, 85
Kotrč, P., Kashapova, L. K., & Kuprjakov, Y. A. 2008, 12th European Solar Physics Meeting, Freiburg, Germany, held September, 8–12, http://espm.kis.uni-freiburg.de/, 2.61, 12, 2
Nagai, F., & Emslie, A. G. 1984, ApJ, 279, 896
Nejezchleba, T. 1998, A&AS, 127, 607
Oran, E. S., & Boris, J. P. 1987, NASA STI/Recon Technical Report A, 88, 44860
Oran, E. S., & Boris, J. P. 2000, Numerical Simulation of Reactive Flow, ed. E. S. Oran, & J. P. Boris, ISBN 0521581753 (Cambridge, UK: Cambridge University Press), 550
Peres, G., Serio, S., Vaiana, G. S., & Rosner, R. 1982, ApJ, 252, 791
Radziszewski, K., Rudawy, P., & Phillips, K. J. H. 2007, A&A, 461, 303
Rosner, R., Tucker, W. H., & Vaiana, G. S. 1978, ApJ, 220, 643
Rybicki, G. B., & Hummer, D. G. 1991, A&A, 245, 171
Shibata, K. 1996, Advances in Space Research, 17, 9
Sturrock, P. A. 1968, in Structure and Development of Solar Active Regions, ed. K. O. Kiepenheuer, IAU Symp., 35, 471
Tandberg-Hanssen, E., & Emslie, G. A. 1988, The physics of solar flares (Cambridge University Press)
Trottet, G., Rolli, E., Magun, A., et al. 2000, A&A, 356, 1067
Turkmani, R., Vlahos, L., Galsgaard, K., Cargill, P. J., & Isliker, H. 2005, ApJ, 620, L59
Štěpán, J., Kašparová, J., Karlický, M., & Heinzel, P. 2007, A&A, 472, L55
Vernazza, J. E., Avrett, E. H., & Loeser, R. 1981, ApJS, 45, 635

ISSN 1845–8319

FAR-IR AND RADIO THERMAL CONTINUA IN SOLAR FLARES

J. KAŠPAROVÁ[1], P. HEINZEL[1], M. KARLICKÝ[1], Z. MORAVEC[2] and M. VARADY[2,1]

[1] *Astronomický ústav Akademie věd České republiky, v.v.i., Fričova 298, 251 65 Ondřejov, Czech Republic*
[2] *Katedra fyziky, Universita J. E. Purkyně, České mládeže 8, 400 24 Ústí nad Labem, Czech Republic*

Abstract. With the invention of new far-infrared (FIR) and radio mm and sub-mm instruments (DESIR on SMESE satellite, ESO-ALMA), there is a growing interest in observations and analysis of solar flares in this so far unexplored wavelength region. Two principal radiation mechanisms play a role: the synchrotron emission due to accelerated particle beams moving in the magnetic field and the thermal emission due to the energy deposit in the lower atmospheric layers. In this contribution we explore the time-dependent effects of beams on thermal FIR and radio continua. We show how and where these continua are formed in the presence of time dependent beam heating and non-thermal excitation/ionisation of the chromospheric hydrogen plasma.

Key words: solar flares - radiative hydrodynamics - continuum emission

1. Introduction

New ground-based and space-borne instruments are being designed to observe the Sun in so-far unexplored wavelength windows or with unprecedented spatial and/or temporal resolution. Here we are motivated by the planned observations of solar flares in the far infrared (FIR) region and in sub-millimetre/millimetre (SMM) radio wavelengths. A specific FIR window where the radiation is not observable from the Earth is between 35 and 250 μm and this is expected to be explored by the DESIR telescope on board the SMESE satellite (SMall Explorer for Solar Eruptions – Vial *et al.* (2007)). At SMM wavelengths, observations were already performed by Kaufmann *et al.* (2000) and Lüthi *et al.* (2004). However, new data are expected soon from ALMA (Atacama Large Millimeter Array) radio-interferometer. In both FIR and SMM domains a superposition of two radi-

ation components is expected: the high-frequency part of the microwave spectrum from ultra-relativistic electrons and/or positrons (non-thermal synchrotron emission) and the low-frequency part of the thermal flare continuum. As suggested in Vial *et al.* (2007), these emissions provide, respectively, a unique diagnostic of the non-thermal particles (beams) and of the thermal response of the lower flare atmosphere to the energy deposit. In the FIR domain, the relative importance of both processes was estimated by Ohki and Hudson (1975). Recently, Loukitcheva *et al.* (2004) and Heinzel and Avrett (2009) computed the microwave thermal continua formed in dynamic and static semi-empirical atmospheres, respectively.

In this study, we concentrate on formation of such thermal emission in the 35 μm – 1 cm wavelength range originating in a highly dynamical flare atmosphere heated by short-duration electron beam pulses. Section 2 describes the mechanisms responsible for the thermal emission, characteristics of the emission corresponding to simulations of the beam heated atmosphere are presented in Section 3. Section 4 summarizes our results.

2. Mechanisms of the FIR and SMM Thermal Continuum Formation

Depending on the wavelength, various atmospheric depths can contribute to the emergent FIR and SMM intensity (Heinzel and Avrett, 2009). In the chromosphere, the dominant source of opacity is the hydrogen free-free continuum. The absorption coefficient is given as (Rybicki and Lightman, 1979)

$$\kappa_\nu(\mathrm{H}) = 3.7 \times 10^8 T^{-1/2} n_\mathrm{e} n_\mathrm{p} \nu^{-3} g_\mathrm{ff} \tag{1}$$

where n_e and n_p are the electron and proton densities, respectively, T is the temperature, and $g_\mathrm{ff} \approx 1$ is the Gaunt factor. At lower temperatures, around the temperature minimum region, H^- free-free opacity plays an important role. The H^- absorption is (Kurucz, 1970)

$$\kappa_\nu(\mathrm{H}^-) = \frac{n_\mathrm{e} n_\mathrm{H}}{\nu}(1.3727\times10^{-25}+(4.3748\times10^{-10}-2.5993\times10^{-7}/T)/\nu) \tag{2}$$

where n_H is the neutral hydrogen density. The total absorption corrected for stimulated emission is then

$$\kappa_\nu = \left[\kappa_\nu(\mathrm{H}) + \kappa_\nu(\mathrm{H}^-)\right](1 - \mathrm{e}^{-h\nu/kT}) \ , \tag{3}$$

where h and k are the Planck and Boltzmann constants, respectively. The source function for these free-free processes is the Planck function B_ν. However, the absorption has to be evaluated using number densities coming from non-LTE calculations. Finally, the emergent intensity I_ν can be obtained as

$$I_\nu = \int \eta_\nu \mathrm{e}^{-\tau_\nu} \mathrm{d}z \qquad \eta_\nu = \kappa_\nu B_\nu \quad \mathrm{d}\tau_\nu = -\kappa_\nu \mathrm{d}z \ , \tag{4}$$

where z is the geometrical height.

3. Flare Models

We have evaluated the FIR and SMM continuum emission for non-LTE radiative hydrodynamic models which describe the atmospheric response to the time dependent electron beam heating. In these simulations electron beams of a varying beam flux and power-law spectra are injected into a loop which corresponds to an initially hydrostatic VAL C atmosphere (Vernazza *et al.*, 1981). Then, the time evolution of the beam particles and plasma properties are followed. We also consider the so-called non-thermal collisional rates, C^{nt}, which account for the changes of the atomic level populations due to the collisions with the beams. For more details on the models see Varady *et al.* (2005); Kašparová *et al.* (2009).

3.1. Time variation

Our simulations show that the continuum emission is well correlated with the beam flux on the time scale of the beam flux variation, e.g. on a sub second time scale. Longer wavelengths (1 cm) exhibit larger relative intensity increase than shorter wavelengths (35 μm) when compared to the the preflare (VAL C) intensities – see Figure 1. Furthermore, emission in the $\lambda < 0.2$ mm range depends also on the beam parameters, i.e. the power-law index and the beam flux. Generally, maxima of the emission lag behind the beam flux maxima, the time lag lies within the 0.1 – 0.3 s interval for present simulations.

3.2. Influence of non-thermal collisional rates

Although the non-thermal rates can significantly affect the hydrogen level populations and electron densities in some atmospheric layers (Kašparová

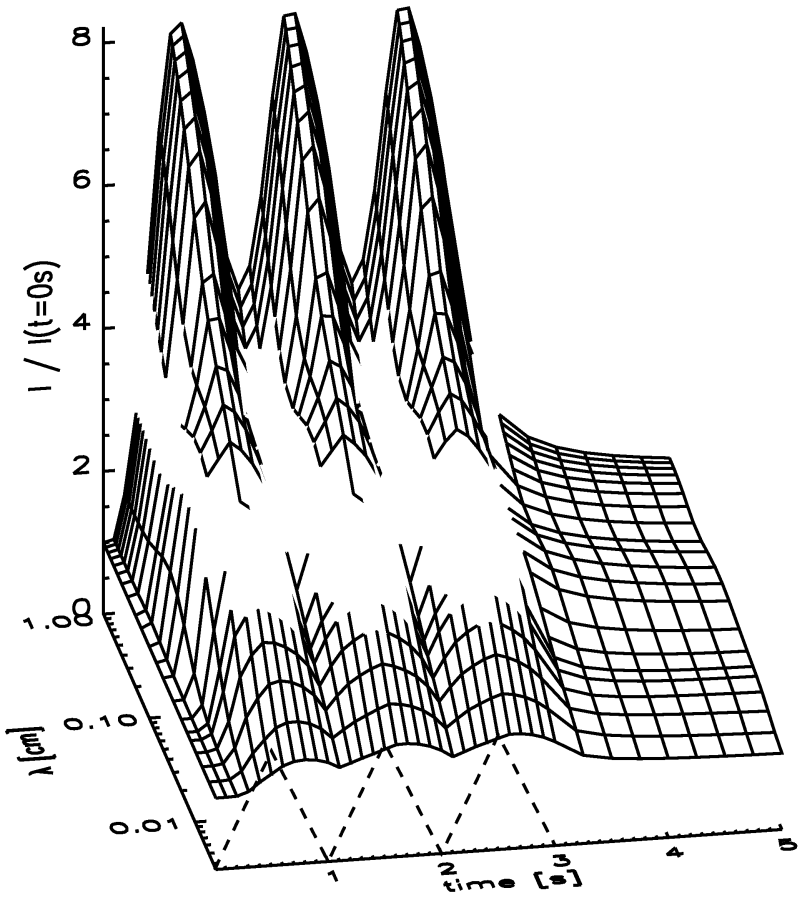

Figure 1: Time evolution of relative continuum intensities scaled to the intensity at $t = 0$ s, i. e. of the VAL C atmosphere, for an electron beam of a power-law index $\delta = 3$ and a maximum beam flux $F_{\max} = 6 \times 10^{10}$ erg cm^{-2} s^{-1}. The dashed line indicates the beam flux time variation.

et al., 2005), their influence on FIR and SMM continuum emission is almost negligible. The $C^{\rm nt}$ cause only a moderate and temporary increase of the continuum intensity shortly after the beam injection into the VAL C atmosphere. Additionally, the influence of $C^{\rm nt}$ for $\lambda < 0.2$ mm depends on the beam parameters and it is modulated by the beam flux time variation – see Figure 2.

3.3. Formation depths

The atmospheric layers which contribute the most to the outgoing intensity, i.e. the formation depths, can be understood in terms of the so-called

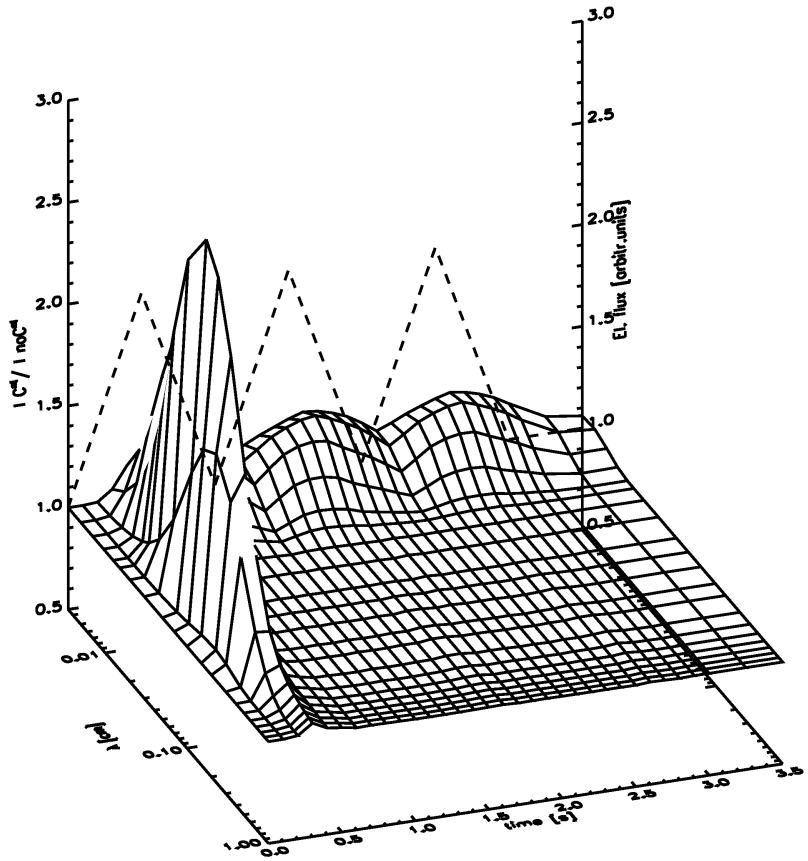

Figure 2: Influence of the non-thermal collisional rates C^{nt}. The plot shows the ratio of intensities with and without C^{nt}. The dashed line indicates the beam flux time variation. The beam parameters are the same as in Fig. 1. Note the reversed wavelength scale with regard to Figure 1.

contribution function CF

$$CF = \eta_\nu \mathrm{e}^{-\tau_\nu} \qquad I_\nu = \int CF \, \mathrm{d}z \,, \tag{5}$$

compare with Equation (4). In the initial atmosphere, emission at wavelengths shorter than $\lambda \approx 1$ mm comes from deep, photospheric layers, whereas the continuum at other wavelengths is formed at the upper part of the atmosphere. However, as the atmosphere is heated by the beams, the emission is formed mainly at the chromospheric heights (above $z \approx$ 1000 km). The emission which comes from these layers can be influenced also by C^{nt} since the beams deposit their energy there. On the other hand, the emission in the 35 – 200 μm range partially originates from the photosphere – see Figure 3.

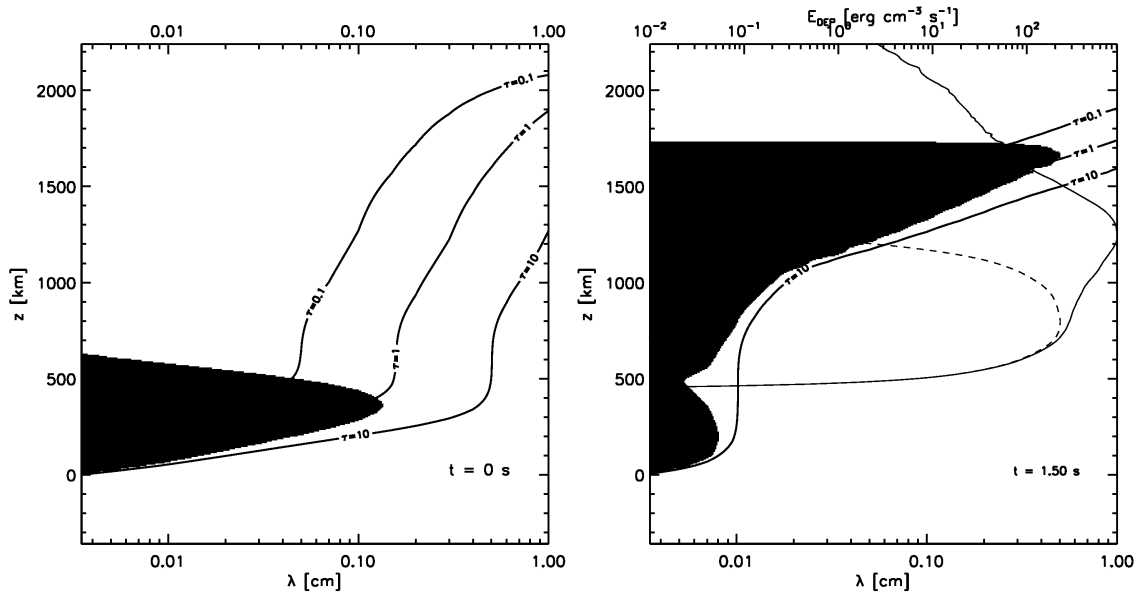

Figure 3: An example of the time evolution of contribution function *CF* (Equation 5) for an electron beam of $\delta = 3$ and $F_{\max} = 4.5 \times 10^{10}$ erg cm^{-2} s^{-1}. *Left: CF* for the VAL C atmosphere, i.e. at $t = 0$ s. *Right: CF* at $t = 1.5$ s corresponding to the model with included $C^{\rm nt}$. Colour scale going from white to black represents the range of log *CF* values (from minimum to maximum). Black solid curve indicates the total energy deposit of the beam, dashed curve is for the energy deposit on hydrogen $E_{\rm H}$. $C^{\rm nt}$ are proportional to $E_{\rm H}$, therefore the dashed line marks the layers which are affected by $C^{\rm nt}$. Gray lines display the levels of optical depth $\tau = 0.1, 1, 10$.

4. Conclusions

Using the results of non-LTE radiative hydrodynamic simulations we have found that the rapidly varying beam flux can manifest itself in the thermal FIR and SMM continuum intensities. We show that the continuum intensities do vary on the beam flux variation time scales. However, the direct influence of the beam electrons via the non-thermal collision is moderate only. The emission is mainly affected by the temperature variations which result from the time dependent heating by the beams. Concerning the formation of the emission, in the heated atmosphere or due to the non-thermal collisions the continua are formed in the upper atmosphere. The intensities in the 35 – 200 μm range partially originate also from the photosphere.

In this work we did not consider effects related to the situation when the frequency of the emitted electromagnetic waves is close to the local plasma frequency. In the case of the solar atmosphere plasma, these effects must be

taken into account at the radio frequency range. We will address this issue for the FIR and SMM emission in a future study.

Acknowledgements

We acknowledge grants 205/04/0358, 205/06/P135, 205/07/1100 (GA CR) and the research project AV0Z10030501 (Astronomický ústav). The non-LTE radiative hydrodynamic simulations were performed on OCAS (Ondřejov Cluster for Astrophysical Simulations) and Enputron, a computer cluster for extensive computations (Universita J. E. Purkyně).

References

Heinzel, P. and Avrett, E. H.: 2009, *Astrophys. J., in preparation* .

Kaufmann, P., Costa, J. E. R., Correia, E., Giménez de Castro, C. G., Raulin, J.-P., and Silva, A. V. R.: 2000, *in* R. Ramaty and N. Mandzhavidze (eds.), *High Energy Solar Physics Workshop - Anticipating Hessi*, Vol. 206 of *ASP Conf. Ser.*, p. 318.

Kašparová, J., Varady, M., Heinzel, P., Karlický, M., and Moravec, Z.: 2009, *Astron. Astrophys., submitted* .

Kašparová, J., Varady, M., Karlický, M., Moravec, Z., and Heinzel, P.: 2005, *in* D. Danesy, S. Poedts, A. De Groof, and J. Andries. (eds.), *ESA SP-600: The Dynamic Sun: Challenges for Theory and Observations*, ESA Publication Division. published on CDROM.

Kurucz, R. L.: 1970, *SAO Special Report* **309**.

Loukitcheva, M., Solanki, S. K., Carlsson, M., and Stein, R. F.: 2004, *Astron. Astrophys.* **419**, 747.

Lüthi, T., Magun, A., and Miller, M.: 2004, *Astron. Astrophys.* **415**, 1123.

Ohki, K. and Hudson, H. S.: 1975, *Solar Phys.* **43**, 405.

Rybicki, G. B. and Lightman, A. P.: 1979, *Radiative Processes in Astrophysics*, Wiley-Interscience, New York, p. 393.

Varady, M., Kašparová, J., Karlický, M., Heinzel, P., and Moravec, Z.: 2005, *Hvar Obs. Bull.* **29**, 167.

Vernazza, J. E., Avrett, E. H., and Loeser, R.: 1981, *Astrophys. J., Suppl. Ser.* **45**, 635.

Vial, J.-C., Auchère, F., Chang, J., Fang, C., Gan, W. Q., Klein, K.-L., Prado, J.-Y., Trottet, G., Wang, C., and Yan, Y. H.: 2007, *Adv. Space Res.* **40**, 1787.

Hinode-3: The 3rd Hinode Science Meeting
ASP Conference Series, Vol. 454
T. Sekii, T. Watanabe, and T. Sakurai eds.

Formation of Balmer Lines in Impulsively Heated Flare Atmosphere by Neutral Beams

M. Varady,[1,2] J. Kašparová,[2] Z. Moravec,[1] M. Karlický,[2] and P. Heinzel[2]

[1]*Department of Physics, J.E. Purkyně University, České mládeže 8, 400 24 Ústí nad Labem, Czech Republic*

[2]*Astronomický ústav Akademie věd České republiky, v.v.i, Fričova 298, 251 65 Ondřejov, Czech Republic*

Abstract. In the context of interpreting non-thermal hard X-ray emission and γ lines emanating from the footpoints of flare loops, most contemporary flare models assign a fundamental role during the flare energy release, transport and deposition to the high energy non-thermal particle beams. In this contribution we concentrate on modelling of the spectroscopic properties of chromospheric flare emission in optical hydrogen lines generated due to the bombardment of the chromosphere and photosphere by neutral beams with power-law spectra. In order to obtain an estimate of the neutral beam flare heating in the solar atmosphere we produced a simple model describing the propagation and thermalisation of neutral beams. We compare the neutral beam flare heating with the flare heating produced by corresponding pure electron and proton beams. Further we compare the contribution functions for Hα line obtained for neutral and electron beam heating.

1. Introduction

In the impulsive phase of flares, the beams formed by charged particles are guided from the acceleration site, wherever it is located, downwards along the magnetic field lines into the transition region, chromosphere and photosphere. In the lower atmospheric layers, due to the high density of local plasma, their kinetic energy is efficiently dissipated, the corresponding regions are rapidly heated, and dramatic changes of temperature and hydrogen ionisation occur.

It is well known from observations of γ lines in some flares that high energy particle beams may contain protons and ions accelerated to energies up to tens of GeV (Lin et al. 2003). It has been also proposed that not only electron beams, but also neutralised particle beams (constituted from electron, proton and ion components) may play the role of the flare heating in some flares (Martens 1988; Brown et al. 1990; Simnett & Haines 1990). In this contribution we present a simple test-particle code which was used to estimate the flare heating function of neutral beams. The main features of the neutral beam flare heating are discussed. The heating function obtained by the test-particle code was then used by the radiative-hydrodynamic code (Kašparová et al. 2009) and contribution functions for chromospheric Hα line were calculated. Besides the heating, also the influence of non-thermal collisional rates to the excitation and ionisation processes have been included. The contribution functions obtained for neu-

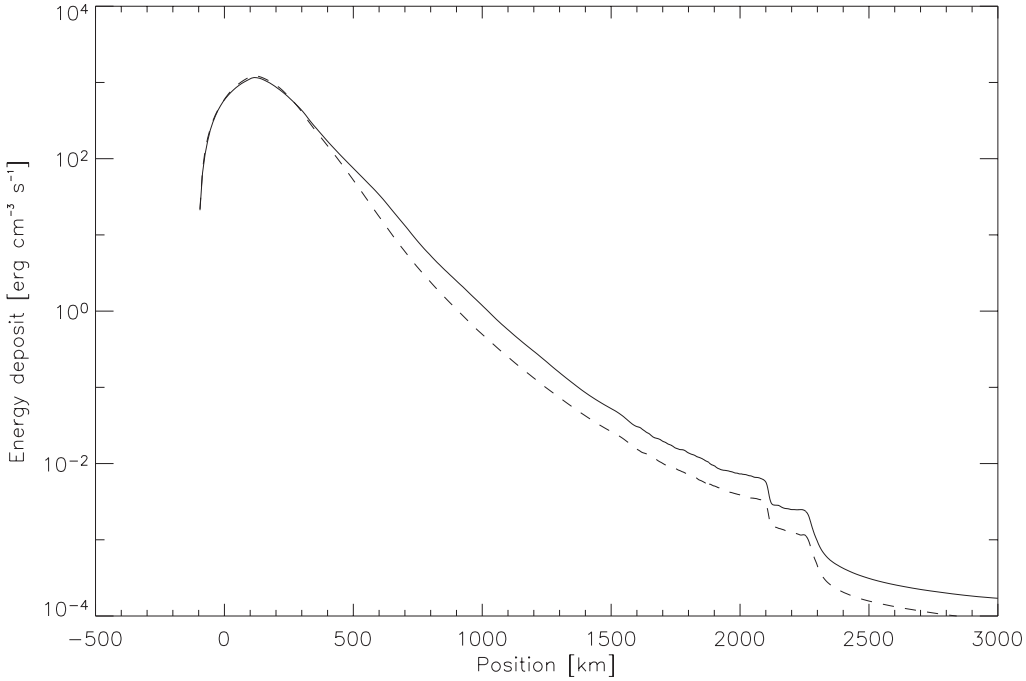

Figure 1. Comparison of energy deposits of neutral (solid line) and proton (dashed line) beams $F_{\max} = 4.5 \times 10^{10}$ erg cm^{-2} s^{-1}, $E_0 = 35$ MeV, $\delta = 3$.

tral beam flare heating are compared with the contribution functions obtained for pure electron beam heating.

2. Model

The propagation and energy deposit (flare heating) of neutral beams is calculated using a test-particle approach based on the following simple scenario. We assume that the neutral beam is formed from electrons and protons. During the beam propagation the beam electrons are dragged by the beam protons (Karlický et al. 2000) and the parallel velocity components (to the magnetic fieldlines) of beam protons and electrons are equal, i.e. $v_{\parallel}^{\mathrm{p}} = v_{\parallel}^{\mathrm{e}}$ and the current density related to the beam propagation vanishes (Martens 1988), so the beam electron and proton densities are identical $n_{\mathrm{e}} = n_{\mathrm{p}}$. Due to the high proton mass the proton scattering can be neglected, so the scattering only for the electron component of the beam is taken into account. The electron scattering is modelled using the approximation given by Bai (1982). An obvious consequence of our model is the energy and momentum exchange between the electron and proton component. During the energy and momentum exchange the electron component is gaining energy on the account of the proton component of the of the neutral beam. The energy losses of proton and electron components are calculated using the formulas given by Emslie (1978). The total energy loss of the neutral beam is given by the sum of the proton and electron component energy losses.

The flare heating given by the total energy loss of the neutral beam enters a radiative hydrodynamic code. Using the code, the response of the solar atmosphere to the flare heating is simulated using a 1-D hydrodynamic code and at the same time the

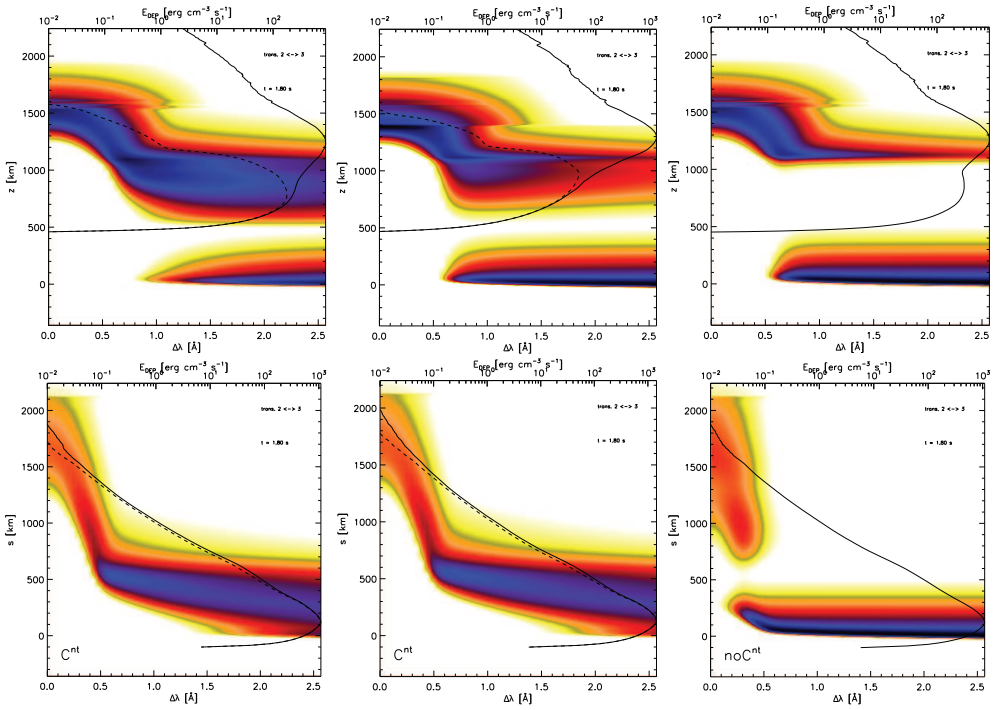

Figure 2. A comparison of Hα contribution functions for an electron beam of $F_{\max} = 4.5 \times 10^{10}$ erg cm^{-2} s^{-1}, $E_0 = 20$ keV (top panels) and for a neutral beam of $F_{\max} = 4.5{\times}10^{10}$ erg cm^{-2} s^{-1}, $E_0 = 35$ MeV (bottom panels). Solid curves indicates the total energy deposit, dashed curves are for the energy deposit on hydrogen. Left and centre: Models with non-thermal collisional rates $C^{\rm nt}$ included for beams of $\delta = 3$ and $\delta = 5$. Right: Models without $C^{\rm nt}$ for $\delta = 3$.

non-LTE radiative transfer for five level plus continuum hydrogen atom is calculated in the chromosphere and photosphere in order to obtain the contribution functions of Hα line. The radiative part of the code includes the influence of the non-thermal collisional rates of neutral beam protons (Hénoux et al. 1993) and electrons (Fang et al. 1993). The radiative-hydrodynamic and test-particle codes are in a detail described in Kašparová et al. (2009).

3. Results

The flare heating function for a neutral beam with parameters $F_{\max} = 4.5 \times 10^{10}$ erg cm^{-2} s^{-1}, $E_0 = 35$ MeV, $\delta = 3$ is shown in Fig. 1. The flare heating corresponding to the neutral beam is similar to the pure proton beam heating. During the beam propagation the beam protons drag the electrons and an energy transfer from the proton to the electron beam component takes place. The energy transferred from protons to electron corresponds to $\sim 3\%$ of the total energy of the proton beam component, i.e. the ratio of the total energy deposited by only the electron component to the total original energy of the electron component before thermalisation is ~ 55. The consequence is, that the beam electrons propagate into the depths comparable with the penetration depth of beam protons (compare the penetration depths of electron and neutral beams in

Fig. 2) and substantially contribute to the non-thermal collisional rates which influence the formation of spectral lines.

The comparison of the contribution functions for Hα line for pure electron and for neutral beam are shown in Fig. 2. Due to the high penetration depth of the neutral beam and efficient radiative losses in the corresponding region almost all the beam energy is deposited into neutrals. Because the radiative losses in the region corresponding to the maximum of the heating function are very efficient (Kašparová et al. 2009), almost all energy deposited by the considered beam is radiated away, i.e. the heating itself does not cause a change of the Hα contribution funcion or line profile. On the other hand, it is the non-thermal collisional rates which result in modification of the Hα line formation.

4. Conclusions

We present an attempt to model the flare heating function for neutral beams using a simple model for its propagation and thermalisation which has been implemented into a test-particle code. We showed that the neutral beam heating resembles to the proton bem heating, but due to the exchange of energy between the proton and electron component, the beam electrons propagate much deeper than in the case of electron beams with corresponding low-energy cutoff. Using the new flare heating we have calculated the contribution functions of Hα line with and without the non-thermal collisional rates. The results are very sensitive to the model of radiative losses in the deep layers of the solar atmosphere, where the the heating reaches its maximum.

Acknowledgments. This work was supported by grants P209/10/1680, 205/06/P135, 205/07/1100 of the Grant Agency of the Czech Republic and by the research project AV0Z10030501 (Astronomical Institute).

References

Bai, T. 1982, ApJ, 259, 341
Karlický, M., et al. 2000, A&A , 333, 1147
Brown, J. C., et al. 1990, ApJS , 73, 729
Emslie, A.G. 1978, ApJ 224, 241
Fang, C., et al. 1993, A&A, 274, 917
Hénoux, J. C., Fang, C., & Gan, W. Q. 1993, A&A, 274, 923
Kašparová, J., et al. 2009, A&A, 499, 923
Martens, P. C. H. 1988, ApJ, 330, L131
Lin, R. P., et al. 2003, ApJ, 595, L69
Simnett, G. M., & Haines, M. G. 1990, Solar Phys., 130, 253

PROBLEM OF THE RETURN CURRENT IN ENERGY DEPOSIT IN FLARES

M. Varady[1,2], **M. Karlický**[2], **and J. Kašparová**[2]

[1]*Department of Physics, J. E. Purkyně Univerzity, České mládeže 8, 400 96 Ústí nad Labem, Czech Republic, mvarady@physics.ujep.cz*

[2]*Astronomical Institute, Academy of Sciences of the Czech Republic, 25165 Ondřejov, Czech Republic*

ABSTRACT

The return current (RC) represents one of the important mechanisms of high energy electron beams thermalisation in flares. The influence of the RC on the propagating electron beam is discussed from two points of view: from the microphysics and using a macroscopic parametric approximation. Using a modified 1–D particle in cell model, details of the RC formation on the microscales are discussed. Based on the results from microphysics, a parameter giving the ratio of background electron density to the density of electrons forming the RC is introduced. Using the parametric approximation, the influence of the RC on the energy deposit of the high energy electron beams into the ambient solar plasma is discussed.

Key words: electron beams; return current; flare heating.

1. INTRODUCTION

According to contemporary solar flare models, electron beams are considered to be important agents responsible for energy transport and deposition in flares. The propagation of electron beams is inevitably connected with origin of enormous electric currents, which according to the Maxwell's theory have to be balanced by RCs formed by the plasma background electrons (van den Oord, 1990). RCs are driven by electric fields which contribute, beside the Coulomb collisions, to the energy dissipation of the electron beams (Emslie, 1980). Although the contribution of the RC effects to the beam energy dissipation can in some approximations even exceed the effect of Coulomb collisions, it has never been considered in calculations of flare heating functions which have been used in the 'standard' 1–D hydrodynamic flare models.

In this contribution we first examine the microphysics of RC formation using a 1–D particle in cell code. Then we calculate the influence of the RC related effects on the energy deposit of the electron beams into the ambient solar plasma using a test particle code in two different approximations.

2. MICROSCOPIC RC MODELLING

2.1. 1–D current-in-cell model

We consider a 1–D system of numerical background plasma electrons, whose charge is neutralized by static protons, into which from one side a beam of numerical electrons penetrates. The considered electric field has only one component oriented in the direction of the beam propagation, thus $\nabla \times \mathbf{E} = \partial \mathbf{B}/\partial t = 0$ and therefore no magnetic field $\mathbf{B}$ exists if $\mathbf{B} = 0$ at $t = 0$. Neglecting the current of the background protons a set of the Maxwell equations (in Gaussian units) can be rewritten to one equation only

$$\frac{\partial \mathbf{E}}{\partial t} = -4\pi(\mathbf{j}_\mathrm{b} + \mathbf{j}_\mathrm{e}), \tag{1}$$

where $\mathbf{j}_\mathrm{b}$ is the beam current and $\mathbf{j}_\mathrm{e}$ is the electric current carried by the background electrons. The electric current in the model is computed as a sum of contributions from individual numerical electrons ($-ev_\mathrm{e}$), distributed over the model grids. Since the electric field acts on electrons, the equations of their motion are used in the following form

$$\frac{\mathrm{d}v_\mathrm{e}}{\mathrm{d}t} = -\frac{e}{m_\mathrm{e}}E - C(v_\mathrm{e})\,, \tag{2}$$

$$x_\mathrm{new} = x_\mathrm{old} + v_\mathrm{e}\Delta t, \tag{3}$$

where m_e is the electron mass, v_e is the velocity of the beam as well as background plasma electrons, x_new and x_old are the new and old positions of the electron during the time step Δt. $C(v_\mathrm{e})$ is the electron velocity loss due to the collisions with the background plasma

$$C(v_\mathrm{e}) = \frac{4\pi\Lambda e^4 n_\mathrm{e} \mid v_\mathrm{e} \mid}{m_\mathrm{e}^2(v_\mathrm{e}^2 + v_{T_\mathrm{e}}^2)^{3/2}}, \tag{4}$$

where Λ is the Coulomb logarithm and v_{T_e} is the thermal plasma velocity.

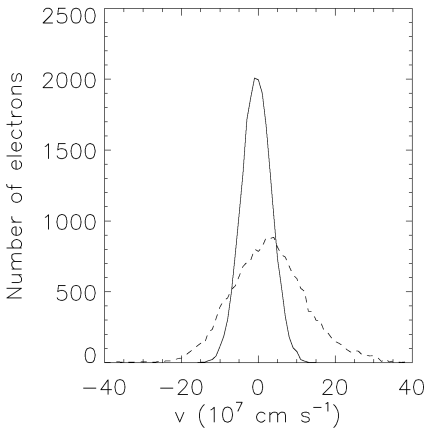

Figure 1. Distribution functions of electrons of the background plasma at the position 70 – 80 *cm in the beam-plasma system at the initial state (full line) and at* 10^{-8} *s (dashed line).*

2.2. Results

We carried out calculations for cold plasma with density corresponding to the upper chromosphere, where the optical chromospheric lines are formed, i.e. for the plasma density $n_e = 10^{12}$ cm^{-3}. To see all the details of the RC formation the time step of the code has to be very short, $\Delta t = 5 \times 10^{-13}$ s in our case.

The simulations showed that an electric field at the beam head is formed and its value corresponds to the relation analytically derived by van den Oord (1990)

$$E = 4\pi j_b/\omega_p, \tag{5}$$

where j_b is the electron beam current and ω_p is the plasma frequency of background plasma. Using the relation $k = 2\pi/L = \omega_p/v_b$, where v_b is the beam velocity, the wavelength of plasma oscillations $L = 1.11$ cm is in agreement with the simulation. The mean velocity of the accelerated background electrons times their density equals to the initial electron beam velocity times n_b (equality of the electric currents).

In the following times, e.g. at $t = 5 \times 10^{-10}$, the amplitude of the electric field of the background plasma oscillations grows. This is due to the two-stream instability. The analytical expression for the growth rate of this instability is (Michailovskij, 1975):

$$\gamma = \omega_p \frac{\sqrt{3}}{2^{4/3}} \left(\frac{n_b}{n_p}\right)^{1/3}, \tag{6}$$

which gives $\gamma = 0.148\omega_p$. This value is in a good agreement with the simulated values.

Under the influence of growing electric field, the beam electrons are trapped in the generated electrostatic wave. This trapping process leads to the saturation of the two-stream instability. The energy level of saturation can be estimated as (Birdsall & Langdon, 1985):

$$W_s = \frac{|E|^2}{8\pi} = \frac{1}{2} n_b m_e v_b^2 \left(\frac{R}{2}\right)^{1/3}, \tag{7}$$

(where $R = n_b/n_e$) which gives $E = 44.3$ cgs units. This value is reached at $t = 5 \times 10^{-10}$ s, later on the electric field amplitude is even greater. A detailed analysis shows that this is due to the fact that the two-stream instability near the injection position is in reality forced by the continuously injected beam. It gives greater value of electric field than in the 'normal' two-stream instability. Simultaneously, the wavelengths of plasma oscillations become shorter at these positions and the waves with higher k–vectors appear.

Then a model with the hot background chromospheric plasma ($n_e = 10^{12}$ cm^{-3}, $T_e = 10^4$ K) and the electron beam ($n_b = 3 \times 10^9$ cm^{-3}, $v_b = -10^{10}$ cm s^{-1}) was considered. We prolonged computations up to the time 1×10^{-8} s and we compared the electron distribution functions of the background plasma at the positions of 70 – 80 cm in the model at the initial state (full line) and at 1×10^{-8} s after a beam injection into the numerical model (dashed line) (Fig. 1). The absolute value of the electric current corresponding to the distribution function at 1×10^{-8} s equals to the beam electric current.

Summarizing the results, we can conclude that a RC of the same magnitude as the beam current is formed on very short time scales. Its electron distribution function deviates strongly from that of the initial state. The RC is not formed by a simple velocity shift which is the same for all background plasma electrons (as sometimes assumed) but the velocity shift is strongly velocity dependent as shown by Rowland & Vlahos (1985).

We defined the measure of collisional losses Q in the system as

$$Q = \sum_{i=1}^{n} \frac{4\pi\Lambda e^4 n_e v_e}{m_e^2 (v_e^2 + v_{T_e}^2)^{3/2}}, \tag{8}$$

where n is the number of electrons in the distribution function. Note that the symmetric distribution function with respect to the static protons (zero electric current) gives $Q = 0$. We compared it for the computed distribution function (the dash line in Fig. 1) with that as at the initial state, but which is as a whole shifted in the velocity space and carrying the same RC as the computed one. We found that Q for the computed distribution function (the dash line in Fig. 1) is about $1/5$ of that which was formed by a simple velocity shift. Therefore, we can expect that the electric field given by the Ohm's law for the RC is also reduced. In the following the electric field decrease is taken into account by defining a free parameter α.

3. MACROSCOPIC RC EFFECTS

3.1. Test Particle Code (TPC)

The electron beams with power law energy spectra in the range 30 – 100 keV are modeled using test particles (TP), each representing a big number of electrons and energy bins (typically from 10 to 30). The positions, energies and pitch angles (Bai, 1982) of all TPs with non-zero energy are calculated in each timestep. The energy losses and the change of the electron pitch angle due to the Coulomb collisions (Emslie, 1978) and RC effects are calculated on a fine ($\sim 10^5$) equidistant grid to which temperature, density and ionisation of the VAL C (Vernazza et al. 1981) atmosphere was interpolated. The current density generated by the beam j_b is assumed to be completely balanced by the RC density $j = -j_b$ and the beam current density is calculated on the grid by the TPC.

To calculate the effect of the RC on flare heating, it is necessary to know the electric intensity E which drives the RC and decelerates the beam electrons at the same time. For the change of beam electron velocity component parallel to the magnetic field we obtain

$$\Delta v_{\parallel} = \frac{eE\Delta t}{m_{\rm e}} \quad . \tag{9}$$

From $\Delta v_{\parallel}$ the change of the pitch angle can easily be calculated. The electric field E is calculated in two approximations: providing the RC obeys the Ohm's law and providing that the RC is predominantly formed by runaway electrons.

3.2. Ohmic RC

In this approximation validity of the Ohm's law is assumed

$$j_{\rm e} = \sigma E, \tag{10}$$

where σ is the classical electrical conductivity which depends only on the background plasma temperature. Knowing σ and $j_{\rm e}$ ($j_{\rm e} = j_{\rm b}$), the electric field can be calculated. Because σ is derived under conditions that $v_{\rm d}^2 \ll v_{T_{\rm e}}^2$, where v_d is the drift velocity of the background electrons, this approximation can be used only for small currents (energy fluxes) when the corresponding electrical intensity is much smaller then the Dreicer field $E_{\rm D}$. Norman & Smith (1978) showed that even for field ratios $E/E_{\rm D} \sim 0.2$, 10 % of background electrons are runaway and the Ohm's law approximation is inappropriate. It follows from our calculations that for $F = 10^{11}$ erg cm^{-2} s^{-1} the field ratio is ≥ 1 and for $F = 10^{10}$ erg cm^{-2} s^{-1} it is ≥ 0.1 in the corona.

3.3. Runaway RC

In this approximation we assume that the RC is formed by only a fraction of fast background electrons. According to Karlický et al. (2004), we introduce a free parameter α, which gives the ratio

$$\alpha = \frac{n_{\rm rc}}{n_{\rm e}} \tag{11}$$

where $n_{\rm rc}$ is the number density of the background electrons carrying the RC and $n_{\rm e}$ is the total number density of the background electrons. We assume that if the parameters of the electron beam remain constant with time, formation of a stationary state on macroscopic scales can be expected. In this case, the RC on macroscopic scales remains constant and for the mean electric field we get equation

$$0 = \frac{{\rm d}\langle v_{\rm e}\rangle}{{\rm d}t} = -\frac{e}{m_{\rm e}}\langle E\rangle - \langle C(v_{\rm e})\rangle \tag{12}$$

where $\langle C(v_{\rm e})\rangle$ can be calculated from Eq. 4. The electric field is now proportional to $\langle C(v_{\rm e})\rangle$. Because we are not able to model the distribution function of the RC electrons in this approximation, we assume the same velocity for all the electrons forming the RC

$$\langle v_{\rm e}\rangle = \frac{j}{n_{\rm rc}e} = \frac{j}{\alpha n_{\rm e}e}. \tag{13}$$

Using Eq. 4 to calculate $\langle C(v_{\rm e})\rangle$ we take into account the fact that the condition $v_{\rm d}^2 \ll v_{T_{\rm e}}^2$ is not fulfilled and it leads to the decrease of the corresponding electric field. Considering the fact that the collisional cross-section of electrons decreases with the square of their velocity, it is an expected result.

3.4. Results – flare heating functions

The flare heating functions calculated in both approximations for power–law index $\delta = 3$ and energy fluxes $F = 10^{10}$ erg cm^{-2} s^{-1} and $F = 10^{11}$ erg cm^{-2} s^{-1} are shown in Figs. 2, 3. The blue line shows the energy deposit when only Coulomb collisions are included, the solid red line shows the total energy deposit (i.e. RC effects plus Coulomb collisions), the dashed line shows only the deposit from RC and the dotted line the deposit from Coulomb collisions. It can be seen that in the approximation using the classical electric conductivity Fig. 2, which as we showed above is not realistic, the penetration depths of the beams are strongly reduced and the RC effects clearly dominate over the contribution of Coulomb collisions. Also the RC losses in the corona are large. In the second approximation, see Fig. 3, the effect of the RC is reduced and even more for the higher flux. This is due to the fact that the velocity of the background electrons, in order to compensate the beam current, has to be higher than it would correspond to the lower flux. Also the penetration depth of the beam increases and becomes comparable with the penetration depth for pure Coulomb collisions.

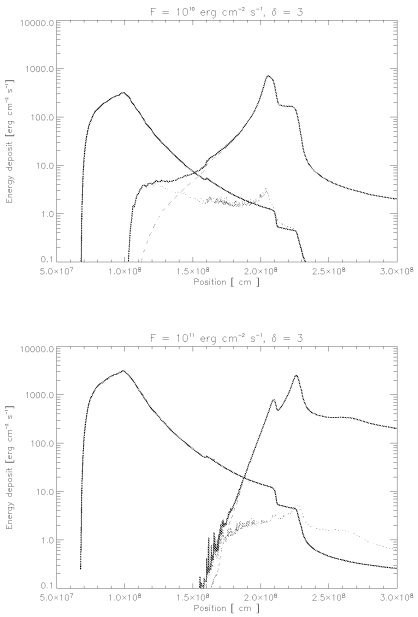

Figure 2. Flare heating functions for VAL C atmosphere (Vernazza et al. 1981) calculated providing the RC obeys the Ohm's law (see description in the text).

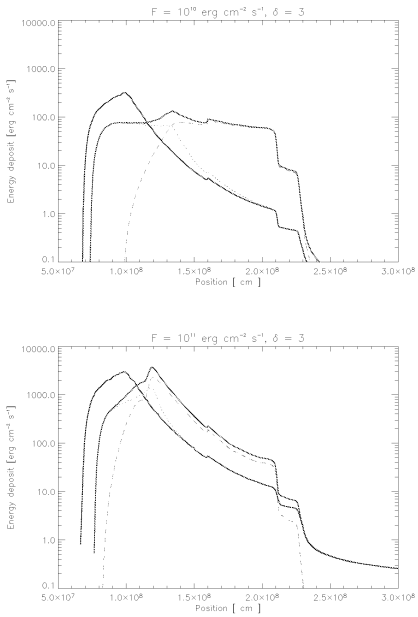

Figure 3. Flare heating functions for VAL C atmosphere (Vernazza et al. 1981) calculated using the alternative method for $\alpha = 0.1$ and (see description in the text).

4. CONCLUSIONS

We discussed the effects of RC on the flare heating functions in two approximations. The detailed simulations of RC formation confirmed that the beam current is almost immediately balanced by the RC. The distribution function of the background electrons forming the RC deviates strongly from Maxwellian so it is not possible to approximate it simply as a velocity shifted Maxwellian. From the macroscopic approximation of the RC we conclude that the approach using the Ohm's law and classical electric conductivity is unrealistic, because the electric fields corresponding to the typical flare energy fluxes $\sim 10^{11}$ erg cm^{-2} s^{-1} are in some regions in the solar atmosphere close or even greater than the corresponding Dreicer fields. So, the electrons carrying RC would quickly become runaway. We proposed a new approximation assuming that only a part of the background electrons carries the RC and that the electric field driving the RC is proportional to the collisional losses of RC electrons. Because we are still unable to calculate the velocity distribution function of RC electrons routinely along the path of the beam, we compute the average collisional losses of the RC electrons for their average velocity. Because $C(v_e)$ reaches its maximum for $v_e = v_{T_e}/\sqrt{2}$, for higher velocities the magnitude of the electric field is substantially reduced and the effect of the RC on the flare heating function as well (see Fig. 3). In the limit case when the number densities and velocities of the RC electrons reach the number densities and velocities of the beam electrons, the contribution of the RC to the beam energy losses would be equal to the beam collisional losses. For more realistic approximation of RC effects on flare heating function, it is necessary to calculate the RC electrons velocity distribution functions along the electron beam trajectory.

ACKNOWLEDGMENTS

This work was supported by a grant number 205/04/0358 of the Grant Agency of the Czech Republic.

REFERENCES

Bai, T., 1982, ApJ, 259, 341

Birdsall, Ch.K., Langdon, A.B., 1985, Plasma physics via computer simulations, McGraw–Hill, Ins., New York

Emslie, A.G., 1978, ApJ, 224, 241

Emslie, A.G., 1980, ApJ, 235, 1055

Karlický, M., Kašparová, J., Heinzel, P., 2004, A&A, 416, L13

Michajlovskij, A.B., 1975, Teorija plazmennych neustojchivostej, Atomizdat, Moskva

Norman, C.A., Smith, R.A., 1978, A&A, 68, 145

Rowland, H.L., Vlahos, L., 1985, A&A, 142, 219

van den Oord, G.H.J., 1990, A&A, 234, 496

Vernazza, J.E., Avrett, E.H., Loeser, R., 1981, ApJS, 45, 635

The Physics of Chromospheric Plasmas
ASP Conference Series, Vol. 368, 2007
Petr Heinzel, Ivan Dorotovič and Robert J. Rutten, eds.

Return Current and Energy Deposit in Flares

Michal Varady[1,2], Marian Karlický[2] and Jana Kašparová[2]

[1]*Department of Physics, Faculty of Natural Sciences, Purkinje University, Ústí nad Labem, Czech Republic*
[2]*Astronomical Institute AS, Ondřejov, Czech Republic*

Abstract. The return current (RC) related effects represent in flares one of the possible mechanisms of conversion of the kinetic energy of electron beams into the thermal energy of flare plasma. Using a 1-D current-in-cell model, details of formation and properties of the RC driven by monoenergetic electron beams are calculated. Based on results of the simulations, the influence of the RC on the energy deposit in flares is discussed.

1. Introduction

According to the standard flare model the flare energy is released in the corona due to the reconnection of coronal magnetic fields and consequently transported by energetic beams of charged particles along the magnetic fieldlines downwards to the transition region, chromosphere and photosphere where the bulk of the beam kinetic energy is converted into the thermal energy of the flare. Due to the diagnostics of non-thermal hard X–ray bremsstrahlung emitted by flares, the electron beams are the best studied agents transporting energy in flares. The propagation of electron beams with power–law spectra and energies in the range from $\approx 15\,\mathrm{keV}$ to several $100\,\mathrm{keV}$ and energy fluxes from $\approx 10^{10}$ erg cm^{-2} s^{-1} to almost 10^{12} erg cm^{-2} s^{-1} observed in flares is inevitably connected with an origin of enormous electric currents which according to the Maxwell's theory have to be *exactly balanced* by RCs created by the plasma background electrons (Knight & Sturrock 1977, Hoyng et al. 1978, van den Oord 1990).

RCs in flares are powered by electric field originating as a result of the beam current injection into the ambient plasma in the solar atmosphere. According to the majority of RC models, the induced electric field accelerates the background electrons, generates the RC and the accelerated RC electrons then via collisions with ions contribute to the flare heating of the ambient plasma. At the same time the induced electric field tends to decelerate the beam electrons and besides the Coulomb collisions it thereby contributes to the dissipation of the electron beam kinetic energy. Although the contribution to the flare heating from the Coulomb collisions is fairly known (Emslie 1978) the contribution from the RC remains unclear and the conclusions obtained by various models are rather controversial, depending on the considered mode of propagation of the RC. The models using the Ohm's law in connection with either the classical (Emslie 1980) or anomalous (Emslie 1981, Duijveman et al. 1981, Cromwell et al. 1988, Matthews et al. 1996) electrical conductivity attribute an important role to the flare heating due to the RC, whereas other models (e.g., Rowland & Vlahos 1985) based on detailed

theoretical considerations of kinetic collective effects related to the RC formation conclude that the bulk of the plasma background electrons is trapped and the RC is carried only by a small population of fast, supra-thermal (runaway) electrons. Collisional losses of such electrons are due to their high velocities substantially reduced and therefore the effects of the RC on the flare heating function as well.

In this contribution we concentrate on a microscopic modeling of the formation of the RC generated by a monoenergetic electron beam in a typical chromospheric plasma. Using a 1-D current-in-cell code we calculate the distribution functions of electrons carrying the RC. We follow evolution of the electric field powering the RC from the transient, unstable state towards a stationary state. The final mean values of the stationary field driving the RC are compared with the electric field which would correspond to the field obtained from the Ohm's law and the classical Spitzer conductivity for the same current.

2. Model Description

We consider a 1-D system of numerical background plasma electrons whose charge is neutralized by static protons. The simulations are initiated by a penetration of a beam of numerical electrons from one side of the computational domain. The details concerning of the code, adopted methods and physical approach are given in Varady et al. (2005).

3. Results

All the simulations were carried out for *monoenergetic* electron beams and as a typical value of plasma density in the chromosphere was taken $n_\mathrm{e} = 10^{12}$ cm^{-3}. To see all the details of the RC formation, the time step of the code had to be shorter than the period of the electron plasma oscillations, i.e. $\Delta t = 5 \times 10^{-13}$ s. Three distinct models have been calculated:

1. Model A: RC formation at the very onset of the interaction of cold chromospheric plasma $T = 0\,\mathrm{K}$, ($v_{T_\mathrm{e}} = 0$ cm s^{-1}) with the electron beam.
2. Model B: RC formation for a constant beam flux propagating through chromospheric plasma, $T_\mathrm{e} = 10^4\,\mathrm{K}$. Model includes only Coulomb collisions, collective effects are *not* taken into account.
3. Model C: RC formation for a constant beam flux propagating through chromospheric plasma $T_\mathrm{e} = 10^4\,\mathrm{K}$. Model includes both the Coulomb collisions and the collective plasma effects.

3.1. Model A: initial phases of the beam injection – cold plasma

Several runs with different densities of the electron beam and with different numbers of numerical electrons (20000 and 200000) were carried out. The real densities were simulated by weighting of the numerical electrons. In the initial state of the system with length 100 cm the background plasma electrons were uniformly distributed into 1000 grid cells in order to resolve the collective plasma effects. Then the beam electrons with velocity $v_\mathrm{b} = -10^{10}$ cm s^{-1} were continuously injected into the domain at its right boundary (i.e. at the position

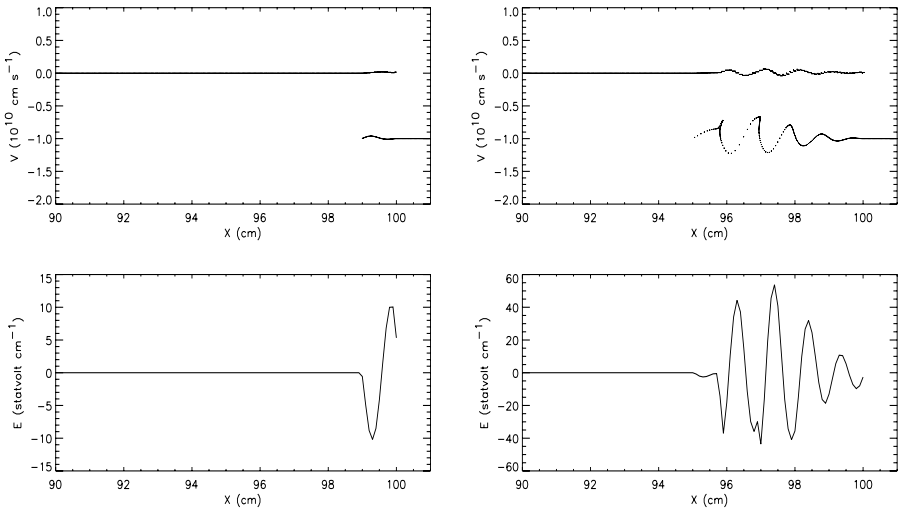

Figure 1. *Left:* The state of the system at 1×10^{-10} s. Upper panel: The distribution of electrons in the phase-space. The initial velocity of background and beam electrons is zero and -10^{10} cm s^{-1}, respectively. Bottom panel: The electric field generated along the beam path. *Right:* The state of the system at 5×10^{-10} s. Upper: The distribution of electrons in the phase-space. Bottom: The electric field generated along the beam propagation.

100 cm). The result of the simulation with $n_\mathrm{b} = 10^{10}$ cm^{-3} at t=10^{-10} s, i.e. immediately after the beam injection when the beam penetrates only 1 cm into the system, is shown on the left side in Fig. 1. The magnitude of the electric field formed at the beam front corresponds to the value analytically derived by van den Oord (1990)

$$E = 4\pi j_\mathrm{b}/\omega_\mathrm{p} \quad , \tag{1}$$

where j_b is the electron beam current and ω_p is the plasma frequency. The corresponding wavelength L of plasma oscillations is (from the relation $k = 2\pi/L = \omega_\mathrm{p}/v_\mathrm{b}$, where v_b is the beam velocity) $L = 1.11$ cm which in agreement with the simulation. Moreover, the mean velocity of the accelerated background electrons times their density equals to the initial electron beam velocity times n_b, i.e. the beam current is equal to the RC.

In the following times, e.g., at $t = 5 \times 10^{-10}$ s (see the right side of Fig. 1) the amplitude of the oscillations grows due to the two-stream instability. The analytical expression for the growth rate of the instability is (Michajlovskij 1975)

$$\gamma = \omega_\mathrm{p} \frac{\sqrt{3}}{2^{4/3}} \left(\frac{n_\mathrm{b}}{n_\mathrm{e}} \right)^{1/3} \quad , \tag{2}$$

which gives $\gamma = 0.148\ \omega_\mathrm{p}$. The theoretical value is again in a good agreement with the value given by the model.

As a consequence of the growing electric field the beam electrons are getting trapped in the generated electrostatic wave. The trapping process leads to the

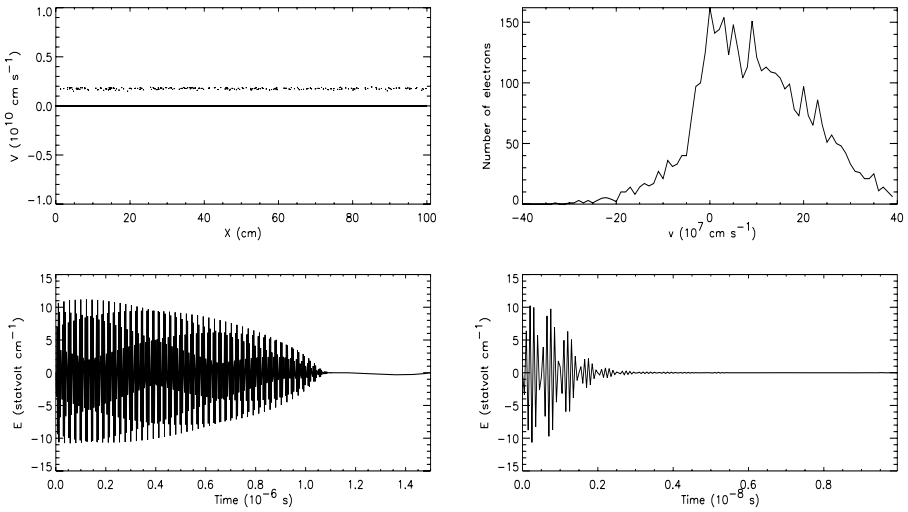

Figure 2. *Left:* Results of Model B. Upper: Phase-space diagram showing two parts of background plasma electrons at 10^{-6} s. The RC is carried by electrons with a mean velocity 1.69×10^9 cm s^{-1}. Bottom: The time evolution of the electric field. *Right:* Results of Model C: Upper: The distribution function of the background plasma at 10^{-8} s. Bottom: The evolution of the mean electric field in the system.

saturation of the two-stream instability. The energy level of the saturation can be estimated by Birdsall & Langdon (1985)

$$W_s = \frac{|\,E\,|^2}{8\pi} = \frac{1}{2} n_\mathrm{b} m_\mathrm{e} v_\mathrm{b}^2 \left(\frac{R}{2}\right)^{1/3} \quad , \tag{3}$$

where $R = n_\mathrm{b}/n_\mathrm{e}$, which gives $E = 44.3$ statvolt cm^{-1} at time $t = 5 \times 10^{-10}$ s.

3.2. Model B: RC including collisions only

The model is almost identical with Model A. The only changes are that the boundary conditions are now periodic in space and there is no spatial grid. The consequence of the latter change results in elimination of the collective plasma processes (e.g., RC instability) from the system, so only the global electric field and the collisional deceleration of electrons are considered. The beam having an arbitrary distribution in the velocity space is always represented by a constant electron flux (current) so this is a good approximation of power-law beams commonly used in the interpretation of hard X-ray emission. The initial distribution function of the background plasma is Maxwellian with temperature $T_\mathrm{e} = 10^4$ K. The RC formation for electron flux $n_\mathrm{b}v_\mathrm{b} = 10^{20}$ cm^{-2} s^{-1} is shown on the left side in Fig. 2. From the figure it is also apparent that due to the collisions, the background plasma electrons are divided into two populations: a) a bulk of electrons with zero velocity; b) a population of fast electrons carrying the RC. The ratio of their densities is $n_\mathrm{RC}/n_\mathrm{bulk} = 5.98 \times 10^{-2}$. The mean velocity of the electrons forming the RC is 1.69×10^9 cm s^{-1}, i.e. the RC again balances

the beam current. During the simulation electric field in the system oscillates with gradually decreasing amplitude and finally (after $\approx 1.1 \times 10^{-6}$ s) a weak and constant electric field driving the RC is formed. The final electric field $E_{\rm final}$ is much less than the electric field calculated from the Ohm's law using the classical conductivity and the same electric current (see Table 1). Similar calculations have been carried out also for beam flux $n_{\rm b}v_{\rm b} = 10^{19}$ cm^{-2} s^{-1} and results are listed in Table 1.

3.3. Model C: RC including collisions and collective effects

The model remains again almost the same as Model B only the computational domain has been divided into 1000 grid cells. The consequence is inclusion of the RC instabilities (i.e. plasma collective effects). The formation of the RC for the electron beam flux $n_{\rm b}v_{\rm b} = 10^{20}$ cm^{-2} s^{-1} is shown on the right panel in Fig. 2. The formation of a stationary RC is much shorter than in Model B due to the waves generated by the instability of the RC. The resulting distribution function has an extended tail for $v > 0$ and strongly deviates from the Maxwellian. The extended tail formed from the background plasma electrons carries the RC. The final, stationary electric field is higher than that in the Model B, but still lower than the Ohm's electric field calculated for the same electric current. Similar calculations have been made also for beam flux $n_{\rm b}v_{\rm b} = 10^{19}$ cm^{-2} s^{-1} and results are listed in Table 1.

Table 1. A comparison of the RC parameters obtained from Model B and Model C. The values $n_{\rm RT}$ and $n_{\rm bulk}$ are the densities of the RC and the bulk populations, $\overline{v_{\rm RT}}$ is the mean velocity of the electron population carrying the RC, $E_{\rm final}$ is the final stationary electric field and $E_{\rm Ohm}$ is the corresponding electric field calculated from the Ohm's law and the classical conductivity.

Electron flux [cm^{-2} s^{-1}]	$n_{\rm RC}/n_{\rm bulk}$	$\overline{v_{\rm RC}}$ [cm s^{-1}]	$E_{\rm final}$ [statvolt cm^{-1}]	$E_{\rm Ohm}$ [statvolt cm^{-1}]
		Model B		
10^{20}	5.98×10^{-2}	1.69×10^{9}	-1.42×10^{-4}	-5.19×10^{-2}
10^{19}	2.01×10^{-2}	4.97×10^{8}	-1.76×10^{-4}	-5.19×10^{-3}
		Model C		
10^{20}	—	—	-6.32×10^{-3}	-5.19×10^{-2}
10^{19}	—	—	-2.08×10^{-3}	-5.19×10^{-3}

4. Conclusions

Using a simple model based on a 1-D current-in-cell code describing the formation of the RC on microscopic scales, we were able to reproduce several important aspects of the RC formation which have been earlier found analytically. All the presented models, in accordance with theory, produced RCs which exactly balanced the beam current. The oversimplified model with cold background plasma (Model A) successfully mimics the magnitude of the electric field formed at the beam front and the properties of the current instabilities (generation of

the plasma waves with the expected parameters, correct grows of two-stream instability, etc.) which are generated immediately after the beam enters the plasma. Model B and Model C showed that the distribution function of the background electrons are strongly non–Maxwellian. Considering only Coulomb collisions and neglecting the collective effects, Model B gives two populations of background electrons: standing bulk and a fast population of background electrons carrying the RC. At this point our the results resemble the results of Rowland & Vlahos (1985). A more realistic Model C taking into account both, collisions and collective effects gives distribution functions which strongly deviate Maxwellian and the RC is here carried by the electrons from an extended tail of the distribution. So the RC is not formed by a simple velocity shift which is the same for all background plasma electrons as sometimes assumed. An obvious consequence is that due to the considerable velocities of the electrons forming the RC their collisional frequency decreases (see Eq. 4 in Varady et al. 2005). Consequently, the electric field which powers the RC and dissipates the kinetic energy of the beam decreases as well (relative to the electric field obtained for the same current using the Ohm's law and classical conductivity). The main conclusion is that according to our simulations, the RC related flare heating calculated using the Ohm's law and classical conductivity overestimates the role of the RC contribution in the calculations of flare heating.

Acknowledgments. This work was supported by grants 205/04/0358 of the Grant Agency of the Czech Republic (GAČR) and 1ET400720409 of the Grant Agency of Academy of Sciences of the Czech republic (GAAV ČR).

References

Birdsall Ch.K., Langdon A.B., 1985, Plasma physics via computer simulations, McGraw-Hill, New York
Cromwell D., McQuillan P., Brown J.C., 1988, Solar Phys. 115, 289
Duijveman A., Hoyng P., Ionson J.A., 1981, ApJ245, 721
Emslie A.G., 1978, ApJ 224, 241
Emslie, A.G. 1980, ApJ 235, 1055
Emslie A.G. 1981, ApJ 249, 817
Hoyng P., Knight J.W., Spicer D.S., 1978, Solar Phys. 58, 139
Knight J.W., Sturrock P.A., 1977, ApJ 218, 306
Matthews S.A., Brown J.C, Melrose D.B., 1996, A&A 305, L49
Michajlovskij A.B., 1975, Teorija plazmennych neustojchivostej, Atomizdat, Moskva
van den Oord G. H. J., 1990, A&A 234, 496
Rowland H.L., & Vlahos L., 1985, A&A 142, 219
Spicer D.S., 1982, Space Sci. Rev. 31, 388
Varady M., Karlický M., Kašparová J., 2005, in: Proceedings of the 11th European Solar Physics Meeting (ESA SP-600), Leuven, Belgium. Editors: D. Danesy, S. Poedts, A. De Groof and J. Andries, 146.1

The Physics of Chromospheric Plasmas
ASP Conference Series, Vol. 368, 2007
Petr Heinzel, Ivan Dorotovič and Robert J. Rutten, eds.

Hα with Heating by Particle Beams

J. Kašparová[1], M. Varady[1,2], M. Karlický[1], P. Heinzel[1] and Z. Moravec[2]

[1] *Astronomical Institute AS, Ondřejov, Czech Republic*
[2] *Department of Physics, J. E. Purkinje University, Czech Republic*

Abstract. Using 1D NLTE radiative hydrodynamics we model the influence of the particle beams on the Hα line profile treating the beam propagation and the atmosphere evolution self-consistently. We focus on the influence of the non-thermal collisional rates and the return current. Based on our results, we propose a diagnostic method for determination of the particle beam presence in the formation regions of the Hα line.

1. Introduction

Some of the flare models assign a fundamental role to the high energy particle beams in the flare energy transport. As the beams interact with the ambient plasma, their energy is dissipated and transformed mainly into the thermal energy of the transition region and chromosphere plasma. Several models studied electron and proton beams as heating agents (e.g., Mariska et al. 1989; Emslie et al. 1998) as well as their influence on spectral line profiles (e.g., Allred et al. 2005). The propagation of electron beams is inevitably connected with the so-called return current (RC, van den Oord 1990) which also contributes to the beam energy dissipation. Besides the heating, the beams influence atomic level populations of the ambient plasma via collisional excitation and ionization. The work presented here concentrates on these two effects which are commonly neglected in the flare modeling and assesses their importance on the formation of Hα line in solar flares.

2. Model

The beam propagation and energy deposition is modelled by a test particle approach consistently with the hydrodynamics of the atmosphere and NLTE radiative transfer in the transition region, chromosphere, and photosphere. Details of the model and the methods used are described in Kašparová et al. (2005).

We study the response of quiet Sun atmosphere (VAL C from Vernazza et al. 1981) to beam pulses of short duration, 1 s with sinus-like time modulation, and power-law energy spectrum with $\delta = 3$.

3. Hydrodynamics and Beam Propagation

The model takes into account Coulomb collisions of the beam with ambient neutrals and electrons, scattering of beam electrons, and optionally RC for the

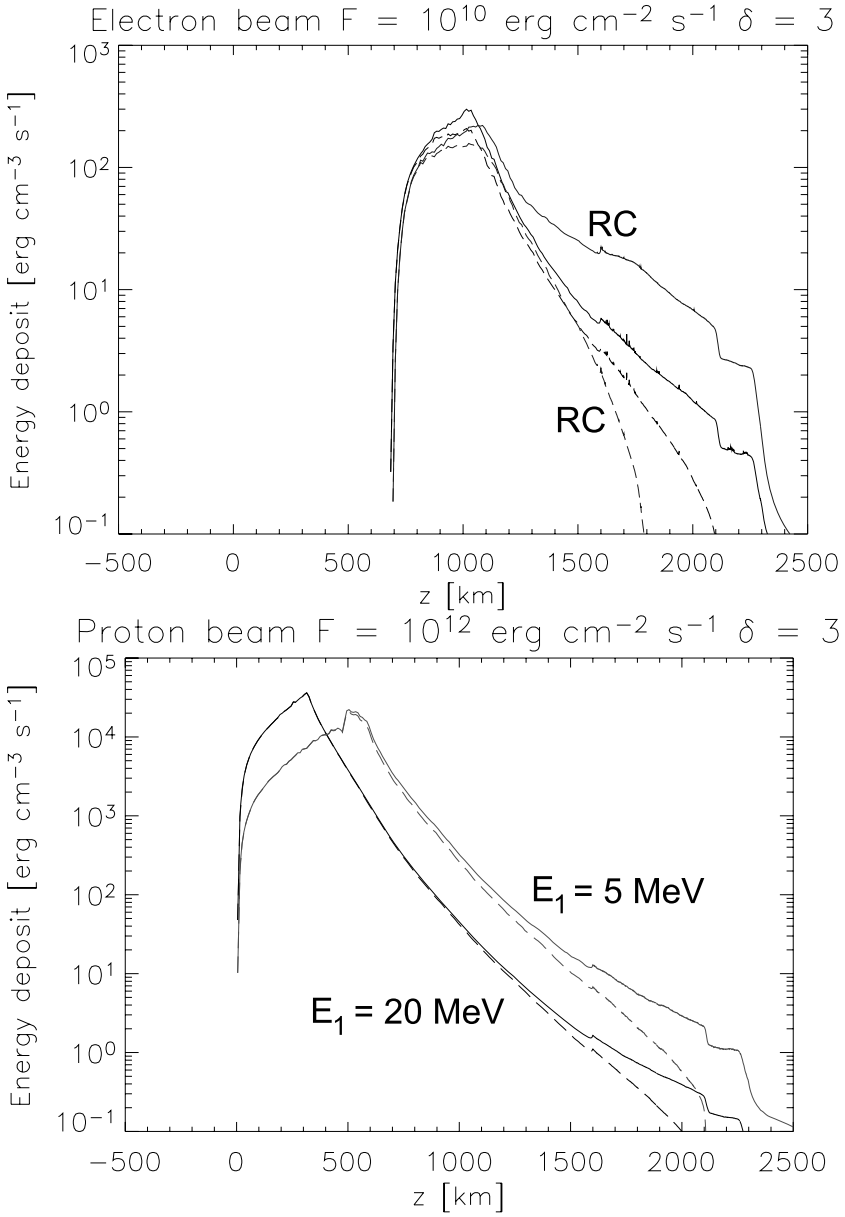

Figure 1. Total energy deposit (solid) and energy deposit to hydrogen (dashed) at beam flux maximum. *Top*: electron beam with and without RC included. *Bottom*: proton beam with $E_1 = 5$ MeV and $E_1 = 20$ MeV.

case of an electron beam (return current is a factor of E_e/E_p lower for protons carrying the same power as electrons (Brown et al. 1990) and is neglected). The return current is included in a runaway approximation assuming $\alpha = 0.1$, i.e. 10% of ambient electrons carry RC. For details and other approximations of RC in solar atmosphere conditions see Varady et al. (2005, 2007).

Figure 1 shows that RC significantly increases the energy deposit of electron beams at heights > 1500 km leading to corresponding increase of the tempera-

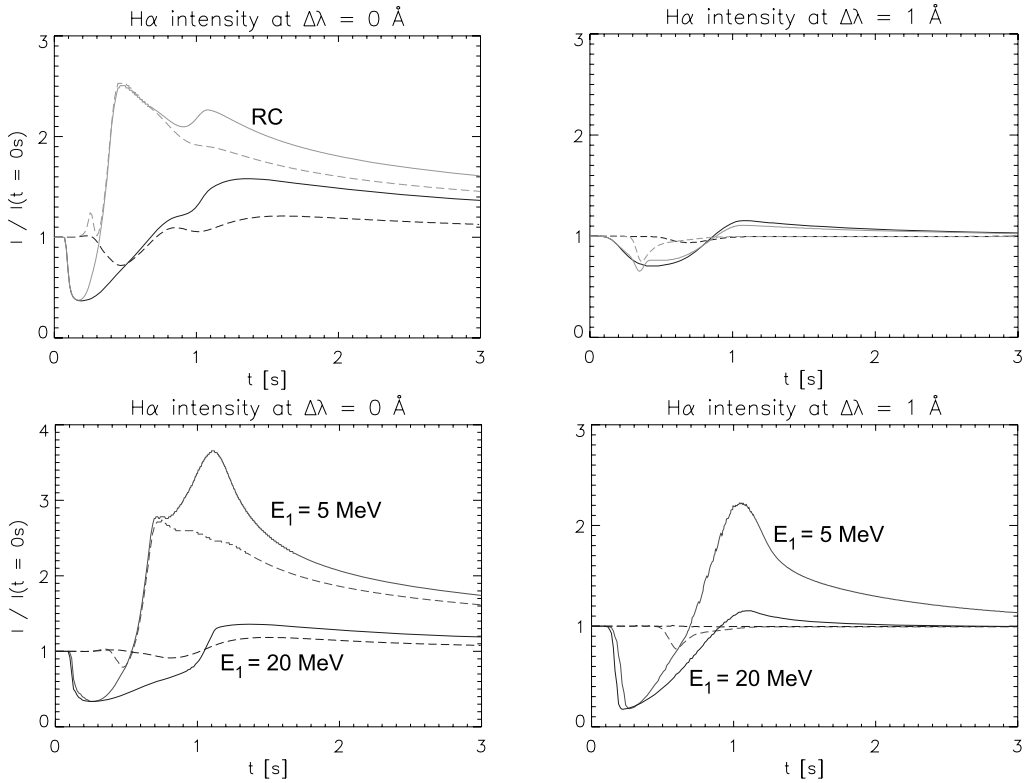

Figure 2. Time evolution of the Hα line center (left column) and wing (right column) intensities. *Top*: electron beam for $F = 10^{10}$ erg cm^{-2} s^{-1} and $\delta = 3$ with and without RC. *Bottom*: proton beam for $F = 10^{12}$ erg cm^{-2} s^{-1}, $\delta = 3$, and $E_1 = 5,\ 20$ MeV. The solid curves refer to cases with $C^{\rm nt}$ included, dashed lines to cases without $C^{\rm nt}$.

ture and ionization. The atmospheric response to proton beams was modelled for two different values of the low-energy cutoff $E_1 = 5,\ 20$ MeV. Note that deka-MeV protons produce approximately the same amount of hard X-rays as deka-keV electrons (Emslie & Brown 1985). Figure 1 illustrates that proton beams deposit their energy into deeper layers than electron beams (Emslie et al. 1996). The energy deposit of proton beams with lower value of E_1 peaks at higher atmospheric layers and is larger at heights above in comparison with a proton beam of $E_1 = 20$ MeV. Consequently, the temperature at these layers is substantially increased.

4. Hα Line Profiles

The hydrogen level populations are affected also by non-thermal collisional ionization and excitation. The corresponding rates $C^{\rm nt}$ are directly proportional to the beam's energy deposit on hydrogen (see Fang et al. 1993 for electron beams, and Hénoux et al. 1993 for proton beams). Their influence on the temporal evolution of the Hα profile was studied for electron beams by Heinzel (1991); Kašparová et al. (2005). Here, we describe in detail their effect for proton beams

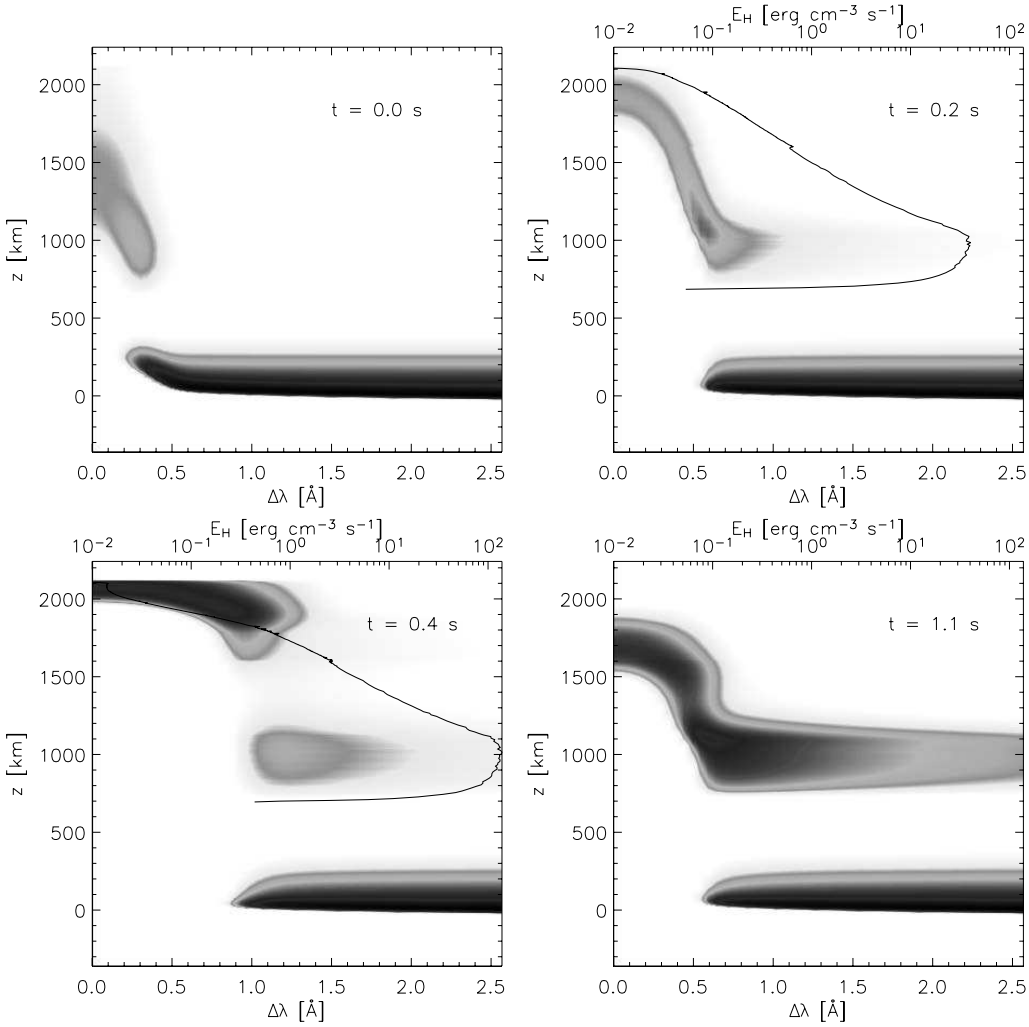

Figure 3. Hα contribution function CF for an electron beam. RC and $C^{\rm nt}$ were included. Solid curve: energy deposit on hydrogen.

and the influence of RC for electron beams. The temporal evolution of the Hα line-center ($\Delta\lambda = 0$ Å) and wing ($\Delta\lambda = 1$ Å) intensities are shown in Fig. 2. As discussed in Heinzel (1991) and Kašparová et al. (2005) for the case of electron beams, $C^{\rm nt}$ cause a decrease of the line-center intensity at the very start of the beam propagation and enhance the wing intensity later on (mainly for fluxes $\gtrsim 10^{11}$ erg cm^{-2} s^{-1}). The line behaviour can be understood in terms of contribution functions CF to the outgoing intensity given by $I_\lambda = \int CF_\lambda \, {\rm d}z$, where z is the height.

Figure 3 shows the evolution of Hα CF for the case of an electron beam with RC and $C^{\rm nt}$ included. A decrease of the line center intensity is caused by an increase of opacity due to $C^{\rm nt}$ (see CF at 0.2 s). Later on, a new region of wing formation occurs at the layers where the energy deposit peaks (see CF at 0.4 s). Such a layer is not formed if $C^{\rm nt}$ are not considered. Since RC causes heating of the top parts of the atmosphere, it is responsible for the increase

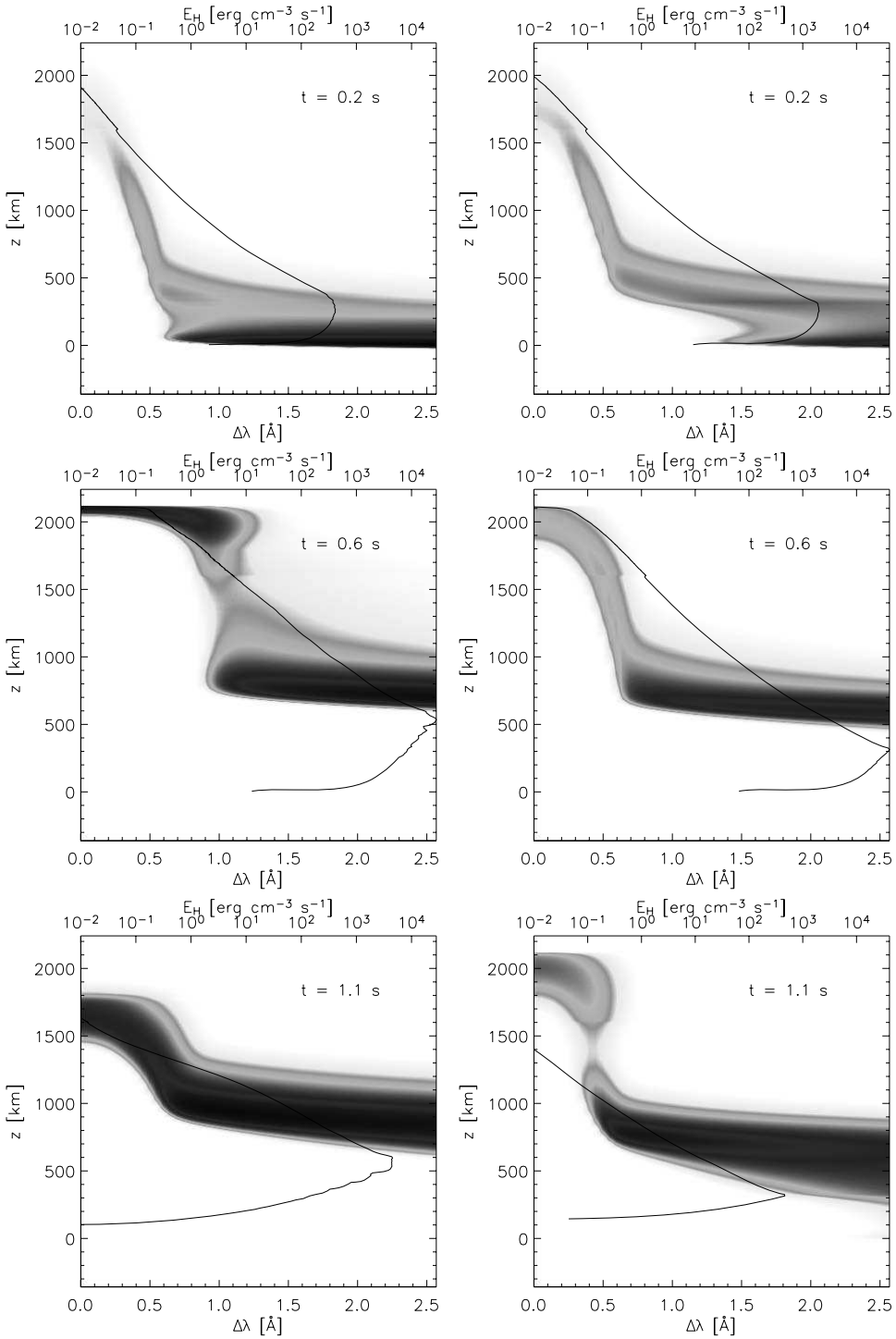

Figure 4. Comparison of Hα contribution function CF for proton beams with $E_1 = 5$ MeV (first column) and $E_1 = 20$ MeV (second column). $C^{\rm nt}$ were included.

of the line center intensity at 0.4 s (see Fig. 2) forming in a narrow region at $\sim$ 2000 km (see Fig. 3).

The situation for a proton beam is shown in Fig. 4. In the case of $E_1 =$ 20 MeV, the beam energy is deposited in regions where the line wings are formed. If $C^{\rm nt}$ are included, they cause increase of opacity which leads to a drop of both the wing and the line-center intensities (see CF at 0.2 s). Later on, a new wing region occurs. Neglecting $C^{\rm nt}$, the line intensity does almost not change because the temperature structure is not significantly affected by the beam propagation.

However, for a proton beam of $E_1 = 5$ MeV, the temperature increase is large enough to form a new region of the line center intensity, as in the case of RC for an electron beam. Also, the energy deposit is large enough to create a new layer of strong wing intensity (see CF at 0.4 and 1.1 s and Fig. 2). The second peak of the line center intensity at about 1.1 s is due to broadening of the formation region. Similarly to the electron beams, the line wings are not changed if $C^{\rm nt}$ are not considered.

5. Conclusions

The Hα line is influenced by temperature structure resulting from the beam propagation and return current as well as the non-thermal collisional rates. We propose to use the decrease of Hα line-center intensity as diagnostic indicating the presence of particle beams. We also predict that proton beams with deka-MeV low-energy cutoffs produce only *decrease* of the Hα in comparison with quiet-sun intensities.

Acknowledgments. This work was mainly supported by the grants 205/04/0358 and 205/06/P135 (GA CR), partially by grants IAA3003202, IAA3003203 (GA AS), and by the key project AV0Z10030501 (AI AS).

References

Allred J. C., Hawley S. L., Abbett W. P., Carlsson M., 2005, ApJ 630, 573
Brown J. C., Karlický M., MacKinnon A. L., van den Oord G. H. J., 1990, ApJS 73, 343
Emslie A. G., Brown J. C., 1985, ApJ 295, 648
Emslie A. G., Henoux J.-C., Mariska J. T., Newton E. K., 1996, ApJ 470, L131
Emslie A. G., Mariska J. T., Montgomery M. M., Newton E. K., 1998, ApJ 498, 441
Fang C., Hénoux J.-C., Gan W. Q., 1993, A&A 274, 917
Heinzel P., 1991, Sol. Phys. 135, 65
Hénoux J.-C., Fang C., Gan W. Q., 1993, A&A 274, 923
Kašparová J., Varady M., Karlický M., Moravec Z., Heinzel P., 2005, in ESA SP-600: The Dynamic Sun: Challenges for Theory and Observations
Mariska J. T., Emslie A. G., Li P., 1989, ApJ 341, 1067
van den Oord G. H. J., 1990, A&A 234, 496
Varady M., Karlický M., Kašparová J., 2005, in ESA SP-600: The Dynamic Sun: Challenges for Theory and Observations
Varady M., Karlický M., Kašparová J., 2007, in P. Heinzel, I. Dorotovič, R. J. Rutten (eds.), The Physics of Chromospheric Plasmas, ASP Conf. Ser. 368, 473
Vernazza J. E., Avrett E. H., Loeser R., 1981, ApJS 45, 635

A&A 563, A51 (2014)
DOI: 10.1051/0004-6361/201322391

Astronomy & Astrophysics

Modifications of thick-target model: re-acceleration of electron beams by static and stochastic electric fields

M. Varady[1,2], M. Karlický[2], Z. Moravec[1], and J. Kašparová[2]

[1] J.E. Purkyně University, Physics Department, České mládeže 8, 400 96 Ústí nad Labem, Czech Republic
e-mail: mvarady@physics.ujep.cz
[2] Astronomical Institute of the Academy of Sciences of the Czech Republic, v.v.i., 25165 Ondřejov, Czech Republic
e-mail: karlicky@asu.cas.cz

Received 29 July 2013 / Accepted 21 November 2013

ABSTRACT

Context. The collisional thick-target model (CTTM) of the impulsive phase of solar flares, together with the famous Carmichael, Sturrock, Hirayama, and Kopp-Pneuman (CSHKP) model, presented for many years a "standard" model, which straightforwardly explained many observational aspects of flares. On the other hand, many critical issues appear when the concept is scrutinised theoretically or with the new generation of hard X-ray (HXR) observations. The famous "electron number problem" or problems related to transport of enormous particle fluxes though the corona represent only two of them. To resolve the discrepancies, several modifications of the CTTM appeared.
Aims. We study two of them based on the global and local re-acceleration of non-thermal electrons by static and stochastic electric fields during their transport from the coronal acceleration site to the thick-target region in the chromosphere. We concentrate on a comparison of the non-thermal electron distribution functions, chromospheric energy deposits, and HXR spectra obtained for both considered modifications with the CTTM itself.
Methods. The results were obtained using a relativistic test-particle approach. We simulated the transport of non-thermal electrons with a power-law spectrum including the influence of scattering, energy losses, magnetic mirroring, and also the effects of the electric fields corresponding to both modifications of the CTTM.
Results. We show that both modifications of the CTTM change the outcome of the chromospheric bombardment in several aspects. The modifications lead to an increase in chromospheric energy deposit, change of its spatial distribution, and a substantial increase in the corresponding HXR spectrum intensity.
Conclusions. The re-acceleration in both models reduces the demands on the efficiency of the primary coronal accelerator, on the electron fluxes transported from the corona downwards, and on the total number of accelerated coronal electrons during flares.

Key words. Sun: flares – acceleration of particles – Sun: X-rays, gamma rays – Sun: chromosphere

1. Introduction

The CTTM of the impulsive phase of solar flares (Brown 1971) for many years presented a successful tool not only for interpreting the processes related to the energy deposition and HXR production in the footpoint regions of flare loops, but also for naturally explaining many other observational aspects of flares like the Neupert effect (Dennis & Zarro 1993), the time correlation of footpoint HXR intensity and intensities of chromospheric lines (Radziszewski et al. 2007, 2011), or the radio signatures of particle transport from the corona towards the chromosphere (Bastian et al. 1998). Nevertheless, especially with the onset of modern HXR observations such as Yohkoh/HXT, RHESSI (Kosugi et al. 1991; Lin et al. 2002), a continuously growing number of discrepancies with the CTTM were beginning to appear. The most striking one is the old standing problem concerning the very high electron fluxes required to explain the observed high HXR footpoint intensities. This problem is particularly acute in the context of the "standard" CSHKP flare model when assuming a single coronal acceleration site (Sturrock 1968; Kopp & Pneuman 1976; Shibata 1996), where enormous numbers of electrons involved in the impulsive phase have to be gathered, accelerated, and then transported to the thick-target region located in the chromosphere (Brown & Melrose 1977; Brown et al. 2009). Another serious class of problems appears as a consequence of enormous electric currents arising from the transport of high electron fluxes through the corona down to the chromosphere and the inevitable generation of the neutralising return current (van den Oord 1990; Matthews et al. 1996; Karlický 2009; Holman 2012). Also the recent measurements of the vertical extent of chromospheric HXR sources (Battaglia et al. 2012) are inconsistent with the values predicted by the CTTM.

Generally, it is very difficult to explain energy transport by means of electron beams with enormous fluxes from the primary coronal acceleration sites assumed to be located in highly structured coronal current sheets (Shibata & Tanuma 2001; Bárta et al. 2011a,b) to the thermalisation regions that lie relatively deep in the atmosphere and that produce the observed intensities of footpoint HXR emission in the frame of classical CTTM. Therefore various modifications of the CTTM have been proposed to solve the problems. Fletcher & Hudson (2008) suggest a new mechanism of energy transport from the corona downwards by Alfvén waves, which in the chromosphere accelerate electrons to energies for X-ray emission. Furthermore, Karlický & Kontar (2012) have investigated an electron acceleration in the beam-plasma system. Despite efficient beam energy losses

A&A 563, A51 (2014)

to the thermal plasma, they have found that a noticeable part of the electron population is accelerated by Langmuir waves produced in this system. Thus, the electrons accelerated during the beam propagation downwards to the chromosphere can reduce the beam flux in the beam acceleration site in the corona requested for X-ray emission. Another modification of the CTTM is the local re-acceleration thick-target model (LRTTM) that has been suggested by Brown et al. (2009). The model assumes a primary acceleration of electrons in the corona and their transport along the magnetic field lines downwards to the thick-target region. Here they are subject to secondary local re-acceleration by stochastic electric fields generated in the stochastic current sheet cascades (Turkmani et al. 2005, 2006) excited by random photospheric motions.

Karlický (1995) studied another idea – the global re-acceleration thick-target model (GRTTM). The beam electrons accelerated in the primary coronal acceleration site are on their path from the corona to the chromosphere constantly re-accelerated. Such a re-acceleration is caused by small static electric fields generated by the electric currents originating due to the helicity of the magnetic field lines forming the flare loop (e.g. Gordovskyy & Browning 2011, 2012; Gordovskyy et al. 2013). The magnitude of the static electric field reaches its maximum in the thick-target region owing to the sharp decrease in electric conductivity in the chromosphere and to the prospective convergence of magnetic field in this region.

In this paper we study the effects of the local and global re-acceleration of beam electrons at locations close to the hard X-ray chromospheric sources. Section 2 describes our approximations of LRTTM and GRTTM and their implementation to a relativistic test-particle code. In Sect. 3 we compare both modifications with CTTM in terms of electron beam distribution functions, chromospheric energy deposits, and HXR spectra. Modelled HXR spectra are also forward-fitted to obtain beam parameters under the assumption of pure CTTM regardless of any re-acceleration. The results are summarised and discussed in Sect. 4.

2. Model description

2.1. Beam properties and target atmosphere

The simulations presented in this work start with an injection of an initial electron beam into a closed magnetic loop at its summit point using a test-particle approach (Varady et al. 2010). Physically, the initial beam represents a population of non-thermal electrons generated at the primary acceleration site located in the corona above the flare loop. Our simulations do not treat the primary acceleration itself. The non-thermal electrons are assumed to obey a single power law in energy, so their initial spectrum (in units: electrons $\mathrm{cm}^{-2}\ \mathrm{s}^{-1}\ \mathrm{keV}^{-1}$) is

$$F(E,z_0)=\begin{cases}(\delta_\mathrm{p}-2)\frac{\mathcal{F}_0}{E_0^2}\left(\frac{E}{E_0}\right)^{-\delta_\mathrm{p}}, & \text{for}\quad E_0\le E\le E_1\\ 0, & \text{for other } E\end{cases} \tag{1}$$

(Nagai & Emslie 1984). The electron flux at the loop top, which corresponds to the column density $z_0 = 0$, is determined by the total energy flux $\mathcal{F}_0$, the low and high-energy cutoffs E_0, E_1 and the power-law index δ_p. All the models presented in this work start with the same initial beam parameters $\delta_\mathrm{p} = 3$, $E_0 = 10$ keV and $E_1 = 400$ keV. For $\mathcal{F}_0$ we use two values $\mathcal{F}_0 = 5\times10^9$ and 10^{11} erg cm^{-2} s^{-1}, with the latter only as the CTTM reference flux for a comparison with the models of secondary re-acceleration.

We study two various cases of initial pitch angle distribution. The pitch angle ϑ determines the angle between the non-thermal electron velocity component parallel to the magnetic field line $v_\parallel$ and the total electron velocity v

$$\mu\equiv\cos\vartheta=\frac{v_\parallel}{v}. \tag{2}$$

The initial μ-distribution is given by function $M(\mu_0)$ and must be normalised. The angularly dependent initial electron flux is then

$$F(E,\mu_0,z_0)=M(\mu_0)F(E,z_0),\qquad \int_{-1}^{1}M(\mu_0)\mathrm{d}\mu_0=1. \tag{3}$$

We consider two extreme cases:

1. a fully focussed beam

$$M^\mathrm{FF}\equiv M(\mu_0)=\frac{1}{2}\delta(\mu_0-\mu_\mathrm{c}), \tag{4}$$

   where δ is the Dirac function and $\mu_\mathrm{c}=\pm1$; and
2. a semi-uniformly distributed beam

$$M^\mathrm{SU}\equiv M(\mu_0)=\begin{cases}1, & \mu_0\in(-1,-0.5)\cup(0.5,1)\\ 0, & \mu_0\in(-0.5,0.5).\end{cases} \tag{5}$$

The initial pitch angle distribution reflects the properties of the primary coronal accelerator. The first distribution may represent an extreme case of an electron beam accelerated in the coronal current sheet with an X-point, and the second is close to the outcome of the acceleration mechanisms involving the plasma wave turbulence in a second-order Fermi process (Winter et al. 2011). The electrons with negative μ_0 propagate to the left, with positive μ_0 to the right half of the loop. Since we study the effects of the electron beam bombardment of the chromosphere, we excluded the population with $\mu_0\in(-0.5,0.5)$ from the uniform distribution. This approximation substantially decreases the computational cost. The choice of $M(\mu_0)$ influences the initial energy flux along magnetic field lines towards a single left or right footpoint. The parallel fluxes towards individual footpoints are $\mathcal{F}_0/2$ for M^FF and $3\mathcal{F}_0/8$ for M^SU, respectively. The total number of non-thermal electrons injected into the loop per unit area and time is $\approx1.6\times10^{17}$ electrons cm^{-2} s^{-1} (relevant to the energy flux $\mathcal{F}_0 = 5\times10^9$ erg cm^{-2} s^{-1} and both pitch angle distributions).

We consider a converging magnetic field along the loop towards the photosphere with a constant mirror ratio $R_\mathrm{m}\equiv B_1/B_0 = 5$, where B_0 and B_1 are the magnetic fields at the loop top in the corona and at the base of the loop in the photosphere, respectively. To model the field convergence we adopted the formula proposed by Bai (1982), where the magnetic field strength B is only a function of the column density z calculated from the loop top downwards

$$\frac{B(z)}{B_0}=\begin{cases}1+(R_\mathrm{m}-1)(z/z_\mathrm{m})^2, & \text{for}\quad z\le z_\mathrm{m}\\ R_\mathrm{m}, & \text{for}\quad z\ge z_\mathrm{m},\end{cases} \tag{6}$$

where $z_\mathrm{m}=4\times10^{19}$ cm^{-2}. For the VAL C atmosphere (Vernazza et al. 1981) z_m is located in the chromosphere – corresponding position $s_\mathrm{m}=1.36$ Mm, temperature $T_\mathrm{m}=6270$ K and density $n_\mathrm{m}=2\times10^{12}$ cm^{-3}. The adopted configuration of the magnetic field is shown in Fig. 1. The convergence of the magnetic field in the vicinity of the loop footpoints influences the model in two aspects. First, only part of the beam electrons with low pitch angles satisfying the condition $\sin^2\vartheta\le\frac{1}{R_\mathrm{m}}$ passes through the magnetic mirror. Second, the corresponding flux is focussed

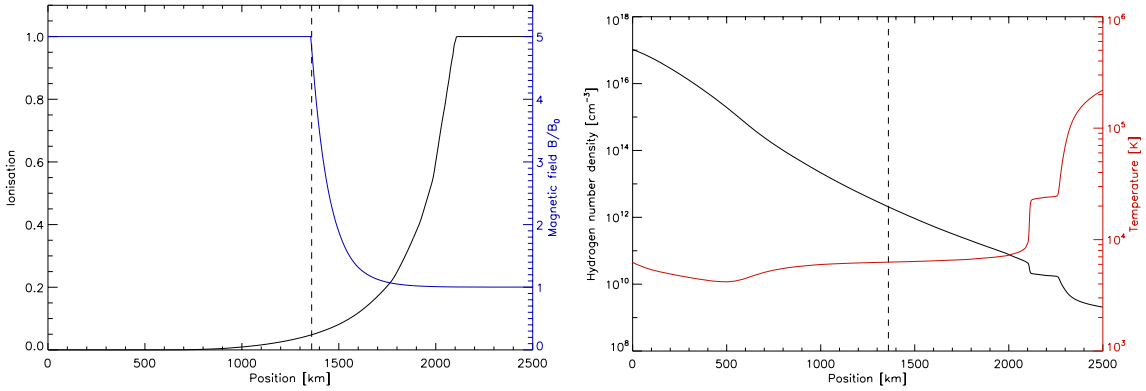

Fig. 1. *Left*: hydrogen ionisation (black line) and relative magnetic field strength B/B_0 (blue line), *right*: temperature (red line), and hydrogen density (black line) in the lower parts of the VAL C atmosphere. The dashed line indicates the lower boundary of the magnetic mirror.

thanks to the field convergence that results in an increase in the energy deposit per unit volume in the constricted flux tube. The remaining beam particles are reflected by the mirror and move back to the loop top and further to the second part of the loop (Karlický & Henoux 1993).

The corresponding energy deposits, non-thermal electron distribution functions, and the HXR spectra are determined primarily by the parameters of the electron beam itself, but also by the properties of the target atmosphere. The results are obtained for the VAL C atmosphere (see Fig. 1) (Vernazza et al. 1981), which was extrapolated to the hot ~1 MK and low density 10^8–10^9 cm^{-3} corona. The length of the whole loop is $L = 20$ Mm, so the source of the energetic particles (primary coronal acceleration site) is located at $s = 10$ Mm.

The hydrodynamic flare models show that a rapid and massive flare energy release in the thick-target region dramatically changes the temperature and ionisation structure in the chromosphere on very short timescales ≤1 s (Abbett & Hawley 1999; Allred et al. 2005; Kašparová et al. 2009). Therefore it also influences the thermalisation rate of the non-thermal electrons (Emslie 1978; Kašparová et al. 2009) and thus the outcome of the bombardment (Varady et al. 2013). Using a hydrodynamic flare code combined with a test-particle code (Varady et al. 2010), we tested the influence in increased temperature and change of ionisation due to the flare heating on the HXR spectra produced in the thick-target region and on the corresponding energy deposits. We found only relatively minor changes in comparison with the results for the quiet VAL C atmosphere. Therefore only results for the quiet VAL C atmosphere are presented in this study.

2.2. Test-particle approach

The problem of collisional particle transport in a partially ionised atmosphere in the cold target approximation was analysed by Emslie (1978). Bai (1982) presented a Monte-Carlo method that is useful for computer implementation of the transport of energetic electrons in a fully ionised hydrogen plasma in a non-uniform magnetic field. It has been shown by MacKinnon & Craig (1991) that the coupled system of stochastic equations presented in Bai (1982) is formally equivalent to the corresponding Fokker-Planck (FP) equation, therefore the method proposed by Bai (1982) has to give equivalent results as the direct solution of the FP equation. We modified the approach of Bai (1982) for a partially ionised cold target and developed a relativistic test-particle code. The code follows the motion of a chain of beam electron clusters, test-particles with a power-law spectrum along a magnetic field line described with the following equation of motion

$$\frac{\mathrm{d}\boldsymbol{p}_\mathrm{e}}{\mathrm{d}t} = -\boldsymbol{C}_\mathrm{e}(v_\mathrm{e}) + \boldsymbol{F}_\mathrm{m} - e\boldsymbol{E}, \tag{7}$$

where $\boldsymbol{p}_\mathrm{e}$ is the momentum of the electron cluster, $-\boldsymbol{C}_\mathrm{e}(v_\mathrm{e})$ is the collisional drag also responsible for the effects of scattering, $\boldsymbol{F}_\mathrm{m}$ is the magnetic mirror force, and the term $-e\boldsymbol{E}$ expresses the force controlling the secondary acceleration.

2.3. Collisional thick-target model – CTTM

In the scenario of classical CTTM, the non-thermal electrons lose their energy and are scattered by the Coulomb collisions with the particles of the ambient plasma (see the term $-\boldsymbol{C}_\mathrm{e}(v_\mathrm{e})$ in Eq. (7)). The energy loss of a non-thermal electron ΔE with kinetic energy E and velocity v caused by Coulomb collisions in a partly ionised hydrogen cold target, per time-step Δt, can be approximated by

$$\Delta E = -\frac{2\pi e^4}{E}\left[\Lambda x + \Lambda'(1-x)\right] n\, v\, \Delta t, \tag{8}$$

where $n = n_\mathrm{p} + n_\mathrm{n}$ is the number density of equivalent hydrogen atoms, n_p and n_n are the proton and hydrogen number densities, respectively, $x = n_\mathrm{p}/n$ is the hydrogen ionisation, and Λ, Λ' are the Coulomb logarithms (Emslie 1978).

The scattering due to Coulomb collisions is simulated using the Monte Carlo method. According to Bai (1982), the relation between the rms of the scattering angle $\Delta\vartheta_\mathrm{C}$, the ratio $\Delta E/E$, and the Lorentz factor γ_L is

$$\overline{\Delta\vartheta_\mathrm{C}^2} = \left(\frac{\Delta E}{E}\right)\left(\frac{4}{\gamma_\mathrm{L}+1}\right), \tag{9}$$

when $\overline{\Delta\vartheta_\mathrm{C}^2} \ll 1$ (or equivalently, $\Delta E/E \ll 1$). The value of scattering angle $\Delta\vartheta_\mathrm{C}$ is given by a Gaussian distribution, the rms of which is computed by the Eq. (9).

The change in the pitch angle caused by the magnetic force $\boldsymbol{F}_\mathrm{m}$, see Eq. (7), in the region of magnetic field convergence is

$$\Delta\vartheta_\mathrm{B} = \frac{B_{i+1} - B_i}{2B_i}\tan\vartheta_i, \tag{10}$$

providing $(\Delta\vartheta_B)^2 \ll 1$ in a single time-step, where B_i and B_{i+1} are the magnetic field strengths at the beginning and end of the particle path, and ϑ_i is the initial pitch angle. The total change of the pitch angle in a single time-step due to collisions and magnetic field non-uniformity is $\Delta\vartheta = \Delta\vartheta_C + \Delta\vartheta_B$, and the new electron pitch angle ϑ is then obtained using the cosine rule from the spherical trigonometry

$$\cos\vartheta = \cos\vartheta_i \cos\Delta\vartheta + \sin\vartheta_i \sin\Delta\vartheta \cos\varphi, \quad (11)$$

where φ is the azimuthal angle given by a uniform distribution $0 \le \varphi < 2\pi$. More details concerning computer implementation can be found in Varady et al. (2005, 2010) and Kašparová et al. (2009).

2.4. Secondary accelerating mechanisms

To include the secondary acceleration mechanisms, we added either the static or stochastic electric fields that re-accelerate or decelerate the test-particles with respect to the mutual directions of the electric field and instantaneous test-particle velocities. The interaction of the non-thermal particles with the re-accelerating electric field, the $-e\boldsymbol{E}$ term in Eq. (7), is calculated using the Boris relativistic algorithm (see Peratt 1992, Sect. 8.5.2). The effects of the return current are not considered. Relatively low electron fluxes transported from the corona ($\mathcal{F}_0/2 = 2.5 \times 10^9$ erg cm^{-2} s^{-1} towards each footpoint) partially justify this negligence.

2.4.1. Static electric field – GRTTM

We now consider a situation where electric currents flow in the flare loop before and during the flare impulsive phase due to the non-zero helicity of the pre-flare magnetic field (Karlický 1995). Furthermore, at the very beginning of the flare, the current-carrying loops are unstable to the kink and tearing-mode instabilities, which produce filamented electric currents in a natural way (Kuijpers et al. 1981; Karlický & Kliem 2010; Kliem et al. 2010; Gordovskyy & Browning 2011). If electrons are accelerated in the coronal part of the individual current thread, they propagate along it and interact with the corresponding global re-acceleration resistive static electric field $\boldsymbol{E}_G$ driving the current. The field corresponding to the current density $\boldsymbol{j}$ is

$$\boldsymbol{E}_G = \boldsymbol{j}/\sigma, \quad (12)$$

where σ is the plasma electric conductivity. The general formula for plasma conductivity is

$$\sigma = \frac{\omega_{pe}^2}{4\pi\nu_e}, \quad (13)$$

where $\omega_{pe}^2 = 4\pi e^2 n_e/m_e$ is the electron plasma frequency, and ν_e the electron collisional rate. In case electric currents propagate in plasma free of any plasma waves, the collisional frequency corresponds to the classical value

$$\nu_e = 2.91 \times 10^{-6} \frac{n_e}{T_e^{3/2}} \Lambda, \quad (14)$$

in the SI units, where T_e is the electron temperature. On the other hand, the presence of plasma waves can increase the collisional frequency to anomalous values: for the anomalous resistivity see Heyvaerts (1981).

To assess the influence of static electric field on the outcome of the chromospheric bombardment by non-thermal electrons, we assume a single thread of constant current density with magnitude below any current instability thresholds. Then we calculate the magnitude of corresponding direct field $\boldsymbol{E}_G$ along the thread using the classical isotropic electric conductivity obtained by Kubát & Karlický (1986). The conductivity was calculated using the updated values of proton–hydrogen scattering cross-section for the quiet VAL C atmosphere (see Fig. 2). Owing to temperature dependence of σ and the convergence of magnetic field in the chromosphere, contributing to the increase in the local current density, the resulting $\boldsymbol{E}_G$ grows rather quickly in the chromosphere (see Fig. 2). Furthermore, $\boldsymbol{E}_G$ tends to accelerate the beam electrons towards one footpoint and to decelerate them towards the second one, providing an asymmetric flare heating of the individual thread footpoints. From now on, we refer to the individual footpoints as the primary and the secondary footpoints, respectively and to this model as the global re-accelerating thick-target model (GRTTM).

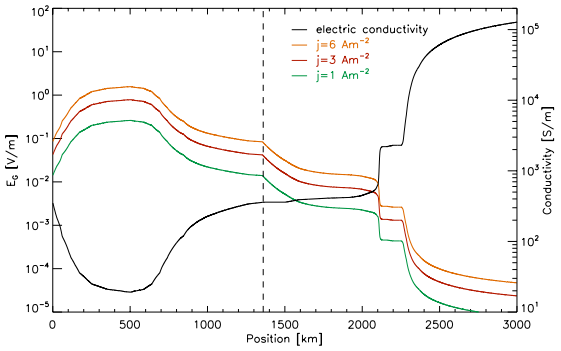

Fig. 2. Classical electric conductivity σ in the lower VAL C atmosphere according to Kubát & Karlický (1986) and the magnitude of the corresponding $\boldsymbol{E}_G$ for various current densities $\boldsymbol{j}$.

The steep increase in $\boldsymbol{E}_G$, hence the high efficiency of GRTTM, is essentially linked with the decrease in temperature in the chromosphere. In contrast, we have already pointed out that chromospheric plasma in flares is heated to temperatures up to 10^5 K on the timescales $\le$1 s. Such an extreme increase in temperature substantially increases the classical electric conductivity ($\sigma \propto T_e^{3/2}$) in the corresponding region, and by the same factor it decreases the electric field $\boldsymbol{E}_G$, so the flare heating of the chromosphere should basically cease the re-acceleration in the thick-target region very early after the start of the impulsive phase. On the other hand, under the flare conditions, generation of a high anomalous resistivity could be expected due to plasma instabilities, so the accelerating mechanism could continue working.

2.4.2. Stochastic electric fields – LRTTM

Inspired by Brown et al. (2009) and Turkmani & Brown (2012), we produced a simplified local re-acceleration thick-target model (LRTTM). To approximate the distribution of electric fields arising as a consequence of a current sheet cascade in the randomly stressed magnetic fields (Turkmani et al. 2005, 2006), we assume a region (between 1–2 Mm) of stochastic re-acceleration electric field $\boldsymbol{E}_L$, spatially modulated by the function shown in Fig. 3 (bottom). The position of the local re-acceleration region is one of the free parameters of the model. It roughly corresponds to the chromosphere and encompasses

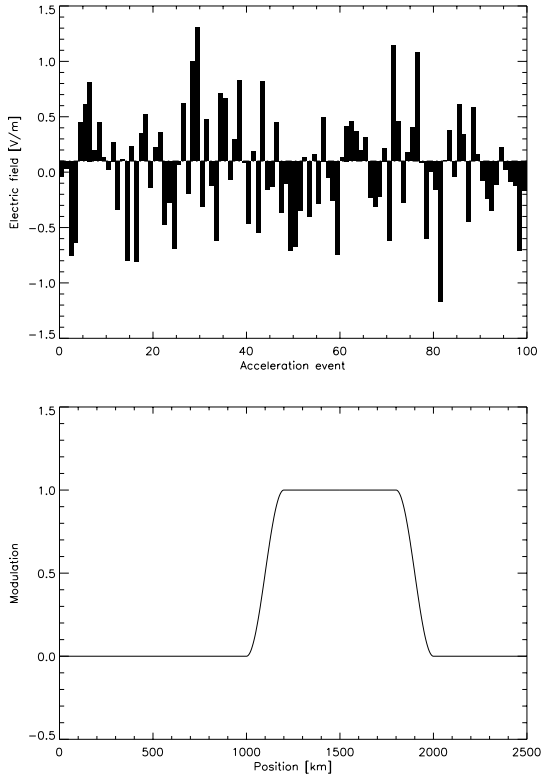

Fig. 3. *Top*: example of $\boldsymbol{E}_{\rm L}$-II type stochastic electric field with $\overline{E_{\rm L}}$ = 0.1 V m^{-1} and var($E_{\rm L}$) = 0.5 V m^{-1} corresponding to the distribution function in Fig. 13. *Bottom*: the spatial modulation of $\boldsymbol{E}_{\rm L}$.

the regions of magnetic field convergence and the rapid change of hydrogen ionisation (see Fig. 1).

The stochastic electric fields $\boldsymbol{E}_{\rm L}$ are generated only in the directions parallel and anti-parallel relative to the loop axis, and their distribution corresponds to Gaussians with various mean values $\overline{E_{\rm L}}$ and variances var($E_{\rm L}$) = $\overline{E_{\rm L}^2} - \overline{E_{\rm L}}^2$. We examine two types of $\boldsymbol{E}_{\rm L}$:

$\boldsymbol{E}_{\rm L}$-I. A stochastic electric field with zero mean value

$$\overline{E_{\rm L}} = 0, \qquad \mathrm{var}(E_{\rm L}) > 0. \tag{15}$$

$\boldsymbol{E}_{\rm L}$-II. A combination of spatially localised static electric field with a stochastic component (see Fig. 3)

$$\overline{E_{\rm L}} \neq 0, \qquad \mathrm{var}(E_{\rm L}) \geq 0. \tag{16}$$

In the case of $\boldsymbol{E}_{\rm L}$-II, the sign of the static component $\overline{E_{\rm L}}$ always assures acceleration of the non-thermal electrons towards the nearest footpoint. This field type can develop in the thick-target region if stochastic fields are present in a globally twisted magnetic loop. In comparison with the GRTTM, the LRTTM is characterised by abrupt changes in magnitude and orientation of the accelerating or decelerating electric fields representing the individual current sheets in the thick-target region (Turkmani et al. 2006) (compare Figs. 2 and 3).

The integration of motion of individual beam electron clusters for the LRTTM is performed in the following way. In each time-step (corresponding to $\Delta t = 5 \times 10^{-5}$ s), we generate a random value of $\boldsymbol{E}_{\rm L}$ for each particle within the acceleration region. In this way we model the situation where the beam electrons are moving in the stochastic electric fields, whose configuration temporally changes. Therefore, the electrons only have a negligible chance of passing through exactly the same configuration of current sheets and of experiencing the same acceleration (deceleration) sequence. The time-step basically determines the spatial extent of the individual current sheets. In order to keep the size independent of particle velocities, we weight $\boldsymbol{E}_{\rm L}$ using a factor v_0/v, where v_0 and v are the velocities corresponding to the low-energy cutoff and to the particular particle, respectively. The time-step $\Delta t = 5 \times 10^{-5}$ s thus corresponds to the current sheet size ~3 km. Simulations with various time-steps showed that the results are not very sensitive to the choice of the time-step. Using the weighted value of $\boldsymbol{E}_{\rm L}$ we relativistically move the electron from the old to the new position. Then we calculate the energy loss and scattering due to the passage of the particle through the corresponding column of plasma and the effects of converging magnetic field. This is done repeatedly for the whole population of test-particles. The corresponding total energy deposit and HXR spectrum are then calculated.

2.5. HXR spectra

The intensity $I(\epsilon, s)$ [photons cm^{-2} s^{-1} keV^{-1}] of HXR bremsstrahlung observed on energy ϵ, emitted by plasma at a position s along the flare loop, detected in the vicinity of the Earth, was calculated using the formula (Brown 1971)

$$I(\epsilon, s) = \frac{n_{\rm p}(s)V(s)}{4\pi R^2} \int_{\epsilon}^{\infty} Q(E, \epsilon)\, v(E)\, n(E, s)\, \mathrm{d}E. \tag{17}$$

Here, $n_{\rm p}(s)V(s)$ is the total number of protons in the emitting plasma volume $V(s)$ at a position s, distance R = 1 AU, $v(E)$ is the electron velocity calculated relativistically from the electron energy, and $n(E, s)$ is the number density of non-thermal electrons per energy in the emitting volume having kinetic energy E. The cross section $Q(E, \epsilon)$ for bremsstrahlung was calculated using a semi-relativistic formula given by (Haug 1997), multiplied by the Elwert factor (Elwert 1939), considering the limit case when the entire electron kinetic energy is emitted. The precision of the method should be better than 1% for energies ≤300 keV (Haug 1997). To calculate the emitting volume $V(s)$ we assume a circular cross section of the converging loop with a radius $r(s) = 1.5\sqrt{B_0/B(s)}$ Mm. The HXR spectra are calculated on a spatial (height) grid $(s, s+\Delta s)$. The individual emitting volumes along the grid are then $V(s) = \pi r(s)^2 \Delta s$.

3. Results

We now concentrate on a comparison of outcomes of chromospheric bombardment for two modifications of CTTM with the CTTM itself. In this section we present the non-thermal electron distribution functions in the vicinity of footpoints and several properties of the corresponding energy deposits and HXR intensities and spectra. The quantitative results for the CTTM, GRTTM, and both considered types of LRTTM are summarised in Figs. 8, 11, and 12 and Tables 1–3, respectively. Here, the factor $\mathcal{F}_{\rm R}/\mathcal{F}_0$ gives the ratio of the reflected (due to the magnetic mirroring, re-acceleration, and backscattering) to the original non-thermal electron energy flux coming from the corona at position s = 3 Mm, measured at t = 0.3 s after the beam injection into the loop at its apex. To assess the magnitude of the energy deposits for the individual models, we calculate the total

Table 1. Summary of results for the CTTM.

$\mathcal{F}_0/2\times10^9$ [erg cm^{-2} s^{-1}]	$\mathcal{F}_R/\mathcal{F}_0$ [%]	$\mathcal{E}_{ch}/10^9$ [erg s^{-1}]	s_{max} [Mm]	$I_{25\,keV}$ [cm^{-2} s^{-1} keV^{-1}]	$\gamma_{25\,keV}$	$\mathcal{F}'_0/2\times10^9$ [erg cm^{-2} s^{-1}]	δ'_p	E'_0 [keV]
				$R_m = 1$				
2.5	0.08 (2.9)	2.3 (2.2)	1.3 (1.4)	0.45 (0.44)	2.4 (2.4)	2.6 (2.4)	3.0 (3.0)	10 (11)
50	0.25 (3.0)	47 (44)	1.3 (1.4)	9.0 (8.8)	2.4 (2.4)	52 (48)	3.0 (3.0)	10 (11)
				$R_m = 5$				
2.5	4.3 (40)	2.2 (1.4)	1.4 (1.4)	0.45 (0.12)	2.4 (2.7)	2.5 (1.3)	3.0 (3.4)	11 (10)
50	3.9 (40)	46 (28)	1.4 (1.4)	9.1 (2.4)	2.4 (2.7)	53 (25)	3.0 (3.4)	10 (10)

Notes. $\mathcal{F}_0$ – the initial energy flux, $\mathcal{F}_R/\mathcal{F}_0$ – ratio of reflected to initial energy flux at $s = 3$ Mm and $t = 0.3$ s, $\mathcal{E}_{ch}$ – integrated chromospheric energy deposit, s_{max} – position of energy deposit maximum, $I_{25\,keV}$, $\gamma_{25\,keV}$ – HXR intensity and power-law index measured at energy 25 keV, $\mathcal{F}'_0$, δ'_p, and E'_0 – the fitted values of energy flux, power-law index, and low-energy cutoff, respectively. The non-parenthetical and parenthetical values are for the M^{FF} and M^{SU} cases of $M(\mu_0)$, respectively. Applies to Tables 2 and 3.

energy deposited into the chromosphere along a magnetic flux tube as

$$\mathcal{E}_{ch} = \int\limits_{\text{chromosphere}} E_{dep}(s)\mathrm{d}V(s) = S_0 B_0 \int\limits_0^{2.3\ \text{Mm}} \frac{E_{dep}(s)}{B(s)}\mathrm{d}s \qquad (18)$$

and give the position of the energy deposit maximum s_{max} in the atmosphere. The factor $B_0/B(s)$ in integral (18) accounts for the convergence of the magnetic field, $E_{dep}(s)$ is the local energy deposit in units [erg cm^{-3} s^{-1}], and the limits of integration correspond to the upper and lower boundaries of the chromosphere. The lower limit lies far below the stopping depths of the beam electrons for all the studied models. When all the beam energy is deposited into the chromosphere and $S_0 = 1$ cm^2, the value of $\mathcal{E}_{ch}$ in units [erg s^{-1}] corresponds to the value of the initial flux $\mathcal{F}_0$.

For HXR we give the intensity $I_{25\,keV}$ and the power-law index $\gamma_{25\,keV}$ measured at energy 25 keV. Furthermore, we applied the RHESSI spectral analysis software[1] (OSPEX) to modelled total X-ray spectra to imitate common spectral analysis. We assumed that these spectra were incident on RHESSI detectors and forward-fitted the "detected" count spectra. In the fitting we used the OSPEX thick-target model and a single power-law injected electron spectrum. In this way we obtained the fitted electron beam parameters. To account for the non-uniform ionisation structure of the X-ray emitting atmosphere, the fitting function `f_thick_nui` in the step-function mode was chosen. When the fitted parameters of `f_thick_nui` were unrealistic and the X-ray emission was formed deep in the layers of almost neutral plasma, `f_thick` with neutral energy loss term was used. Also, we modified the standard OSPEX energy loss term and the ratio of Coulomb logarithms to be consistent with relations used in the test-particle code. The results of this analysis, the fitted energy flux $\mathcal{F}'_0$, the power-law index δ'_p, and the low-energy cutoff E'_0 are listed in Tables 1–3 and displayed in Figs. 8, 11, and 12.

3.1. CTTM

To produce a basis for comparison we present results for the classical CTTM in a converging magnetic field. The information on kinematics of non-thermal electrons for both initial μ-distributions we considered is incorporated into Fig. 4. We first concentrate on the left-hands panels showing the time dependent distributions for M^{FF} case. The top panel for $t = 0.1$ s corresponds to the transition state when the loop is being filled with non-thermal electrons. The process of filling is apparent as a depletion of the distribution function at low energies in the region ranging from approximately 1.4 Mm to 3.7 Mm. The distribution above the low-energy cutoff and the bottom boundary of the magnetic mirror is dominated by red, so a vast majority of particles move downwards with $\mu \approx 1$. At low energies ($E < 20$ keV), a low-energy tail of particles starts to form in the region under the lower boundary of the magnetic mirror. It consists of particles with originally higher energies that lost part of their energy owing to their interactions with the target plasma. The tail is rich in particles with $\mu \approx 0$ (green), and it also contains a few back-scattered particles with $\mu \approx -1$ (blue). Coulomb scattering leads to an increase in pitch angles of low-energy electrons in the region above the magnetic mirror. These particles do not satisfy the condition for passing through the mirror. They are reflected and propagate back to the loop top and fill the loop with a population of low-energy electrons (<20 keV) with $-1 \le \mu < 0$.

Such a low-energy tail is more clearly pronounced in the subsequent times in the vicinity and slightly above the lower boundary of the magnetic mirror. The following snapshot for $t = 0.15$ s, when even the particles with lowest energies reached the thick-target region, shows the proceeding thermalisation of beam electrons in this region and increase in particle number with $\mu \le 0$ in the low-energy tail. A new population of particles with $\mu \approx -1$ starts to form and propagate upwards, towards the loop top. The snapshot at $t = 0.3$ s roughly corresponds to a fully developed state. The part of the distribution function at the vicinity of the bottom boundary of the magnetic mirror and in the low-energy region $E < 20$ keV is dominated by particles with $\mu \approx 0$. The reflected energy flux propagating upwards is approximately 4% of the original flux $\mathcal{F}_0$ for the M^{FF} case (see Table 1).

The distribution functions corresponding to M^{SU} are shown in Fig. 4 (right). The overall behaviour of the beam electrons is quite similar to the previously discussed case. The most obvious difference is the enhancement of the particle populations with $\mu < 0$ on all energies (corresponding to 40% of the initial flux $\mathcal{F}_0$) and $\mu \approx 0$ predominantly on low energies ($E < 40$ keV) localised above the bottom boundary of the magnetic mirror. The differences between the M^{FF} and M^{SU} cases naturally influence the resulting energy deposits and properties of the corresponding HXR emission (see Figs. 4, 5). The CTTM in the adopted arrangement gives identical results for both footpoints. Therefore

[1] http://hesperia.gsfc.nasa.gov/rhessi2/home/software/spectroscopy/spectral-analysis-software/

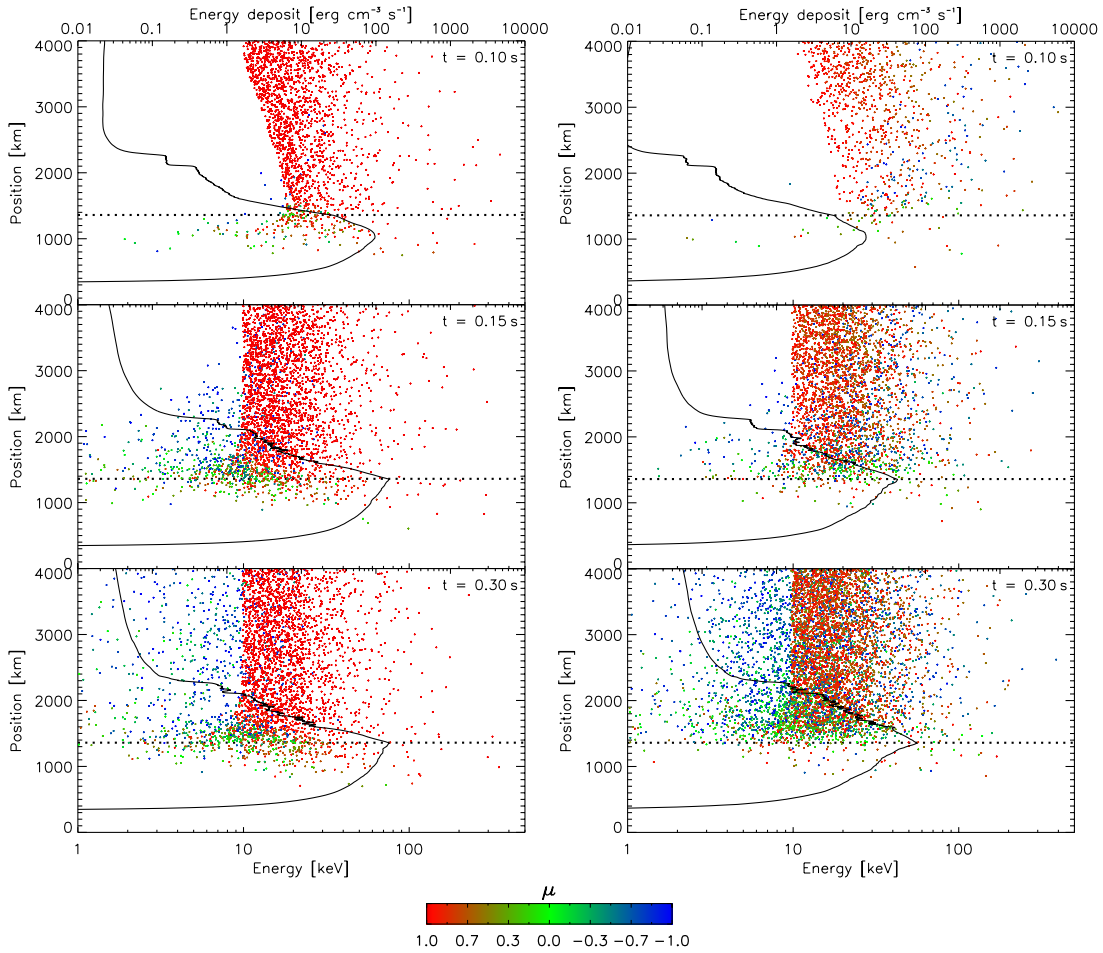

Fig. 4. CTTM time evolution of distribution functions of non-thermal electron energies versus positions with a colour coded $M(\mu_0)$ in the VAL C atmosphere. *Left*: M^{FF}, *right*: M^{SU}. *From top to bottom*: individual snapshots at $t = 0.1, 0.15, 0.3$ s after the beam injection into the loop at its apex. The solid lines indicate the instantaneous energy deposits corresponding to $\mathcal{F}_0/2 = 2.5 \times 10^9$ erg cm^{-2} s^{-1}. The dotted horizontal lines indicate the bottom boundary of the magnetic mirror. Only the lower part of the loop and one footpoint are displayed.

for $t > 0.3$ s the particles reflected at the second footpoint reach the loop top and appear as a new population of particles moving downwards to the first footpoint. For simplicity we only concentrate on times $t \leq 0.3$ s.

To distinguish the effects of the μ-distribution and magnetic field convergence, Table 1 also lists the characteristics of CTTM for the case of no magnetic mirror, i.e. $R_{\mathrm{m}} = 1$. It shows that it is the magnetic field convergence that significantly influences $\mathcal{F}_{\mathrm{R}}/\mathcal{F}_0$ and $\mathcal{E}_{\mathrm{ch}}$ in the case of M^{SU}.

A comparison of energy deposits for both considered initial μ-distributions is shown in Fig. 5 (left). Because the adopted energy flux for both models considering secondary re-acceleration $\mathcal{F}_0/2 = 2.5 \times 10^9$ erg cm^{-2} s^{-1} is unrealistically low in the context of CTTM and flare physics, we also plot energy deposits for the much higher and more realistic value $\mathcal{F}_0/2 = 5 \times 10^{10}$ erg cm^{-2} s^{-1}. The results corresponding to this flux will be used as a basis for comparison with the energy deposits and HXR spectra obtained from the models involving the secondary acceleration mechanisms. The chromospheric energy deposit $\mathcal{E}_{\mathrm{ch}}$ scales linearly with $\mathcal{F}_0$ (see Table 1), and the positions of energy deposit maxima are almost identical for all the considered cases approximately corresponding to the placement of the lower boundary of the magnetic mirror $s_{\mathrm{max}} = 1.36$ Mm. The peak in the energy deposits at s_{max} and their steep decrease above it (see Fig. 5, left) are caused by the constricted magnetic flux tube. The influence of the initial μ-distribution is obvious. For the M^{FF} case, particles have a greater chance of passing through the magnetic mirror and thus of depositing their energy into the deeper layers. In the M^{SU} case, when the particles reach the thick-target region and the region of strongly converging field, their pitch angles are generally higher: compare the left-hand and right-hand panels of Fig. 4. Therefore the probability that an electron passes through the magnetic mirror is strongly reduced. This naturally explains the systematic enhancements in the energy deposits for M^{SU} in the layers above and the decrease in the layers below the lower boundary of the magnetic mirror in comparison with the M^{FF} case.

The corresponding HXR spectra are shown in Fig. 5 (right), and their parameters are summarised in Table 1. As expected, the HXR intensity $I_{25\,\mathrm{keV}}$ scales linearly with the chromospheric deposit $\mathcal{E}_{\mathrm{ch}}$ or the energy flux $\mathcal{F}_0$. Majority of the total X-ray emission, i.e. summed over the whole loop, comes from the regions below the bottom boundary of the magnetic mirror. As explained above, the number of particles passing through the

A&A 563, A51 (2014)

Table 2. Summary of results for the GRTTM with $\mathcal{F}_0/2 = 2.5 \times 10^9$ erg cm^{-2} s^{-1}.

Footpoint	j [A m^{-2}]	$\mathcal{F}_R/\mathcal{F}_0$ [%]	$\mathcal{E}_{ch}/10^9$ [erg s^{-1}]	s_{max} [Mm]	$I_{25\,keV}$ [cm^{-2} s^{-1} keV^{-1}]	$\gamma_{25\,keV}$	$\mathcal{F}_0'/2 \times 10^9$, δ_p', E_0' [erg cm^{-2} s^{-1}], [keV]
Primary	1.0	3.1 (37)	2.8 (1.7)	1.2 (1.4)	0.71 (0.18)	2.4 (2.7)	3.3, 3.0, 12 (1.6, 3.4, 11)
	2.0	2.2 (36)	4.2 (2.1)	1.1 (1.1)	1.2 (0.29)	2.4 (2.7)	4.5, 3.0, 15 (2.2, 3.5, 13)
	3.0	1.6 (33)	5.5 (3.0)	0.98 (1.1)	2.2 (0.56)	2.5 (2.9)	6.7, 3.1, 20 (3.2, 3.6, 17)
	4.0	1.5 (33)	7.7 (4.7)	0.87 (0.94)	5.0 (1.5)	2.40 (2.9)	10, 3.3, 30 (4.7, 3.7, 25)
	5.0	0.92 (32)	15 (7.7)	0.80 (0.83)	13 (4.5)	2.0 (2.3)	17, 3.5, 48 (7.7, 3.9, 39)
	6.0	0.69 (31)	30 (18)	0.60 (0.63)	38 (17)	1.7 (1.7)	35, 4.5, 100 (17, 4.8, 88)
Secondary	1.0	5.1 (42)	1.9 (1.2)	1.4 (1.4)	0.31 (0.086)	2.4 (2.7)	2.0, 3.0, 9 (1.0, 3.5, 10)
	2.0	6.6 (43)	1.5 (1.0)	1.4 (1.4)	0.22 (0.066)	2.4 (2.7)	1.6, 3.1, 9 (0.82, 3.5, 10)
	3.0	8.6 (47)	1.4 (0.89)	1.4 (1.6)	0.16 (0.053)	2.4 (2.7)	1.3, 3.1, 8 (0.70, 3.5, 10)
	4.0	11 (51)	1.2 (0.82)	1.4 (1.6)	0.13 (0.044)	2.4 (2.7)	1.0, 3.1, 8 (0.61, 3.6, 10)
	5.0	12 (55)	1.1 (0.71)	1.4 (1.7)	0.10 (0.034)	2.4 (2.8)	0.87, 3.1, 8 (0.52, 3.6, 10)
	6.0	15 (54)	0.93 (0.64)	1.4 (1.7)	0.081 (0.032)	2.5 (2.8)	0.74, 3.2, 8 (0.47, 3.6, 10)

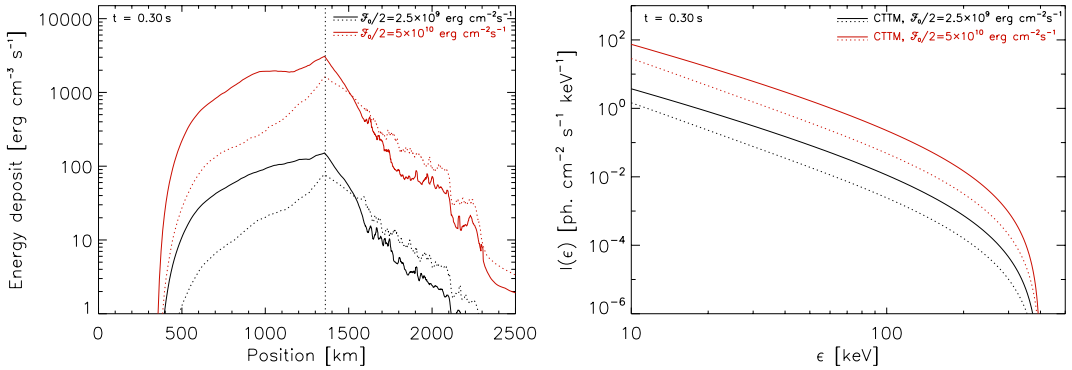

Fig. 5. *Left*: CTTM instantaneous energy deposits into the VAL C atmosphere at $t = 0.3$ s for energy fluxes $\mathcal{F}_0/2 = 5 \times 10^{10}$ erg cm^{-2} s^{-1} (red lines) and $\mathcal{F}_0/2 = 2.5 \times 10^9$ erg cm^{-2} s^{-1} (black lines). The dotted vertical line indicates the bottom boundary of the magnetic mirror. *Right*: the HXR spectra integrated over one half of the loop. In both panels the solid lines represent M^{FF}, the dotted lines M^{SU} case.

magnetic mirror is lower in the M^{SU} case than for M^{FF}, therefore the HXR emission corresponding to M^{FF} is more intense than the emission of M^{SU}.

HXR spectra are steeper in the M^{SU} case owing to presence of magnetic field convergence – compare $R_m = 1$ and 5 in Table 1. Fitted beam injected energy flux agrees well (within 20%) with the $\mathcal{E}_{ch}$, whereas δ_p' and E_0' are the same as those of the injected power law. An exception is the larger δ_p' in the M^{SU} case, which corresponds to the mentioned HXR spectral behaviour and the fact that the spectral fitting does not take the scattering induced by change in B into account.

3.2. GRTTM

The effects of static (global) electric field $\boldsymbol{E}_G$ was studied for current densities in the range from 1 A m^{-2} to 6 A m^{-2}. The distribution functions of non-thermal electrons for current density $j = 6$ A m^{-2} and time $t = 0.3$ s after the beam injection into the loop at its apex are shown in Fig. 6. In the upper left-hand panel, two tails of particles can be identified in the primary footpoint and the M^{FF} case. A faint low-energy tail at energies $E < 20$ keV, located above the bottom boundary of the magnetic mirror, is predominantly formed of particles with $\mu \leq 0$ (see the regions labelled L in Fig. 6). Its formation mechanism corresponds to the CTTM, i.e. to the particle deceleration related to the collisional energy losses in the target plasma and to the combined effects of particle scattering and magnetic field convergence, compare with Fig. 4 (left). This tail becomes more apparent for distributions that correspond to lower j (see Fig. 4). On the other hand, a prominent high-energy tail, on energies from 20 to 300 keV stretching from 1.7 to 0.5 Mm (see the regions labelled H in Fig. 6), does not have any counterpart in Fig. 4 for the CTTM. The tail is formed of re-accelerated and relatively focussed particles with $\mu \approx 1$. Another obvious effects of $\boldsymbol{E}_G$ are the increase in beam penetration depth with growing j and a weakening of the population of reflected and back-scattered particles propagating towards the secondary footpoint that corresponds to 0.7% of the initial beam flux only, see Fig. 8 (left).

Figure 6 (top right, M^{SU} case) exhibits essentially the same features. The most apparent distinctions between the two distributions are a much richer population of particles in the low-energy tail located above the bottom boundary of the magnetic mirror and the existence of a relatively rich population of reflected and back-scattered particles with $\mu < 0$ (on all energies) propagating towards the secondary footpoint reaching approximately 30% of the initial flux (see Fig. 8, bottom left). The differences between the distributions corresponding to M^{FF} and M^{SU} cases are solely effects of the initial μ-distribution.

The situation at the secondary footpoint is shown in Fig. 6 (bottom). In addition to the effect of Coulomb collisions, the field $\mathbf{E}_G$ constantly decreases the parallel velocity component of the particles propagating towards the secondary footpoint. This results in the formation of an enhanced low-energy tail in the particle distribution functions located above the bottom boundary of the magnetic mirror. Another obvious feature is a rich

Table 3. Summary of results for the LRTTM with $\mathcal{F}_0/2 = 2.5 \times 10^9$ erg cm^{-2} s^{-1}.

$\overline{E_L}$ [V m^{-1}]	var(E_L) [V m^{-1}]	$\mathcal{F}_R/\mathcal{F}_0$ [%]	$\mathcal{E}_{ch}/10^9$ [erg s^{-1}]	s_{max} [Mm]	$I_{25\,keV}$ [cm^{-2} s^{-1} keV^{-1}]	$\gamma_{25\,keV}$	$\mathcal{F}_0'/2 \times 10^9$, δ_p', E_0' [erg cm^{-2} s^{-1}, keV]
0.0	0.1	5.8 (41)	2.2 (1.4)	1.3 (1.4)	0.46 (0.12)	2.4 (2.7)	2.2, 3.0, 12 (1.2, 3.5, 11)
	0.5	21 (78)	3.0 (1.7)	1.0 (1.1)	0.79 (0.32)	2.8 (3.3)	2.9, 3.7, 24 (1.5, 4.4, 25)
	1.0	31 (120)	3.9 (2.5)	0.87 (0.96)	2.0 (1.2)	2.4 (2.5)	4.1, 4.4, 41 (2.6, 4.9, 42)
	2.0	44 (130)	6.4 (4.5)	0.78 (0.76)	4.8 (3.6)	1.9 (1.9)	6.2, 4.8, 70 (4.7, 5.0, 71)
	3.0	68 (140)	7.0 (5.5)	0.69 (0.71)	7.5 (6.0)	1.8 (1.8)	7.9, 4.6, 93 (6.4, 4.8, 93)
	4.0	77 (170)	9.1 (7.5)	0.66 (0.70)	10 (8.3)	1.7 (1.7)	9.7, 4.5, 110 (7.9, 4.6, 110)
	5.0	90 (160)	12 (8.6)	0.61 (0.68)	13 (11)	1.6 (1.6)	11, 4.3, 130 (9.8, 4.4, 130)
0.1	0.0	0.05 (23)	7.5 (6.5)	0.91 (0.94)	4.2 (2.8)	2.4 (2.6)	8.7, 6.0, 47 (6.5, 9.0, 48)
	0.5	0.63 (37)	8.3 (6.1)	0.88 (0.89)	4.7 (3.3)	2.3 (2.40)	8.7, 5.7, 51 (6.6, 7.0, 52)
	1.0	3.2 (55)	8.7 (8.2)	0.82 (0.84)	6.2 (4.6)	2.1 (2.1)	9.5, 5.6, 61 (7.3, 6.0, 61)
	2.0	17 (78)	10 (8.7)	0.72 (0.74)	8.7 (7.3)	1.9 (1.9)	10, 5.8, 84 (8.6, 5.8, 85)
	3.0	37 (100)	12 (8.7)	0.68 (0.70)	11 (9.8)	1.7 (1.7)	11, 4.8, 100 (9.9, 5.0, 110)
	4.0	65 (120)	9.0 (12)	0.63 (0.63)	13 (12)	1.6 (1.6)	12, 4.6, 120 (11, 4.7, 130)
	5.0	76 (150)	13 (11)	0.63 (0.65)	16 (14)	1.6 (1.6)	13, 4.4, 140 (12, 4.4, 140)

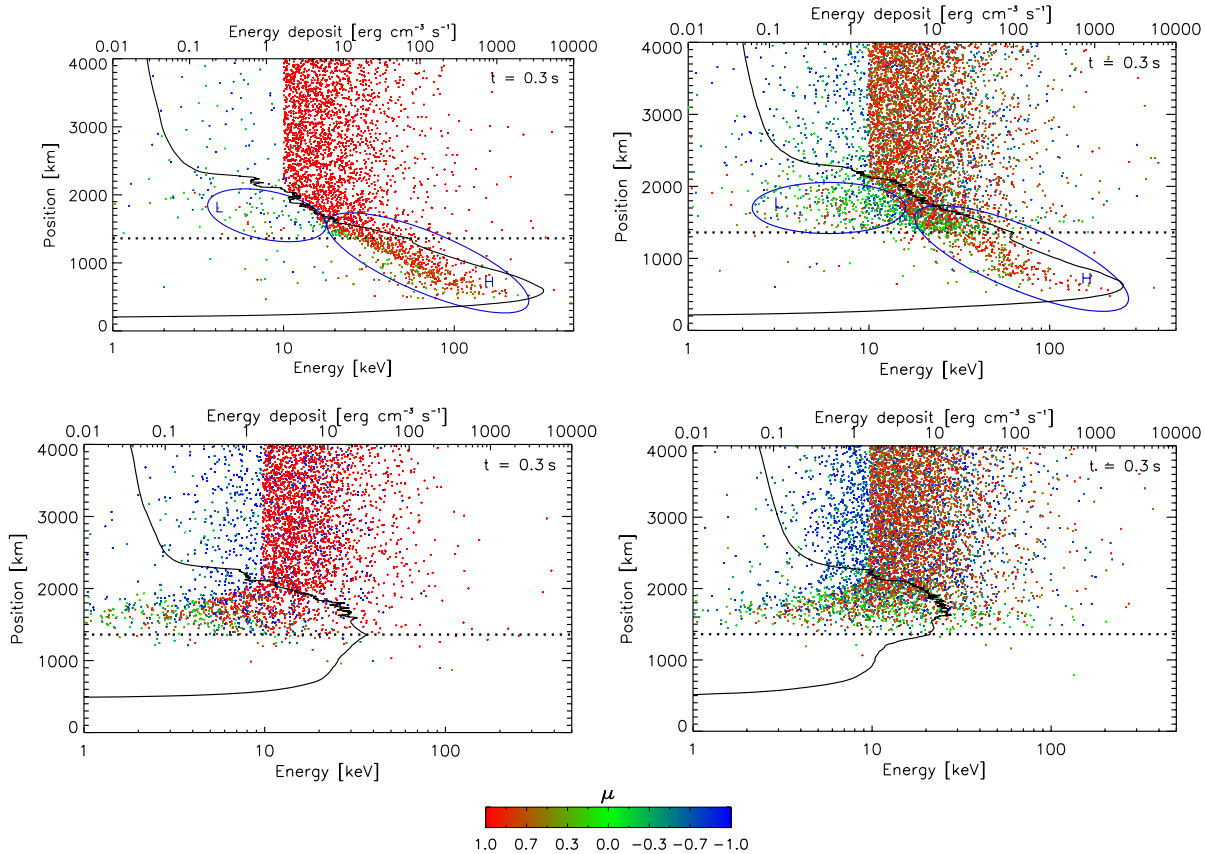

Fig. 6. GRTTM distribution functions of non-thermal electron energies versus positions with a colour coded $M(\mu_0)$ corresponding to the current density $j = 6\,\mathrm{A\,m^{-2}}$ in the VAL C atmosphere at time $t = 0.3$ s after the beam injection into the loop at its apex. *Top*: primary footpoint, *bottom*: secondary footpoint, *left*: M^{FF}, *right*: M^{SU}. The solid lines indicate the instantaneous energy deposits corresponding to $\mathcal{F}_0/2 = 2.5 \times 10^9$ erg cm^{-2} s^{-1}, the dotted horizontal lines the bottom boundary of the magnetic mirror and the blue ellipses labelled L and H denote tails in the particle distribution function. Only the vicinity of the footpoints are displayed.

population of reflected or back-scattered particles corresponding approximately to 15% and 54% of the initial beam flux for the M^{FF} and M^{SU} cases, respectively (see Fig. 8, bottom left). These particles are accelerated by the global field $\boldsymbol{E}_G$ back, towards the primary footpoint.

The instantaneous energy deposits and HXR spectra for both the primary and secondary footpoints and various current densities are shown in Fig. 7, and the quantitative results, some of them only for the primary footpoint, are summarised in Fig. 8 (see Table 2 for complete results). The magnitudes and spatial

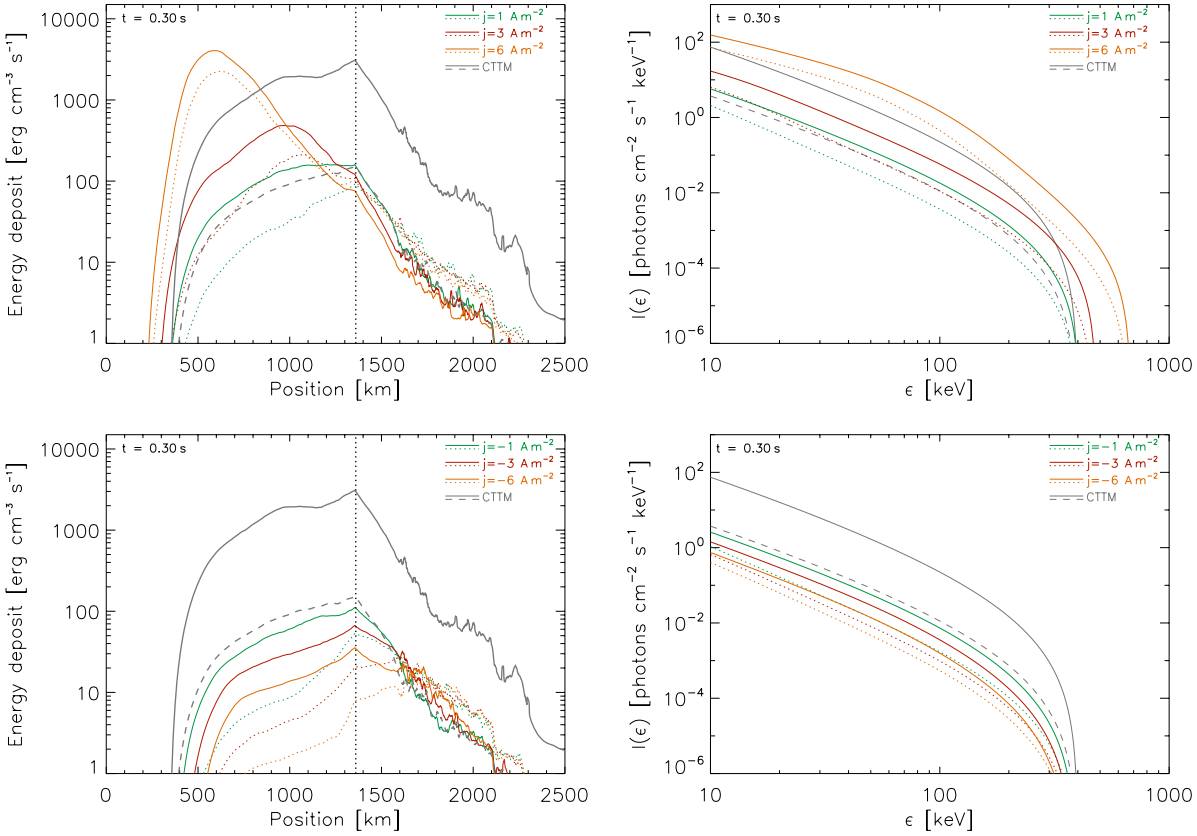

Fig. 7. GRTTM instantaneous energy deposits (*left*) and HXR spectra (*right*) for the primary (*top*) and secondary (*bottom*) footpoints and the VAL C atmosphere at $t = 0.3$ s. The green, red, and orange solid ($M^{\rm FF}$) and dotted ($M^{\rm SU}$) lines correspond to the current densities $j = 1, 3, 6\,{\rm A\,m^{-2}}$, respectively, and to the energy flux $\mathcal{F}_0/2 = 2.5 \times 10^9$ erg cm^{-2} s^{-1}. The grey dashed and solid lines correspond to the CTTM with $\mathcal{F}_0/2 = 2.5 \times 10^9$ and 5×10^{10} erg cm^{-2} s^{-1}, respectively. The dotted straight vertical line indicates the bottom boundary of the magnetic mirror. The HXR spectra are integrated over one half of the loop.

distributions of energy deposits in the atmosphere, as well as the production of HXR photons, are extremely sensitive to the current densities in the threads. According to our simulations, the current density $j = 6\,{\rm A\,m^{-2}}$ increases $\mathcal{E}_{\rm ch}$ at the primary footpoint of one order and $I_{25\,{\rm keV}}$ of approximately two orders (see Fig. 8). Moreover, this HXR spectrum is more intense than the spectrum of pure CTTM with $\mathcal{F}_0/2 = 5 \times 10^{10}$ erg cm^{-2} s^{-1} (see Fig. 7, top right). The presence of j also considerably changes the distribution of the energy deposit in the thick-target region. The maximum of the energy deposit $s_{\rm max}$ is substantially shifted towards the photosphere (compare the results for $j = 0$ corresponding to the CTTM and for $j > 0$ in the top right of Fig. 8), and the energy is deposited in a much narrower region in the chromosphere (see the top left of Fig. 7). In the case of $j = 6\,{\rm A\,m^{-2}}$, $\mathcal{E}_{\rm ch}$ is comparable to $\mathcal{F}_0/2 = 5 \times 10^{10}$ erg cm^{-2} s^{-1} of pure CTTM, however the spatial distribution is completely different.

HXR emission of the primary footpoint comes predominantly from regions well below the bottom of the magnetic mirror, close to temperature minimum for $j \gtrsim 3\,{\rm A\,m^{-2}}$ and photon energies $\gtrsim$50 keV. As j increases, HXR spectra get more intense and flatter at deka-keV energies, and the maximum photon energy is shifted to higher energies. This is all consistent with the presence of the high-energy electrons accelerated by $\boldsymbol{E}_{\rm G}$ below the magnetic mirror. Although the HXR power-law index $\gamma_{25\,{\rm keV}}$ tends to harden as j increases, the fitted CTTM injected electron power-law index $\delta'_{\rm p}$ becomes steeper. However, at the same time, the low-energy cutoff E'_0 rises to deka-keV values, causing decrease in $\gamma_{25\,{\rm keV}}$ – see fitted parameters in Fig. 8 (bottom right).

The model of $j = 1\,{\rm A\,m^{-2}}$ is similar to the CTTM situation; i.e. similar formation heights of HXR, spectral shape of photon spectrum (Fig. 7, left), and fitted electron distribution (Fig. 8, bottom right). In the case of $j = 6\,{\rm A\,m^{-2}}$, the HXR spectra are extremely flat below ~40 keV with $E'_0 \sim 100$ keV. Such low-energy cutoffs are not found from observations, therefore this case could represent a limit of possible j in flare loops.

The situation at the secondary footpoint is different (see Fig. 7, bottom). Because a part of energy carried by non-thermal particles is drained due to the actuation of $\boldsymbol{E}_{\rm G}$, the resulting chromospheric energy deposits for a particular j are smaller than at the primary footpoint. As expected, this behaviour steeply increases with j. Although the HXR spectra of the secondary footpoint are less intense than the spectrum of pure CTTM, the overall spectral shape is not changed significantly. Consequently, the fitted injected electron beam parameters show only a decrease in $\mathcal{F}'_0$ consistent with lower $\mathcal{E}_{\rm ch}$ (see Fig. 8, top left) and Table 2.

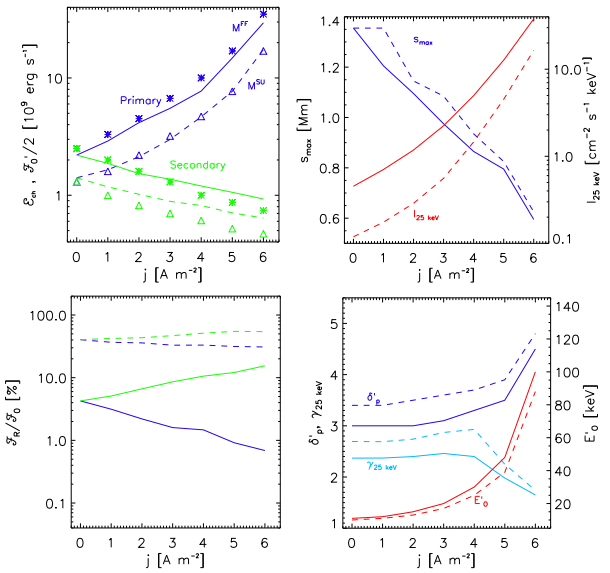

Fig. 8. GRTTM summary of calculated parameters of chromospheric bombardment for various current densities j. The solid lines and asterisks denote the M^{FF}, the dashed lines and triangles denote the M^{SU}. *Left*: chromospheric energy deposit $\mathcal{E}_{\mathrm{ch}}$ (lines) and fitted energy flux $\mathcal{F}'_0$ (symbols) *(top)*, the ratio $\mathcal{F}_{\mathrm{R}}/\mathcal{F}_0$ *(bottom)* for the primary (blue) and secondary (green) footpoints. *Right*: position of energy deposit maximum $s_{\max}$ and HXR intensity $I_{25\,\mathrm{keV}}$ (*top*), HXR spectral index $\gamma_{25\,\mathrm{keV}}$, fitted electron beam spectral index δ'_{p} and low-energy cutoff E'_0 (*bottom*) only for the primary footpoint.

3.3. LRTTM

3.3.1. $\mathrm{E_L}$-I type

The non-thermal electron distribution functions for the stochastic field with $\overline{E_{\mathrm{L}}} = 0\ \mathrm{V\,m^{-1}}$ and $\mathrm{var}(E_{\mathrm{L}}) = 1\ \mathrm{V\,m^{-1}}$ in the VAL C atmosphere and time $t = 0.3$ s after the beam injection into the loop at its apex are shown in Fig. 9. In both panels two kinds of particle populations can be identified: a conspicuous high-energy tail fuzzy in energies at particular height sections (see the regions labelled H), and an inconspicuous low-energy tail (see the regions labelled L).

The high-energy tail is located within the re-acceleration region on energies from 10 to 100 keV. It indicates that the net re-acceleration of particles occurs even though any electron in the re-acceleration region has an equal probability of encountering stochastic field $\boldsymbol{E}_{\mathrm{L}}$ (normally distributed) of parallel or anti-parallel orientation relative to $\mu = 1$. The net acceleration in this type of electric field is a consequence of inverse proportionality between the electron collisional energy loss and energy $\mathrm{d}E/\mathrm{d}z \propto 1/E$, z being the column density (Emslie 1978). The energy gain of re-accelerated electrons increases with $\mathrm{var}(E_{\mathrm{L}})$ similar to the fuzziness of the high-energy tails and the fluxes of backwards moving electrons (with $\mu < 0$). The ratio $\mathcal{F}_{\mathrm{R}}/\mathcal{F}_0$ corresponding to $\mathrm{var}(E_{\mathrm{L}}) = 1\ \mathrm{V\,m^{-1}}$ is approximately 31% and 120% for the M^{FF} and M^{SU} cases, respectively; i.e., in the latter case the backward energy flux exceeds the initial flux propagating downwards from the corona (see Fig. 11, right). Another effect of growing $\mathrm{var}(E_{\mathrm{L}})$ is a decrease in the electron population having μ distinct from 1 or -1. Ultimately, for high values of $\mathrm{var}(E_{\mathrm{L}})$, only particles with μ either close to 1 or -1 are present in the distribution, so the μ-distribution then copies the directional distribution of the re-accelerating field.

The inconspicuous low-energy tail spreads from the top of the re-acceleration region to the lower boundary of the magnetic mirror, and it is formed of particles of all possible pitch angles with energies under 20 keV. It is shifted higher into the chromosphere in comparison to the low-energy tail in the CTTM case (see Fig. 4). As $\mathrm{var}(E_{\mathrm{L}})$ increases, the low-energy tail becomes less distinct and its location is shifted higher towards the upper boundary of the re-acceleration region. The low-energy tail is formed by concerted actuation of Coulomb collisions and alternating stochastic field.

The energy deposits and HXR spectra corresponding to various values of $\mathrm{var}(E_{\mathrm{L}})$ in the range from 0.1 to 5 $\mathrm{V\,m^{-1}}$ are shown in Fig. 10 and their main parameters $\mathcal{E}_{\mathrm{ch}}$, $s_{\max}$, $I_{25\,\mathrm{keV}}$, and $\gamma_{25\,\mathrm{keV}}$ are displayed in left-hand panels of Figs. 11 and 12 and summarised in Table 3.

The behaviour of the energy deposits is similar to the GRTTM of the primary footpoint. They increase with $\mathrm{var}(E_{\mathrm{L}})$, $s_{\max}$ are shifted to the deeper layers, and the energy is deposited into an even narrower chromospheric region. For the lowest studied value $\mathrm{var}(E_{\mathrm{L}}) = 0.1\ \mathrm{V\,m^{-1}}$, we obtained practically no change in all followed parameters relative to the CTTM with an identical initial flux (see Figs. 10–12).

On the other hand, for the maximum value $\mathrm{var}(E_{\mathrm{L}}) = 5\ \mathrm{V\,m^{-1}}$ there is half an order increase in $\mathcal{E}_{\mathrm{ch}}$ and a substantial shift of $s_{\max}$ towards the photosphere (~750 km) for both initial μ-distributions. The value of $I_{25\,\mathrm{keV}}$ increases considerably (28× for the M^{FF} and $10^2\times$ for the M^{SU} case) relative to the CTTM with an identical initial flux (see Fig. 12, left).

Again, hard X-ray emission comes from the regions below the magnetic mirror. As for GRTTM case, as $\mathrm{var}(E_{\mathrm{L}})$ increases, the LRTTM hard X-ray spectra at ~25 keV become flatter (see $\gamma_{25\,\mathrm{keV}}$ in Fig. 12, left). Values of $\mathrm{var}(E_{\mathrm{L}}) \geq 2\ \mathrm{V\,m^{-1}}$ result in extremely flat photon spectra. On the other hand, the LRTTM X-ray spectra exhibit a double break or a local sudden decrease; see e.g. the spectrum in the ~50–100 keV range corresponding to $\mathrm{var}(E_{\mathrm{L}}) = 1.0\ \mathrm{V\,m^{-1}}$ in Fig. 10, right. Such spectral shapes affect the fitted CTTM electron distributions and result in high values of E'_0 (located approximately at the energy of a double break) and higher values of δ'_0 (see Fig. 12, bottom left). As $\mathrm{var}(E_{\mathrm{L}})$ rises, E'_0 still increases but δ'_0 stays almost constant, i.e. 4–5. The model of $\mathrm{var}(E_{\mathrm{L}}) = 5\ \mathrm{V\,m^{-1}}$ presents a limit, and the hard X-ray spectrum is consistent with a rather flat electron flux spectrum of high E'_0. Although the spectrum is more intense than the spectrum of pure CTTM with $\mathcal{F}_0/2 = 5 \times 10^{10}\ \mathrm{erg\,cm^{-2}\,s^{-1}}$ (i.e. 20× higher than the initial flux used in this model), owing to the high value of E'_0, the fitted electron flux is lower and consistent with the energy deposit in the chromosphere $\mathcal{E}_{\mathrm{ch}}$ (see Fig. 11, left).

3.3.2. $\mathrm{E_L}$-II type

The effects of local re-acceleration due to the stochastic field $\boldsymbol{E}_{\mathrm{L}}$ with $\overline{E_{\mathrm{L}}} \neq 0$ are demonstrated for the case with $\overline{E_{\mathrm{L}}} = 0.1\ \mathrm{V\,m^{-1}}$ and $\mathrm{var}(E_{\mathrm{L}}) = 0.5\ \mathrm{V\,m^{-1}}$ (see the distribution functions for M^{FF} and M^{SU} cases in Fig. 13). The re-acceleration process again results in formation of fuzzy high-energy tail of particles situated in the secondary acceleration region and covering the energy range from 10 to 100 keV approximately (see the regions labelled H). The mean energy reached by the re-accelerated electrons at the lower boundary of the re-acceleration region steeply increases with $\overline{E_{\mathrm{L}}}$, and at the same time the maximum of energy deposit shifts towards the deeper layers. The mean value of $\boldsymbol{E}_{\mathrm{L}}$ also has a strong focussing effect on the re-accelerated electrons. The latter effect reduces the ratio of backscattered and reflected

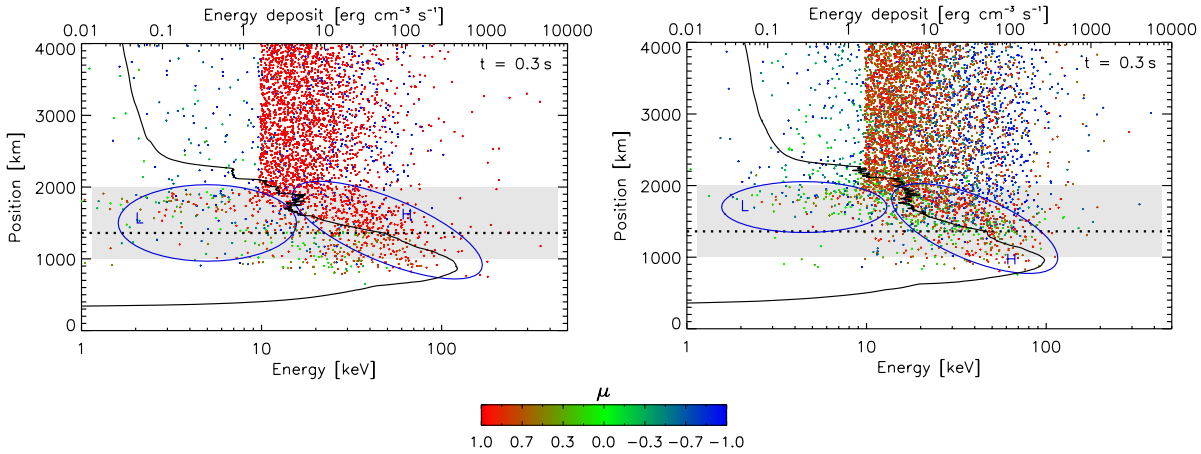

Fig. 9. LRTTM $\boldsymbol{E}_{\rm L}$-I type distribution functions of the non-thermal electron energies versus positions with a colour-coded $M(\mu_0)$ corresponding to $\overline{E_{\rm L}} = 0$ V m^{-1} and var($E_{\rm L}$) = 1 V m^{-1} in the VAL C atmosphere at time $t = 0.3$ s after the beam injection into the loop at its apex. *Left*: $M^{\rm FF}$; *right*: $M^{\rm SU}$. The solid lines indicate the instantaneous energy deposits corresponding to $\mathcal{F}_0/2 = 2.5 \times 10^9$ erg cm^{-2} s^{-1}, the dotted horizontal lines the bottom boundary of the magnetic mirror, the grey area the secondary re-acceleration region, and the blue ellipses labelled L and H denote tails in the particle distribution function. Only the vicinity of the footpoints is displayed.

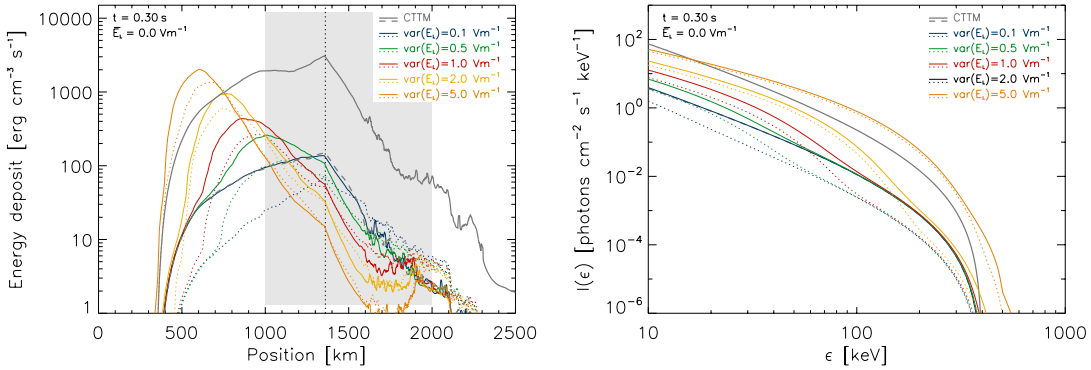

Fig. 10. LRTTM $\boldsymbol{E}_{\rm L}$-I type instantaneous energy deposits (*left*) and HXR spectra (*right*) for the VAL C atmosphere at $t = 0.3$ s. The solid ($M^{\rm FF}$) and dotted ($M^{\rm SU}$) blue, green, red, yellow, and orange lines correspond to $\overline{E_{\rm L}} = 0$ V m^{-1} and var($E_{\rm L}$) = 0.1, 0.5, 1, 2, 5 V m^{-1}, respectively, and energy flux $\mathcal{F}_0/2 = 2.5 \times 10^9$ erg cm^{-2} s^{-1}. The dashed and solid grey lines correspond to the CTTM with $\mathcal{F}_0/2 = 2.5 \times 10^9$ and 5×10^{10} erg cm^{-2} s^{-1}, respectively. The dotted straight vertical line indicates the bottom boundary of the magnetic mirror, the grey area the secondary re-acceleration region. The HXR spectra are integrated over one half of the loop.

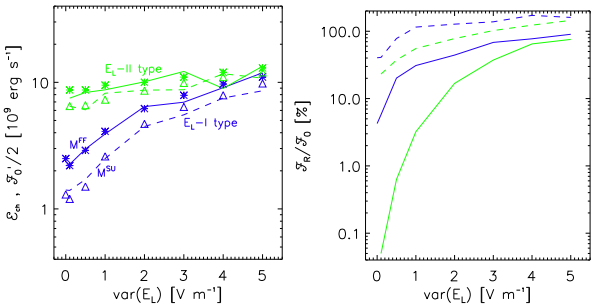

Fig. 11. LRTTM $\boldsymbol{E}_{\rm L}$-I (blue) and $\boldsymbol{E}_{\rm L}$-II (green) (for $\overline{E_{\rm L}} = 0.1$ V m^{-1}) chromospheric energy deposits $\mathcal{E}_{\rm ch}$ (lines) and fitted energy flux $\mathcal{F}_0'$ (symbols) (*left*) and the ratio $\mathcal{F}_{\rm R}/\mathcal{F}_0$ (*right*) for various var($E_{\rm L}$). Solid lines and asterisks denote $M^{\rm FF}$; dashed lines and triangles denote $M^{\rm SU}$.

particle flux to the initial flux $\mathcal{F}_{\rm R}/\mathcal{F}_0$ to less than 1% for the $M^{\rm FF}$ and to 37% for the $M^{\rm SU}$ case, respectively: compare values of $\mathcal{F}_{\rm R}/\mathcal{F}_0$ for the individual field types and parameters of $\boldsymbol{E}_{\rm L}$ displayed in Fig. 11 (right). The value of var($E_{\rm L}$) plays a similar role to what is described above for the $\boldsymbol{E}_{\rm L}$-I type. In comparison with the effects of $\overline{E_{\rm L}}$, it only weakly influences the energy gain of electrons at the lower boundary of the re-acceleration region, it increases the fuzziness of the high-energy tail and the flux of backwards moving electrons (with $\mu < 0$). For high values of var($E_{\rm L}$) we also see a decrease in electrons having μ other than close to 1 and -1, which is again the effect of imprint of the directional distribution of $\boldsymbol{E}_{\rm L}$ on the electron μ-distribution, which was also found for the stochastic field type $\boldsymbol{E}_{\rm L}$-I.

The stochastic field of $\overline{E_{\rm L}} = 0.1$ V m^{-1} and var($E_{\rm L}$) = 0.5 V m^{-1} (see Fig. 13) practically ceases the formation of the low-energy tail of particles located in the region between the upper boundary of the re-acceleration region and the lower boundary of the magnetic mirror found in the distribution functions corresponding to the CTTM, GRTTM, and LRTTM $\boldsymbol{E}_{\rm L}$-I type (see Figs. 4, 6, and 9). It forms either for lower values of $\overline{E_{\rm L}}$, which is too small to compensate for the

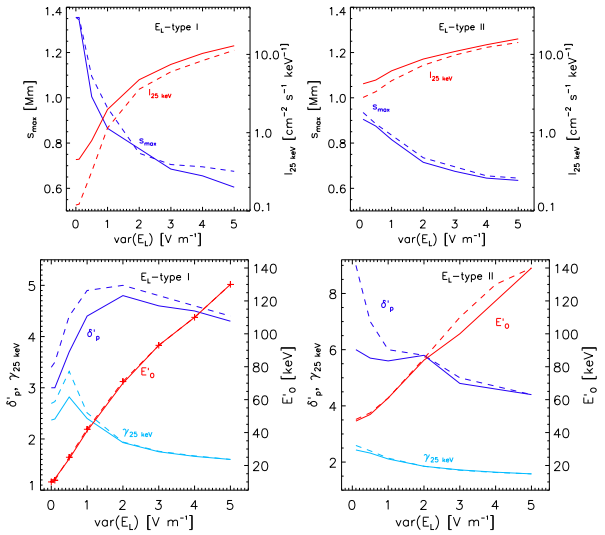

Fig. 12. LRTTM $\boldsymbol{E}_{\rm L}$-I (*left*) and $\boldsymbol{E}_{\rm L}$-II (*right*) (for $\overline{E_{\rm L}} = 0.1$ V m^{-1}) summary of calculated and fitted parameters of chromospheric bombardment for various values of var($E_{\rm L}$). *Top*: position of energy deposit maximum $s_{\rm max}$ and HXR intensity $I_{25\,\rm keV}$. *Bottom*: HXR spectral index $\gamma_{25\,\rm keV}$ and fitted electron beam spectral index $\delta'_{\rm p}$ and low-energy cutoff E'_0. The solid and dashed lines denote $M^{\rm FF}$ and $M^{\rm SU}$, respectively.

collisional energy losses of the electrons in the region above the lower boundary of the magnetic mirror, or for greater values of var($E_{\rm L}$), when the interactions of beam electrons with the stochastic component of $\boldsymbol{E}_{\rm L}$ lead to its formation. On the other hand, a new tail of particles is formed on energies from approximately 1 to 100 keV in the region under the lower boundary of the re-acceleration region where the re-accelerated particles are quickly thermalised (see the regions labelled L).

The energy deposits and HXR spectra for $\overline{E_{\rm L}} = 0.1$ V m^{-1} and various values of var($E_{\rm L}$) from 0 to 5 V m^{-1} are plotted in Fig. 14, and the parameters $\mathcal{E}_{\rm ch}$, $s_{\rm max}$, $I_{25\,\rm keV}$, and $\gamma_{25\,\rm keV}$ are displayed in the left-hand and right-hand panels of Figs. 11 and 12, respectively, and summarised in Table 3. The general behaviour of $\mathcal{E}_{\rm ch}$ and $s_{\rm max}$ is similar to the GRTTM of primary footpoint and LRTTM $\boldsymbol{E}_{\rm L}$-I type. They are very sensitive to the static component $\overline{E_{\rm L}}$ of the stochastic field and only moderately sensitive to the stochastic component var($E_{\rm L}$). Even for var($E_{\rm L}$) = 0 and $\overline{E_{\rm L}} = 0.1$ V m^{-1}, there is an appreciable increase in $\mathcal{E}_{\rm ch}$ (3.6× for the $M^{\rm FF}$ and 5.5× for the $M^{\rm SU}$ case) and a shift of $s_{\rm max}$ of approximately 450 km towards the photosphere and substantial growth in HXR production ($I_{25\,\rm keV}$ increases of by an order of magnitude for both initial μ-distributions relative to the CTTM with an identical initial flux). For the identical value of $\overline{E_{\rm L}}$ and the maximum value of var($E_{\rm L}$) = 5 V m^{-1}, the increase in $\mathcal{E}_{\rm ch}$ is 5.5× for the $M^{\rm FF}$ and 10× for the $M^{\rm SU}$ case, the shift of $s_{\rm max}$ towards the photosphere of approximately 750 km (for both initial μ-distributions), and a substantial increase in $I_{25\,\rm keV}$ (35× for the $M^{\rm FF}$ and almost 130× for the $M^{\rm SU}$ case) relative to the CTTM with an identical initial flux. The power-law index $\gamma_{25\,\rm keV}$ tends to harden with increasing var($E_{\rm L}$).

HXR spectra corresponding to the $\boldsymbol{E}_{\rm L}$-II type are distinct from the previous ones. Here, two re-accelerating processes are involved. The static component causes a significant increase in spectra at deka-keV energies, up to ∼40 keV, and a steep double break at energies above. Therefore, the corresponding fitted electron flux spectrum assuming pure CTTM shows quite a steep δ'_0 (see Fig. 12, bottom right). Such a steep double break is a consequence of a re-acceleration by a constant electric field. The energy at which it appears is related to the length of the re-acceleration region, i.e. the current sheet size. The larger the size, the steeper the double break and the higher energies at which it is located. The presence of the stochastic component introduces another shift of the double break to higher energies, likewise for the type I; as var($E_{\rm L}$) increases, the double break is less prominent. Consequently, E'_0 increases and δ'_0 decreases (see Figs. 12 and 14). When the stochastic component prevails, i.e. var($E_{\rm L}$) $\geq$ 2 V m^{-1}, the hard X-ray spectra are of similar spectral shape to the $\boldsymbol{E}_{\rm L}$-I model but more intense.

4. Conclusions

We studied modifications of the CTTM by considering two types of secondary particle acceleration: GRTTM and LRTTM. In both cases the re-acceleration takes place during the transport of non-thermal particles, which are primarily accelerated in the corona. According to Brown et al. (2009), such a re-acceleration generally reduces collisional energy loss and Coulomb scattering and increases the life-time and penetration depth of particles.

In the case of GRTTM, the spatially varying direct electric field spreading along the whole magnetic strand from first to second footpoint re-accelerates the beam electrons towards the primary footpoint and decelerates them towards the secondary footpoint, thus producing an asymmetric heating of footpoints. The low electric plasma conductivity and increased current density due to magnetic field convergence are the key constraints for the functionality of this mechanism. The model was studied for the mirror ratio $R_{\rm m} = 5$ and current densities $j \leq 6$ A m^{-2}. Significant re-acceleration is present for $j \gtrsim 3$ A m^{-2}, and for lower j the model is similar to CTTM. However, a question arises as to whether such current densities are realistic. Although the current densities derived from magnetic field observations are two orders of magnitude lower (Guo et al. 2013), in the magnetic rope, especially in their unstable phase at the beginning of the flare, the current density in some filaments could reach these values: see the processes studied in Gordovskyy & Browning (2011, 2012); Gordovskyy et al. (2013). On the other hand, a current filamentation also means a decrease in the area where this re-acceleration can operate effectively. Finally, the GRTTM model inherently introduces an asymmetry on opposite sites of the magnetic rope. More observations are needed to check that some asymmetrical X-ray sources are caused by this effect.

Two types of electric field were considered for LRTTM: a purely stochastic field var($E_{\rm L}$) $\leq$ 5 V m^{-1} ($\boldsymbol{E}_{\rm L}$-I type) and a combination of var($E_{\rm L}$) and a static component $\overline{E_{\rm L}} = 0.1$ V m^{-1} ($\boldsymbol{E}_{\rm L}$-II type). It has been shown that both types of electric fields produce a substantial secondary re-acceleration ($\boldsymbol{E}_{\rm L}$-I type for var($E_{\rm L}$) $\gtrsim$ 0.5 V m^{-1}, $\boldsymbol{E}_{\rm L}$-II type for all considered field parameters due to the static field component) with dominant energy propagating towards the photosphere.

Generally in all presented models, HXR spectra gets flatter below ∼30 keV and more intense on all energies as re-accelerating fields increase. The flattening then corresponds to an increase in the low-energy cutoff E'_0 of the fitted electron distribution. The effect of flattening of HXR spectra below the low-energy cutoff can be seen in Brown et al. (2008, Fig. 1e). Extremely flat HXR spectra (related to $E'_0 \gtrsim 50$ keV) were obtained for GRTTM of $j = 6$ A m^{-2} and LRTTM var($E_{\rm L}$) $\geq$ 2 V m^{-1} ($\boldsymbol{E}_{\rm L}$-I type). Such flat spectra or high values

A&A 563, A51 (2014)

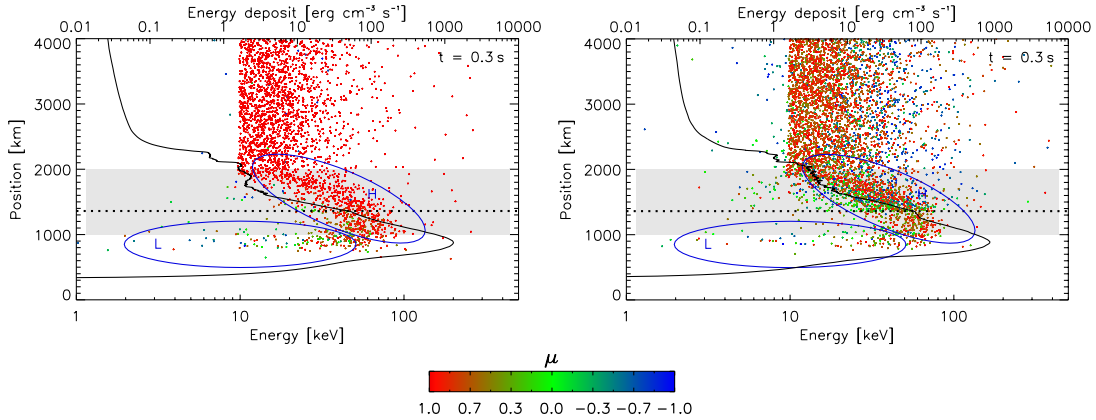

Fig. 13. LRTTM $\boldsymbol{E}_{\rm L}$-II type distribution functions of the non-thermal electron energies versus positions with a colour coded $M(\mu)$ corresponding to $\overline{E_{\rm L}} = 0.1$ V m^{-1} and var$(E_{\rm L}) = 0.5$ V m^{-1} in the VAL C atmosphere at time $t = 0.3$ s after the beam injection into the loop at its apex. *Left*: $M^{\rm FF}$, *right*: $M^{\rm SU}$. The solid lines indicate the instantaneous energy deposits corresponding to $\mathcal{F}_0/2 = 2.5 \times 10^9$ erg cm^{-2} s^{-1}, the dotted horizontal lines the bottom boundary of the magnetic mirror, the grey area the secondary re-acceleration region, and the blue ellipses labelled L and H denote tails in the particle distribution function. Only the vicinity of the footpoints is displayed.

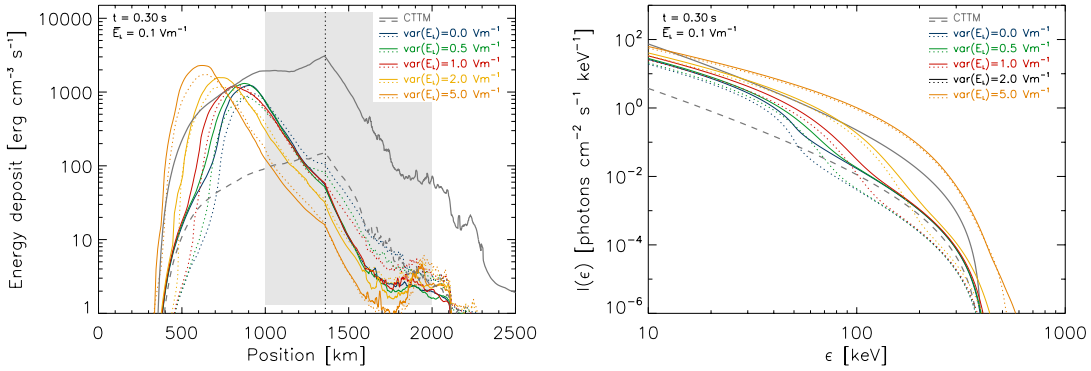

Fig. 14. LRTTM $\boldsymbol{E}_{\rm L}$-II type instantaneous energy deposits (*left*) and HXR spectra (*right*) for the VAL C atmosphere at $t = 0.3$ s. The solid ($M^{\rm FF}$) and dotted ($M^{\rm SU}$) blue, green, red, yellow, and orange lines correspond to $\overline{E_{\rm L}} = 0.1$ V m^{-1} and var$(E_{\rm L}) = 0.1, 0.5, 1, 2, 5$ V m^{-1}, respectively and energy flux $\mathcal{F}_0/2 = 2.5 \times 10^9$ erg cm^{-2} s^{-1}. The dashed and solid grey lines correspond to the CTTM with $\mathcal{F}_0/2 = 2.5 \times 10^9$ and 5×10^{10} erg cm^{-2} s^{-1}, respectively. The dotted straight vertical line indicates the bottom boundary of the magnetic mirror, the grey area the secondary re-acceleration region. The HXR spectra are integrated over one half of the loop.

of E_0' are not reported from the observation, therefore those j and var$(E_{\rm L})$ could represent limiting values. In addition, prominent double breaks at keV energies, present in the $\boldsymbol{E}_{\rm L}$-II cases, are not observed in HXR spectra. This suggests that our model of a constant re-accelerating field over a larger spatial scale, ∼1 Mm, is probably too simplistic.

For upper limit of model parameters, both models give similar results in several aspects (although the values are probably extreme, at least from the HXR signatures). At energies above 20 keV, the corresponding HXR spectra are more intense than the spectrum of pure CTTM with 20× higher initial energy flux. GRTTM gives a comparable total chromospheric energy deposit. For the LRTTM the total energy deposits reach only about 30% of the latter value. The re-acceleration also leads to spatial redistribution of the chromospheric energy deposit with the bulk energy being deposited much deeper into the chromosphere and into a narrower layer in comparison to the CTTM. The heights of the energy-deposit maxima are thus substantially shifted towards the photosphere (of ≈800 km for both models). It is a consequence of the re-accelerating fields pushing the non-thermal electrons under the magnetic mirror and under the beam-stopping depth corresponding to the CTTM. The height above the photosphere decreases with both the current density for the GRTTM and with the mean value and variance of the stochastic field for the LRTTM. For the upper values of model parameters, we obtained the heights of energy-deposit maxima as only approximately 600 km. This is not far from the upper limits on heights of the flare white-light sources (305 ± 170 km and 195 ± 70 km) found from observations (Martínez Oliveros et al. 2012).

To demonstrate how the secondary accelerating processes may lead to artificially high CTTM input energy fluxes, we followed a standard forward-fitting procedure for determining the injected electron spectrum from an observed X-ray spectrum. Although the spectral fitting does not take any re-acceleration into account, the fitted $\mathcal{F}_0'$ agrees well (within 30%) with $\mathcal{E}_{\rm ch}$ in all simulations. This value can differ substantially from the injected total energy flux, therefore the fitted total energy flux (under assumption of pure CTTM) is related more to the energy

deposit of re-accelerated particles than to the injected energy flux.

In general, both the considered models with secondary re-acceleration, GRTTM and LRTTM, allow loosening the requirements on the efficiency of coronal accelerator, thus decreasing the total number of particles involved in the impulsive phase of flares and the magnitude of the electron flux transported from the corona towards the photosphere, as needed to explain the observed HXR footpoint intensities. These findings agree with the results obtained by Brown et al. (2009) and Turkmani et al. (2006, 2005).

Acknowledgements. This work was supported by grants P209/10/1680 and P209/12/0103 of the Grant Agency of the Czech Republic. The research at the Astronomical Institute, ASČR, leading to these results has received funding from the European Commission's Seventh Framework Programme (FP7) under the grant agreement SWIFF (project number 263340).

References

Abbett, W. P., & Hawley, S. L. 1999, ApJ, 521, 906
Allred, J. C., Hawley, S. L., Abbett, W. P., & Carlsson, M. 2005, ApJ, 630, 573
Bai, T. 1982, ApJ, 259, 341
Bárta, M., Büchner, J., Karlický, M., & Kotrč, P. 2011a, ApJ, 730, 47
Bárta, M., Büchner, J., Karlický, M., & Skála, J. 2011b, ApJ, 737, 24
Bastian, T. S., Benz, A. O., & Gary, D. E. 1998, ARA&A, 36, 131
Battaglia, M., Kontar, E. P., Fletcher, L., & MacKinnon, A. L. 2012, ApJ, 752, 4
Brown, J. C. 1971, Sol. Phys., 18, 489
Brown, J. C., & Melrose, D. B. 1977, Sol. Phys., 52, 117
Brown, J. C., Kašparová, J., Massone, A. M., & Piana, M. 2008, A&A, 486, 1023
Brown, J. C., Turkmani, R., Kontar, E. P., MacKinnon, A. L., & Vlahos, L. 2009, A&A, 508, 993
Dennis, B. R., & Zarro, D. M. 1993, Sol. Phys., 146, 177
Elwert, G. 1939, Ann. Physik, 34, 413
Emslie, A. G. 1978, ApJ, 224, 241
Fletcher, L., & Hudson, H. S. 2008, ApJ, 675, 1645
Gordovskyy, M., & Browning, P. K. 2011, ApJ, 729, 101
Gordovskyy, M., & Browning, P. K. 2012, Sol. Phys., 277, 299
Gordovskyy, M., Browning, P. K., Kontar, E. P., & Bian, N. H. 2013, Sol. Phys., 284, 489
Guo, Y., Démoulin, P., Schmieder, B., et al. 2013, A&A, 555, A19
Haug, E. 1997, A&A, 326, 417
Heyvaerts, J. 1981, in Solar Flare Magnetohydrodynamics, ed. E., Priest (New York, USA: Gordon and Breach Science Publishers), 429
Holman, G. D. 2012, ApJ, 745, 52
Karlický, M. 1995, A&A, 298, 913
Karlický, M. 2009, ApJ, 690, 189
Karlický, M., & Henoux, J.-C. 1993, A&A, 278, 627
Karlický, M., & Kliem, B. 2010, Sol. Phys., 266, 71
Karlický, M., & Kontar, E. P. 2012, A&A, 544, A148
Kašparová, J., Varady, M., Heinzel, P., Karlický, M., & Moravec, Z. 2009, A&A, 499, 923
Kliem, B., Linton, M. G., Török, T., & Karlický, M. 2010, Sol. Phys., 266, 91
Kopp, R. A., & Pneuman, G. W. 1976, Sol. Phys., 50, 85
Kosugi, T., Makishima, K., Murakami, T., et al. 1991, Sol. Phys., 136, 17
Kubát, J., & Karlický, M. 1986, Bull. Astr. Inst. Czechosl., 37, 155
Kuijpers, J., van der Post, P., & Slottje, C. 1981, A&A, 103, 331
Lin, R. P., Dennis, B. R., Hurford, G. J., et al. 2002, Sol. Phys., 210, 3
MacKinnon, A. L., & Craig, I. J. D. 1991, A&A, 251, 693
Martínez Oliveros, J.-C., Hudson, H. S., Hurford, G. J., et al. 2012, ApJ, 753, L26
Matthews, S. A., Brown, J. C., & Melrose, D. B. 1996, A&A, 305, L49
Nagai, F., & Emslie, A. G. 1984, ApJ, 279, 896
Peratt, A. L. 1992, in Physics of the Plasma Universe (Berlin, Heidelberg, New York: Springer-Verlag), 294
Radziszewski, K., Rudawy, P., & Phillips, K. J. H. 2007, A&A, 461, 303
Radziszewski, K., Rudawy, P., & Phillips, K. J. H. 2011, A&A, 535, A123
Shibata, K. 1996, Adv. Space Res., 17, 9
Shibata, K., & Tanuma, S. 2001, Earth Planets Space, 53, 473
Sturrock, P. A. 1968, in Structure and Development of Solar Active Regions, ed. K. O. Kiepenheuer, IAU Symp., 35, 471
Turkmani, R., & Brown, J. 2012, in ASP Conf. Ser. 454, eds. T. Sekii, T. Watanabe, & T. Sakurai, 349
Turkmani, R., Vlahos, L., Galsgaard, K., Cargill, P. J., & Isliker, H. 2005, ApJ, 620, L59
Turkmani, R., Cargill, P. J., Galsgaard, K., Vlahos, L., & Isliker, H. 2006, A&A, 449, 749
van den Oord, G. H. J. 1990, A&A, 234, 496
Varady, M., Kašparová, J., Karlický, M., Heinzel, P., & Moravec, Z. 2005, Hvar Observatory Bulletin, 29, 167
Varady, M., Kašparová, J., Moravec, Z., Heinzel, P., & Karlický, M. 2010, IEEE Trans. Plasma Sci., 38, 2249
Varady, M., Moravec, Z., Karlický, M., & Kašparová, J. 2013, J. Phys. Conf. Ser., 440, 012013
Vernazza, J. E., Avrett, E. H., & Loeser, R. 1981, ApJS, 45, 635
Winter, H. D., Martens, P., & Reeves, K. K. 2011, ApJ, 735, 103

ISSN 1845–8319

SIMULATIONS OF HXR FOOT-POINT SOURCE SIZES FOR MODIFIED THICK-TARGET MODELS

Z. MORAVEC[1], M. VARADY[1,2], M. KARLICKÝ[2] and J. KAŠPAROVÁ[2]

[1] *Department of Physics, Faculty of Science, J. E. Purkyně University, České mládeže 8, 400 96 Ústí nad Labem, Czech Republic*
[2] *Astronomický ústav Akademie věd České republiky, v.v.i, Fričova 298, 251 65 Ondřejov, Czech Republic*

Abstract. We study vertical sizes of foot-point hard X-ray (HXR) sources using a relativistic test particle approach in a flare loop with a converging magnetic field. We compare results for the Collisional Thick Target Model (CTTM) with recently proposed modifications of the CTTM comprising a secondary acceleration of beam electrons. Our preliminary results indicate that none of the proposed modifications of the CTTM can explain the observed sizes of the HXR sources in a single loop flare scenario.

Key words: Sun: solar flares – hard X-rays – foot-point sources

1. Introduction

The recent RHESSI observations enabled to measure the vertical size (along the magnetic field-lines) of flare foot-point HXR sources. The measurements of Battaglia et al. (2012) showed that the vertical size spans the range from 1.3 to 8 arcseconds. These values are in contradiction with the predictions given by the Collisional Thick Target Model (CTTM, Brown 1971) which predicts values up to a factor 4 smaller (Battaglia et al. 2011).

In this work we compare foot-point sizes given by the CTTM with those given by two modifications of the CTTM: the Local Re-acceleration Thick Target Model (LRTTM, Brown et al. 2009) and the Global Re-acceleration Thick Target Model (GRTTM, discussed in Karlický 1995). The concept of both modified models is discussed in Varady et al. (2012).

2. Model description

In all our models, an initial electron beam with power-law index $\delta = 3$, low-energy cutoff $E_0 = 10$ keV, high-energy cutoff $E_1 = 400$ keV, total

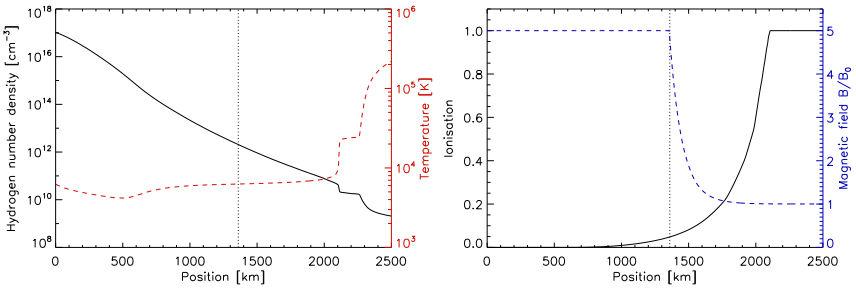

Figure 1: *Left:* The hydrogen number density (solid) and temperature (dashed) along the magnetic field-line in the lower atmosphere. *Right:* The hydrogen ionisation (solid) and relative magnetic field strength (dashed) along a magnetic field-line in the lower atmosphere. The dotted vertical lines indicate position of the bottom of the magnetic mirror.

energy flux $\mathcal{F}_0 = 2.5 \times 10^9$ erg cm^{-2} s^{-1} and uniform distribution of the pitch angle cosine $\mu_0 = \cos\vartheta \in (0, 0.5)$, is accelerated at the primary (coronal) acceleration site (for details see Kašparová et al. 2009, Varady et al. 2010). Using a test particle approach, the beam then propagates through a static VAL C atmosphere (Vernazza et al. 1981, see Fig. 1) in a converging magnetic field with mirror ratio $R_m = 5$ (Fig. 1 right). The bottom of the magnetic mirror at 1360 km (see vertical lines in Fig. 1) corresponds to temperature $T = 6270$ K. The HXR flux produced in the vicinity of loop foot-points is computed according to Brown (1971) using the cross-section given by Haugh (1997). In this work we present steady state HXR fluxes at time $t = 0.5$ s since the beam injection into the loop at its apex for three models:

1. **CTTM:** Beam electrons are accelerated at the primary (coronal) acceleration site and interact with the ambient plasma purely via Coulomb collisions.

2. **GRTTM:** We assume that helicity of the pre-flare magnetic fields results in the presence of electric currents in the flare loop before and during the impulsive phase (Karlický 1995). The electric currents are fragmented into thin insulated current threads and the current densities in the individual threads are below the thresholds of any

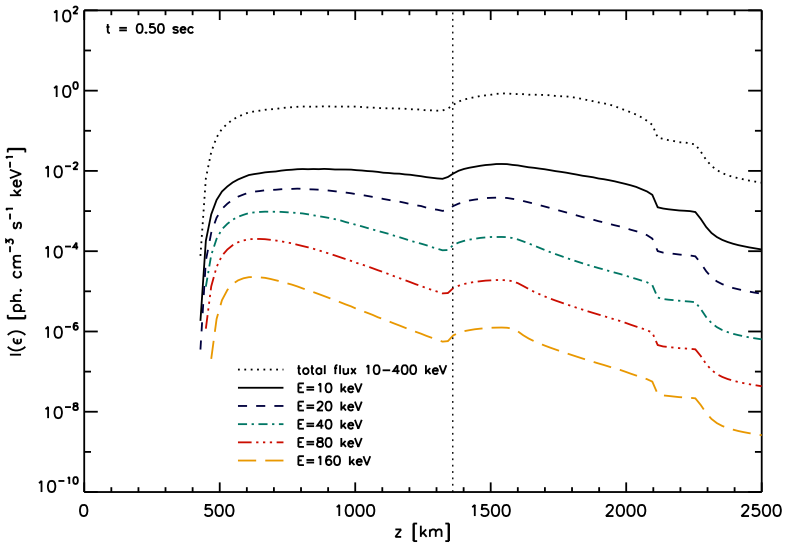

Figure 2: HXR photon flux as a function of height for selected photon energies in the CTTM. The dotted vertical line indicates the position of the bottom of the magnetic mirror. The total photon flux per unit height is given in photons cm^{-3} s^{-1}.

current instabilities. The beam electrons propagate along the magnetic field-lines corresponding to the threads and the current densities j in the individual threads produce resistive electric fields $\mathbf{E} = \mathbf{j}/\sigma$. We study a case of a single thread using the classical plasma conductivity σ and $j = 6$ A m^{-2}.

3. **LRTTM:** We assume normally distributed stochastic electric fields in the directions parallel and antiparallel relative to the loop axis, i.e. a simplified model of the electric field distribution due to the current sheet cascade in a randomly stressed magnetic loop in the chromosphere (Brown et al. 2009, Turkmani et al. 2006). In the presented model the mean value of the stochastic field is $E_{mean} = 0$ and its variance is var$(E) = 1$ V m^{-1}.

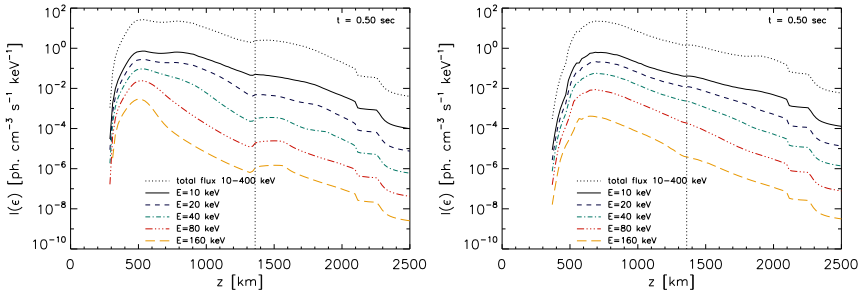

Figure 3: HXR photon flux as a function of height for selected photon energies in the GRTTM (left panel) and LRTTM (right panel). The line coding is the same as in Fig. 2.

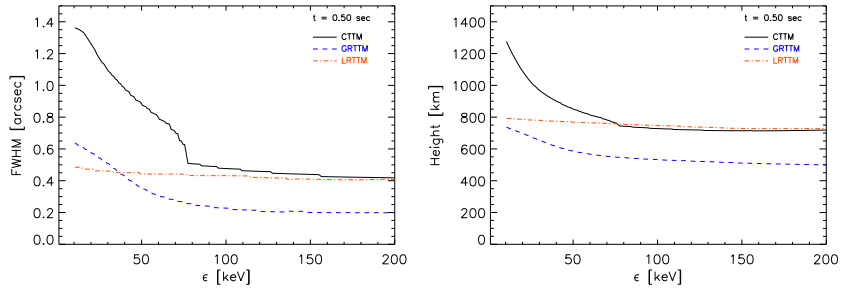

Figure 4: FWHM vertical size of the foot-point source (left panel) and the position of the HXR maximum emission (right panel) versus photon energy for the three presented models – CTTM, GRTTM and LRTTM.

3. Results

The HXR photon fluxes as a function of height above the photosphere are shown in Fig. 2 and 3. From these profiles, the HXR source height and vertical size are calculated as the first and second moments, respectively. The results are shown in Fig. 4.

The vertical size of HXR sources in the CTTM is about 1.3 arcsec for energies 10 – 20 keV and the source size decreases with increasing energy down to 0.4 – 0.5 arcsec for energies above 80 keV.

The GRTTM gives the sizes of HXR sources significantly smaller in com-

parison with the CTTM. The difference is more than 50 % for all energies.

For the LRTTM we found the HXR sources to be more compact on all energies with a typical vertical size 0.4 – 0.5 arcsec, which is less then 50 % of the size for energies below 50 keV, but comparable with the CTTM results for energies above 80 keV.

The heights of the HXR emission maxima for GRTTM and LRTTM are sensitive to j and var(E), respectively. For the GRTTM, the heights of maxima are significantly lower than those for the CTTM for all energies. For the LRTTM, the heights of the maxima are lower for energies 10 – 70 keV than those for the CTTM. For the LRTTM and energies above 70 keV, the heights of the maxima are roughly the same as for the CTTM. For energies 10 – 200 keV the CTTM gives the source height 700 – 1300 km, the GRTTM 500 – 700 km and the LRTTM 750 km. With increasing values of both parameters (j and var(E)) the heights of the sources above the photosphere decrease.

4. Conclusions

Our preliminary results indicate that the heights above the photosphere of the HXR emission maxima for the GRTTM are more than 200 km lower than those for the CTTM for all energies. None of the proposed modifications of the CTTM in frame of a single monolithic flare loop can explain the observed sizes of the HXR sources. Taking the multi-threaded nature of the chromosphere into account could converge the modeled values to observations (Kontar et al. 2010).

Acknowledgements

This work was supported by grants P209/10/1680 and P209/12/0103 of the Grant Agency of the Czech Republic.

References

Battaglia, M., Kontar, E.P., 2011, *Astrophys. J.* **735**, 42.

Battaglia, M., Kontar, E.P., Fletcher, L., and MacKinnon, A.L., 2012, *Astrophys. J.* **752**, 4.

Brown, J.C., 1971, *Solar Phys.* **18**, 489.

Brown, J.C., Turkmani, R., Kontar, E.P., MacKinnon A.L., and Vlahos, L., 2009, *Astron. Astrophys.* **508**, 993.

Haugh, E., 1997, *Astron. Astrophys.* **326**, 417.

Karlický, J., 1995, *Astron. Astrophys.* **298**, 913.

Kašparová, J., Varady, M., Heinzel, P., Karlický, M., and Moravec, Z., 2009, *Astron. Astrophys.* **499**, 923.

Kontar, E.P., Hannah, I.G., Jeffrey, L.S., and Battaglia, M., 2010, *Astrophys. J.* **717**, 250.

Turkmani, R., Vlahos, L., Galsgaard, K., Cargill, P., J., and Isliker, H., 2005, *Astrophys. J.* **620**, L59.

Varady, M., Kašparová, J., Moravec, Z., Heinzel, P., and Karlický, M., 2010, *IEEE Transactions on Plasma Science* **38**, 2249.

Varady, M., Karlický, M., Moravec, Z., Kašparová, J., 2012, *The Fifth Hinode Science Meeting "Explore the active Sun", ASP Conference Series* **456**, 203.

Vernazza, J.E. et al., 1981, *Astrophys. J., Suppl. Ser.* **45**, 635.

Eclipse on the Coral Sea: Cycle 24 Ascending (GONG 2012, LWS/SDO-5, and SOHO 27) IOP Publishing
Journal of Physics: Conference Series **440** (2013) 012013 doi:10.1088/1742-6596/440/1/012013

Observational consequences of the local re-acceleration thick-target model

M Varady[1], Z Moravec[1], M Karlický[2], J Kašparová[2]

[1]Faculty of Science, J.E. Purkyně University, Physics Department, České mládeže 8, 400 75 Ústí nad Labem, Czech Republic

[2]Astronomical Institute of the Academy of Sciences of the Czech Republic, v.v.i., 251 65 Ondřejov , Czech Republic

E-mail: mvarady@physics.ujep.cz

Abstract. In our contribution we compare the efficiency of the hard X-ray production and the vertical sizes and positions of the hard X-ray sources for the classical collisional thick-target model and for its recently proposed modification, the local re-acceleration thick-target model. The latter model has been proposed in order to ease some of the severe theoretical problems of the collisional thick-target model related to interpretation of the observational properties of the foot-point HXR sources in solar flares. The results are obtained using a relativistic test-particle approach for a fully ionised atmosphere with a converging magnetic field and a single (compact) flare loop.

1. Introduction

The Collisional Thick-Target Model (CTTM) of the impulsive phase of solar flares [1] presented for many years a quite successful tool to interpret the fundamental processes related to the energy deposition and hard X-ray (HXR) production at the foot-point regions of flare loops due to the interaction of chromospheric plasma with electron beams. On the other hand, in order to explain the energetics of flares and observed intensities of HXR, many serious theoretical problems emerged (see [2] and the Introduction in [3]), especially in combination with the idea that the beam acceleration site corresponds to the coronal reconnection site [4], [5], [6] and consequently with the inevitability to transport enormous fluxes of accelerated charged particles from the corona to the thick-target region. Moreover novel RHESSI measurements of HXR chromospheric albedo [7] or of the vertical sizes and positions of the HXR sources are inconsistent with the predictions given by the CTTM [8], [9].

To resolve the discrepancies a modification of the CTTM known as the Local Re-acceleration Thick-Target Model (LRTTM) has recently been proposed [3], [10], [11]. The model assumes an existence of a secondary re-acceleration region located within the thick-target region in the chromosphere. The non-thermal electrons initially accelerated at the primary coronal acceleration site experience, in addition to the energy losses and scattering due to the Coulomb collisions, also sequences of re-acceleration events at the secondary re-acceleration region due to the stochastic electric fields generated in the current sheet cascades [10], [11] excited by random photospheric motions.

In our contribution we concentrate on a comparison of outcomes of the chromospheric bombardment by electron beams with a power-law spectrum modelled in frame of the CTTM

Eclipse on the Coral Sea: Cycle 24 Ascending (GONG 2012, LWS/SDO-5, and SOHO 27) IOP Publishing
Journal of Physics: Conference Series **440** (2013) 012013 doi:10.1088/1742-6596/440/1/012013

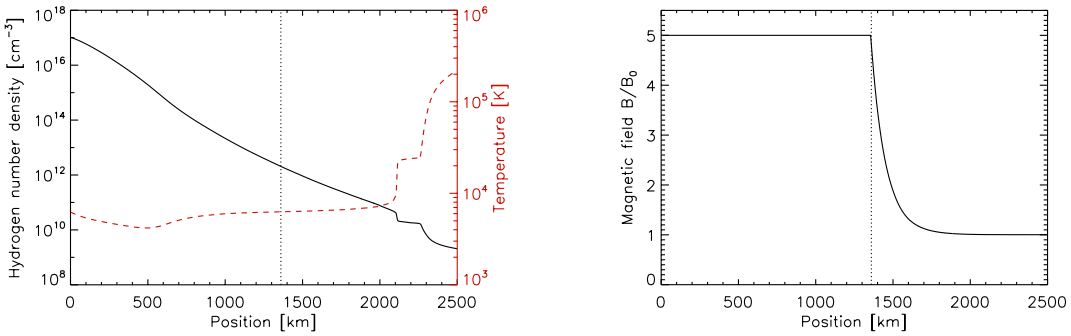

Figure 1. Left: Density (black solid line) and temperature (red dashed line) profiles of the VAL C atmosphere [12]. The dotted line indicates the bottom boundary of the magnetic mirror. Right: Relative magnetic field strength along the loop. Only the lower part of the atmosphere is plotted.

and LRTTM. We compare the non-thermal electron distribution functions in the vicinity of the thick-target region, corresponding chromospheric energy deposits, HXR production, spectra and vertical sizes and heights above the photosphere (corresponding to $\tau = 1$ at 5000 Å) of the HXR foot-point sources calculated for a fully ionised VAL C atmosphere [12] and a single (compact) loop with a converging magnetic field towards the photosphere. The results are obtained using a relativistic test-particle code [13], [14], [15].

2. Model description

The starting point of our simulations is a generation of an electron beam with a power-law spectrum and with parameters: power-law index $\delta = 3$, low-energy cutoff $E_0 = 10$ keV, high-energy cutoff $E_1 = 400$ keV, initial energy flux $\mathcal{F}_0 = 2.5 \times 10^9$ erg cm^{-2} s^{-1} (or 5×10^{10} erg cm^{-2} s^{-1} – the reference flux for the CTTM) and a normalised semi-uniform initial distribution of the pitch angle cosine $\mu_0 = \cos\vartheta \in (0.5, 1)$. In order to demonstrate the potential of secondary re-acceleration we selected a very small value of $\mathcal{F}_0$ in context of flare physics. As the target atmosphere in the presented approximation is static, by changing $\mathcal{F}_0$ the vertical structure of the distribution function remains the same and the energy deposits and HXR intensities scale linearly. In our model we assume that the beam is accelerated at the primary acceleration site localised in the corona. Using a relativistic test-particle code [13], [14], [15], we model the propagation of beam electrons through a fully ionised, static atmosphere with a converging magnetic field with the mirror ratio $R_m = 5$ (see right panel of Fig. 1). The temperature and density profiles of the atmosphere correspond to the VAL C model [12] (see left panel of Fig. 1) with an extension into the corona, the ionisation is artificially set to one in the whole atmosphere. The code calculates the corresponding Coulomb collisional energy losses and scattering and the effects of the magnetic mirroring in the converging field for the CTTM. For the LRTTM it also includes the effects of the secondary re-acceleration events due to the presence of the stochastic electric fields in the vicinity of the thick-target region. Only one-half of the loop is considered.

We assume normally distributed stochastic electric fields in the directions parallel and antiparallel relative to the loop axis, i.e. a simplified model of the electric field distribution due to the current sheet cascade in a randomly stressed magnetic loop in the chromosphere [3], [11]. We present results for zero mean value of the stochastic field and for its variances var$(E) = 0.5, 1$ and 5 V m^{-1}. The secondary re-acceleration region is placed into the chromosphere in range of

Eclipse on the Coral Sea: Cycle 24 Ascending (GONG 2012, LWS/SDO-5, and SOHO 27) IOP Publishing
Journal of Physics: Conference Series **440** (2013) 012013 doi:10.1088/1742-6596/440/1/012013

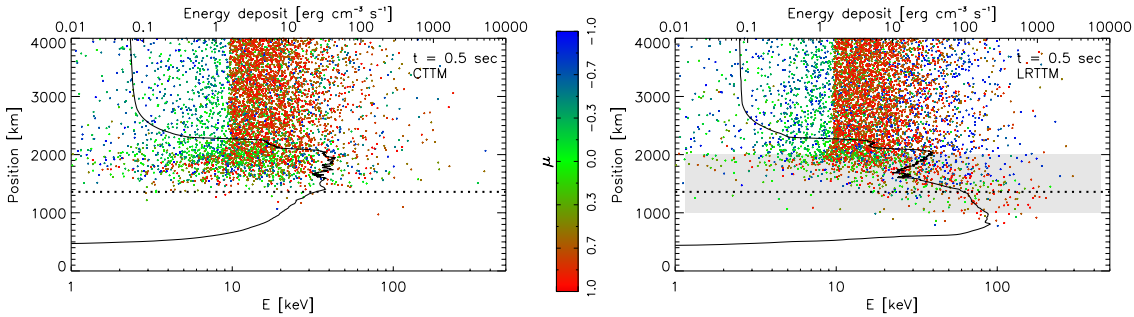

Figure 2. The distribution functions of non-thermal electron energies versus positions with a colour coded μ-distribution for the classical the CTTM (left panel) and LRTTM (right panel) for $\mathrm{var}(E) = 1$ V m^{-1} at time $t = 0.5$ s after the beam injection into the loop at its apex. The solid lines indicate the instantaneous energy deposit corresponding to $\mathcal{F}_0 = 2.5 \times 10^9$ erg cm^{-3} s^{-1} in the logarithmic scale. The dotted horizontal line indicates the bottom boundary of the magnetic mirror, the grey area corresponds the secondary re-acceleration region. Only the lower parts of the loop are captured.

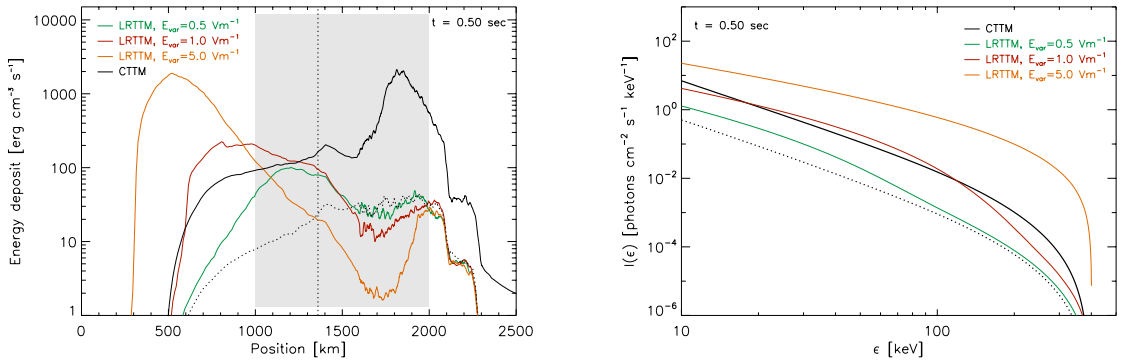

Figure 3. The energy deposits (left) and HXR spectra (right) at $t = 0.5$ s. The green, red and orange lines correspond to the LRTTM with the initial beam energy flux $\mathcal{F}_0 = 2.5 \times 10^9$ erg cm^{-2} s^{-1} and field variances $\mathrm{var}(E) = 0.5, 1$ and 5 V m^{-1}, respectively. The black lines indicate the energy deposits and HXR spectra for the CTTM, where the black solid and dotted lines correspond to the initial energy fluxes $\mathcal{F}_0 = 5 \times 10^{10}$ erg cm^{-2} s^{-1} and 2.5×10^9 erg cm^{-2} s^{-1}, respectively. The grey area indicates the secondary re-acceleration region, the vertical dotted line the bottom boundary of the magnetic mirror.

heights from 1000 km to 2000 km.

The HXR fluxes and spectra produced in the vicinity of loop foot-points are computed according to [1] using the semi-relativistic cross-section given by [16]. All the results are presented at time $t = 0.5$ s after the beam injection into the loop at its apex, when the model is close to a quasi-steady state.

Eclipse on the Coral Sea: Cycle 24 Ascending (GONG 2012, LWS/SDO-5, and SOHO 27) IOP Publishing
Journal of Physics: Conference Series **440** (2013) 012013 doi:10.1088/1742-6596/440/1/012013

3. Results

The distribution functions of non-thermal electrons for the CTTM and LRTTM are shown in left and right panel of Fig. 2, respectively. The electrons propagating from the loop apex towards the photosphere ($\mu \sim 1$) are coded with shades of red, the electrons with $\mu \sim 0$ are coded with shades of green and the electrons reflected by the magnetic mirror or backscattered ($\mu \sim -1$) are coded with shades of blue. For the CTTM case, it is evident that the majority of electrons arriving from the primary acceleration site (colour coded red to brown), into the higher density region between the upper chromosphere ($s \approx 2000$ km) and the bottom boundary of the magnetic mirror ($s = 1360$ km), quickly lose their energies and increase their pitch angles due to the Coulomb collisions and the effects of converging magnetic field. As a consequence a low energy tail is formed in the chromosphere above the bottom boundary of the magnetic mirror. The tail is dominated by particles of $\mu \sim 0$ and these particles either completely thermalise their kinetic energies or are reflected by the magnetic mirror back towards the second foot-point. Only few particles with higher energies penetrate behind the bottom boundary of the magnetic mirror.

The right panel of Fig. 2 shows the distribution function for the LRTTM. Two tails in the distribution function can be identified. A low energy tail corresponding to the tail identified in the distribution function for the CTTM, but less distinct, and a tail aiming towards high energies, spatially located within the re-acceleration region. This tail is formed by the particles re-accelerated by the stochastic electric fields. Another obvious effect of the stochastic fields is the enhancement of the number of backscattered electrons, particularly at higher energies. Comparing the corresponding energy deposits, it is apparent that the presence of the re-acceleration field substantially increases the energy deposit and shifts its maximum towards deeper layers.

The energy deposits for several variances of the stochastic field are shown in the left panel of Fig. 3. The model indicates that an increase of var(E) results in a dramatic increase of the energy deposit into the lower atmosphere and also the maxima of the energy deposits can be shifted to very deep layers (see the deposit for var(E) = 5 V m^{-1}). If the deposits are integrated over the chromosphere and photosphere we can conclude that the latter mentioned variance of stochastic field can increase the integrated deposit of almost one and half order in comparison with the deposit obtained using the CTTM and equal initial beam energy flux (dotted black line in the left panel of Fig. 3).

In flares the non-thermal electron distribution functions, the spatial position, and the extent of the energy deposits are influenced by the instantaneous state of the target flare atmosphere, in particular by the density profile of the chromosphere, which corresponds to the history of flare heating [14], [17], [18]. Due to the interaction of the low-energy electrons, which are predominant in the beam, with the evaporated flare plasma a shift of their penetration depth higher into the atmosphere can be expected. Similar effects would be also present using a static flare chromosphere (e.g. models F1 or F2 [19]).

The corresponding HXR spectra are shown in the right panel of Fig. 3. The HXR intensities and power-law indices are dependent on the values of var(E). With increasing variances $I_{10\,\mathrm{keV}}$ (the intensity at 10 keV) increases and the power-law indices harden. Comparing the intensity $I_{10\,\mathrm{keV}}$ for the LRTTM with var(E) = 5 V m^{-1} and for the CTTM with equal initial beam energy flux (dotted black line in the right panel of Fig. 3) we again obtain an increase in $I_{10\,\mathrm{keV}}$ of one and half order.

The HXR photon fluxes at various energies as a function of height above the photosphere for the CTTM and LRTTM are shown in Fig. 4. These profiles are used to calculate the HXR source heights and vertical sizes as the profile first and second moments, respectively. It is apparent that the placement and parameters of the magnetic mirror strongly influence the size and position of the CTTM HXR source. The results are shown in Fig. 5. The vertical sizes of

Eclipse on the Coral Sea: Cycle 24 Ascending (GONG 2012, LWS/SDO-5, and SOHO 27) IOP Publishing
Journal of Physics: Conference Series **440** (2013) 012013 doi:10.1088/1742-6596/440/1/012013

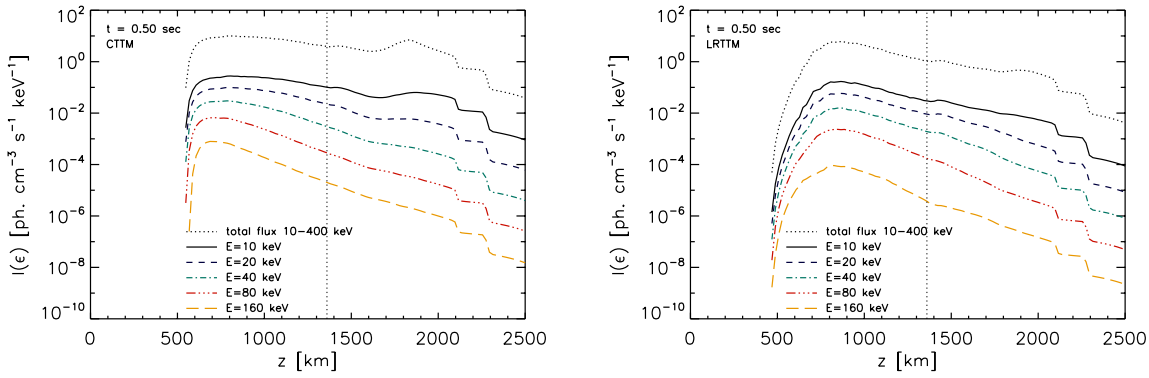

Figure 4. HXR photon flux emanating from the thick-target region as a function of height for selected photon energies (colour coded). Left for the CTTM, right for the LRTTM and $\mathrm{var}(E) = 1\ \mathrm{V\,m^{-1}}$. The dotted vertical line indicates the position of the bottom boundary of the magnetic mirror.

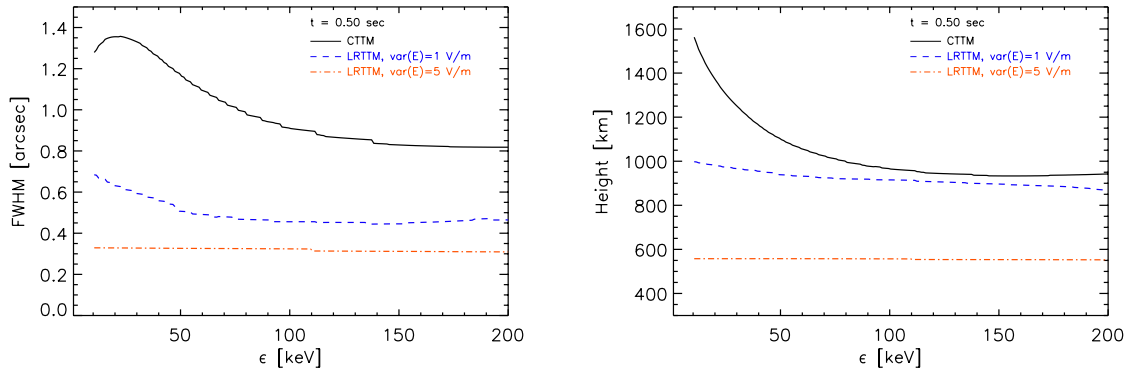

Figure 5. FWHM vertical sizes of the foot-point HXR sources (left panels) and the positions of the HXR emission maxima (right panels) versus photon energy for the CTTM (black solid lines) and the LRTTM (red dash-dotted lines) with $\mathrm{var}(E) = 1\ \mathrm{V\,m^{-1}}$ (upper panels) and $\mathrm{var}(E) = 5\ \mathrm{V\,m^{-1}}$ (lower panels).

HXR sources for the CTTM (left panel of Fig. 5 solid black lines) are about 1.2 arcsec for energies 10 – 30 keV. The source sizes decrease with increasing energy down to approximately 0.8 arcsec for energies above approximately 130 keV. For the LRTTM we found the HXR sources to be much more compact with increasing $\mathrm{var}(E)$ on all energies (compare dashed blue and dashed-dotted red lines in the left panel of Fig. 5) with a typical vertical source size 0.5 – 0.7 arcsec for $\mathrm{var}(E) = 1$ V m^{-1} and approximately 0.3 arcsec for $\mathrm{var}(E) = 5$ V m^{-1} on all energies.

Also the heights of the HXR emission maxima for the LRTTM are sensitive to the variance of stochastic field. With increasing $\mathrm{var}(E)$ the maxima tend to be placed deeper in the atmosphere (compare the blue dashed and red dash-dotted lines in the right panel of Fig. 5). The height of the HXR emission maximum for $\mathrm{var}(E) = 1$ V m^{-1} is 1000 – 900 km for all energies. It corresponds to the height of the CTTM emission maximum for energies above 90 keV. The height for $\mathrm{var}(E) = 5$ V m^{-1} is even only about 550 km for all energies and the source is thus much deeper than the CTTM source on all energies.

Eclipse on the Coral Sea: Cycle 24 Ascending (GONG 2012, LWS/SDO-5, and SOHO 27) IOP Publishing
Journal of Physics: Conference Series **440** (2013) 012013 doi:10.1088/1742-6596/440/1/012013

4. Conclusions

It has been shown that the presence of secondary re-acceleration in the region close to the flare loop foot-points reduces by one or one and half orders of magnitude (depending on the stochastic field parameters) the particle flux from the corona required to explain the observed HXR foot-point intensities. It also decreases the vertical size of the foot-point HXR sources. While the first findings agree with the results obtained by [3], [10], [11], the latter presents a problem.

Namely, the vertical sizes of HXR sources computed for the LRTTM are only 0.5 – 0.7 arcsec for $\mathrm{var}(E) = 1$ V m^{-1}, and even only 0.3 arcsec for $\mathrm{var}(E) = 5$ V m^{-1} on all energies. These values are much smaller than those obtained from the recent RHESSI observations (1.3 – 8 arcsec), see [9] and [8]. However, a comparison of the vertical sizes of X-ray sources for the LRTTM and CTTM models together with the multi-threaded chromosphere [20] offer a solution. Besides different densities in the multi-thread structure of the flaring chromosphere (which increases the vertical source size), in different threads a different distribution of the localised electric field can be expected; even with zero electric field (as in the case of the CTTM model). Therefore, integrating the vertical sizes of HXR sources for both considered models (LRTTM and CTTM) the observed vertical source sizes might be obtained. This suggestion will be tested in future models.

The heights of the HXR emission maxima for the LRTTM are in comparison with the CTTM substantially shifted towards the photosphere. The height above the photosphere, corresponding to height 0 km in the VAL C atmosphere model [12], decreases with the variance of the stochastic field. For $\mathrm{var}(E) = 5$ V m^{-1} we obtained the source height only approximately 550 km, which is not far from the heights of the white-light sources (305 ± 170 km and 195 ± 70 km) found from observations of white-light flares [21].

5. Acknowledgments

This work was supported by grants P209/10/1680 and P209/12/0103 of the Grant Agency of the Czech Republic. The research at the Astronomical Institute, ASČR leading to these results has received funding from the European Commission's Seventh Framework Programme (FP7) under the grant agreement SWIFT (project number 263340).

References

[1] Brown J C 1971 *Sol. Phys.* **18** 489
[2] Brown J C, Karlicky M, MacKinnon A L and van den Oord G H J 1990 *ApJS* **73** 343–348
[3] Brown J C, Turkmani R, Kontar E P, MacKinnon A L and Vlahos L 2009 *A&A* **508** 993–1000
[4] Sturrock P A 1968 A Model of Solar Flares *Structure and Development of Solar Active Regions* (*IAU Symposium* vol 35) ed Kiepenheuer K O p 471
[5] Kopp R A and Pneuman G W 1976 *Sol. Phys.* **50** 85–98
[6] Shibata K 1996 *Advances in Space Research* **17** 9
[7] Kontar E P and Brown J C 2006 *ApJ* **653** L149–L152 (*Preprint* `arXiv:astro-ph/0611170`)
[8] Battaglia M, Kontar E P, Fletcher L and MacKinnon A L 2012 *ApJ* **752** 4
[9] Battaglia M and Kontar E P 2011 *ApJ* **735** 42 (*Preprint* `1104.2997`)
[10] Turkmani R, Vlahos L, Galsgaard K, Cargill P J and Isliker H 2005 *ApJ* **620** L59
[11] Turkmani R, Cargill P J, Galsgaard K, Vlahos L and Isliker H 2006 *A&A* **449** 749–757
[12] Vernazza J E, Avrett E H and Loeser R 1981 *ApJS* **45** 635–725
[13] Varady M, Kašparová J, Moravec Z, Heinzel P and Karlický M 2010 *IEEE Transactions on Plasma Science* **38** 2249–2253
[14] Kašparová J, Varady M, Heinzel P, Karlický M and Moravec Z 2009 *A&A* **499** 923–934
[15] Varady M, Karlický M, Moravec Z and Kašparová J 2012 Influence of Static and Stochastic Electric Fields on Electron Beams Bombarding the Chromosphere *Fifth Hinode Science Meeting* (*Astronomical Society of the Pacific Conference Series* vol 456) ed Golub L, De Moortel I and Shimizu T p 203
[16] Haug E 1997 *A&A* **326** 417–418
[17] Abbett W P and Hawley S L 1999 *ApJ* **521** 906–919
[18] Allred J C, Hawley S L, Abbett W P and Carlsson M 2005 *ApJ* **630** 573–586

[19] Machado M E, Avrett E H, Vernazza J E and Noyes R W 1980 *ApJ* **242** 336–351
[20] Kontar E P, Hannah I G, Jeffrey N L S and Battaglia M 2010 *ApJ* **717** 250–256 (*Preprint* 1005.0599)
[21] Martínez Oliveros J C, Hudson H S, Hurford G J, Krucker S, Lin R P, Lindsey C, Couvidat S, Schou J and Thompson W T 2012 *ApJ* **753** L26 (*Preprint* 1206.0497)

Astron. Astrophys. 355, 769–780 (2000)

ASTRONOMY AND ASTROPHYSICS

Decaying post–flare loops system observed by SOHO/CDS and Yohkoh/SXT

M. Varady[1], **A. Fludra**[2], **and P. Heinzel**[1]

[1] Astronomical Institute of the Academy of Sciences of the Czech Republic, 25165 Ondřejov, Czech Republic
[2] Space Science Department, Rutherford Appleton Laboratory, Chilton, OX11 0QX, UK

Received 20 September 1999 / Accepted 21 January 2000

Abstract. The results of an analysis of joint SOHO/CDS and Yohkoh/SXT observations of a decaying post–flare loops system with a rapid time evolution are presented. The loop system was a remnant of a small single loop flare (GOES class C2.9). Using the CDS raster taken in several EUV lines with different formation temperatures and a temperature sensitive line pair Fe XVI 360.8/Si XII 520.7 we confirmed the existence of the vertical stratification in the loop system according to the line formation temperature. The analysis of the SXT data showed a strong decay of the system with time. While the temperature of the hot part of the system ($T \simeq 2.5$ MK) decreased only slightly, the total emission measure dropped by more than a factor of four in approximately 10^3 s. This could be explained by a plasma outflow from the loops with velocity approximately 10 km/s. On the other hand, signs of rapid, probably radiative cooling can be identified in the images obtained from the CDS raster taken in cool lines of O V and O III. Using the density sensitive line pair of Fe XIV 334.2/353.8 and the integrated intensity of Fe XIV 334.2 line we determined the electron densities and emission measures across the top of the loop system. From the results of these measurements, taking all known uncertainties into account, we obtained that the geometrical filling factor at the top of the system in the regions with maximum electron density in the Fe XIV line lies in the interval from $\simeq 0.01$ to $\simeq 0.2$. A simple theoretical approximation of the energy balance in the post–flare plasma gives a total cooling time $\simeq 750$ s.

Key words: Sun: corona – Sun: flares – Sun: UV radiation – Sun: X-rays, gamma rays

1. Introduction

Systems of flare loops appear shortly after the onset of solar flares first in the soft X–ray and the EUV band and later on, Hα loop prominences for events on the limb or typical dark loops on the disk usually appear (Bray et al. 1991). These loops are most conspicuous in the gradual phase of flares and can persist for many hours. This is also the reason why they are called in literature 'post–flare loops – PFL' although their appearance during the impulsive phase is not unusual.

Sturrock (1968), Kopp & Pneumann (1976), Forbes & Malherbe (1986) and others proposed that PFL can result from a gradual reconnection of magnetic fields high in the solar corona which produces successively higher magnetic arches in the corona and at the same time, energy is released at the reconnection site (cusp) above the loop system. This energy is then transported downwards, along the magnetic field lines, either by thermal conduction or by beams of accelerated particles. As a consequence, the chromosphere and transition region are heated and a flow of evaporated hot plasma fills the corresponding magnetic loop system. A hot PFL is thus created. As the reconnection continues, this loop is separated from the energy input and starts to cool. In the meantime, a new hot PFL is originating above it.

PFL systems have been extensively observed particularly in Hα and in soft X–rays, especially after the launch of Yohkoh with its Soft X–ray Telescope (SXT) (Tsuneta et al. 1991). Hα images show plasma at temperatures around 10^4 K and provide very good spatial resolution useful for studies of the structural and dynamic properties of PFL (e.g. Wiik et al. 1996). From these observations it is also possible to determine the emission measure of cool plasma in the loop system (Schmieder et al. 1996). On the other hand, soft X–ray images, which lack the spatial resolution of Hα images, show plasma with temperatures of the order of 10^6 – 10^7 K and they are useful for approximate temperature and emission measure analysis. The relation between cool (Hα) and hot plasma in PFL systems was described in Schmieder et al. (1995).

Observations of PFL systems in EUV lines provide an excellent opportunity to study the behaviour of post–flare loop plasma at intermediate temperatures. EUV spectra also allow to apply efficient electron density, emission measure and temperature diagnostic methods (e.g. Mason & Monsignori Fossi 1994). Several studies of this kind have been published. Dere & Cook (1979) studied the time evolution of differential emission measure and electron density during the decay of a flare using data from Solrad 9 and Skylab. The spatial distribution of EUV emission and electron density was studied by Cheng (1980) using Skylab data. A displacement of loops visible in lines with high and low formation temperatures was found. Similar re-

Send offprint requests to: varady@asu.cas.cz

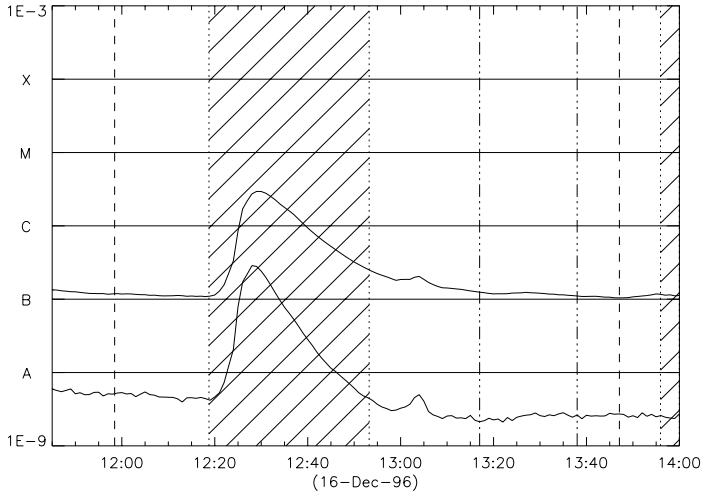

Fig. 1. GOES–9 X–ray fluxes and times of CDS and SXT observations. The hatched regions correspond to the times when the Yohkoh satellite was in the shadow of the Earth, the region between the two dashed lines corresponds to the time when the whole CDS raster was built and the region between the two dot–dash lines to the times when the loop system itself was scanned.

sults based on data from SMM and Hα observations were also published by Švestka et al. (1987).

Using observations from SOHO Coronal Diagnostic Spectrometer (CDS) and Yohkoh SXT, we examine in this paper a decaying PFL system in its final phase when the loops are fading and becoming invisible. From SXT observations we derive the time evolution of the temperature and the emission measure in the hot part of the system during its decay. The CDS data was used to determine the vertical thermal structure of the examined loop system using the temperature sensitive line pair of Fe XVI at 360.8 Å and Si XII at 520.7 Å and its electron density from the density sensitive line pair of Fe XIV 334.2/353.8. From integrated intensities of several allowed lines with different formation temperatures the emission measures were calculated. From these measurements we estimated the geometrical filling factor at the top of the PFL system in Fe XIV lines. The values of the temperature and the electron density were then used to estimate the cooling time of the system from its initial temperature down to $\simeq 2 \times 10^4$ K.

2. Observations

The analysed PFL system was a remnant of a small flare (GOES class C2.9) which occurred on 16th December 1996 on the south-west limb of the Sun. GOES X–ray fluxes showed that the flare started at 12:20 UT, its maximum occurred at 12:29 UT and the GOES event finished at approximately 13:00 UT. There are no direct observations of the flare itself because during the flare Yohkoh was in the shadow of the Earth and the slit of CDS was high above the flare region. The data concerning the PFL system was taken only before and after the GOES event and its time distribution is presented on the background of GOES–9 X–ray fluxes in the Fig. 1.

2.1. CDS

The Coronal Diagnostic Spectrometer – CDS on board SOHO is fully described in Harrison et al. (1995) and Harrison & Fludra (1995). The analysed raster was taken using the Normal Incidence Spectrometer (NIS) with the 2×240 arcsec slit oriented in the N–S direction.

The size of the raster analysed in this work is 243.8×240.2 arcsec, the spatial dimensions of one raster element are 2.032 arcsec in the E–W direction and 1.68 arcsec in the N–S direction. The exposure time of one spectrum was 45 s and the scanning started at 11:58:27 UT and finished at 13:47:05 UT (see also Fig. 1). The whole raster consists of 120 exposures and the total raster duration was 1h 48min 38s. This gives the CDS scanning speed $\simeq 54$ s per one N–S stripe. It is clear that when highly dynamic phenomena are observed, as for example PFL, a long scanning time can influence the shape of the observed structures and one has to be very careful when interpreting such observations. The observation was carried out in 16 spectral windows 20 pixels wide, in the spectral direction. Each window corresponds to spectral width approximately 1.33 Å for NIS I and 2.23 Å for NIS II. The spectral lines are usually in the middle of these windows. A list of the 14 spectral lines available and their approximate formation temperatures is given in Table 1. In addition to the 14 lines referred to in Table 1, there are two more spectral windows which are adjacent to the important density sensitive line pair of Fe XIV at 334.2 Å and 353.8 Å. These windows were used for determination of the scattered light level.

2.2. SXT

The Soft X–ray Telescope – SXT on board Yohkoh is described in detail in Tsuneta et al. (1991). The SXT is able to obtain time sequences of images in one of five filters with the time resolution better than one second. The pixel size of the CCD detector is 2.45 arcsec.

As we mentioned above, the Yohkoh satellite was in the shadow of the Earth during the flare (see Fig. 1), so that the only SXT images available were taken before and after the flare. In this analysis we used only the SXT data obtained after the flare.

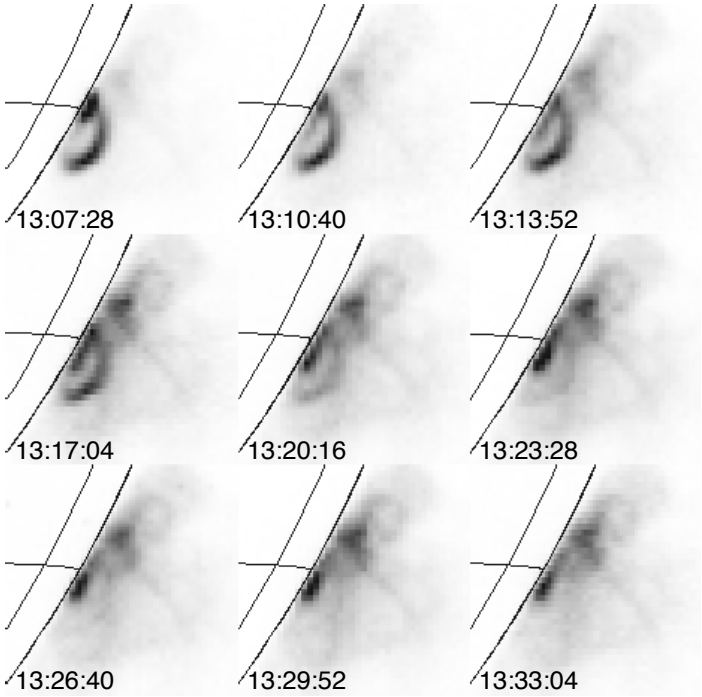

Fig. 2. A time sequence of Yohkoh SXT images taken in Al1 filter showing the time evolution of the hot part of the PFL system. The times when the majority of these images was taken correspond to the times when the slit of CDS scanned the loop system (compare with Fig. 3).

Table 1. List of available lines and their formation temperatures. Asterisks indicate the density and crosses the temperature sensitive line pairs used in this analysis.

Ion	Wavelength Å	Temperature K
He I	584.33	2×10^4
O III	599.59	10^5
O V	629.73	2.5×10^5
Ca X	557.77	6×10^5
Mg IX	368.06	10^6
Mg X	624.94	1.1×10^6
Si X	347.40	1.3×10^6
Si X	356.04	1.3×10^6
Fe XII	364.47	1.6×10^6
Fe XIII	348.18	1.6×10^6
Si XII$^+$	520.67	1.8×10^6
Fe XIV*	334.17	1.8×10^6
Fe XIV*	353.83	1.8×10^6
Fe XVI$^+$	360.75	2.2×10^6

The first usable, not overexposed SXT image of the sequence of interest was taken at 13:07:28 UT and the last one a long time after the examined PFL system had disappeared. The time gap between two consecutive images was 64 s. The observational sequence was carried out in two filters. One image taken in Al1 filter was followed by two images taken in AlMg filter. From the intensity ratio in these two filters the time evolution of the temperature and emission measure of the observed hot PFL plasma was determined.

3. Structure and time evolution of the PFL derived from SXT and CDS observations

The time evolution of the hot parts of the PFL system ($T \simeq 2.5$ MK), at approximately the same time when the slit of CDS scanned it, is very well visible in the images obtained by SXT (Fig. 2). A rapid evolution of the hot part of the loop system is seen in the first pictures of the sequence, while very little change is seen in the last images. The length of the loop determined from these pictures is approximately 2.5×10^9 cm. It is also apparent that the examined loop system is surrounded by a hot rare coronal plasma. An influence of this plasma has to be taken into account when the temperature, emission measure and electron density are determined. Apart from the PFL system and the rare coronal plasma around it, it is also possible to recognize some loops above PFL and two bright points; one above the northern footpoint of the loop and the second under it. These two bright points brighten when the PFL system is disappearing. In this analysis we discuss only the behaviour of the conspicuous loop–like structure visible in the first images of the sequence.

The CDS images of the PFL system, in eight selected lines which cover the temperature range from 2×10^4 K to 2.2 MK, are shown in Fig. 3. Here, in all lines roughly only one half of the loop system is clearly visible. Why this happens in the hot lines ($T > 1$ MK) is apparent from a comparison of the CDS images with the time sequence of images obtained by SXT (Fig. 2). The hot loops in the raster are visible until approximately 13:22 UT, which corresponds to the time when the hot loop observed by SXT starts to disappear as well. It will be shown in the next

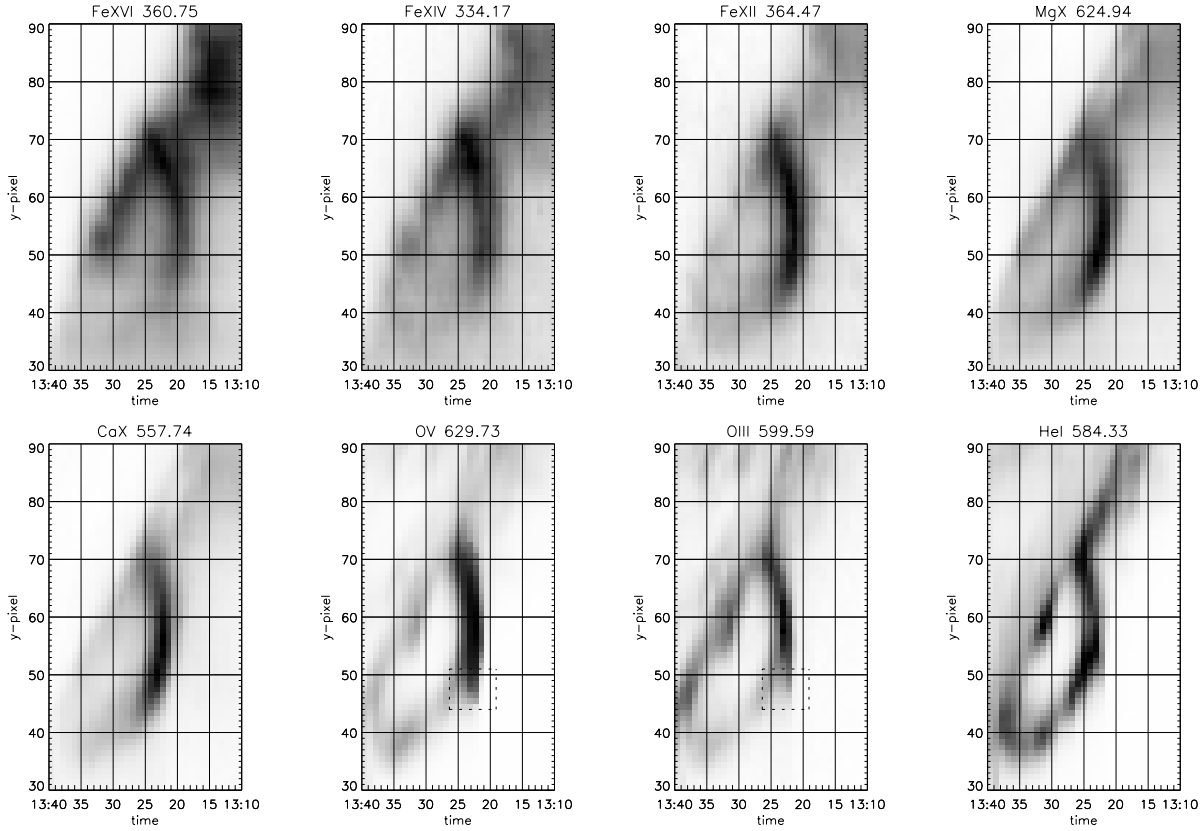

Fig. 3. Part of the CDS raster with the PFL system in eight chosen lines spanning the temperature range from 2×10^4 K to 2.2×10^6 K (image in negative). The times on the x–axes correspond to the positions of the CDS slit in the raster. The time goes from right to left because the CDS slit scans from W to E and is oriented in N–S direction.

section that this is mainly due to plasma depletion from the loop. In the cooler lines this could be due to the combined effect of plasma depletion and cooling.

It follows from the way the CDS rasters are built that the eight images with the loop–like structures in Fig. 3 are exactly cospatial. When the positions of the tops of the semi–loops taken in different lines are compared, it is apparent that those in the images which are taken in lines having higher formation temperature lay *above* those formed at lower temperatures. On the other hand, the structures visible in different lines are not spatially separated, but they are overlapping, which is demonstrated in Fig. 4. This temperature stratification with height can be either real, as it is supposed in theoretical models of PFL (Kopp & Pneumann 1976, Forbes & Malherbe 1986, etc.), or it could be mimicked by the combined effect of cooling and scanning the loop system with the CDS with a finite speed. The scanning across the loop tops in all available lines took approximately 5 min (see Fig. 3). In contrast, SXT measurements (Sect. 4) show that plasma cooling in the hot part of the system is very slow. Also the theoretical estimate of the PFL plasma cooling rate (Sect. 7) does not show any fast cooling in the temperature region above $\simeq 1$ MK which could explain the thermal stratification of the loop system by the combined effect of cooling and scanning speed. We believe that at least in the lines with formation temperature above 1 MK we observe a real temperature stratification with height, as a 'snapshot' of the PFL system evolution.

When the shapes of the semi–loop structures visible in hot and cool lines are compared (Fig. 3), it is apparent that they are much smoother in the hot lines while in the cool lines there are some irregularities in their shapes (structures inside the dotted boxes). They are clearly not a part of the loop system, so they have to result from a combined effect of the PFL system time evolution and the finite scanning speed of CDS. We interpret these irregularities as a manifestation of a rapid cooling of PFL plasma visible in cool lines. If we admit that there is a real temperature stratification with height in the observed PFL system, then plasma with temperature a little higher than the formation temperature of the particular line is located above the bright loop tops seen in that line, and this hotter plasma is at that moment invisible in this line. But since the CDS slit scans the loop system with a finite speed approximately one step per minute (in Fig. 3 from right to left), the plasma with temperature just greater than the formation temperature of the particular line manages to cool

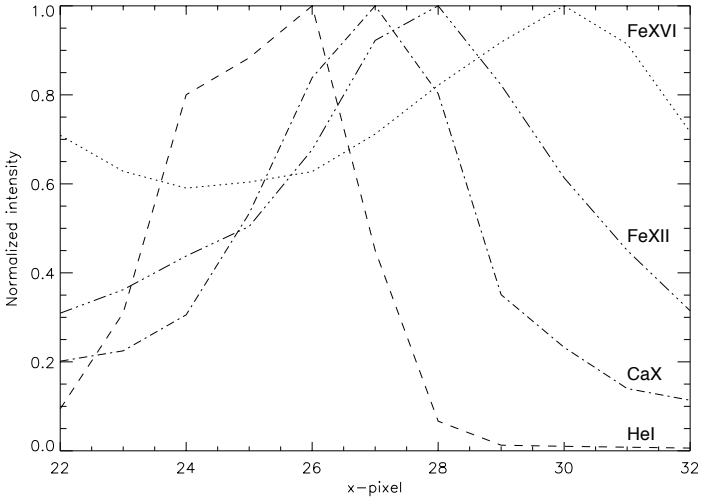

Fig. 4. Normalized intensity profiles of the CDS semi–loop structures taken in four selected lines He I, Ca X, Fe XII and Fe XVI. The intensity profiles are plotted along a horizontal line $y = 55$ in range from $x = 22$ (scanning time $\sim 13 : 27$) to $x = 32$ (scanning time $\sim 13 : 18$) (see also the raster plotted in the Fig. 6). To improve the S/N ratio we added to the corresponding $y = 55$ intensity intensities from two adjacent y pixels 54 and 56.

down and becomes visible as the irregularities in the loop-like structures. Because the time necessary for the completion of one N–S stripe exposure is approximately only one minute we can interpret these irregularities as a manifestation of very rapid, probably radiative plasma cooling visible in O V, O III and perhaps also He I lines. Since in the hot lines no similar features are seen, we believe that plasma visible here cools much more slowly compared to the CDS scanning speed.

Another prominent feature is the dependence of the sharpness (or diffusivity) of the PFL images on the formation temperature of the line which was used to take the image. From the CDS data available it follows that the images taken in hotter lines tend to be more diffused than the ones taken in cool lines, which are much sharper. On the other hand, for example, in the image taken in He I line (Fig. 3), the loop top where the CDS slit was parallel to the scanned structure is quite sharp but the part of the loop in the lower left corner, where the CDS slit was perpendicular to the scanned structure, is rather diffused. So we believe that this is probably caused by the combined effect of CDS scanning and different speed of plasma cooling in different lines, rather than by a real structural difference of hot and cool loops, although using this data we can not completely exclude the possibility of real structural difference of hot and cool loops.

4. Analysis of the SXT data

The SXT data and filter ratio method (Hara et al. 1992) were used to derive the time evolution of mean temperature and emission measure during the decay of the loop system. The intensity, in each filter (Al1, AlMg), was integrated from an area of 189 pixels which lay inside an intensity contour 39% above the background containing the whole loop (see Fig. 5). However, during the analysis we found out that the general behaviour of the mean plasma temperature and emission measure is almost independent of the chosen area of the loop system where the intensity was integrated from. A similar result was obtained by Schmieder et al. (1996).

The time evolution of the mean plasma temperature in the loop (upper graph in Fig. 5) looks rather complicated. At the beginning of the observational sequence, from 13:07:28 UT to 13:17:04 UT, a manifestation of slow plasma cooling from the initial temperature 2.8 MK down to 2.5 MK in approximately 600 s can be seen. Then the temperature behaves rather chaotic. We believe that this could be accounted for by the influence of hot rare coronal plasma surrounding the PFL system, the existence of which we mentioned in the previous section. When the emission measure of plasma inside the examined loop was much greater than the emission measure of other plasma along the line of sight, the manifestation of plasma properties in the examined loop prevailed over the manifestation of properties of surrounding plasma. But as the emission measure of plasma inside the loop was decreasing with time (see lower plot in Fig. 5), the measured quantities were more and more influenced by the properties and behaviour of other plasma lying along the line of sight. So we believe that plasma inside the PFL could continue cooling even after 13:17:04 UT because the values of the temperature later on are probably very strongly influenced by other hot coronal plasma along the line of sight (see Fig. 2).

The behaviour of the total emission measure along the line of sight averaged over the area of the whole loop $\langle EM_{tot} \rangle$, presented in the lower graph of Fig. 5, looks much simpler. It decreases very quickly (in approximately 960 s) from its original value $(9.2 \pm 0.3) \times 10^{28}$ cm^{-5} at 13:07:28 UT to its final value $(2.2 \pm 0.2) \times 10^{28}$ cm^{-5} at 13:23:28 UT. Because such a rapid decrease of $\langle EM_{tot} \rangle$ can be explained only by plasma depletion from the PFL (see also Fig. 2), we can expect a strong down-flow of hot plasma from the loop to its footpoints along the magnetic field lines. Later on, the behaviour of $\langle EM_{tot} \rangle$ becomes slightly chaotic again, which we believe can be accounted for by rare hot coronal plasma along the line of sight, with a mean emission measure $\langle EM_{cor} \rangle$, which does not belong to the PFL system. Because the emission measure is an additive quantity, the mean emission measure of plasma inside the loop system itself is

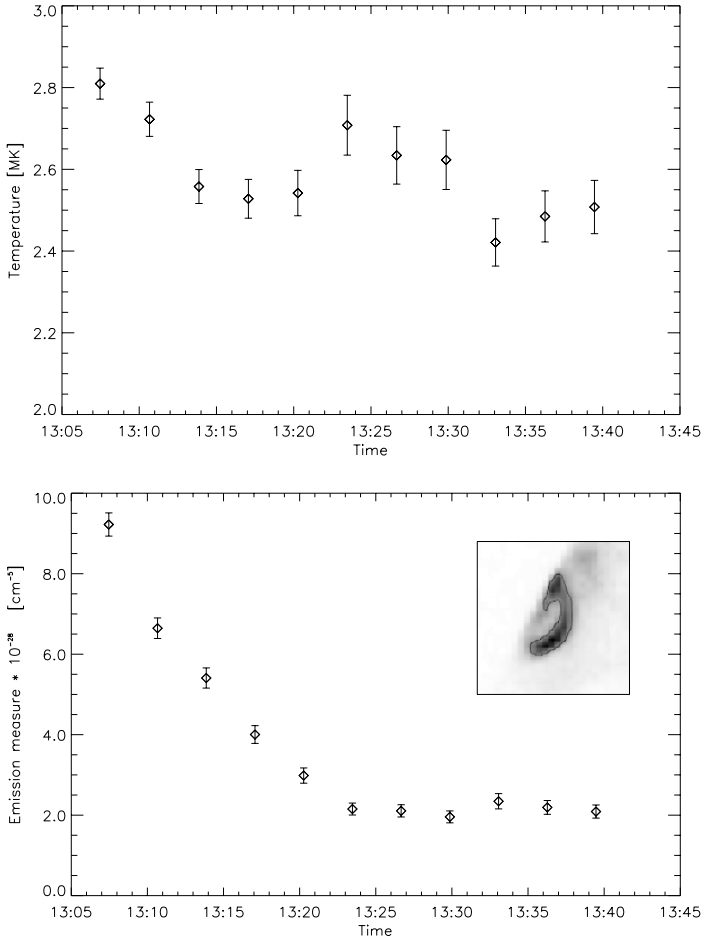

Fig. 5. The time evolution of mean temperature and emission measure for the whole loop (the region inside the intensity contour containing 189 pixels) obtained from the SXT observations using filter ratio method. The error bars include the decompression and statistical errors. The systematic errors are not included.

$$\langle EM_{pfl}\rangle = \langle EM_{tot}\rangle - \langle EM_{cor}\rangle \quad . \tag{1}$$

If the mean emission measure of plasma inside the loop system $\langle EM_{pfl}\rangle$ is known and if it is possible to estimate the size of the loop system D along the line of sight, a simple formula

$$\langle EM_{pfl}\rangle = \frac{1}{S_{pfl}} \int_{S_{pfl}} \int_0^D n_e^2 \, \mathrm{d}l \, \mathrm{d}S \approx \langle n_e^2\rangle \, D \tag{2}$$

can be used to estimate the mean value of the second power of the electron density $\langle n_e^2\rangle$ in the loop system. If we suppose that all the emitting plasma is deposited inside some filaments, which are not resolved by SXT and which have the same electron density, we can calculate the mean electron density in the volume occupied by the loop system: $\langle n_e\rangle = \sqrt{\langle n_e^2\rangle}$. S_{pfl} is the area over which the intensity is integrated.

From the SXT images and CDS rasters (Figs. 2, 3) we determined the apparent diameter of the loop system in the plane perpendicular to the line of sight $D_{app} = (4.0 \pm 0.7) \times 10^8$ cm. If we assume that this apparent diameter obtained above equals D and $\langle EM_{pfl}\rangle = \langle EM_{tot}\rangle$, so that all the emitting plasma along the line of sight is concentrated in the loop system, the maximum mean electron density is $(1.5 \pm 0.2) \times 10^{10}$ cm^{-3} and the minimum density is $(7.0 \pm 1.0) \times 10^9$ cm^{-3}. On the other hand, if we suppose that $\langle EM_{cor}\rangle$ equals one half of the almost constant value of $\langle EM_{tot}\rangle$ at times from 13:23:28 UT to 13:39:28 UT, which is approximately $\langle EM_{tot}\rangle = (2.1 \pm 0.5) \times 10^{28}$ cm^{-5} then the maximum mean electron density in the loop is $(1.4 \pm 0.2) \times 10^{10}$ cm^{-3} and the minimum density is $(5.0 \pm 2.0) \times 10^9$ cm^{-3}, for the same value of D as in the previous case.

From the emission measure analysis we found that there has to be a plasma outflow from the examined loop system. Using the quantities obtained above and with the help of the continuity equation it is possible to estimate, though very roughly, the velocity of plasma outflow along the magnetic field at the base of the loop. If we suppose that the cross-sectional area along the loop is constant, we get for a velocity of a symmetrical plasma outflow to both footpoints ~ 10 km s^{-1}. If the plasma outflow is directed only to one footpoint of the loop system then the velocity would be approximately twice larger. This rather low velocity contrasts with much stronger flows ($v \sim 10^2$ km s^{-1}) observed in cool Hα loops (Wiik et al. 1996). This could be

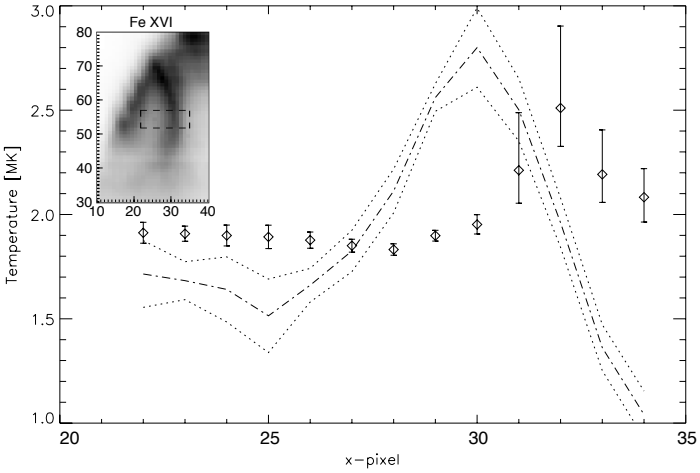

Fig. 6. The vertical thermal structure across the loop tops determined from the temperature sensitive ratio of Fe XVI 360.8 and Si XII 520.7 lines. The error bars correspond to 3σ probability of the fits. This graph is overplotted by the normalized intensity profile of Fe XVI loop–like structure (dash-dot line) and by the errors in the intensities (dotted lines). In the upper left corner of the graph a part of the CDS raster was plotted. Its axis are in pixels which we refer all the measurements from CDS to. The dashed box is the region where the line intensities were measured.

explained by quite different pressure scale–heights in these two cases.

5. Analysis of the CDS data

5.1. Fitting the CDS spectral profiles

All results in this section were derived from integrated line intensities, taking their uncertainties into account. Because the way we obtained them was common in all following subsections, we will discuss it briefly here. We supposed that the spectra in individual spectral windows (covering the wavelength interval 1.33 Å for NIS I and 2.33 Å for NIS II) can be approximated by a sum of a constant b_0 representing the background (stray light) and L Gaussian components representing the individual spectral lines centered at wavelengths λ_k:

$$I_i = b_0 + \sum_{k=1}^{L} a_k \exp - \left(\frac{\lambda_i - \lambda_k}{\alpha c_k} \right)^2 . \qquad (3)$$

I_i is the intensity observed in the i-th spectral pixel at the wavelength λ_i, a_k is the amplitude, c_k is the FWHM of the k-th Gaussian and $\alpha \doteq 0.6$.

To obtain the best fit of parameters b_0, a_k, λ_k and c_k, we used the least square method and minimized the function:

$$\sum_{i=1}^{N} \left[\frac{I_i}{\sigma_i} - \frac{1}{\sigma_i} \left(b_0 + \sum_{k=1}^{L} a_k \exp - \left(\frac{\lambda_i - \lambda_k}{\alpha c_k} \right)^2 \right) \right]^2 , \qquad (4)$$

where σ_i are the statistical errors in intensities collected in individual spectral pixels of the detector obtained from the photon statistics (Thompson 1997) and N is the number of spectral pixels. The searched integrated intensity of a given k-th line can be then easily calculated from fitted parameters a_k and c_k.

The statistical errors of the fitted parameters were calculated only for the parameters concerning the spectral line of interest which directly influence the searched integrated line intensity (i.e. a_s, c_s and b_0). These errors were obtained by a standard method described in detail in Press et al. (1989). Another source of errors is the unknown accuracy in the calibration curves of CDS which can introduce a systematic error into the line intensities. Because this error is unknown, it could not be included, but when one is interested in a ratio of two line intensities with similar wavelengths lying on the same detector, these errors tend to cancel each other. This is the case of the density sensitive pair Fe XIV. On the other hand, for a ratio of two distant lines or two lines lying on different detectors it can be quite significant. This is the case of the temperature sensitive pair Fe XVI/Si XII.

5.2. CDS temperature diagnostics

To get information on the temperature distribution of hot plasma in the system across the loop tops we used the intensity ratio of lines Fe XVI at 360.8 Å and Si XII at 520.7 Å which is temperature sensitive in the interval from 1 MK to 3.2 MK. The theoretical intensity ratio is also dependent on the relative chemical abundance of iron to silicon which is not very well known (Meyer 1985) and which can also vary from flare to flare (Fludra & Schmelz 1995). Moreover, as we already mentioned above, the observed intensity ratio can be quite significantly influenced by the systematic error resulting from the uncertainty in the CDS calibration. These reasons prevented us from calibrating the temperature using only theoretical data and we had to use another method based on our knowledge of the temperature obtained from SXT data. Therefore, we supposed that the maximum temperature of plasma in the PFL system, measured using the line ratio, corresponds to the plasma temperature measured by SXT at the same time.

The ratios of Fe XVI and Si XII lines were determined in 13 pixels along the x axis from pixel numbers 22 – 34 (see Fig. 6). To improve the S/N ratio the signal was integrated from 6 pixels along the y axis from pixels 52 – 57. The error bars correspond to 3σ probability of the line fits and they do not contain any uncertainties in values of theoretically calculated emissivities. Their very variable length is given by the theoretical dependence of the temperature on the emissivities ratio. The emissivities were calculated using ADAS (Summers et al. 1996).

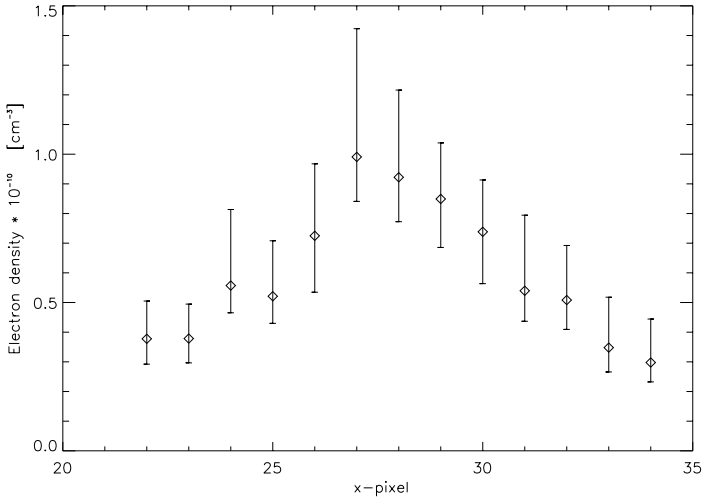

Fig. 7. The course of electron density determined from the ratio of intensities of the electron density sensitive line pair Fe XIV 334.2/353.8 across the top of the loop system. The error bars correspond to 3σ probability of the fits.

The results of this analysis are presented in Fig. 6, where the intensity profile of the Fe XVI loop was also plotted. It is clearly visible that the temperature increases with height and reaches its maximum above the Fe XVI loop. Plasma with lower density is probably located here. This distribution of temperature in the PFL system is in full agreement with the classical formation theory of PFL systems. The course of temperature under the Fe XVI loop reflects the temperature of rare hot coronal plasma surrounding the PFL system rather then the temperature of plasma located in the loops visible in lines having lower formation temperatures.

5.3. CDS electron density diagnostics

The CDS data was used to determine the electron density of the hot part of the PFL system, using the density sensitive line pair of Fe XIV 334.2/353.8 (Mason et al. 1997, Mason 1998). This line pair is electron density sensitive in range approximately from 10^9 cm^{-3} to 10^{11} cm^{-3}, where also the expected values of electron densities of PFL lie.

The disadvantage of this line pair is that when plasma with temperature greater than $\simeq$ 4 MK is present in the analysed region, the Fe XIV line at 353.8 Å is strongly blended with a very bright Ar XVI line. Fortunately the temperature analysis of the SXT data and also the comparison of observed spectra with the synthetic spectra calculated with CHIANTI (Dere et al. 1997, Mason 1998) showed that the plasma temperature in the analysed region is lower than $\simeq$ 3 MK, so that the blending is not prohibitive. The theoretical dependence of the electron density on the intensity ratio was calculated using CHIANTI.

The electron densities were determined in 13 different positions along the x axis across the loop top, in pixel numbers 22 – 34 (see the raster in Fig. 6). To improve the S/N ratio the intensity was integrated from 6 pixels along the y axis from pixels 52 – 57. To determine the level of scattered light we connected the spectral windows containing the given diagnostic lines with the adjacent spectral windows, and the minimum signal from these two windows was taken as the background. The error bars correspond to 3σ probability of the line fits. No uncertainties are included in the theoretical dependence of electron density on the intensity ratio. The course of the electron density across the loop top is shown in Fig. 7. These values were used to estimate the geometrical filling factor in the top of the loop system.

5.4. CDS emission measure diagnostics

The integrated intensities of allowed lines with different formation temperatures were used to obtain the plasma emission measure using the method originally designed by Pottasch (1963). We assumed an isothermal plasma at temperature T, which corresponds to the maximum of the contribution function (emissivity) of the given line. Then the integrated intensity of the line can be approximated by a simple formula:

$$I = \frac{1}{4\pi}\, A\ G(T)\, EM\ , \tag{5}$$

where A is the elemental abundance relative to the hydrogen and I is the integrated intensity of the particular spectral line. The contribution functions $G(T)$ were calculated using ADAS (Summers et al. 1996) and the elemental abundances for a solar flare were taken from Fludra & Schmelz (1995). These abundances are subject to a 30% combined statistical and systematic uncertainty. The errors of integrated line intensities resulting from the photon statistics correspond to 3σ probability of the line fits.

The values of the emission measure were determined at the brightest regions at the tops of the loop–like structures visible in CDS raster in different spectral lines. These regions were one pixel broad in the x direction and the intensity was integrated from six pixels in the y direction. The results are summarized in Table 2 and the dependence of the emission measure on line formation temperature is shown in the upper plot in Fig. 8. Under the assumptions adopted in the Sect. 4 it is possible to determine the mean electron densities from these val-

Table 2. The results of the emission measure analysis.

Ion	Wavelength Å	Abundance	Emissivity $\times 10^{20}$ erg cm^3 s^{-1}	x, y-coordinates pixels	Intensity erg cm^{-2} s^{-1} sr^{-1}	$\langle EM \rangle \times 10^{-27}$ cm^{-5}
O III	599.59	2.5×10^{-4}	1.45	26, 54-59	63.8±4.6	0.2 ± 0.1
Ca X	557.77	4.4×10^{-6}	5.57	26, 47-52	89.9±9.7	4.6 ± 1.9
Mg X	624.94	4.0×10^{-5}	2.23	27, 50-55	323.8±11.4	4.6 ± 1.5
Si XII	520.67	4.2×10^{-5}	1.64	28, 51-56	170.3±7.9	3.1 ± 1.1
Fe XIV	334.17	4.8×10^{-5}	1.52	29, 52-57	153.4±10.7	2.6 ± 1.0
Fe XVI	360.75	4.8×10^{-5}	2.19	30, 52-57	557.4 ± 37.8	6.7 ± 2.5

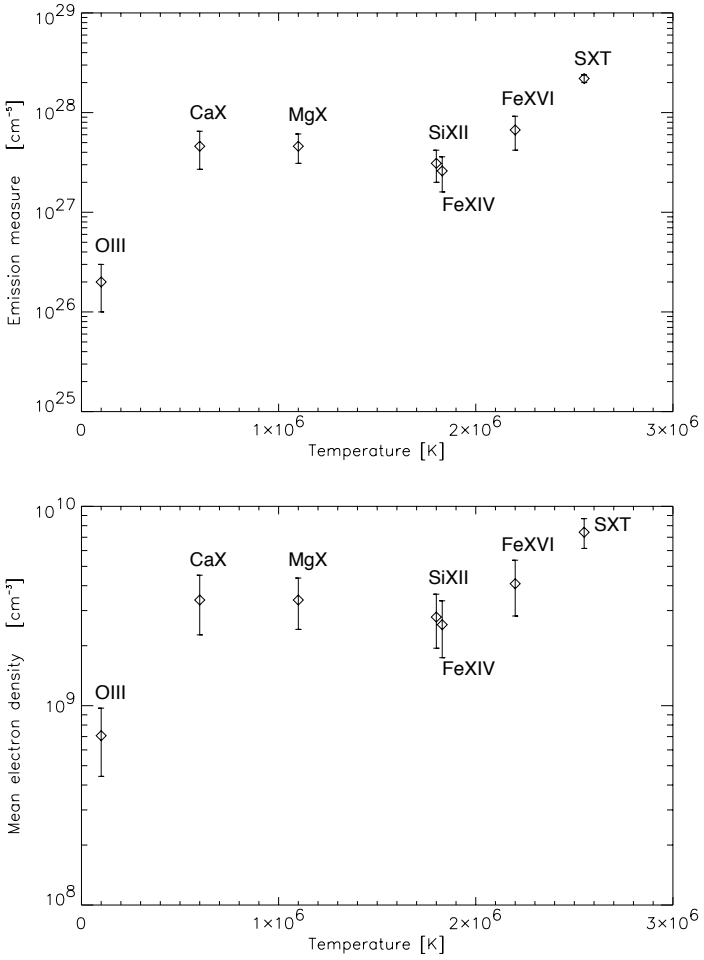

Fig. 8. The mean emission measures and electron densities obtained from allowed lines and SXT measurements versus the formation temperature of the lines. The emission measure is calculated for the brightest parts in the tops of corresponding loops (see Table 2).

ues of emission measure. We assumed that the size of the loop system along the line of sight corresponds to the apparent diameter of the loop system obtained from SXT and CDS images $D_{app} = (4.0 \pm 0.7) \times 10^8$ cm. The dependence of the electron density, obtained in this way, on the formation temperature is shown in the lower plot in Fig. 8. The mean electron densities for lines with formation temperatures from 2.2 MK (Fe XVI) to 0.6 MK (Ca X) remain almost constant with the temperature ($\simeq 3 \times 10^9$ cm^{-3}). In contrast, the mean electron density calculated from the emission measure derived from the intensity of O III is substantially smaller $\simeq 7 \times 10^8$ cm^{-3}.

6. Plasma filling factor at the top of the PFL system

The results obtained from CDS electron density and emission measure analysis were used to estimate the geometrical filling factor of the examined PFL system in the Fe XIV line. If we assume that the plasma is isothermal and concentrated in fil-

aments with a typical electron density n_e, we can rewrite the formula for emission measure in this way:

$$EM = n_e^2 D_{real} = \left\langle n_e^2 \right\rangle D_{app} \ , \tag{6}$$

where

$$D_{real} = \int_{rad} \mathrm{d}l \ . \tag{7}$$

In this integral we calculate the total thickness of the radiating elements along the line of sight. Using these quantities we can define the geometrical filling factor as

$$f \equiv \frac{D_{real}}{D_{app}} = \frac{\left\langle n_e^2 \right\rangle}{n_e^2} \ . \tag{8}$$

The density n_e in Eq. 8 has been derived from the density sensitive line ratio Fe XIV 334.2/353.8. This ratio measures the real electron density. The value of $\left\langle n_e^2 \right\rangle$ has been derived by dividing the emission measure EM, calculated from the allowed line intensity, by the apparent size of the system along the line of sight, D_{app}.

The quantities n_e^2 and $\left\langle n_e^2 \right\rangle$ are identical only in the case of homogeneous distribution of plasma along the line of sight. In this case the filling factor would be equal to one. If plasma is not distributed uniformly, the electron density obtained from line ratio is greater than the density obtained from the emission measure and the filling factor is less than one.

Using this method we determined the filling factor in pixels 26 – 30 (x axis) which correspond to the brightest parts of the Fe XIV loop–like structure. The uncertainties in n_e and $\left\langle n_e^2 \right\rangle$ obtained in previous subsections were used to calculate the uncertainty of the geometrical filling factor. The results are summarized in Table 3. From our measurements it follows that the geometrical filling factor at the top of the examined PFL system in the regions with maximum electron density in Fe XIV line (formation temperature $\simeq 1.8$ MK) lies in the interval from $\simeq 0.01$ to $\simeq 0.2$. The great range of its possible values reflects the realistic uncertainties in our knowledge of elemental abundance, integrated intensities and D_{app}.

The value of the geometrical filling factor in flare loops has an important consequence. The majority of flare loops observations have been made by Yohkoh/SXT. However, SXT can measure only the emission measure and not the electron density in observed regions. An approximation which assumes a homogeneous and isothermal plasma $n_e = \sqrt{EM/D}$ is often used to derive the electron density. This approximation does not take into account the possibility that the spatial plasma distribution can be filamentary. If we assume that the typical electron density in such filaments is approximately the same for all of them and the electron density outside the filaments is much smaller than inside, knowing the filling factor we can estimate the real electron density $n_e = \sqrt{EM/fD}$ of emitting elements with a much better accuracy.

Table 3. Geometrical filling factor across the top of the loop system determined using the Fe XIV 334.2 and 353.8 lines.

x-pixel	$n_e^2 \times 10^{-19}$ cm^{-6}	$\left\langle n_e^2 \right\rangle \times 10^{-18}$ cm^{-6}	f
26	$5.25^{+3.51}_{-2.76}$	4.3 ± 2.4	$0.08^{+0.10}_{-0.08}$
27	$9.81^{+8.57}_{-2.97}$	5.3 ± 2.8	$0.05^{+0.08}_{-0.04}$
28	$8.50^{+5.42}_{-2.76}$	6.1 ± 3.2	$0.07^{+0.08}_{-0.06}$
29	$7.21^{+3.21}_{-2.78}$	6.6 ± 3.5	$0.09^{+0.09}_{-0.08}$
30	$5.45^{+2.58}_{-2.58}$	5.9 ± 3.2	$0.11^{+0.11}_{-0.11}$

7. Cooling of the PFL system

It is generally believed that the post–flare loop plasma cools mainly due to thermal conduction and radiation. To get a simple estimate of the time scale which a hot PFL with temperature of the order 10^6 K needs to reach temperature of the order 10^4 K, we used a simple formula of Švestka (1987) and we applied a correction to the temperature gradient introduced by Varady & Heinzel (1997). The formula was derived from the energy equation under the assumption of static ($n_e(t) = const$), fully ionized plasma. The first and the second term on the right hand side of the equation are approximations of conductive and radiative losses:

$$-3 n_e k_B \frac{\mathrm{d}T}{\mathrm{d}t} = a\kappa_0 \frac{T^{7/2}}{L^2} + n_e^2 \chi T^{\alpha} \ . \tag{9}$$

In this equation $a = 0.4$ is the correction applied to the temperature gradient, k_B is the Boltzmann constant, L is the semi-length of the loop, $\kappa = 10^{-6}$ (in CGS units) is the thermal conductivity coefficient and χ and α fit the radiative losses. The latter were taken from Cargill (1994) and are based on the model of Cook et al. (1989):

$$\begin{aligned}
\chi\, T^{\alpha} &= 2 \times 10^{-23} \ , & T &> 10^{6.5} \ , \\
\chi\, T^{\alpha} &= 3.5 \times 10^{-7} T^{-2.5} \ , & 10^6 < T &< 10^{6.5} \ , \\
\chi\, T^{\alpha} &= 3.5 \times 10^{-22} \ , & 10^5 < T &< 10^6 \ , \\
\chi\, T^{\alpha} &= 1.1 \times 10^{-27} T^{1.1} \ , & T &< 10^5 \ .
\end{aligned} \tag{10}$$

Using the formula above and quantities obtained in previous sections we calculated the theoretical time dependence of plasma temperature in the PFL. The model was calculated for the initial temperature 2.8 MK, which was obtained from the SXT temperature analysis and a constant electron density 10^{10} cm^{-3}, which corresponds to the value obtained at the top of the loop system using the density sensitive line pair of Fe XIV. The theoretical time dependence of temperature in the loop is shown in Fig. 9. It follows from this model that the total cooling time required to achieve the temperature of the order 10^4 K is approximately 750 s. In fact the cooling time will probably be longer, because from the SXT emission measure analysis we have an evidence of a rapid decrease of emission measure in the loop system which reduces the radiative losses.

8. Discussions and conclusions

In this paper we used simultaneously taken CDS and SXT data to examine a decaying PFL system resulting from a small single

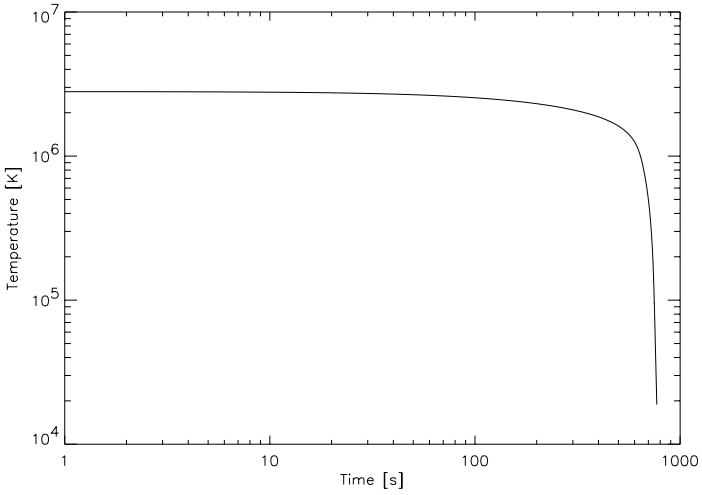

Fig. 9. Theoretical time dependence of the temperature of hot PFL, cooled conductively and radiatively from an initial temperature 2.8 MK. The electron density $n_e = 10^{10}$ cm^{-3} in the loop is assumed to be constant with time.

loop flare GOES class C2.9. From the structural features contained in the CDS images taken in lines with different formation temperature we were able to confirm that plasma with higher temperature tends to lie over plasma with lower temperature, as it is expected by the PFL formation theory and which was earlier observed by Cheng (1980) and Švestka et al. (1987). Using the time evolution of temperature of hot plasma in the loop system derived from the SXT data and the theoretical estimate of the cooling time of the hot plasma in the PFL system we ruled out the possibility that the observed thermal distribution of plasma, emitting at different formation temperatures, could be mimicked by a combined effect of PFL plasma cooling and the CDS scanning speed. Another argument which supports the reality of the thermal stratification in the loop system is the existence of the irregularities observed in lines with formation temperatures under 0.5 MK which are protruding from the CDS loop–like structures. Providing the distribution of plasma temperature discussed above is real, these structures can be naturally explained as a result of a very fast plasma cooling, which can be expected at these temperatures. A similar result was obtained using the temperature sensitive line pair Fe XVI at 360.8 Å and Si XII at 520.7 Å. Using this line pair we found that the hottest plasma in the loop system is placed above the maximum intensity of the highest loop visible in Fe XVI line.

From the SXT emission measure and temperature analysis we obtained that the main role during the decay of the hot part of the loop system was played by a plasma outflow from the system. During approximately 10^3 s the mean emission measure in the loop decreased to roughly one fourth of its original value. The velocity of the plasma outflow from the loop system at the footpoints was estimated to be approximately 10 km s^{-1}, for a uniform cross-sectional area along the loop. The time evolution of temperature obtained from SXT data shows some signs of slow cooling at the beginning of the observational sequence. Later on, when the emission measure in the loop system substantively decreased, the temperatures are strongly influenced by the behaviour of the surrounding hot coronal plasma. When we admit that the decrease of temperature observed at the beginning of the observational sequence represents a real plasma cooling and compare its speed to the speed of the emission measure loss, we can conclude that this part of the system decayed mainly due to plasma depletion from the system and the decrease of the temperature played a minor or perhaps a triggering role in the decay of the system. From the CDS data also follows that the plasma outflow from the PFL system, responsible for its decay, started in all lines at approximately the same moment.

To obtain the geometrical filling factor at the top of the PFL system in Fe XIV line ($\simeq$ 1.8 MK), we first determined the electron density and its uncertainty using the density sensitive line pair of Fe XIV. This method reflects the collisional rate in plasma and is not dependent on geometrical fine structural features in the system. Then we calculated emission measure of plasma in the system from the integrated intensities of an allowed line of Fe XIV at 334.2 Å (at the same locations where the electron densities using the density sensitive pair were measured). The emission measure was used to calculate the $\langle n_e^2 \rangle$ and its error. Because during the whole procedure of fitting and calculating of all the quantities necessary to determine the filling factor we took a great care to proper treatment of all errors which can influence the results, we obtained a great, but realistic uncertainty of the resulting filling factor. The results of our measurements are that the upper limit of the geometrical filling factor at the top of the loop system in Fe XIV line is $\simeq 0.2$ while the lower limit at least in regions of maximum electron density is $\simeq 0.01$. Of course, the filling factor can be different for loops with different temperatures. Unfortunately the CDS data available did not allow us to carry out a similar study in lines with different formation temperatures. The results show that if the electron density is estimated from for example a SXT emission measure without knowledge of the filling factor, the results can differ of factor from $\simeq 2$ to 10 from the real electron density in the observed region. This can strongly influence any theoretical interpretation of such observations.

Acknowledgements. MV acknowledges the financial support of ESA during his stay at the SOHO EOF where a substantial part of this study was carried out. MV is also indebted to P. C. Martens and A. J. C. Beliën for many fruitful discussions and to the whole CDS team for creating the excellent instrument. AF is supported by the United Kingdom PPARC. SOHO is a project of international cooperation between ESA and NASA. We thank B. Schmieder for useful comments. A part of this project was supported by a grant A3003902 of GA AV ČR.

References

Bray R.J., Cram L.E., Durrant C.J., et al., 1991, Plasma loops in the solar corona. Cambridge Astrophysics Series 18, Cambridge University Press
Cargill P.J., 1994, ApJ 422, 381
Cheng C.-C., 1980, Sol. Phys. 65, 347
Cook J.W., Cheng C.-C., Jacobs V.L., et al., 1989, ApJ 338, 1176
Dere K.P., Cook J.W., 1979, ApJ 229, 772
Dere K.P., Landi E., Mason H.E., et al., 1997, A&AS 125, 149
Fludra A., Schmelz J.T., 1995, ApJ 447, 936
Forbes T.G., Malherbe J.M., 1986, ApJ 302, L67
Hara H., Tsuneta S., Lemen S., et al., 1992, PASJ 44, L135
Harrison R.A., Sawyer E.C., et al., 1995, Sol. Phys. 162, 233
Harrison R.A., Fludra A., 1995, The Coronal Diagnostic Spectrometer for the Solar and Heliospheric Observatory – Scientific Report, SC–CDS–RAL–SN–95–0001
Kopp R.A., Pneumann G.W., 1976, Sol. Phys. 50, 85
Mason H.E., Monsignori Fossi B.C., 1994, A&AR 6, 123
Mason H.E., Young P.R., Pike C.D., et al., 1997, Sol. Phys. 170, No. 1, 143
Mason H.E., 1998, In: Vial J.C., Bocchialini K., Boumier P. (eds.) Space Solar Physics. Lecture notes in physics 507, p. 143
Meyer J.P., 1985, ApJS 57, 173
Pottasch S.P., 1963, ApJ 137, 945
Press W.H., Flannery B.P., Teukolsky S.A., et al., 1989, Numerical recipes. Cambridge University Press
Schmieder B., Heinzel P., Wiik J.E., et al., 1995, Sol. Phys. 156, 337
Schmieder B., Heinzel P., van Driel–Gesztelyi L., 1996, Sol. Phys. 165, 303
Sturrock P.A., 1968, IAU Symp. 35, 471
Summers H.P., Brooks D.H., Hammond T.J., et al., 1996, Atomic Data and Analysis Structure – User Manual, RAL–TR–96–017
Švestka Z., 1987, Sol. Phys. 108, 411
Švestka Z., Fontenla J.M., Machado M.E., et al., 1987, Sol. Phys. 108, 237
Thompson W.T, 1997, CDS software note, No. 49
Tsuneta S., Acton L., Ogawara Y., et al., 1991, Sol. Phys. 136, 37
Varady M., Heinzel P., 1997, In: Wilson A. (ed.) Proc. of the Fifth SOHO Workshop, ESA SP-404, 7p. 05
Wiik J.E., Schmieder B., Heinzel P., et al., 1996, Sol. Phys. 166, 89

EVIDENCE OF MAGNETIC FIELD RECONNECTION IN THE Hα ERUPTIVE PROMINENCE ON 18 SEPTEMBER 1995

P. KOTRČ, M. KARLICKÝ, S. ŠIMBEROVÁ, M. KNÍŽEK and M. VARADY
Astronomical Institute, Academy of Sciences of the Czech Republic, CZ–25165 Ondřejov, Czech Republic

(Received 1 December 1997; accepted 1 May 1998)

Abstract. In this paper we present a detailed study of a violent evolution of the 18 September 1995 eruptive prominence observed by the Hα telescope and the Multichannel Optical Flare Spectrograph in Ondřejov. The fast changes of the prominence structure started immediately after a weak radio burst at 3 GHz. This circumstance shows the presence of non-thermal processes. In the later phase of the prominence evolution a comparison of the Hα filtergrams with the *Yohkoh* Soft X-ray Telescope pictures was made. For a search of fine structures in the Hα images, an image processing technique was used. A detailed analysis of observations indicates magnetic field line reconnection, mainly in space below the rising Hα prominence. These reconnection processes are manifested not only by structural changes of the Hα prominence and X-ray loops but also by the character of Doppler velocities. Evidence of splitting and rotation was found in the Hα spectrum formed close to the reconnection space, and the typical velocities of such plasma movement were evaluated. We estimated amplitudes of rotational velocities, giving evidence about the rearrangement of helical structures during the process of the eruptive prominence activation. In the conclusion we discuss some implications of our results.

1. Introduction

It is commonly believed that eruptive processes in the solar atmosphere – solar flares or eruptive prominences – are physically connected to the magnetic field line reconnection process (see Rompolt, 1990; Švestka and Cliver, 1992; Tandberg-Hanssen, 1995; Tsuneta, 1996).

There are several papers trying to show good evidence of the reconnection or of the loop interactions, analyzing observational data. For example, the Proceedings from Symposium on Current Loop Interaction in Solar Flares (Sakai, 1993) shows several examples of current loop interactions. Furthermore, Šimberová, Karlický, and Švestka (1993) found indications of the reconnection in a large coronal arch. Studying coronal loops at visible wavelengths, Smartt *et al*. (1994) found localized brightenings and interpreted them as indirect evidence of magnetic field reconnection in those structures.

Recently, Pevtsov, Canfield, and Zirin (1996) presented observations of the 8 May 1992 flare associated with an Hα filament eruption. A twisted X-ray structure was formed shortly before the flare and disappeared after it, being replaced by a system of unsheared postflare loops. It was shown that the long S-shaped

Solar Physics **182:** 393–409, 1998.

structure appears to result from the reconnection of two shorter ones just tens of minutes before the filament eruption and flare. This was an example of filament eruption on the solar disk. Another S-shaped flare with possible reconnection has been observed recently by van Driel-Gesztelyi *et al*. (1997). In this case also a large reorganization of the magnetic field in the corona occurred. Such changes are connected with plasma flows ($\pm$ 50 km s^{-1}) as is shown in Wiik *et al*. (1997).

In this paper we present the 18 September 1995 Hα eruptive prominence which reveals fast structural changes. First we describe the eruptive prominence evolution with respect to all observations we have at our disposal. Later we analyse Hα images and spectra as well as soft X-ray pictures of the eruptive prominence structures. Then we study the Doppler velocities derived from the Hα spectra, because they could give more information about the eruptive prominence activation (Engvold *et al*., 1989) compared to simple filtergram analysis. We find fine structures in the prominence, and finally we discuss evidence of a magnetic field reconnection, and we present a schematic model of this phenomenon. Some preliminary results concerning this eruptive promimence study were already presented by Karlický *et al*., (1997).

2. Observations

2.1. Development of the eruptive prominence in optical and radio bands

The 18 September 1995 eruptive prominence (EP) situated on the north-east solar limb was observed by the Hα telescope and the Multichannel Optical Flare Spectrograph (MFS) in Ondřejov. Simultaneously accompanying weak radio emission was observed by the Ondřejov radiospectrograph. The activation of the prominence starts at about 09:15 UT by a slow rise of Hα loops. The slower phase of evolution of the Hα prominence lasts up to 09:40 UT, and then much faster processes followed. At the period from 09:39 UT to 09:41 UT, a weak radio burst on 3 GHz was observed. This circumstance indicates the presence of non-thermal processes. The GOES instrument registered the B 4.3 soft X-ray flare starting at 09:33 UT with a maximum at 09:43 UT.

Hα filtergrams are shown in Figure 1. In the snapshot taken at 09:40:40 UT we can see the prominence consisting of two cusp-shaped structures (see also Figure 9, where a special image processing method was used): a higher one is more open at the top, and the smaller one, which is shifted northwards (upwards on Figure 1), seems to be closed. Just this smaller structure forms a bubble-shaped loop in the following moments, see Figure 1 at 09:41:33 UT. Simultaneously, the bottom ends of this bubble-shaped loop started to interact with the higher cusp-shaped structure. This loop interaction process continues in the time interval from 09:42:36 to 09:43:12 UT, the northern side of the prominence rises to a higher

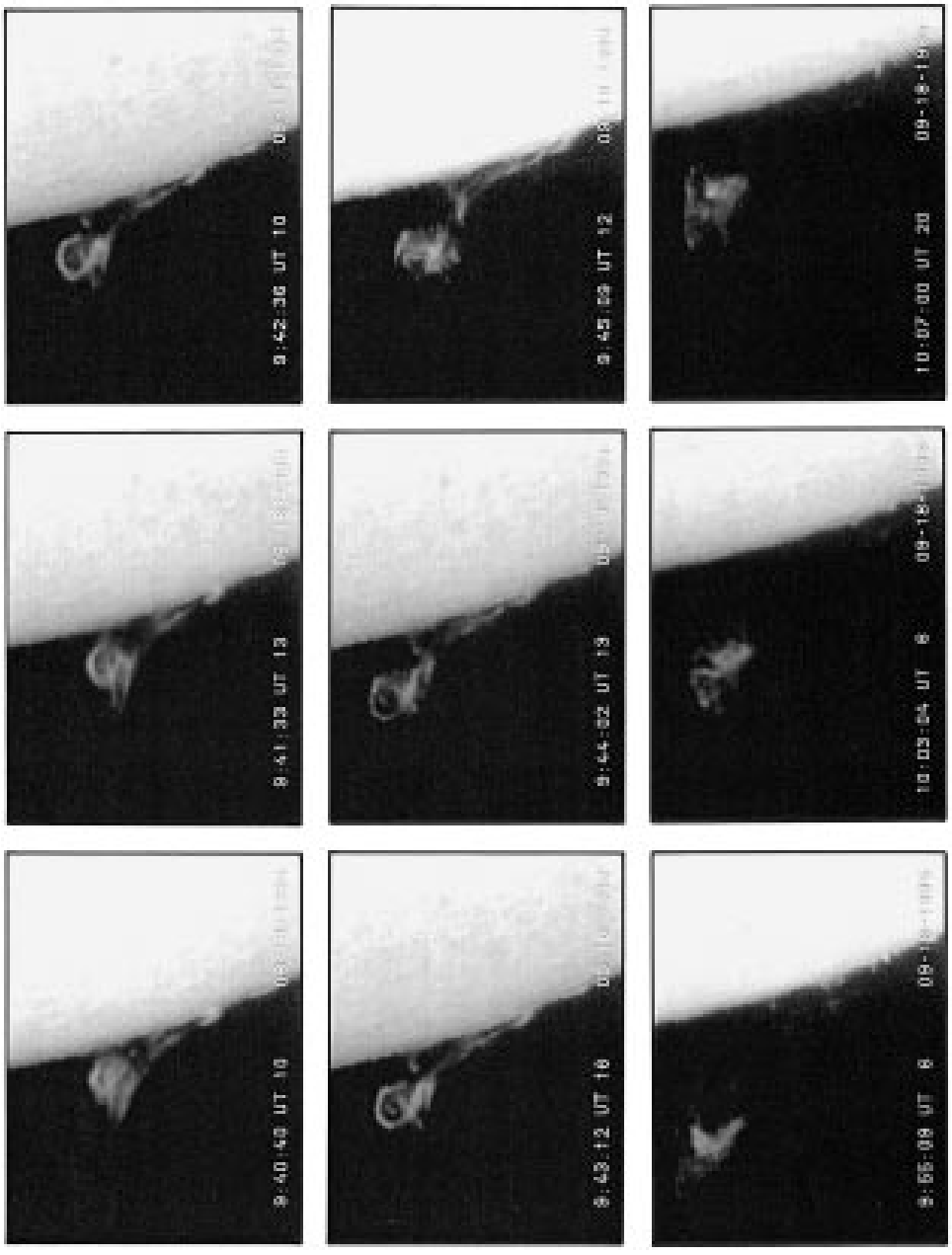

Figure 1. The evolution of the 18 September 1995 eruptive prominence observed by the Ondřejov Hα telescope.

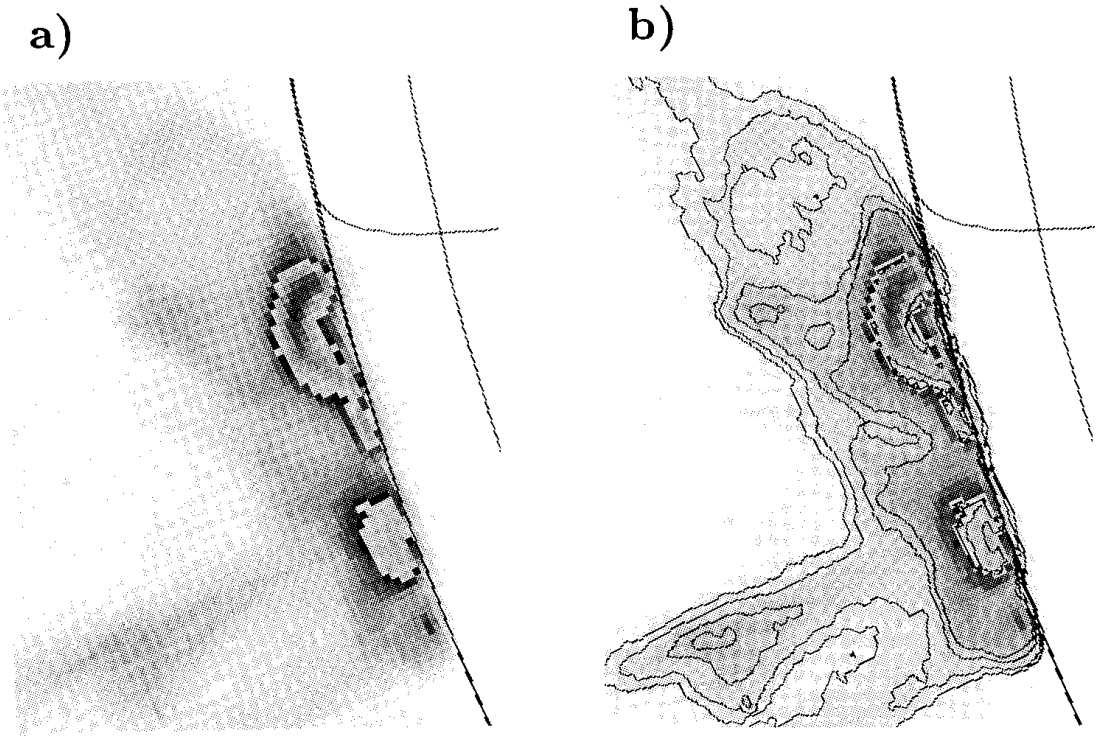

Figure 2. (a) Superposition of 5 pictures taken by *Yohkoh* SXT at times and filters: 10:03:43 UT (Al12), 10:04:15 UT (AlMg), 10:04:47 UT (AlMg), 10:05:19 UT (Al12), and 10:05:55 UT (AlMg). (b) The same as (a) but with contours (levels: 20, 30, 55, and 78 in shades of gray – black is 255).

coronal height and forms a circular structure at 09:44:02 UT. Simultaneously, the open ends of the initially higher cusp-shaped structure on the opposite side of the prominence reconnect. Then during a one-minute time interval (see 09:45:09 UT) a large chaotization of the circular structure takes place. In the following periods the prominence evolution becomes slower, but still its structure changes all the time, e.g., at 09:55:09 and 10:07:00 UT the 'helmet' structure, and at 10:03:04 UT the 'octopus' structure were observed.

2.2. Hα SPECTRA AND SLIT-JAW FILTERGRAMS

Simultaneously, we observed this eruptive prominence also by the Ondřejov MFS, equipped with a videosystem for fast monitoring of the Hα spectrum and slit-jaw pictures (Kotrč, Heinzel, and Knížek, 1993). The spectra registered on the video cassette recorder (VCR) were digitized on the DIPIX frame-grabber at 8 bit dynamical range and in a window of the size 620 × 570 pixels. The angular size of 1 pixel was equivalent to 1 arc sec, while in the direction of dispersion it represented approximately 0.1 Å per pixel. Then the wavelength scale for each spectrum was derived to calibrate the Doppler component velocity scale.

2.3. X-RAY PICTURES

The *Yohkoh* Soft X-ray Telescope (SXT) observed this phenomenon only in its final phase, the first picture was observed at 09:59:37 UT. In the individual pictures one can see that the bright structure near the limb is very dynamic and it is changing substantially from picture to picture. On the other hand, the weak structure located under the Hα prominence is quite static. In order to improve the signal to noise ratio of the weak structure we are interested in, we superposed 5 pictures (see Figure 2). To avoid over-exposure due to the dynamic bright structure near the limb, we removed it from all of the superposed pictures. Then we copied into this empty part of the resulting picture the bright structure taken from picture exposed at 10:05:55 UT. Using this procedure we stressed the weak X-like structure (see Figure 2(a) and 2(b) above the X-ray loop) which is now much more easily visible than in the individual pictures. Thus we can consider it to be a real phenomenon and not only an accidental fluctuation.

To show positions of both Hα and soft X-ray structures, we made a superposition of these pictures giving information about cool and hot plasma. The resulting pictures are shown in Figure 3. Although the times in Figure 3(a) are not just the same as in the optical observations, we present this comparison to show the time evolution of the Hα structure with respect to the hot X-ray loop and to understand better changes of the magnetic field lines.

Besides the Hα interacting loops shown in Figures 1 and 9, interacting X-ray loops were also recognized in Figure 2(a). To relate this hot X-ray structure to the cool Hα one, we made a composite image (see the arrow in Figure 4 showing these interacting X-ray loops in the shape of the letter X). They are situated above the closed X-ray loop but below the Hα erupted prominence material.

3. Doppler Velocity Components

The Hα spectra of the EP obtained with the MFS and registered at high temporal resolution on the video tape recorder were processed to derive Doppler velocity components of both the bulk translational and rotational movement of the prominence plasma. We used an IDL 'curve-fit' procedure to fit the measured line profiles of the EP by a gaussian or a sum of two gaussians. The resulting approximation is relatively good, as can be found in Figure 5 where typical examples of the split Hα line profiles, including evaluated Doppler velocities of the components, can be seen. As the brightness of the erupting prominence in some points increased very much, some Hα slit-jaw pictures and especially the VCR-monitored Hα spectra became over-exposed (see Figure 5 the lower right profile taken at 09:43:24 UT at position 100). This circumstance, however, should not influence the estimation of Doppler velocities as the individual profile components are symmetrical and distinguishable.

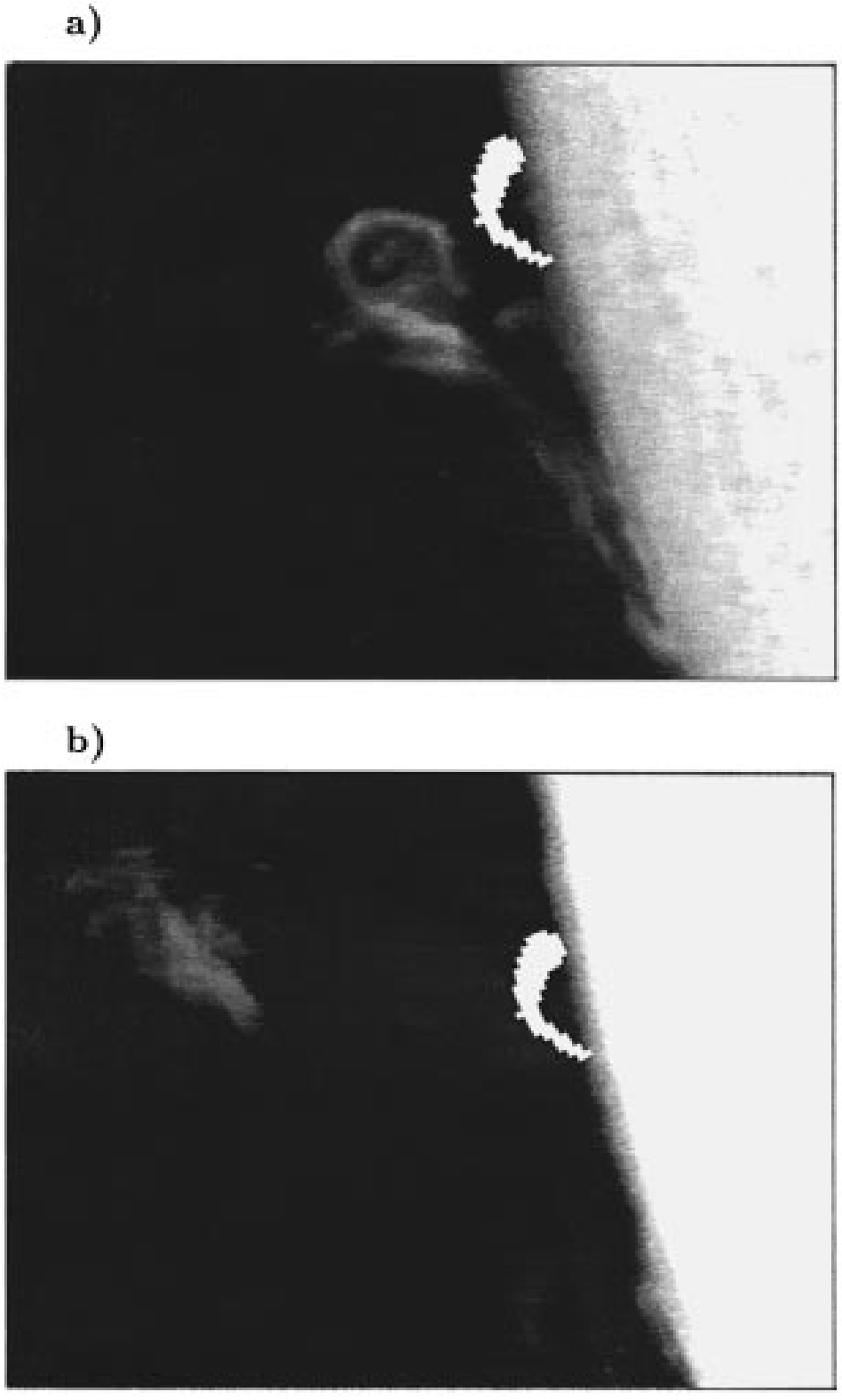

Figure 3. (a) Superposition of the Hα eruptive prominence at 09:43:12 UT and *Yohkoh* SXT flare loop at 09:59:37 UT; (b) superposition of the Hα eruptive prominence at 09:59:15 UT and *Yohkoh* SXT flare loop at 9:59:37 UT.

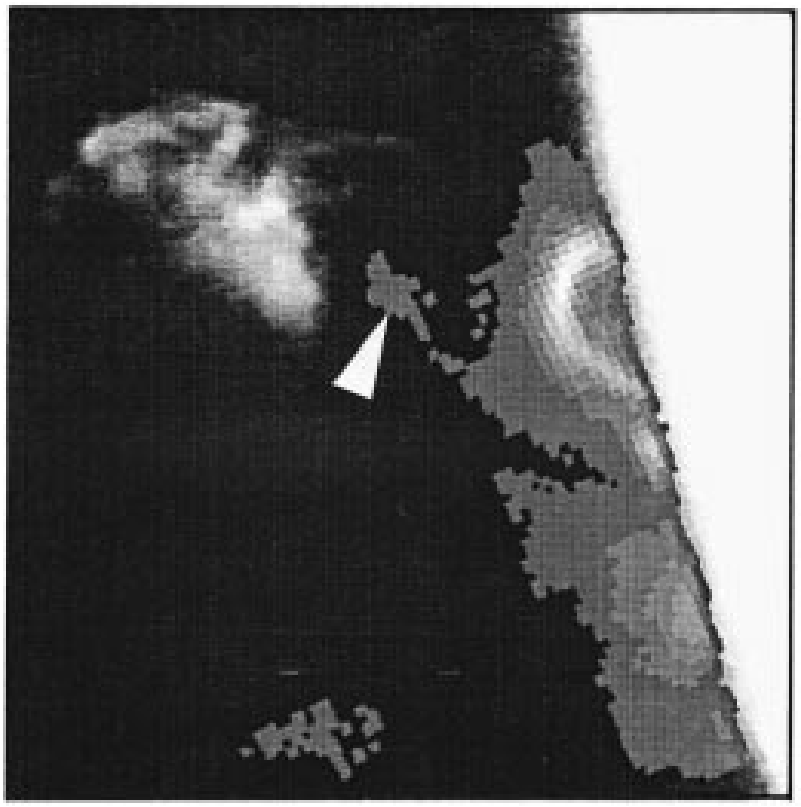

Figure 4. Superposition of the Hα eruptive prominence at 10:04:15 UT and *Yohkoh* SXT flare loops at 10:04:15 UT. The arrow shows interacting soft X-ray loops.

Three interesting Hα spectra with the position of the spectrograph slit are shown in the left-hand side of Figure 6. They display spectral patterns typical for the phase of the dynamic activation of the EP. The spectrograph slit scanning the EP was put just on the interacting loops.

In the top part of the Hα spectrum in Figure 6 we can see an inclined pattern as evidence of the plasma rotation or a plasma movement along a loop. As a matter of fact, such an inclined pattern on a scale of more than 50 000 km could be observed already an hour before the phase of the prominence activation (see top of Figure 7 observed at 08:52:26 UT!), and it lasted in some places and in a changing measure till the latter phases of its development. In the central part of Figure 7, taken at 09:41:58 UT, one can see two inclined patterns that can be interpreted as an effect of combined splitting and rotation in the EP plasma structure. The spectral pattern in the bottom part of Figure 7 shows isolated split nodes with Doppler component velocities even larger than 150 km s^{-1}. This situation was typical for the fast restructuring of the 'octopus' structure.

It is important to point out that when comparing Figure 1 to Figures 6 and 7 one can find a very crucial moment: At the places where the slit of the spectrograph cuts *the contacts of individual loops*, (i.e., at the bottom of the circular prominence structure) the Hα spectra showed large brightening and substantial splitting. Thus

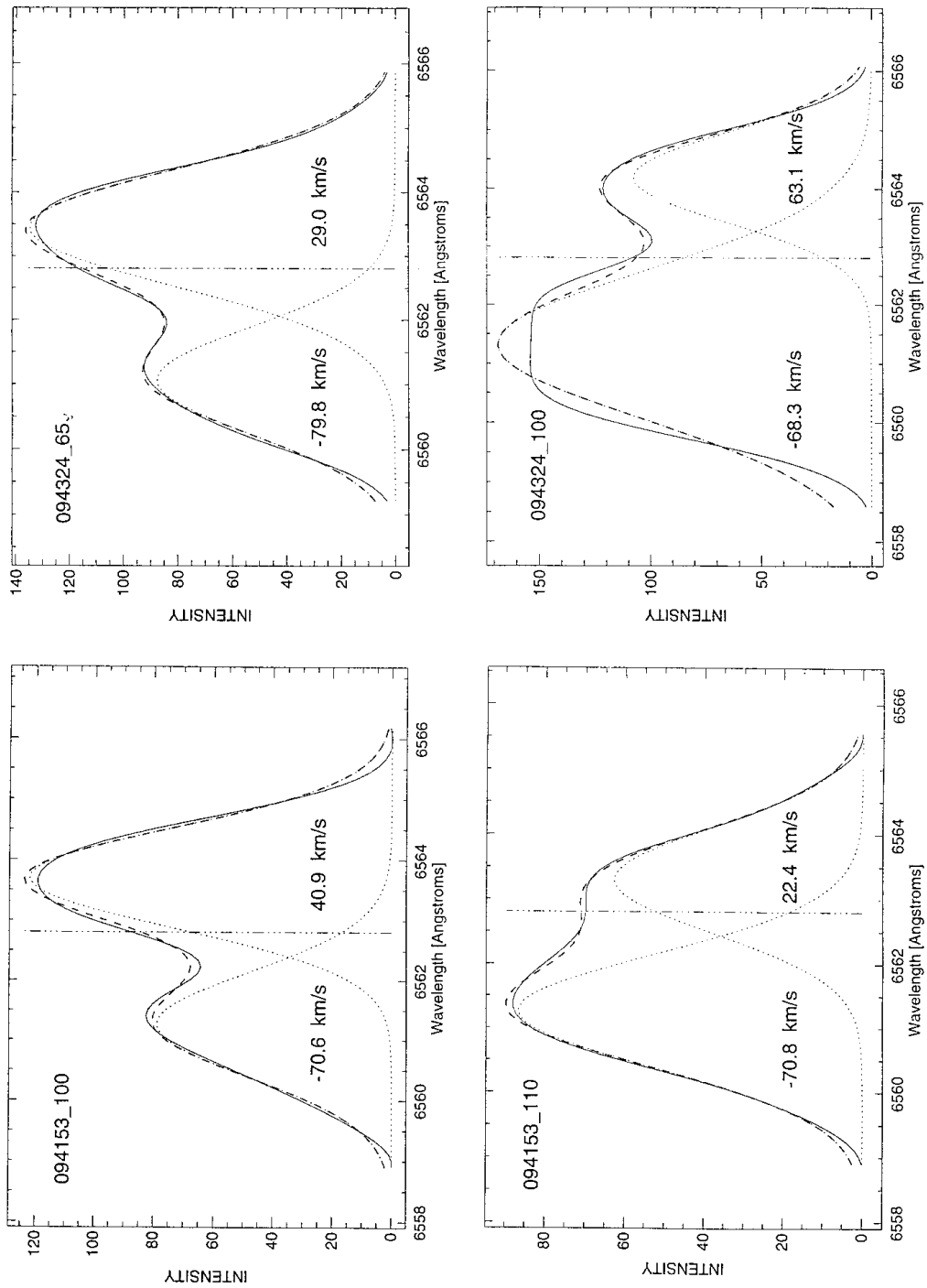

Figure 5. Hα line profiles (full line) were well approximated by the sums (dashed) of two gaussians considered to be the Doppler-velocity-separated components. The vertical line marks the position of the undisturbed Hα line center. The values in the graphs mean time and position in the spectra and the corresponding velocities of the two components.

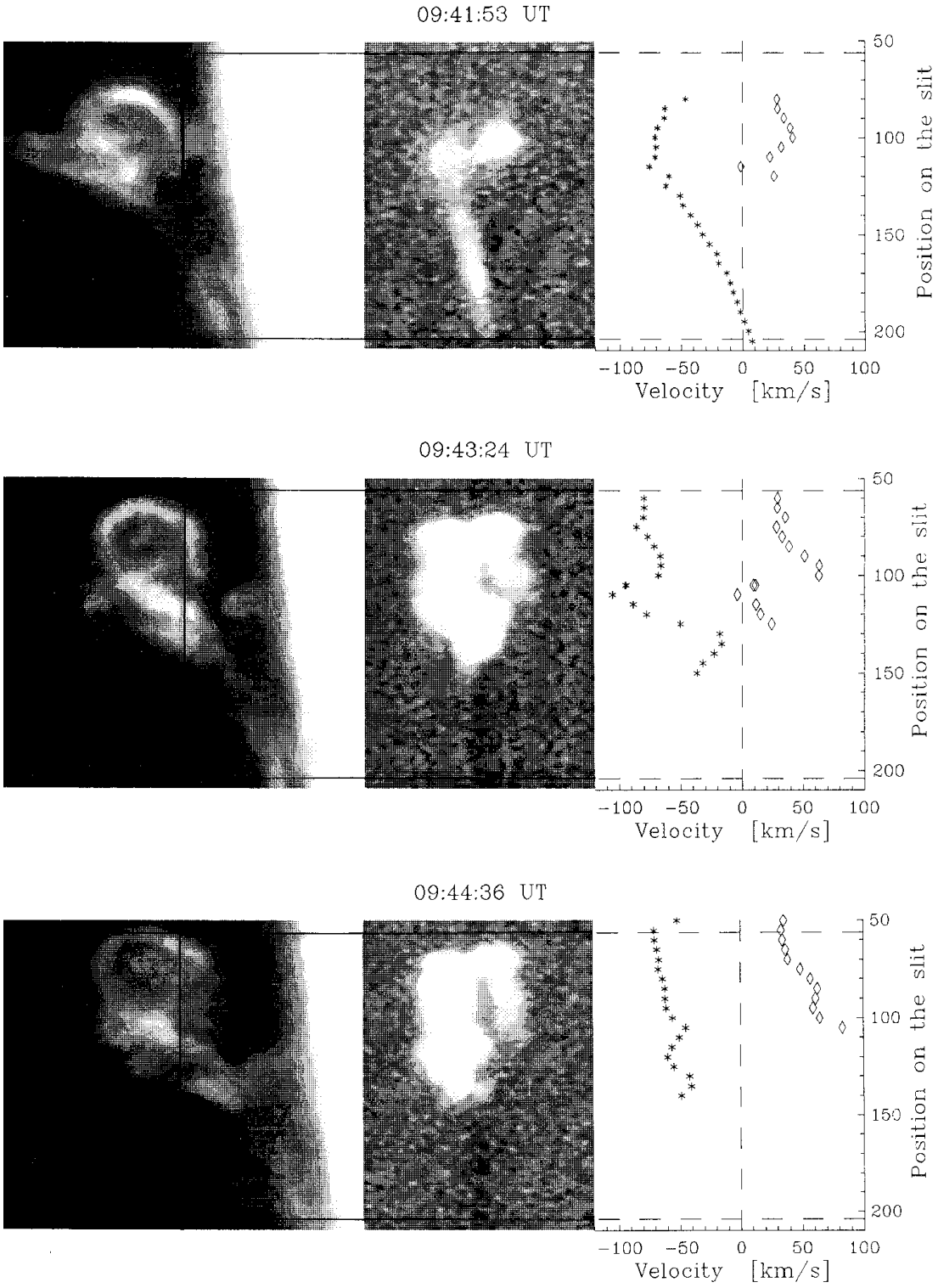

Figure 6. Slit-jaw pictures of the eruptive prominence are on the left-hand side (position of the slit is identical with a black vertical line); corresponding Hα spectra observed by the video system are in the center, while charts of evaluated Doppler velocities are on the right-hand side.

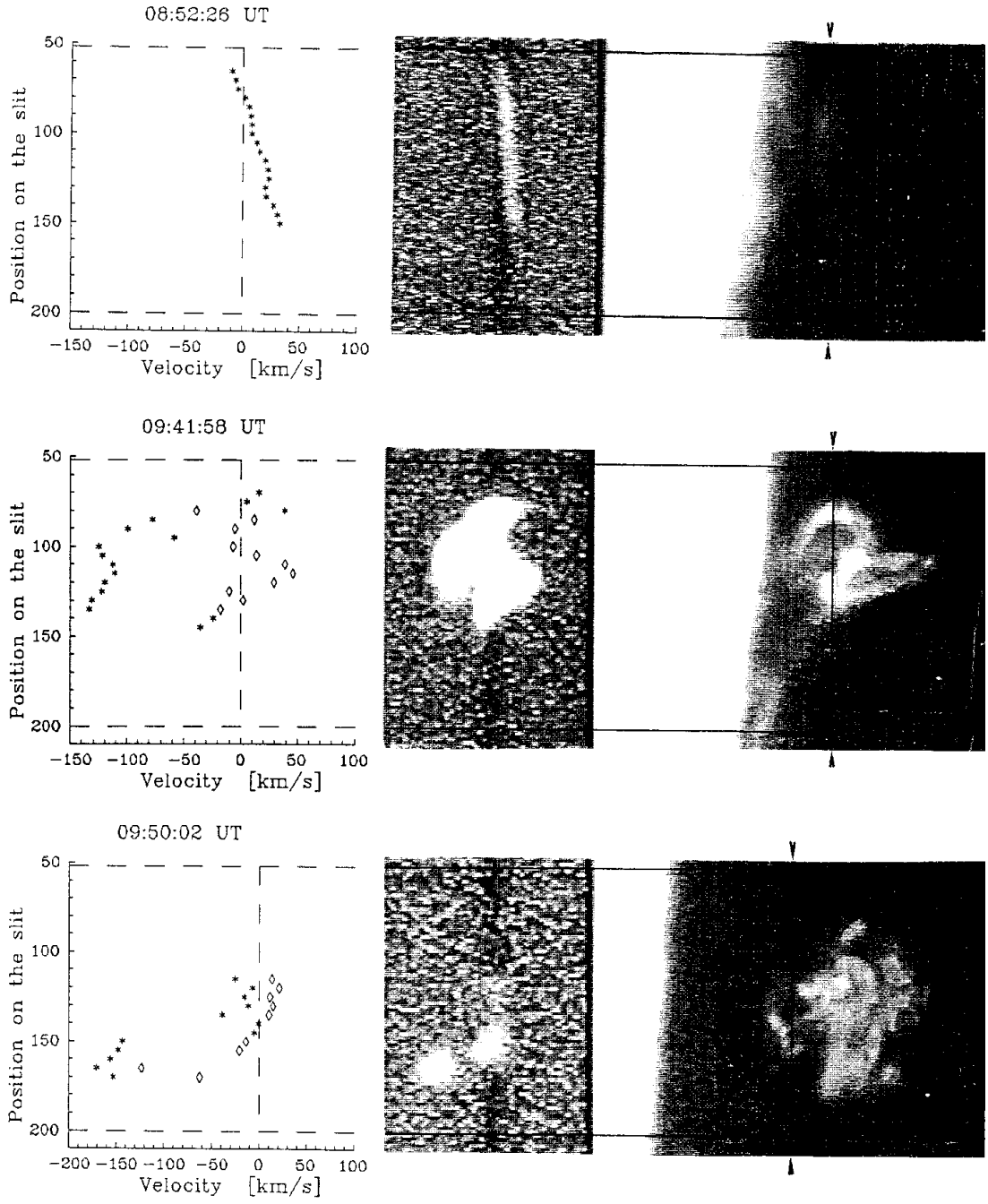

Figure 7. Long-time development slit-jaw pictures of the eruptive prominence (left-right reversed when compared to the previous Figure 6) are on the right-hand side (position of the slit is marked by black arrows); corresponding Hα spectra are in the center and Doppler velocity values are displayed on the left-hand side.

the Hα line was split into two Doppler-velocity-separated red- and blue-shifted and at the same time very bright components. We consider these phenomena to be dynamic interactions of individual loops and/or processes related to the magnetic field reconnection. As a matter of fact, this splitting can be interpreted both as an inflow of the plasma into a central point and as an outflow from such a point. Only a comparison of the data with other facts and taking into account the physics of the supposed processes, can find the right interpretation.

Interpreting the Hα filtergrams (see Figures 1 and 6) one can keep all the time in mind that the passband halfwidths of the Hα filters used were only 0.7 Å, while the Doppler velocity component values obtained from the Hα spectra were often higher than 50 km s^{-1}. This means that those interesting high-velocity structures cannot be principally seen in the Hα filtergrams obtained, as they are out of the filter passband range.

As noticed above, the inclined patterns in the Hα spectrum occurred in some parts of the EP practically during all its development (see top parts of Figures 6 and 7). This effect was studied by Kotrč, Korčáková, and Kupryakov (1998). They supposed it can be explained by movement of the plasma in a rotating cylindrical pattern, as suggested by Rompolt (1975) and Rompolt and Mzyk (1978). For evaluation of the rotational velocities in such a pattern, a simple model of a rotating prominence thread in the shape of a rotating cylinder crossing the slit was constructed. Doppler velocity components in such a rotating cylinder produce a similar inclined spectral pattern. The resulting measured line-of-sight velocity v_l can be expressed as a sum

$$v_l = v_t + v_r \ ,$$

where the bulk translational velocity v_t represents the cylinder movement velocity component and v_r is the rotational velocity component depending linearly on the radius r of the cylinder: $v_r = \omega r$, and ω is the cylinder angular rotational velocity.

The cross-section of the cylinder with the slit can be evaluated from the shape of the spectrum. Two angles between the axes of the cylinder and the slit can be adjusted in the model. Matching both v_t and ω of the cylinder, one can find the best approximation to the rotational pattern of the spectrum. In Figure 8 one can see a good approximation of the inclined top pattern from Figure 6 taken at 09:41:53 UT. We can match the inclined spectrum with either a rotating cylinder or a plasma loop. In the first case the radius of the cylinder is then estimated to be $r = 28\,000$ km, $\omega = 0.0015$ rad s^{-1} and $v_t = -65$ km s^{-1}. In the other case (plasma moving along a loop) we find $\omega = 0.0023$ rad s^{-1}, radius of the loop will be $r = 56\,000$ km and the bulk translational velocity v_t becomes zero. On this assumption, we can estimate typical rotation velocities in the inclined spectral pattern of the order about 50 km s^{-1}.

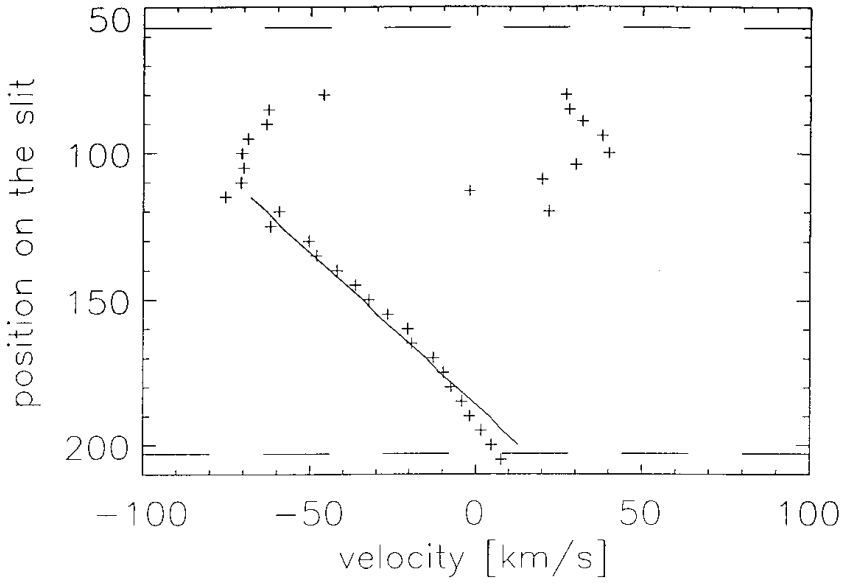

Figure 8. Evaluation of the Doppler velocities in the Hα spectrum of a rotating structure. The inclined pattern is approximated by a line representing a cylindrical rotation.

4. The Search for Hα Prominence Fine Structure

The Hα digital images in the time interval 09:40–10:07 UT were analyzed by an image processing technique to find the fine structures in this event. A special processing method first described by Šimberová and Suk (1993) and applied to *Skylab* image data (see Šimberová, Karlický, and Švestka, 1993) was modified and the new algorithms based on the cumulative histogram (CH) optimization of density in the local area have been designed. The local area (sub-image) is determined around each pixel of an input image. In this sub-image a general idea of histogram equalization mapping has been used (see, e.g., Ballard and Brown, 1982), but differently the cumulative histogram is computed only to the intensity level of the central pixel of the local area. Then the value of CH is given as

$$\mathrm{CH} = \int_0^S h(s)\,\mathrm{d}s\ , \tag{1}$$

where s is a particular gray level in the intensity interval, $h(s)$ the number of pixels in the sub-image with that gray level, and S is the gray level of the central pixel.

The most important processing step is the size and shape options of the local area. Several tests to choose the local area shape (rectangular, triangle, ellipse and circle) led to the optimal shape selection. In the case of prominence analysis a circle shape has been determined. In compliance with our tests, a circle is the most convenient shape for enhancement in the image objects consisting of the circular parts. Another step is the optimal size selection. The various area sizes were tested,

and it was proved that the local size area depends approximately on the image size which the object covers.

Then, using the modified histogram equalization transformation, the new gray level of the central pixel of the circle area is

$$\mathrm{CP} = \frac{M}{\pi R^2} \int_0^{S-1} h(s)\, \mathrm{d}s \ , \tag{2}$$

where R is the radius of the local area in pixels and M is the number of gray levels.

Examples of the processed Hα images are shown in Figure 9. Comparing these images with the original ones, we can see that some features are expressed more distinctly. For example, in Figure 9(a) (at 09:40:40 UT) the small loop shows the cusp structure above its top (see arrow). On the other hand, Figures 9(b) and 9(c) (09:42:36 UT and 09:43:12 UT) show (see arrows) places of probable reconnection. The last example (Figure 9(d), at 10:03:04 UT) represents a very interesting 'octopus' structure, which is very rapidly changing.

5. Interpretation

A simplified scheme of the complex evolution of the 18 September 1995 prominence and places of the magnetic field line reconnection are shown in Figure 10. We assume the magnetic field lines to be parallel to the shape of the Hα loops. Obviously, only their relative orientation is important for reconnection. It is interesting that at the beginning of the evolution, the upper part of the Hα prominence shows cusp structures. When studying the EP development in all the available observations we found three places (I, II, and III – see Figures 9 and 10) where the magnetic field reconnection is very probable.

We think that the reconnection alone can explain the fast changes of the prominence structure as well as the occurring brightenings and patterns of splitting in the spectra. The most important reconnection process was probably at place III. Namely, the reconnection can explain not only changes of the prominence observed in Hα (circular structure), but also the presence of a closed X-ray loop observed below this reconnection place by the *Yohkoh* satellite (Figure 3, in Figure 10 this hot loop is expressed by dotted lines). This reconnection scenario can also be supported by the observation of the X-ray loop interaction pattern (hot loop crossing in the shape of the letter X) in space between the closed X-ray loop and the rising Hα prominence (Figures 2, 4, and 10).

The Hα line splitting into red and blue Doppler-shifted components at place III represents further evidence of the reconnection process. Namely, as known from the theory of magnetic field reconnection in a simple 2-D current sheet, a plasma with the magnetic field flows into the X-point where the reconnection process takes place (e.g., Priest, 1981). We suggest that just in the inflowing plasma (in

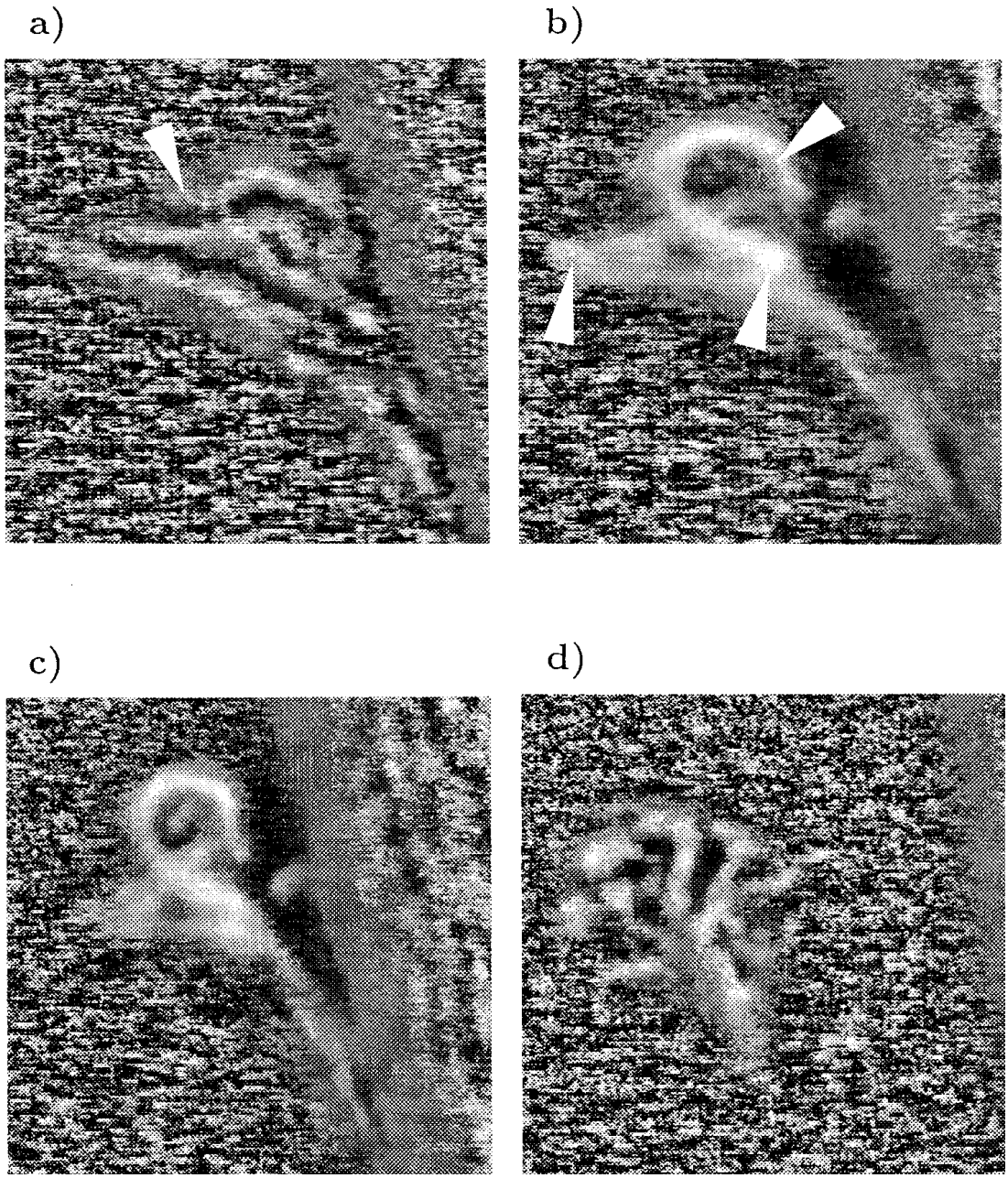

Figure 9. The Hα processed images: (a) 09:40:40 UT, optimization of density in the local circle area with radius $R = 10$ pixels. The arrow shows the cusp structure above a small Hα loop; (b) 09:42:36 UT, and (c) 09:43:12 UT, optimization of density in the local area with radius $R = 40$ pixels. The arrows show places of probable reconnection; (d) an 'octopus structure' at 10:03:04 UT, optimization of density in the local area with radius $R = 16$ pixels.

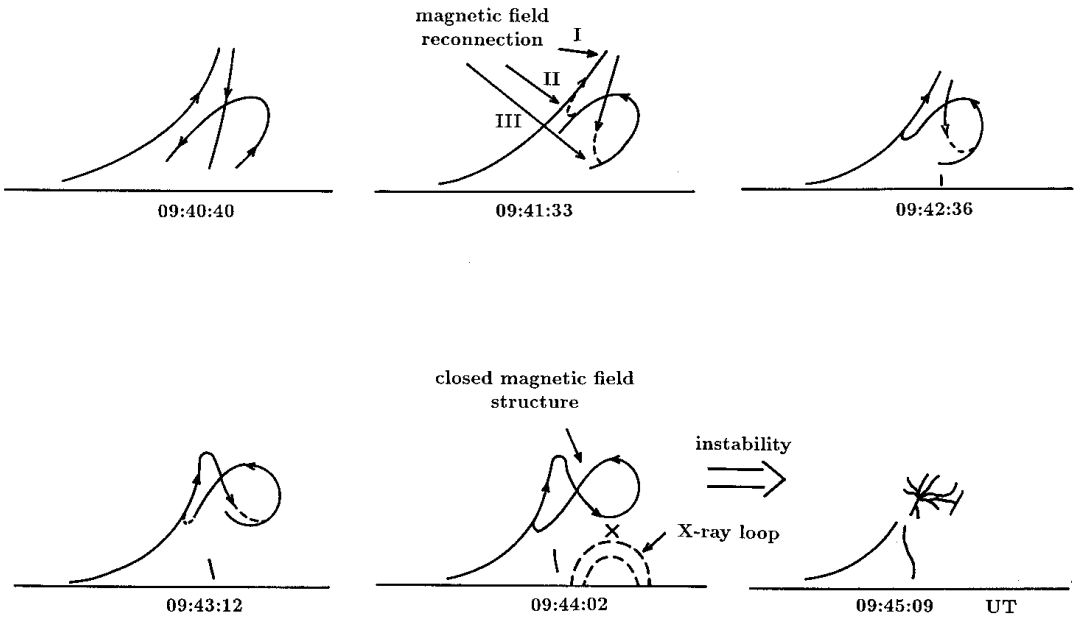

Figure 10. Scenario of the Hα eruptive prominence evolution and magnetic field reconnection. Only relative orientation of the magnetic field lines is important.

the direction from and towards an observer – see Figure 6) the enhanced and split Hα emission is generated at the place III. The other alternative of the spectrum splitting interpretation – the reconnection outflows – was excluded because the outflowing plasma is hot and then it would not be visible in the Hα line. Moreover, the outflow plasma speed corresponds roughly to the Alfvén speed (about 1000 km s^{-1} at the conditions considered) which is much higher than the observed velocities. Therefore the Doppler velocity components in the Hα spectrum are interpreted as a centerward velocity field of the inflowing plasma into the place of reconnection, i.e., center of the plasma contraction. Typical values of the inflow velocity derived from our spectra are of the order 50–100 km s^{-1}. But clearly, in the 3-D reconnection geometry, the plasma flow pattern can be more complicated. Some complexity is found also in this case. For example, the rotational movement detected in the Hα spectra indicates rebuilding of twisted magnetic field lines.

6. Conclusions

The structural changes of the 18 September 1995 Hα eruptive prominence, the 3 GHz radio burst, accompanied X-ray loops and the Doppler velocities derived from spectral observations indicate evidence for the occurrence of magnetic field reconnection in this prominence.

About an hour before the start of the prominence activation inclined patterns in the Hα spectrum were observed and lasted in some places till the prominence disappeared. This gave good evidence about the magnetic field rearrangement dur-

ing and after the process of activation. During the evolution of this prominence the neighbouring prominence loops interacted; a closed hot X-ray loop and a circular Hα structure were generated below and above the interaction point. The X-point of the magnetic field reconnection is expected just between both these structures. This idea was confirmed by an observation of the X-ray interacting loops later on. A unique argument in favour of the reconnection was found as a result of analysis of the Doppler velocities in the Hα spectrum. Namely, the Hα spectrum from the reconnection point was split into red- and blue-shifted bright components. The observation was interpreted as the centerwards plasma inflow into the reconnection place. The inflow plasma velocity was derived to be 50–100 km s^{-1}. The amplitudes of rotational velocities occurring in the eruptive prominence on a spatial scale of more than 50 000 km were estimated to be of the order of about 50 km s^{-1}.

Although in this phenomenon we found several arguments which fit very well with the reconnection scenario, there is a principal limit in the interpretation of the 2-dimensional observations. From the third dimension we have only information concerning the Doppler velocity components, and thus this limitation can be overcome only by stereoscopic, multi-wavelength observations.

Acknowledgements

The authors acknowledge the support of the Grant Agency of the Academy of Sciences of the Czech Republic via grant No. A3003707, the grants of the Grant Agency of the Czech Republic Nos. 205/96/1199 and 205/95/0293, and the Key–Projects K1–003–601 and K1–043–601. Technical help of D. Korčáková and Yu. A. Kupryakov is also highly appreciated.

References

Ballard, D. H. and Brown, M. C.: 1982, *Computer Vision*, Prentice-Hall, Englewood Cliffs, p. 70.

Engvold, O., Jensen, E., Zhang, Yi., and Brynildsen, N.: 1989, *Hvar Obs. Bull.* **13**, 205.

Karlický, M., Kotrč, P., Knížek, M., Šimberová, S., and Varady, M.: 1997, in D. Webb (ed.), 'New Perspectives of Solar Prominences', *Proceedings IAU Colloquium* **167**, *Publications of the Astronomy Society Pacific*, in press.

Kotrč, P., Heinzel, P., and Knížek M.: 1993, in A. v. Alvensleben (ed.), *JOSO Annual Report 1992*, Freiburg, p. 114.

Kotrč, P., Korčáková D, and Kupryakov, Yu. A.: 1998, *Proceedings of the Kanzelhöhe Solar Physics Workshop*, Kluwer Academic Publishers, Dordrecht, Holland, in press.

Pevtsov, A. A., Canfield, R. C., and Zirin, H.: 1996, *Astrophys. J.* **473**, 533.

Priest, E. R.: 1981, *Solar Flare Magnetohydrodynamics*, Gordon and Breach Sci. Publ., New York.

Rompolt, B.: 1975, *Solar Phys.* **41**, 329.

Rompolt, B.: 1990, *Hvar Obs. Bull.* **14**, 37.

Rompolt, B. and Mzyk, S.: 1978, In E. Jensen, P. Maltby, and F. Q. Orrall (eds.), 'Physics of Solar Prominences', *Proc. Colloq. IAU* **44**, 242.

Sakai, J. (ed.): 1993, *Proceedings of Symposium on Current Loop Interaction in Solar Flares*, Toyama University.

Smartt, R. N., Zhang Z., Kim, I. S., and Reardon, K. P.: 1994, in V. Rušin, P. Heinzel, and J.-C. Vial (eds.), 'Solar Coronal Structures', *Proc. IAU Colloq.* **144**, 219.

Šimberová, S. and Suk, T.: 1993, *Lecture Notes in Computer Science*, Vol. 719, Springer-Verlag, Berlin. p. 759.

Šimberová, S., Karlický, M., and Švestka, Z.: 1993, *Solar Phys.* **146**, 343.

Švestka, Z. and Cliver, E. W.: 1992, in Z. Švestka, B. Jackson, and M. Machado (eds.), *Eruptive Solar Flares*, Springer-Verlag, Berlin, p. 1.

Tandberg-Hanssen, E.: 1995, *The Nature of Solar Prominences*, Kluwer Academic Publishers, Dordrecht, Holland.

Tsuneta, S.: 1996, *Astrophys. J.* **456**, L63.

van Driel-Gesztelyi, L., Manoharan, P. K., Pick, M., and Démoulin, P.: 1997, *Adv. Space Res.* **19**, 1883.

Wiik, J. E., Schmieder, B., Kucera, T., Poland, A., Brekke, P., and Simnett, G.: 1997, *Solar Phys.* **175**, 411.

HOLES IN THE Hα ERUPTIVE PROMINENCE STRUCTURE

STANISLAVA ŠIMBEROVÁ[1], MARIAN KARLICKÝ[1], MICHAL VARADY[1] and GERHARD RANK[2]

[1]*Astronomical Institute, Academy of Sciences of the Czech Republic, 25165 Ondřejov, Czech Republic (e-mail: ssimbero@asu.cas.cz)*

[2]*Max-Planck-Institut für extraterrestrische Physik, Postfach 1312, 85741 Garching, Germany*

(Received 10 September 2000; accepted 8 February 2001)

Abstract. The eruptive prominence observed on 27 May 1999 in Hα at Ondřejov Observatory is analyzed using image-processing techniques. To understand the physical processes behind the prominence eruption, heated structures inside the cold Hα prominence material are sought. Two local minima of intensity (holes), the first above and the second below the erupting Hα prominence, have been found in the processed Hα images. A comparison of Hα images with the SOHO/EIT and *Yohkoh*/SXT images showed: (a) the cold Hα prominence is visible as a dark feature in the EIT images, (b) the upper local minimum of intensity in the Hα image corresponds to a hot structure seen in EIT, (c) the lower minimum corresponds to a hot loop observed by SXT. The physical significance of the Hα intensity minima and their relation to the hot structures observed by EIT and SXT is discussed. The time sequence of observed processes is in favor of the prominence eruption model with the destabilization of the loop spanning the prominence. For comparison with other events the velocities of selected parts of the eruptive prominence are determined.

1. Introduction

Due to their close connection to coronal mass ejections (CMEs) interest in all aspects of prominences, especially of eruptive prominences (EPs), is increasing (Schmieder *et al.*, 1997; Wang and Sheeley, 1999; Wood *et al.*, 1999; Ciaravella *et al.*, 2000). Their formation, structure, evolution, and stability have been studied in many papers (Engvold and Rustad, 1974; Tandberg-Hanssen, 1974; Engvold, Malville, and Rustad, 1976; Schmahl and Hildner, 1977; Rompolt, 1978, 1990; Moore, 1988; Vršnak, Ruždjak, and Rompolt, 1991). While the traditional studies tried to explain how the cool and dense prominence material is supported, now, in connection with CMEs, it is often asked why prominences eventually erupt. One possibility based on the critical twist of the prominence magnetic rope was suggested by Vršnak, Ruždjak, and Rompolt (1991). In several recent papers indications of an extended magnetic loop above the Hα prominence have been found (Dere *et al.*, 1999; Plunkett *et al.*, 2000). Furthermore, the statistical results of Feynman and Martin (1995) indicate that prominences erupt due to the emergence of a new magnetic flux. In a recent paper by Wang and Sheeley (1999) it was found that the new flux may act as a strong catalyst, but that it is not a necessary condition for the filament destabilization. On the other hand, during the prominence erup-

Solar Physics **201:** 119–131, 2001.

tion, interactions of magnetic loops and magnetic field reconnections are highly probable. An example of such processes was presented in a paper by Kotrč *et al.* (1998).

Several models of CMEs including EPs were suggested. Chen (1996) presented a model of a prominence eruption based on the instability of an extended magnetic flux rope. Wu, Guo, and Dryer (1997) have developed a $2\frac{1}{2}$-D model with a flux rope in the corona. In the Antiochos, DeVore, and Klimchuk (1999) model the reconnection removes the unsheared field above a low-lying, sheared core flux near the neutral line, thereby allowing this core flux to burst open.

Here, we continue our previous studies of EPs. In accordance with Priest (1982) and Vršnak *et al.* (1988) we assume that the magnetic pressure in the prominence dominates the thermal one; the β parameter expressing the thermal-magnetic pressure ratio is much less than 1. Moreover, the prominence plasma is highly conductive. In this case, the structural features of the observed prominence follow the magnetic field lines. Using special image-processing techniques, the 27 May 1999 prominence is analyzed from a structural and evolutional point of view. We search for the heated hot loops in the structure of the cold Hα prominence during its eruption. Namely, the presence of the hot loops indicates heating processes at these positions. In this way we try to understand processes during the early phases of the prominence eruption, which are according to our knowledge still not well known.

2. Image-Processing Methods

Several image-processing methods have been used to analyze Hα images obtained at the Ondřejov Observatory, and SOHO/EIT 195 Å images of the examined EP.

To process and analyze the development of the prominence in Hα images a method of local optimization of density (LOD) was applied. As known from previous studies (Šimberová, Karlický, and Švestka, 1993; Šimberová and Suk, 1993; Kotrč *et al.*, 1997; Plunkett *et al.*, 2000), the LOD method gives information about hidden structures in 2-D images. It is very efficient in such areas, where the changes of density are small, and where any global method of image restoration cannot give any satisfactory result.

From the image-processing point of view, the most important attributes of the applied LOD method are the size and shape of visible patterns being presented in the image. Statistical recognition of these patterns led to the determination of local area, where the density transformation is performed. The method was tested for rectangular, square, circular and elliptical local areas. It was found that the last two shapes are the most convenient for processing the images of prominences, whose internal texture consists of 'bubbles' and partly curved patterns. The principle of the algorithm, based on computing of the cumulative histogram within the local

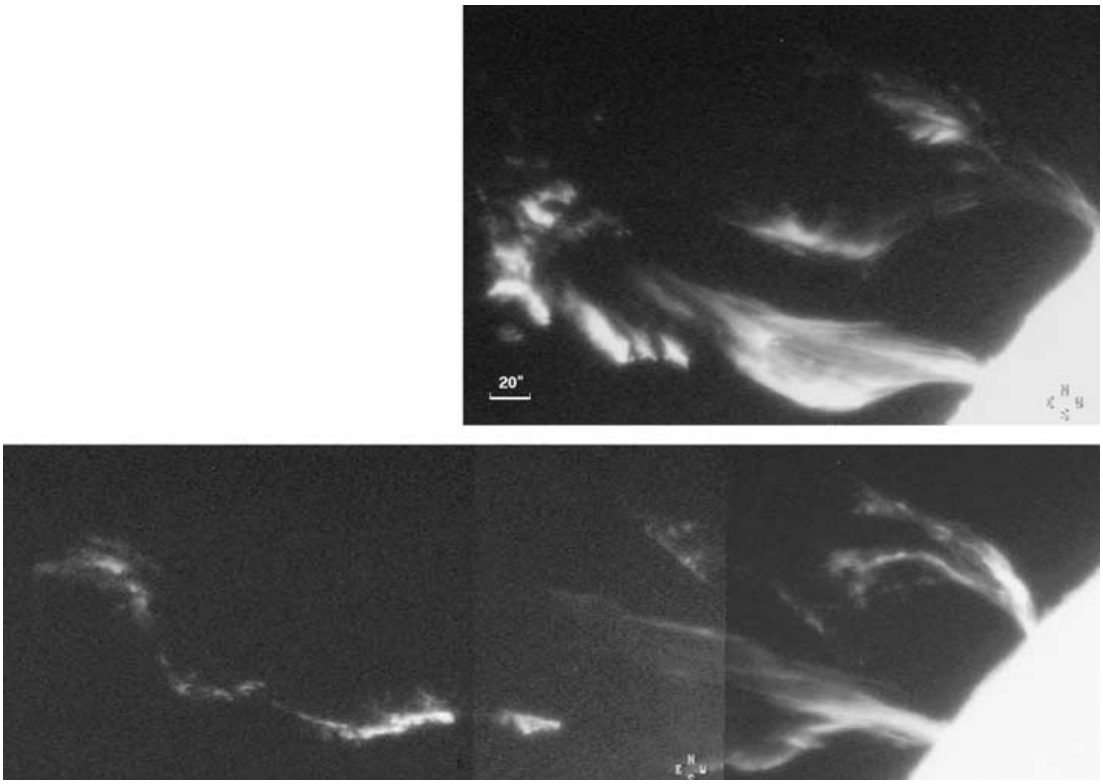

Figure 1. The Hα eruptive prominence observed at Ondřejov Observatory at 14:29:56 UT (*upper panel*) and at 14:36:39 UT (*lower panel*).

areas, is explained in Šimberová and Suk (1993), and a modification of the method was used in Kotrč *et al.* (1997), and Plunkett *et al.* (2000).

Furthermore, the Hα images were processed by a smoothing technique (ST). The smoothing by a wide convolution mask followed by a segmentation into appropriate number of strips of density was performed.

To get more information on the investigated objects in the EIT images, a digital filter technique (DF) was used to sharpen the images. The data was processed in the spatial domain. To enhance the visibility of the prominence structure a Laplacian operator was applied to the sub-images 80×80 pixels. The Laplacian operator is an approximation to the linear second derivative of brightness in directions x and y. It is invariant to rotation and insensitive to the direction in which the discontinuity runs. This highlights the points and edges in the image and suppresses uniform and smoothly varying regions (see, e.g., Russ, 1995).

3. Observed Data Description and Analysis

The Hα images obtained from the Ondřejov Observatory are combined with the images from SOHO/EIT (Delaboudinière *et al.*, 1995), SOHO/LASCO (Brueckner *et al.*, 1995), and *Yohkoh*/SXT (Acton *et al.*, 1989).

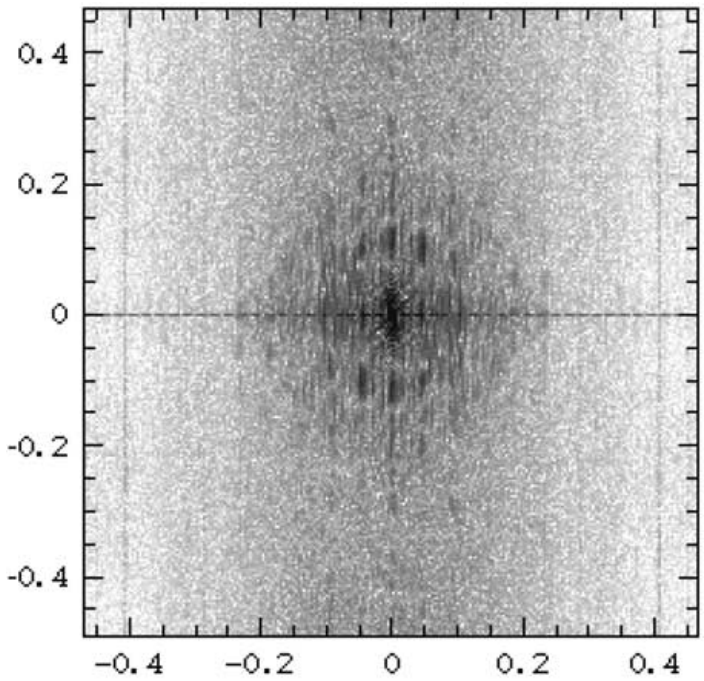

Figure 2. Fourier-transform (inverse log power spectrum) image of the Hα prominence at 14:29:56 UT. The frequency values are relative to the sampling frequency.

The EP under study was observed on 27 May 1999 in the active region NOAA 8555 (N15 E72) close to the north-east solar limb. The eruption started between 14:06–14:08 UT, when a U/III-type radio burst, giving evidence of the presence of accelerated electrons, was observed in the 300–580 MHz frequency range (*Solar Geophysical Data*). As found by Kotrč *et al.* (1997), the accelerated electrons can be considered as a signature of the start of the eruptive processes.

The magnetic field in the active region just before the event was very complex, with intruding magnetic islands of opposite polarity (Kitt Peak magnetic field map). The eruption of the prominence in the Hα line was observed at Ondřejov Observatory from 14:28:48 UT until 15:00:03 UT. Two typical images from this observing sequence obtained at 14:29:56 UT and 14:36:39 UT are shown in Figure 1. In the time interval 14:32–14:40 UT the *Solar Geophysical Data* reports on a small subflare taking place in the same active region (N21 E73) as the observed prominence.

To assure a correct interpretation of the processed images, we tested our observing system. Figure 2 shows the two-dimensional Fourier-transform logarithmic power spectrum of the Hα prominence image obtained at 14:29:56 UT. It gives general information about the image formation during the prominence observation. In the inverse-gray-scale log power spectrum it is evident that there is a well-defined small central figure corresponding to the formation of the prominence. The origin of the frequency domain is shifted to the center of image. The central cross of high values of the spectrum in the axes is a typical result of scanning the image

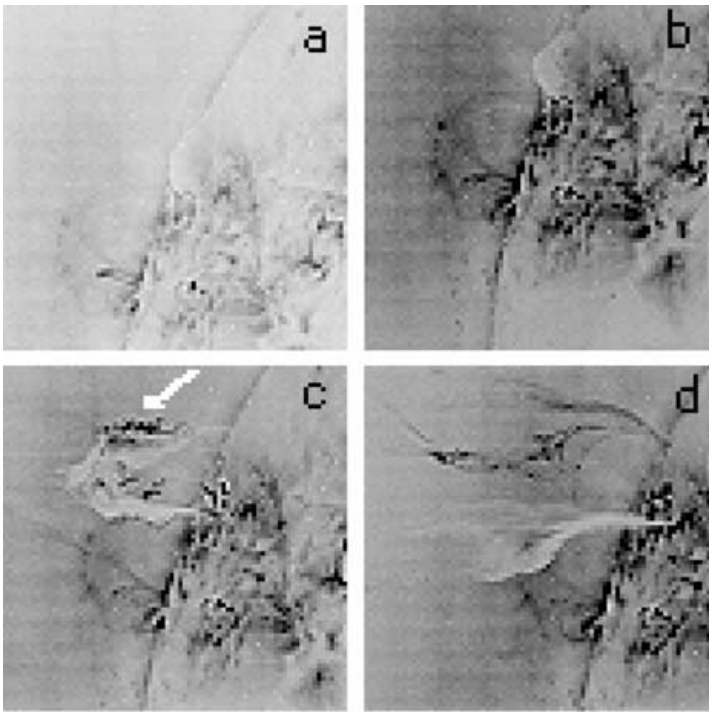

Figure 3. The eruptive prominence as seen by EIT in the Fe XII 195 Å line at (a) 14:03:11, (b) 14:13:18, (c) 14:23:30, and (d) 14:36:10 UT. The images have been sharpened by a Laplacian operator (DF method) 5×5 pixels. The arrow indicates the structure whose position has been plotted into the processed Hα image (see Figure 9). The image is visualized as a negative of the original so the Hα structure is light and the hot structures are dark.

into rows. The relative values of the scale axes represent signal/sample frequency ratio. The peaks in the log power spectrum correspond to periodic structures in the original image. Close to the left and right sides of the image there are two vertical lines corresponding to noise with one typical frequency. It has been found that this noise is caused by the camera.

For the studied time period, four EIT images taken in Fe XII line 195 Å (formation temperature $\simeq$ 1.6 MK) at 14:03:11, 14:13:18, 14:23:30, and 14:36:10 UT are available. We also used three SXT images taken at 14:16:55, 14:21:11, and 14:25:27 UT in the AlMg filter (temperature exceeding $\sim$ 1 MK (Tsuneta *et al.*, 1991)). At the times after 14:50 UT, the LASCO C2 coronagraph observed a coronal mass ejection propagating in the north-east direction from the Sun. The time series of Hα images does not cover the very beginning of the event. The early stages of the prominence eruption are captured in the EIT images taken at 14:13:18 and 14:23:30 UT (compare Figures 3(a–c). The images in Figure 3 are sharpened by the Laplacian operator (DF method with 5×5 mask). The estimated velocity of the EIT filament is 150 km s^{-1}.

It was found that the part of the EIT filament seen in absorption (see the light structure Figures 3(c) and 3(d)) is in good positional agreement with the Hα one (see also Plunkett *et al.*, 2000). Therefore, the evolution of this EIT structure

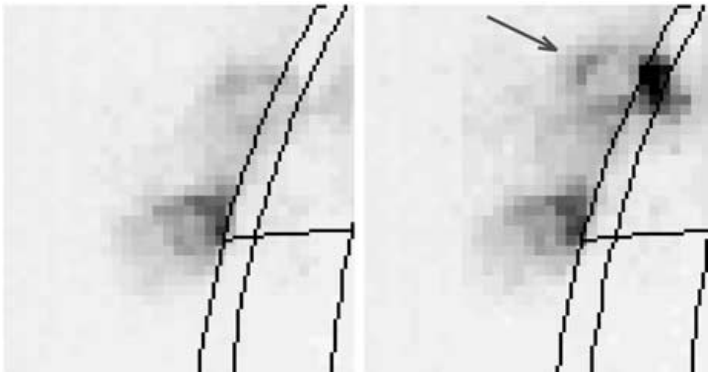

Figure 4. SXT images (raw data) of the region corresponding to the origin of the eruptive prominence at times 14:16:55 (*left*) and 14:25:27 UT (*right*) in the AlMg filter. The arrow in the right image indicates the 'bright' top of the hot SXR loop whose position corresponds to the lower local intensity minimum found in the processed Hα image (see Figure 9).

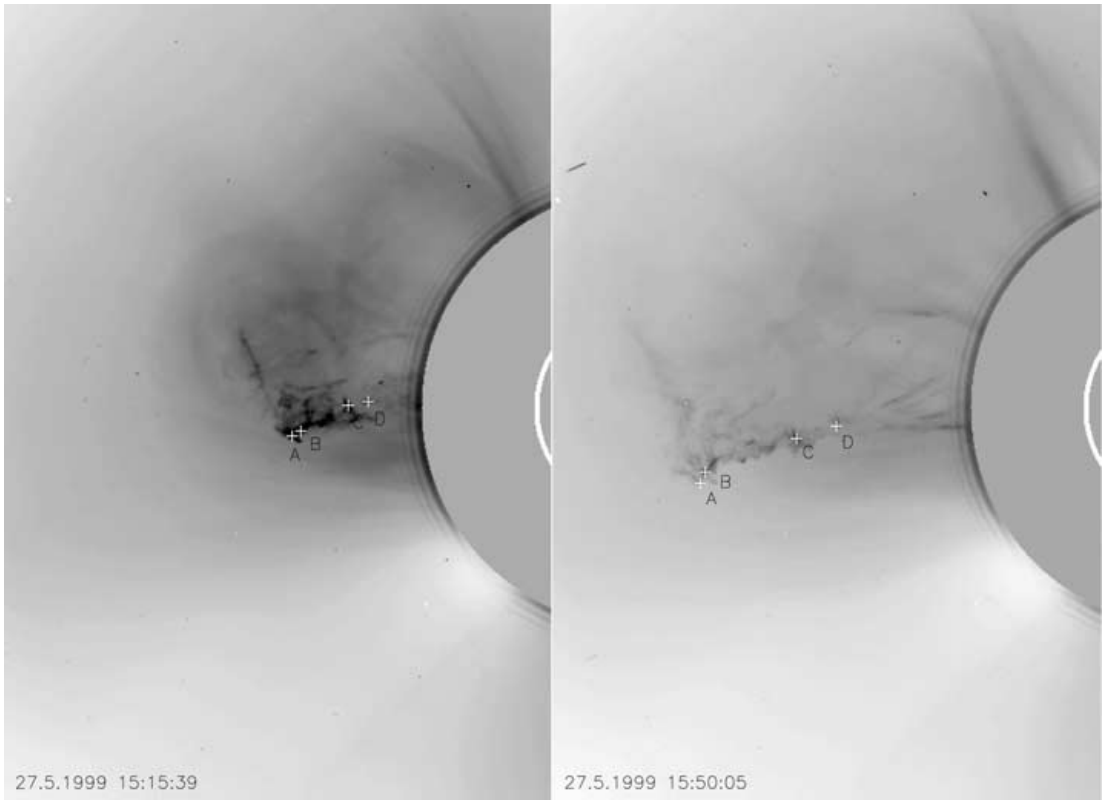

Figure 5. The prominence in the LASCO C2 coronagraph. The 'blobs' signed A, B, C, and D have been used as tracers to follow the expansion of the prominence (see Figure 6). The image has not been processed.

can be directly compared with the Hα EP (compare the Hα and EIT images at 14:36:39 UT – Figure 1 and 14:36:10 UT – Figure 3(d)). The image obtained by SXT at 14:16:55 UT does not show any significant emission at the position of the prominence. Later, however, a soft X-ray brightening appears in the bottom part of the filament and it is visible in the SXT image taken at 14:25:27 UT (compare left and right panel of Figure 4).

As seen in Figure 1 (upper part) and Figure 3(c) the expansion of the prominence is asymmetric and its northern leg becomes much broader (Figure 1 upper panel) than the southern leg. Because the β parameter of the prominence plasma is assumed to be much lower than 1 and the plasma is highly conductive, the same behavior applies to the magnetic field. Moreover, in the upper part of the northern leg the hot structure appears (Figure 3(c), the dark arrowed structure). This fact is in agreement with the disappearance of this part of the prominence in the Hα images (showing plasma with the temperature up to 20 000 K only, Figure 1). Therefore, we think that the processes of the prominence eruption started at the northern leg. Simultaneously, the cold Hα prominence material of the southern leg is rapidly moving upwards (compare Figure 1 upper and lower panels). The estimated velocity of the leading edge of the EP is about 520 km s^{-1}.

The EP was observed later by the LASCO C2 coronagraph as part of a CME (Figure 5). For four 'blobs' (A–D in Figure 5) chosen in the ejected structure of the prominence the heights and radial velocities were measured. The results (early EIT growing loop, Hα expansion, LASCO C2 structures) are summarized in Figure 6. The radial velocity of the LASCO C2 structures corresponding to the prominence reaches its maximum $\simeq$ 530 km s^{-1} at the leading edge of the prominence (tracer A) and gradually decreases with the decreasing distance of tracers from the solar limb (blobs B, C, and D in Figure 6). In our height/velocity measurements we can identify three velocity regimes. Relatively slow growth of the prominence from the onset of the event at ∼14:13 UT till ∼14:26 UT, when a phase of rapid and relatively short acceleration starts. This acceleration phase is followed by the rapid expansion of the structure at an approximately constant velocity.

4. Two Holes in the Hα Eruptive Prominence and Corresponding Hot EIT and SXT Structures

To find more details about the fine structure of the Hα EP, the two image-analysis techniques LOD and ST, as described in Section 2, were applied to the Hα prominence images. In Figure 7, the result of the LOD method is presented showing two considered times 14:29:56 and 14:29:58 UT. Two 'holes' of low emission, one at the bottom part of the EP close to the northern leg and the second above the prominence leg were 'visualized' (see arrows). The reality of these two local intensity minima, which were indistinguishable in the original images, was confirmed by the second image-processing technique ST (Figure 8).

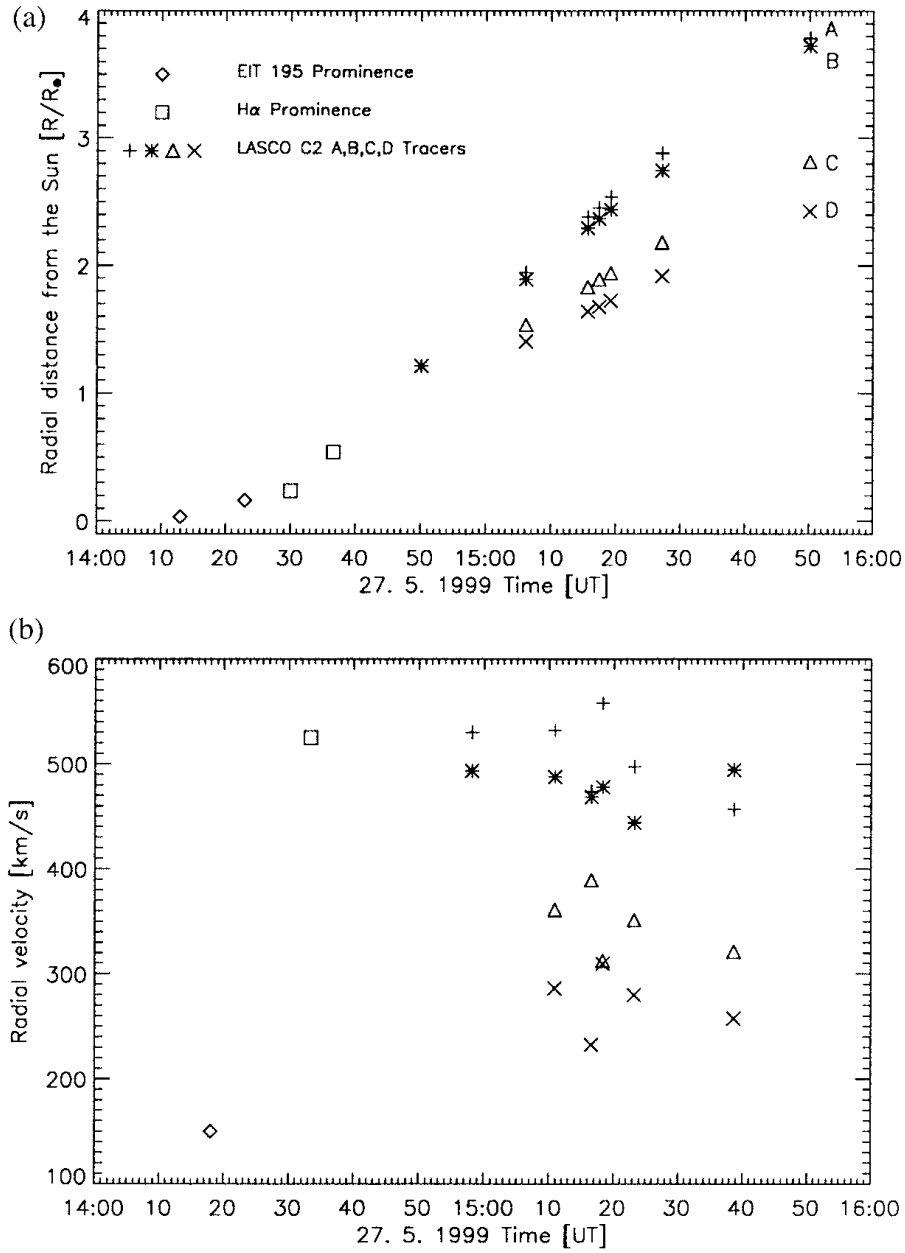

Figure 6. (a) Height vs time plot showing the radial distances of the leading edge of the EIT and Hα prominence and of the LASCO C2 'blobs' (see Figure 5) during the expansion of the eruptive prominence. (b) The corresponding radial velocities.

We compared the processed Hα images with the EIT and SXT observations and looked for the features in the EIT and SXT images which could correspond to the positions of the local intensity minima (holes). We found that the position of the upper and lower local minimum coincides with the EIT and SXT loop structures, respectively (see Figures 7 and 9). Considering the time differences of observations and slow motions in the bottom part of EP at this prominence evolution phase, the precision of the SXT hot loop localization relative to the Hα EP (in the vertical

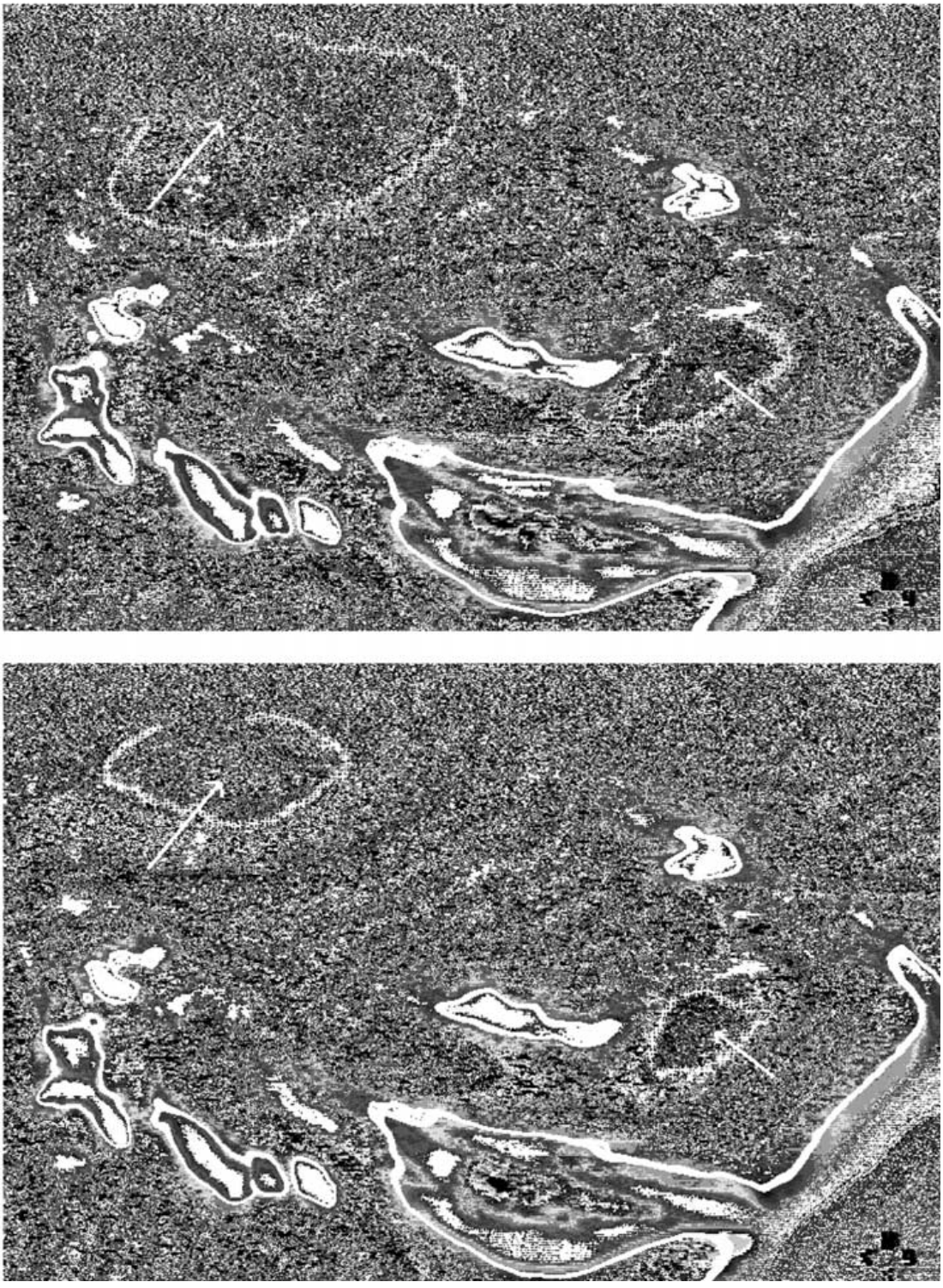

Figure 7. Processed Hα image of the eruptive prominence (LOD method, circular shape of the sub-image with a radius $R = 40$ pixels, thresholded into 36 levels) at 14:29:56 UT, and at 14:29:58 UT. The areas with local intensity minima (holes) are marked by *white arrows*. The original Hα features are outlined by *white stripes*.

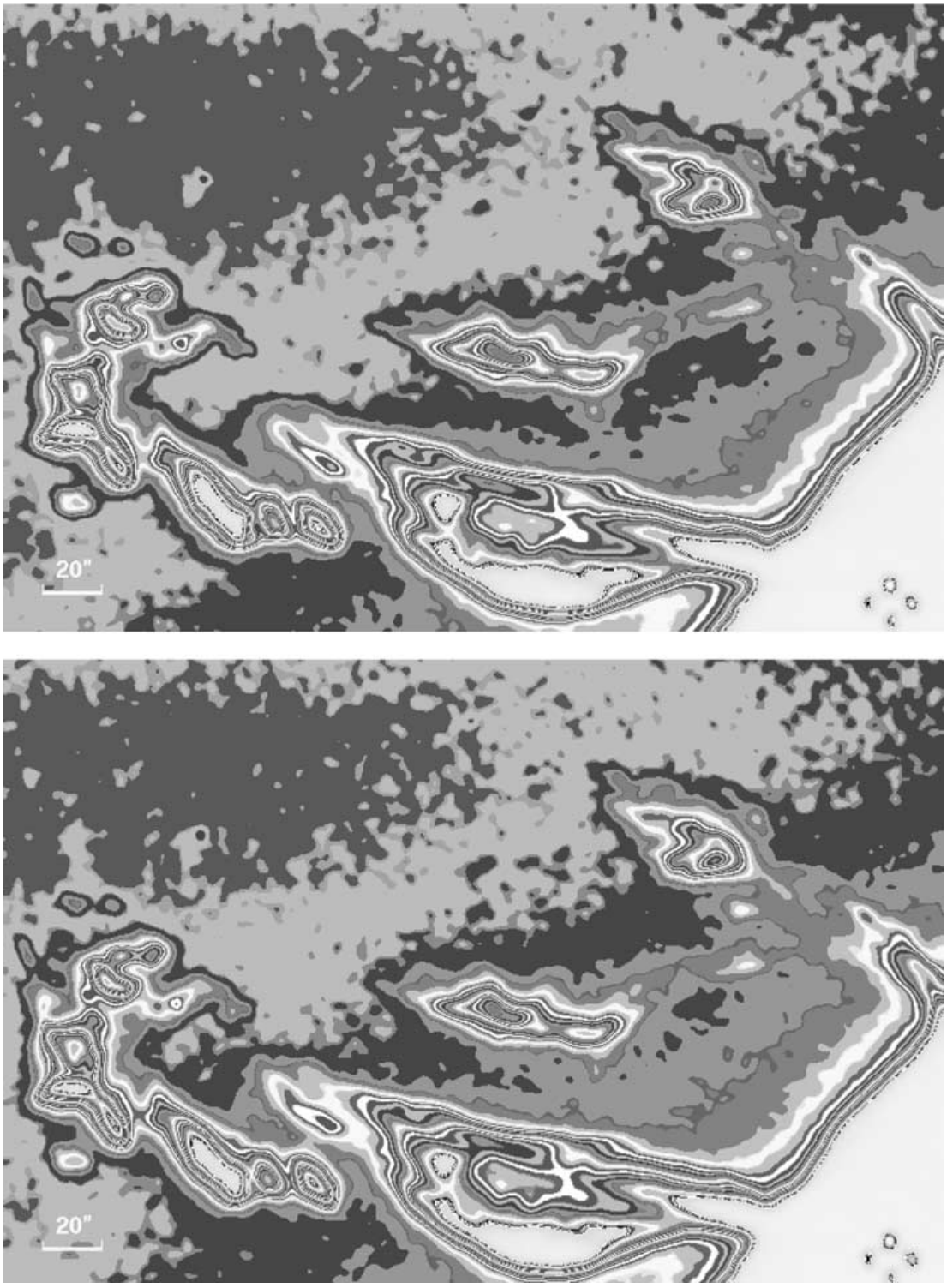

Figure 8. Processed Hα image of the eruptive prominence (smoothing by a large convolution Gauss mask (ST method) of 15 $\times$ 15 pixels, $\sigma = 2.56$, and segmentation into 30 density levels) at 14:29:56 UT, and at 14:29:58 UT. The holes are localized in the areas marked in Figure 7.

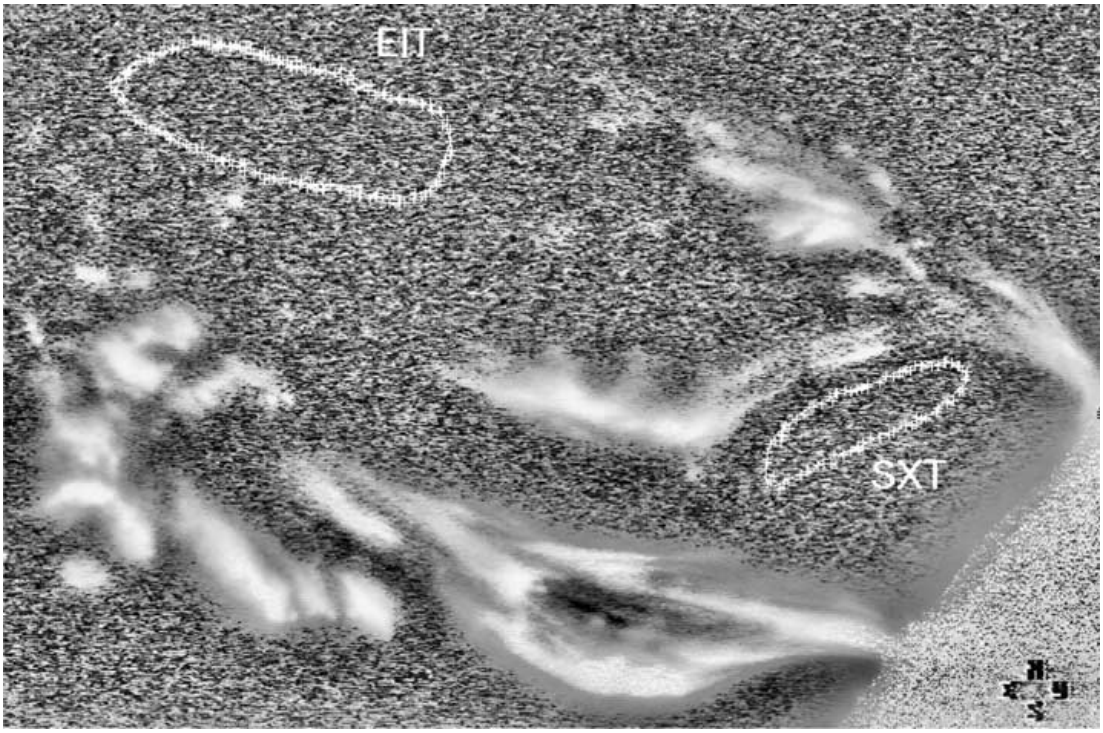

Figure 9. Processed Hα image of the eruptive prominence (LOD method, circular shape of the sub-image with a radius $R = 40$) at 14:29:56 UT. The position of the SXT hot loop observed at 14:25:27 UT, and the structure seen by EIT at 14:23:30 UT are indicated.

direction) is less than 10". The radial velocity increases with height, thus the precision of the relative localization of the EIT loop is lower, but better than 20". The precision in the azimuthal direction, due to low azimuthal velocities, is much better.

The possible uncertainty in the mutual positions of the hot and cold structures qualitatively does not change the results.

5. Discussion and Conclusions

Using the special image-processing techniques mentioned above, two local intensity minima in the Hα EP images were visualized. The lower one appears close to the northern leg at the position where the hot loop observed by SXT was recognized. Although we cannot exclude projection effects, it seems that due to the higher temperature and the probably lower density, the hot SXT loop appears transparent in the Hα images, thus forming the local intensity minimum (hole) in the cold (less than 2×10^4 K) prominence structure. Just the presence of hot structures ($T > 1$ MK) inside the cold prominence material is important from the interpretational point of view. Namely, hot structures indicate active processes as, e.g., plasma heating, release of the energy accumulated in the magnetic field, magnetic field changes and reconnection. The topology at the bottom part of the studied EP is similar to that observed on 18 September 1995 EP (Kotrč *et al.*,

1998). There, similarly, as in the present case, the hot loop was lying below the cold Hα prominence structure. The Doppler velocity pattern indicated a bi-directional plasma motion in the space between the hot and cold interacting loops. In the present case, we accept the same schema and therefore the magnetic reconnection processes are expected at the contact surface between the hot SXT loop (lower local intensity minimum) and the overlying cold Hα prominence structure.

On the other hand, in the upper local minimum of the Hα images the EIT hot structure was localized. In agreement with recent observations of the concave-outwards features (magnetic ropes) (Plunkett *et al.*, 2000, Figure 5) and theoretical expectations (Chen, 1996) we interpret the Hα minimum and corresponding EIT feature as signatures of a huge hot coronal loop spanning the Hα prominence. It is also reminiscent of the geometry which was reported by Ohyama and Shibata (1998) for an X-ray plasma ejection.

Combining the results of 18 September 1995 (Kotrč *et al.*, 1998) and 2 June 1998 (Plunkett *et al.*, 2000) with the present EP it seems that two types of hot loops appear in the EP structure: low-lying hot loops below the Hα prominence and wide-spanning ones located above this prominence. The question arises, which role these hot loops or ropes play in the prominence eruption. Usually, two scenarios are considered: (a) the low hot loop corresponds to a newly emerging magnetic field flux, which interacts with the pre-existing magnetic field structure of the prominence and thus triggers the prominence eruption, or (b) the large magnetic flux rope spanning the prominence is destabilized and starts to move upwards; the low-lying loop is formed and heated due to a driven magnetic field reconnection below the expanding prominence. In our case, first an upward motion of the upper parts of the prominence was observed and then with some time delay the soft X-ray brightening was detected at the bottom part of the prominence. Thus, the second possibility of the prominence eruption scenario looks to be more probable. Namely, in case (a), the opposite sequence of the processes is expected: first the X-ray brightening in the bottom part of the prominence appears due to the magnetic flux emergence and then the upward motion of the upper part of the prominence should be observed.

Acknowledgements

Authors thank the unknown referee for stimulating comments which helped to improve the paper. This work was supported by the Project of Bilateral Cooperation (Germany–Czech Republic) in Science and Technology under Grant TSR-012-98, by the Grant Agency of the Czech Republic (Grants No. 102/00/1711, 205/00/1726) and by the Grant Agency of the Academy of Sciences of the Czech Republic (Grants No. 3003003, S1003006) under the Key Project of the Astronomical Institute No. K2043105. We would like to thank T. Vaněk and M. Knížek for their assistance during the observations at Ondřejov. S. Šimberová is indebted to T.

Suk from the Institute of Information Theory and Automation, Czech Academy of Sciences, for a very stimulating discussion of image analysis in frequency space.

References

Acton, L. W., Bruner, M., Brown, W., Lemen, J., Hirayama, T., Tsuneta, S., Watanabe, T., and Ogawara, Y.: 1989, *Adv. Space Res.* **8**, 93.
Antiochos, S. K., DeVore, C. R., and Klimchuk, J. A.: 1999, *Astrophys. J.* **510**, 485.
Bruekner, G. E. and 14 co-authors: 1995, *Solar Phys.* **162**, 357.
Chen, J.: 1996, *J. Geophys. Res.* **101**, 27499.
Ciaravella, A., Raymond, J. C., Thompson, B. J., van Ballegooijen, A., Strachan, L., Li, J., Gardner, L., O'Neal, R., Antonucci, E., Kohl, J., and Noci, G.: 2000, *Astrophys. J.* **529**, 575.
Delaboudinière, J.-P. and 27 co-authors: 1995, *Solar Phys.* **162**, 291.
Dere, K. P., Brueckner, G. E., Howard, R. A., Michels, D. J., and Delaboudinière, J.-P.: 1999, *Astrophys. J.* **516**, 465.
Engvold, O. and Rustad, B. M.: 1974, *Solar Phys.* **35**, 409.
Engvold, O., Malville, J. M., and Rustad, B. M.: 1976, *Solar Phys.* **48**, 137.
Feynman, J. and Martin, S. F.: 1995, *J. Geophys. Res.* **100**, 3355.
Kotrč, P., Schmieder, B., Karlický, M., and Heinzel, P.: 1997, *Solar Phys.* **172**, 199.
Kotrč, P., Karlický, M., Šimberová, S., Knížek, M., and Varady, M.: 1998, *Solar Phys.* **182**, 393.
Moore, R. L.: 1988, *Astrophys. J.* **324**, 1132.
Ohyama, M. and Shibata K.: 1998, *Astrophys. J.* **499**, 1934.
Plunkett, S. P., Vourlidas, A., Šimberová, S., Karlický, M., Kotrč, P., Heinzel, P., Kupryakov, Yu. A., Guo, W. P., and Wu, S. T.: 2000, *Solar Phys.* **194**, 371.
Priest, E. R.: 1982, *Solar Magnetohydrodynamics*, D. Reidel Publ. Co., Dordrecht, Holland, p. 382.
Rompolt, B.: 1990, *Hvar Obs. Bull.* **14**, 37.
Rompolt, B. and Mzyk, S.: 1978, in E. Jensen, P. Maltby, and F. Q. Orrall (eds.), *Physics of Solar Prominences, Proc. Colloq. IAU* **44**, 242.
Russ, J. C.: 1995, *The Image Processing Handbook*, 2nd ed., CRC Press, Inc., New York.
Schmahl, E. and Hildner, E.: 1977, *Solar Phys.* **55**, 473.
Schmieder, B., van Driel-Gesztelyi, L., Wiik, J. K., Kucera, T., Thompson, B., De Forrest, C., Saint Cyr, C., and Simnett, G. M.: 1997, *Proc. of the Fifth SOHO Workshop*, ESA SP-404, p. 663.
Šimberová S. and Suk, T.: 1993, *Lecture Notes in Computer Science* **719**, Springer-Verlag, Berlin, p. 759.
Šimberová, S., Karlický, M., and Švestka, Z.: 1993, *Solar Phys.* **146**, 343.
Tandberg-Hanssen, E.: 1974, *Solar Prominences*, D. Reidel Publ. Co., Dordrecht, Holland.
Tsuneta, S., Acton, L., Bruner, M., Lemen, J., Brown, W., Caravalho, R., Catura, R., Freeland, S., Jurcevich, B., Morrison, M., Ogawara, Y., Hirayama, T., and Owens, J.: 1991, *Solar Phys.* **136**, 37.
Vršnak, B., Ruždjak, V., and Rompolt, B.: 1991, *Solar Phys.* **136**, 151.
Vršnak, B., Ruždjak, V., Brajša, R., and Džubur, A.: 1988, *Solar Phys.* **116**, 45.
Wang, Y. M. and Sheeley, N. R. Jr.: 1999, *Astrophys. J.* **510**, L157.
Wood, B. E., Karovska, M., Chen, J., Brueckner, G. E., Cook, J. W., and Howard, R. A.: 1999, *Astrophys. J.* **512**, 484.
Wu, S. T., Guo, W. P., and Dryer M.: 1997, *Solar Phys.* **170**, 265.